Numerical Simulations of Droplet Aerobreakup

Thesis by

Jomela C. Meng

In Partial Fulfillment of the Requirements

for the Degree of

Doctor of Philosophy

California Institute of Technology

Pasadena, California

2016

(Defended May 3, 2016)

For my parents who, by lifelong example, have taught me hard work, integrity, and faithfulness.

Without their unconditional love and relentless belief in me, I would not have made it.

Acknowledgments

The sage knows that life begins and ends in mystery. And he apprehends the end of genuine learning, which begins in the fear of God. That end is to know God and enjoy him forever.

Russell Kirk

This thesis would not have been possible without the encouragement, support, and counsel of many individuals. Coming alongside me at different junctures and for various stages in the journey, they have each, in their own way, left an indelible mark on my life.

I owe a debt of gratitude to my thesis advisor, Tim Colonius. Tim's direction and guidance over the past several years have taught me to think more critically, articulate more succinctly, and assert more confidently. His mastery of and intuition for fluid dynamics will always be the standard I aspire to. I am humbled by and profoundly grateful for the immeasurable investment he has made in my professional development.

My thesis committee — Joanna Austin, Guillaume Blanquart, and Joseph Shepherd — have my gratitude for serving in this capacity, and for the valuable feedback they provided on this thesis. In particular, I am indebted to Guillaume for his insightful advice and input during countless research discussions throughout the course of my graduate career. During my time at Caltech, I have had the privilege of being a Keck Institute for Space Studies graduate fellow, and would like to thank KISS for funding my first year, and sponsoring numerous events and seminars where I had the opportunity to interact with industry leaders. All things KISS would not be possible without the inimitable Michele Judd who has my sincere gratitude.

The monotony of graduate research would have been unbearable were it not for the past and

present members of the Computational Flow Physics group: Oliver Schmidt, Thierry Jardin, Georgios Rigas, Aswin Gnanaskandan, Vedran Coralic, Sebastian Liska, Matthew Inkman, Aaron Towne, Jeesoon Choi, Hsieh-Chen Tsai, Ed Burns, Andres Goza, Jay Qi, Kazuki Maeda, Phillipe Tosi, and André Fernando de Castro da Silva. It was a pleasure to work with and learn from each of them, and I am grateful for their comradery.

I would be remiss to not acknowledge my friends and peers in the GALCIT incoming class of 2009, without whom I would not have survived my first year. I am especially indebted to Phares Carroll, Stephanie Coronel, Ignacio Maqueda, and Siddhartha Verma for their friendships and many treasured memories.

Finally, I am forever indebted to my family and friends, both here in the U.S. and in Taiwan. Truly, there are no words to adequately thank these people who have cheered, prayed, and willed me through this doctorate. I am overwhelmed and humbled by their love. And while it is my name that appears on the cover, this thesis ultimately belongs to my family — *we* did it.

This work was supported by NIH Grant 2P01-DK043881 and by a gift to the Institute from Energent Corporation.

Soli Deo gloria.

Abstract

The work presented in this thesis aims to bridge an existing gap in the state of droplet aerobreakup knowledge associated with the fundamental flow physics that govern the experimentally observable droplet morphologies. Using direct numerical simulations of the aerobreakup of water cylinders and droplets in the flow behind shock waves in air, we investigate the behavior of the surrounding gas flow to gain insight into the droplet's deformation and evolution in the stripping breakup regime. The compressible multicomponent Navier-Stokes equations are solved using the Multicomponent Flow Code — a high-order accurate structured finite-volume flow solver with shock- and interface-capturing. Following qualitative descriptions of the aerobreakup process, comparisons are made with available experimental data. In 2D, accurate measurements of the cylinder's center-of-mass acceleration across a range of incident shock Mach numbers allow characterization of the unsteady drag coefficient. Additionally, mass loss measurements from viscous simulations refute a well-known boundary layer stripping theory. The results of a 3D nonaxisymmetric aerobreakup simulation are presented with an emphasis on describing the intricate flow phenomena observable in the wake region. Subsequent analyses of the surface instabilities and a Fourier decomposition of the flow field reveal asymmetrical azimuthal modulations and broadband instability growth that result in the devolution of the wake region into chaotic flow.

Published Content

Journal articles

J. C. Meng and T. Colonius. Numerical simulations of the early stages of high-speed droplet breakup. *Shock Waves*, 25(4):399–414, July 2015. doi: 10.1007/s00193-014-0546-z

Conference proceedings

J. C. Meng and T. Colonius. Droplet breakup in high-speed gas flows. In *Proc. 8th Int. Conf. on Multiphase Flow*, number 488, Jeju, Korea, May 2013

J. C. Meng and T. Colonius. The effects of shock strength on droplet breakup. In R. Bonazza, editor, *Proc. 29th Int. Symposium on Shock Waves*, number 000311, Madison, WI, July 2013

Contents

List of Figures

List of Tables

Nomenclature

Greek letters

α	Volume fraction
Γ	Stiffened gas EOS fitting parameter function
γ	Specific heat ratio or stiffened gas EOS fitting parameter
$\Delta\theta$	Cell width in the azimuthal coordinate
Δr	Cell width in the radial coordinate
Δt	Time step size
Δx	Cell width in the x-coordinate
Δy	Cell width in the y-coordinate
Δz	Cell width in the z-coordinate or axial coordinate
δ	Boundary layer thickness
ϵ	Interface sharpening parameter or machine epsilon
ε	Specific internal energy
η	PLIC plane constant
$\hat{\boldsymbol{\theta}}$	Unit vector in the azimuthal coordinate
θ	Azimuthal coordinate
κ	Kinetic energy or surface curvature
Λ	Wavelength of fastest growing wave
λ	Wavelength
μ	Dynamic viscosity

μ_v	Bulk viscosity
ν	Kinematic viscosity
Π_∞	Stiffened gas EOS fitting parameter function
π_∞	Stiffened gas EOS fitting parameter
ϖ	Wave group velocity
ρ	Density
σ	Surface tension coefficient
ϕ	Flux limiter function
φ	Polar coordinate or numerical schlieren function
χ	Ratio of consecutive gradients of the volume fraction
ψ	Color function
$\boldsymbol{\omega}$	Vorticity vector
Ω	Computational domain
ω	Vorticity component or wave growth rate

Roman letters

A	Area
$\mathbf{a}$	Acceleration vector
$\mathcal{A}$	Amplitude
c	Sound speed
$\mathcal{C}$	CFL number
C_D	Drag coefficient
D	Diameter
$\mathbf{D}$	Deformation rate tensor
$\mathcal{D}$	Diffusion number/coefficient
E	Total energy
$\mathcal{E}$	Mixture total energy
$\mathbf{f}$	Flux vector in the x-coordinate or axial coordinate

$\mathcal{F}$	PLIC function
F_D	Drag force
$\mathbf{g}$	Flux vector in the y-coordinate or radial coordinate
h	Length of PLIC parallelepiped side
$\mathbf{h}$	Flux vector in the z-coordinate or azimuthal coordinate
$\hat{\boldsymbol{\imath}}$	Unit vector in the x-coordinate
$\mathbf{I}$	Identity matrix
$\hat{\boldsymbol{\jmath}}$	Unit vector in the y-coordinate
K	Wavenumber of fastest growing wave
k	Wavenumber
$\hat{\mathbf{k}}$	Unit vector in the z-coordinate
L	Length or norm
$\mathcal{L}$	Interface-locating function
M	Mach number
m	Mass or azimuthal Fourier mode
$\mathbf{m}$	Liquid volume fraction gradient
N	Number of dimensions/cells/fluids
$\mathbf{n}$	Normal vector
N_m	Number of modes retained by azimuthal spectral filter
$\mathcal{O}$	Order of
Oh	Ohnesorge number
p	Pressure
$\mathbf{p}$	Momentum vector
$\mathbf{q}$	Conservative variables vector
R	Radius
r	Radial coordinate
$\hat{\mathbf{r}}$	Unit vector in the radial coordinate

$\mathcal{R}$	Regularization term
Re	Reynolds number
S	Reference/planform/frontal area
s	Wave speed
$\mathbf{s}$	Source term vector
St	Strouhal number
T	Period
t	Time
$\mathbf{T}_\mu$	Viscous stress tensor
$\mathbf{T}_\sigma$	Capillary stress tensor
u	Velocity in x-coordinate or velocity component in cylindrical coordinates
$\mathbf{u}$	Velocity vector
$\mathcal{U}_0$	Characteristic regularization rate
V	Volume
v	Velocity in y-coordinate
W	Relative velocity between the two phases
w	Velocity in z-coordinate
We	Weber number
x	x-coordinate
$\mathbf{x}$	Position vector
y	y-coordinate
z	z-coordinate or axial coordinate
$\hat{\mathbf{z}}$	Unit vector in the axial coordinate

Subscripts

Q_0	Initial value
Q_∞	Far-field property
Q_Ω	Value integrated over computational domain

$Q_{\parallel}$	Value associated with KH instability
$Q_{\perp}$	Value associated with RT instability
Q_{θ}	Azimuthal component
Q_c	Liquid center-of-mass property
Q_d	Deformed droplet property
Q_g	Gas property
Q_I	Interface property
Q_i	Index in the x-coordinate or axial coordinate
Q_j	Index in the y-coordinate or radial coordinate
Q_k	Index in the z-coordinate or azimuthal coordinate
Q_l	Liquid property
Q_o	Forward stagnation point property
Q_r	Radial component
Q_s	Shock or post-shock property
Q_z	Axial component
Q_{proj}	Projected value
$Q_{\max}$	Maximum value
$Q_{\min}$	Minimum value
Q_{br}	Breakup value
Q_{cr}	Critical value

Superscripts

$\hat{Q}$	Unit vector or Fourier transform
$\tilde{Q}$	Redefined coordinate
Q^*	Dimensionless variable
Q^a	Advective flux
Q^d	Diffusive flux
Q^{HI}	High-order flux

Q^{LO}	Low-order flux
Q^{RS}	Riemann solver intercell value
Q^{TVD}	Limited flux

Abbreviations and acronyms

1D	One-dimensional
2D	Two-dimensional
3D	Three-dimensional
AMR	Adaptive mesh refinement
BC	Boundary condition
CFL	Courant-Friedrichs-Lewy
DNS	Direct numerical simulation
EOS	Equation of state
HLLC	Harten-Lax-van Leer-contact
IC	Initial condition
IVP	Initial value problem
KH	Kelvin-Helmholtz
LHS	Left-hand side
MFC	Multicomponent flow code
NRBC	Nonreflective boundary condition
NTP	Normal temperature and pressure
PLIC	Piecewise linear interface calculation
RBC	Reflective boundary condition
RHS	Right-hand side
RMS	Root-mean-square
RT	Rayleigh-Taylor
RTP	Rayleigh-Taylor piercing
SIE	Shear-induced entrainment

TVD	Total variation diminishing
VOF	Volume of fluid
WENO	Weighted essentially nonoscillatory

Chapter 1

Introduction

1.1 Motivation

The study of droplet aerobreakup has historically been motivated by three applications: bulk dissemination of liquid agents, raindrop damage during supersonic flight, and secondary atomization of liquid jets in turbomachinery such as gas turbine and diesel engines. The experimental work of Taylor [86] investigating aerobreakup using an air blast gun, inaugurated the large body of work that has since been dedicated to this phenomenon. Not only did this pioneering work lay the foundation for the boundary layer stripping model of Ranger and Nicholls [69], but it also led to the Taylor analogy breakup model of O'Rourke and Amsden [64]. Taylor's experiments were quickly followed by other seminal works such as those from Engel [16], Hanson et al. [22], Lane [49], Ranger and Nicholls [69], and Simpkins and Bales [79]. The understanding of droplet aerobreakup as it applies to secondary atomization processes (generally used to refer to the breakup of an isolated droplet that arises after an initial disaggregation of the injected liquid jet or sheet) is driven by the desire to predict and control the final droplet size distribution. A detailed understanding of the physical mechanisms of the breakup process, and how they translate into final fragment sizes, is thus crucial to improving engineering design and efficiency. For example, in combustion applications, it is well known that secondary atomization of fuel droplets plays an important role in increasing surface area and enhancing heat and mass transfer between the fuel and ambient gas. However, contrary to intuition, the smallest drop sizes are not necessarily produced by the highest ambient gas velocities [20]. Therefore, an improved understanding of secondary atomization processes is imperative to ultimately predicting and controlling final droplet sizes. Accordingly, much of the aerobreakup literature has focused research efforts on characterizing and mapping various breakup regimes (e.g., [16, 22, 30, 49, 69]), calculating characteristic breakup times (e.g., [29, 69]), quantifying dependence on parameters such as density and viscosity ratios (e.g., [22, 90]), predicting final drop size distributions (e.g., [66, 69]), and quantifying unsteady drag properties (e.g., [16, 43, 79]). Unfortunately, these experimental and theoretical research efforts have resulted in many, and often conflicting, phenomenological models describing the aerobreakup process, and to date, a definitive understanding of aerobreakup remains elusive [46].

The simple setup of the aerobreakup problem belies the complexity of physical processes that intricately relate small length and time scales, unsteady compressible gas dynamics, interfacial dynamics, hydrodynamic instabilities, heat and mass transfer, and multiphase physics. Experimental studies of aerobreakup are hindered by the formidable challenge of achieving the necessary spatial and temporal resolutions, while comprehensive theoretical analyses are made almost impossible by the aforementioned list of interconnected physical phenomena. As an example of the significant challenge facing experimentalists, Theofanous [87] notes that "[f]or low-viscosity liquids, particle size and interfacial features with length scales of approximately tens of micrometers and velocities of a few hundred ms^{-1} are common . . . thus spatial resolutions of over 100 pixels per millimeter and exposure times of a few nanoseconds are basic requirements."

Only since the turn of the millenium has numerical simulation emerged as a valuable and capable tool for studying aerobreakup. Unfortunately, due to the high computational costs of fully three-dimensional (3D) simulations, numerical aerobreakup studies have often invoked two-dimensional (2D) (e.g., [10, 34–36]) or axisymmetric (e.g., [1, 21, 95]) approximations. Additionally, fluid density ratios are often assumed to be small, or the fluids are considered to be incompressible (e.g., [1, 21, 39, 67]).

The overarching goal for the present work, then, is to use direct numerical simulations (DNS) to elucidate the physical breakup mechanisms responsible for aerobreakup in the hopes that such knowledge and understanding can ultimately be exploited to improve secondary atomization models used in larger simulations of practical interest. The remainder of this chapter is organized as follows. A high-level review on the aerobreakup literature (interspersed with qualitative descriptions of the various aerobreakup regimes) is provided in Section 1.2, with a subsequent focus on interface instabilities that arise on the droplet surface (Section 1.2.1). In Section 1.3, the main contributions of this thesis and a comprehensive outline are provided.

1.2 Historical perspective

The nondimensional ratio of inertial (or aerodynamic) to capillary forces, known as the Weber number, We, has historically been the authoritative parameter governing aerobreakup of liquid droplets. Its emergence as the dominant parameter began with the theoretical work of Hinze [24], who found critical values of the Weber number, above which breakup would occur, for cases of a liquid globule exposed to air flows of constant speed and uniformly increasing speed. Hinze's analysis also accounted for viscous effects through the liquid Ohnesorge number, Oh, defined as the ratio of viscous to inertial and capillary forces. For strongly viscous liquids (large Oh), the critical Weber number, We_{cr}, was found to be $We_{cr} = 10$, while $We_{cr} = 6$ for weakly viscous liquids (small Oh). Since then, the Weber number has been the principal parameter used to delineate the various modes of aerobreakup. Traditionally, there exist five distinct regimes that are well established in the literature [20, 66]. They are, in order of increasing We, the vibrational, bag, bag-and-stamen, stripping, and catastrophic regimes.

At low Weber numbers (typically below We_{cr}), the vibrational breakup regime is sometimes observed (e.g., [97]). In this regime, the droplet develops small oscillations at its natural frequency. Under certain conditions, the surrounding gas flow interacts with the droplet so as to amplify these oscillations, which eventually causes the droplet to break into several large fragments. As the Weber number increases beyond We_{cr}, the bag breakup mode (shown in Fig. 1.1) is first observed. This breakup regime is characterized by a thin hollow bag, anchored to a toroidal rim, that is blown

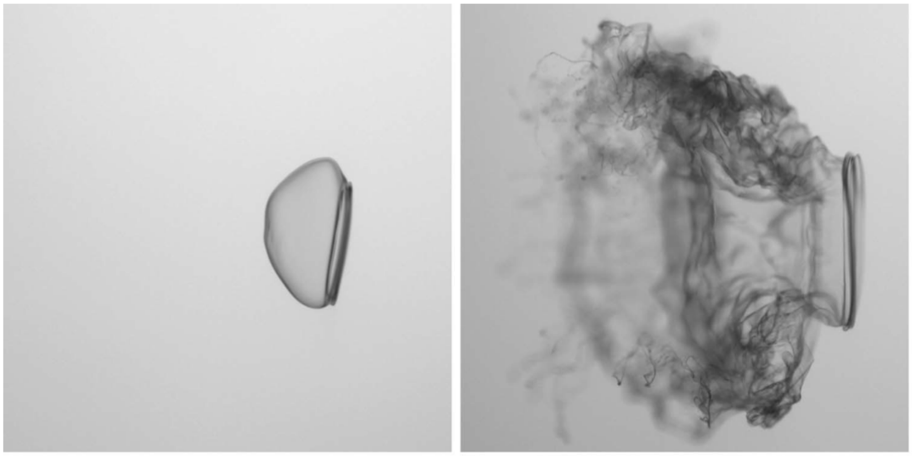

Figure 1.1: Bag breakup. Image reproduced from Fig. 4 of [90]. Flow is from right to left. Reprinted from Theofanous et al. [90] with the permission of AIP Publishing. © 2012 by the American Institute of Physics.

downstream. The bursting of the bag initiates the fragmentation process, and is followed shortly by the disintegration of the rim.

Bag breakup (at relatively low gas velocities) was experimentally observed by Lane [49] for drops falling through a vertical wind tunnel. At higher relative velocities (produced by injecting drops into the transient air flow from an air blast gun), the breakup mode transitioned into that of stripping-type breakup. The blast gun operated much like a conventional shock tube in that a compressed section was filled with gas to a desired pressure. A spike was then used to puncture a diaphragm, resulting in a blast of high-speed air. Lane [49] postulated that boundary layer instability was responsible for the stripping of material from the droplet periphery. Notably in these experiments, bag breakup was not observed in any of the blast gun cases. For a droplet of known size, critical velocities required for breakup were found, and the values corresponding to a sudden air blast were found to be smaller than those for steady wind tunnel flow. By measuring final droplet sizes, Lane [49] found that higher gas velocities resulted in smaller drops; however, for the highest (supersonic) velocity cases, the drop sizes were not as small as predictions from extrapolation of the steady air flow results. The earliest review of the aerobreakup literature was provided in a subsequent publication by Hinze [25]. Studying various types of globule deformation when subjected to different flow conditions, We_{cr} for breakup in an air stream was found to be appreciably smaller than that for

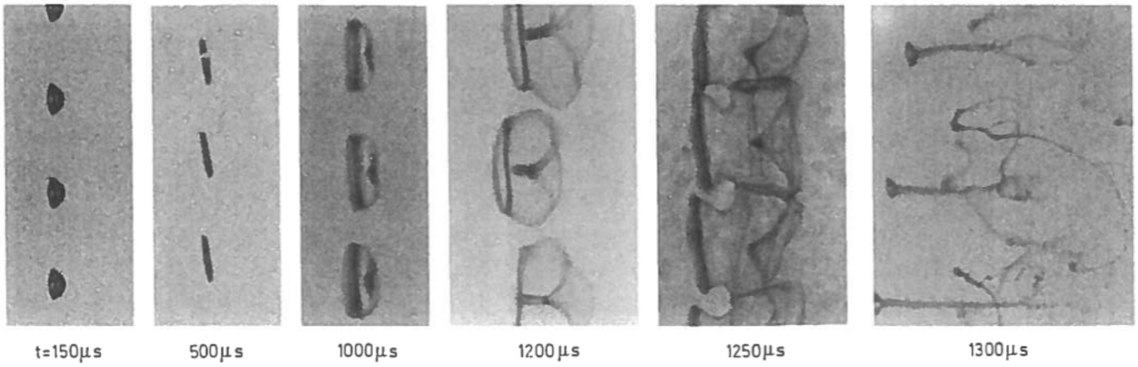

Figure 1.2: Bag-and-stamen breakup. Image reproduced from Fig. 7 of [26]. Flow is from left to right. Reprinted from Hirahara and Kawahashi [26] with the permission of Springer. © 1992 by Springer-Verlag.

viscous shear or turbulent flow. Additionally, the dependence of globule splitting on the Weber and Ohnesorge numbers was again confirmed.

Beginning with the work of Engel [16], several experimental shock tube investigations of aerobreakup were performed covering a wide range of flow and liquid conditions. Motivated by rain erosion damage on supersonic aircraft, Engel [16] visualized aerobreakup of mm-sized water droplets behind $M_s = 1.3, 1.5, 1.7$ shock waves. From the spark pictures taken, detailed stages of the fragmentation process were described. Expanding upon the experimental observations, Engel [16] included a comprehensive discussion of mist formation (see Section 1.2.1.1), radial water flow, drop flattening and drift, and drag coefficients using relatively simple analyses and theoretical considerations. The work of Hanson et al. [22] supplied new experimental data for droplets in the $10^2 < D_0 < 10^3\,\mu$m range using water, methyl alcohol, and viscous oil drops. Contrary to Lane [49] who did not observe bag breakup in transient flow, Hanson et al. [22] found that the bag breakup mode always occured in the transient velocity case except when the air velocity greatly exceeded the critical value. Hanson et al. [22] were also the first to observe the bag-and-stamen breakup regime. As its name suggests, the bag-and-stamen breakup mode (shown in Fig. 1.2) is similar to the bag regime in terms of the formation of a downstream-blown bag attached to a rim. The main difference is the additional formation of a liquid column (stamen) oriented parallel to the flow. Disintegration is again initiated by the bursting of the bag, which is followed by the fragmentation of the rim and stamen.

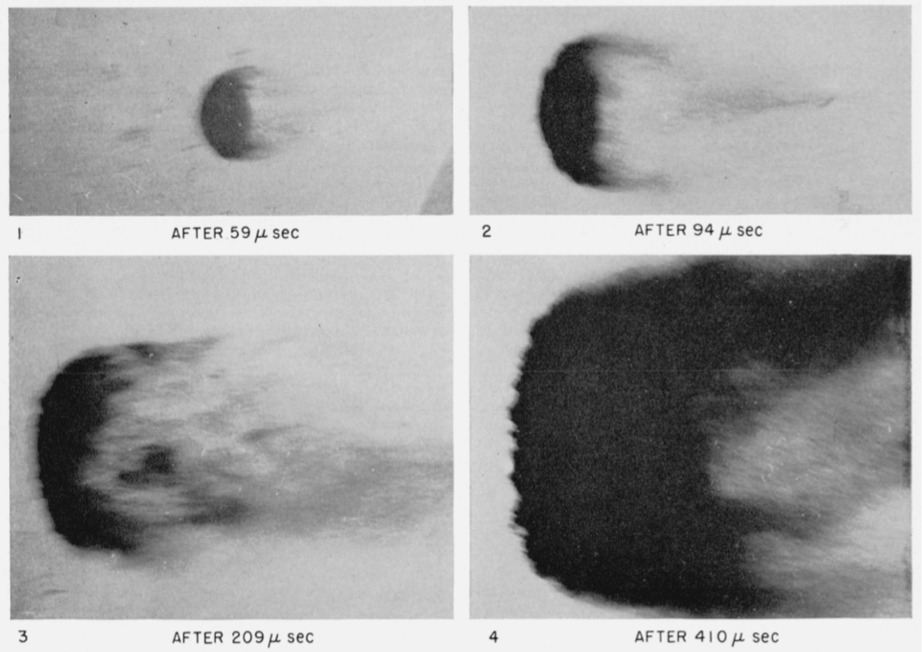

Figure 1.3: Stripping breakup. Image reproduced from Fig. 9 of [16]. Flow is from left to right. Reprinted from Engel [16] courtesy of the National Institute of Standards and Technology, U.S. Department of Commerce. Not copyrightable in the United States.

The stripping regime, experimentally observed in the blast gun cases of Lane [49] and of primary interest in this thesis, marks a transition in breakup physics that fundamentally differs from that of vibrational, bag, and bag-and-stamen breakup. Generally speaking, the stripping regime (shown in Fig. 1.3) is characterized by an initial deformation of the droplet into a disk-like shape. Following the shape change, droplet fluid is observed to be stripped from the droplet's periphery in a region near the droplet equator (defined as a polar, or inclination, angle of $\varphi = \frac{\pi}{2}$). Several mechanisms have been proposed for the stripping of material from the droplet periphery. The "boundary layer stripping" or "shear stripping" model was proposed by Ranger and Nicholls [69], who experimentally studied the aerobreakup of water droplets of diameters $D_0 = 750\text{–}4400\,\mu\text{m}$ in the flow behind shock waves with Mach numbers ranging between $M_s = 1.5\text{–}3.5$. Their work was intended to supplement and extend previous work to find drop-shattering rates and breakup times. As part of their analysis, Ranger and Nicholls [69] postulated that shear forces from the ambient flow result in the formation of boundary layers both inside and outside the drop. Assuming the drop remains spherical, the boundary layers become unstable at the droplet equator, and are subsequently stripped off by the ambient gas flow. A specific expression for mass loss rate based on this theory (see Section 5.4.2) was put forth, in addition to a characteristic breakup time that has become ubiquitous in the aerobreakup literature (see Section 2.3.4). An alternative stripping mechanism, known as "sheet thinning," was later proposed by Liu and Reitz [54]. In sheet thinning, the droplet is initially flattened by the pressure gradient between the drop's poles ($\varphi = 0, \pi$) and equator. Once flattened, the strong inertial drag forces from the surrounding flow draw a thin sheet of liquid off the periphery. This sheet is accelerated, stretched, and bent in the direction of flow, and eventually breaks up into streamwise ligaments that fragment into individual drops. Due to the flattened disk-like shape of the deformed droplet, flow separation occurs for all practical values of the Reynolds number, Re, and the sheet thinning mechanism can be considered an inviscid phenomenon with no dependence on Re [20].

The importance of the sudden accelerations imparted to the droplet were first considered by Simpkins and Bales [79] who used the Bond number (nondimensional ratio of body to capillary forces) to characterize the transition from simple droplet distortion to that of deformation accompanied by exponentially-growing unstable surface waves. Given that the drag coefficient relates the Bond and Weber numbers, particular attention was given to establishing the drag coefficient of deforming droplets. For compressible flows, a mean drag coefficient value of $C_D = 2.5$ was found for large Reynolds numbers. From their analysis, Simpkins and Bales [79] offered support for the existence of a terminal regime beyond that of stripping breakup. "Eventually, the drop response is acceleration dominated and the unstable Taylor waves pierce the drop before it has sufficient time to distort" [79]. Known as the catastrophic breakup regime, this type of breakup had previously been observed by Reinecke and Waldman [70] who used strong $M_s = 3, 6, 11$ shocks applicable for atmospheric reentry conditions. At the largest Weber numbers, the classical catastrophic breakup regime predicts the existence of surface waves of large amplitude and long wavelength that eventually penetrate the droplet resulting in large fragments that subsequently break up (shown in Fig. 1.4). The existence of this terminal regime was primarily evidenced by various experimental shadowgraph visualizations (e.g., [43, 79]). It is unclear who and when first described the catastrophic breakup regime, but it

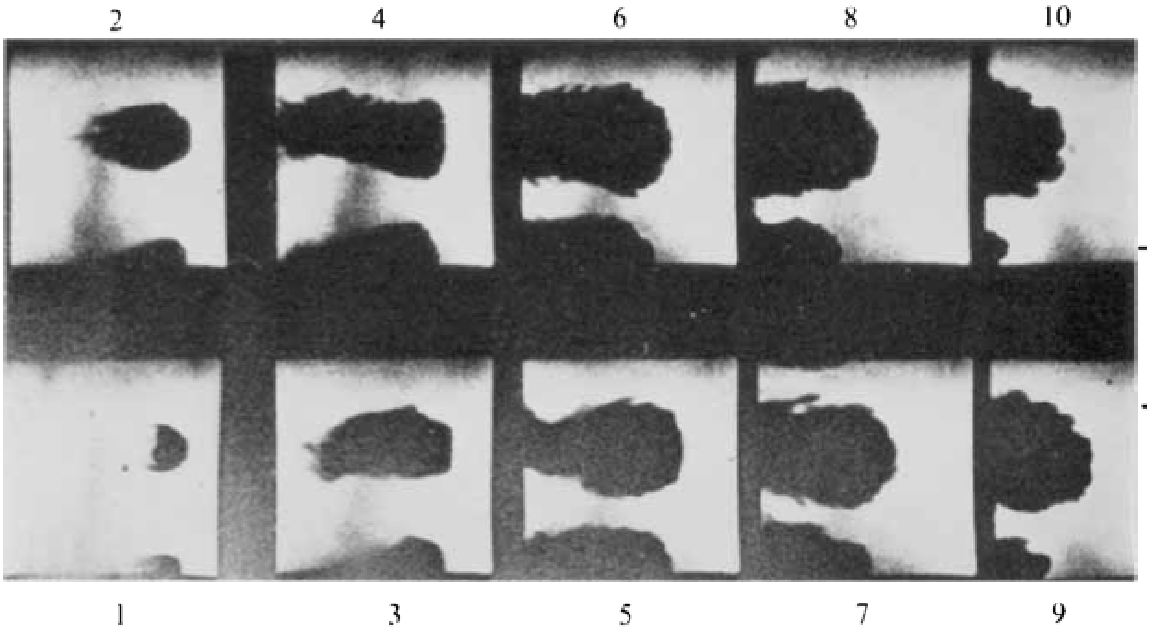

Figure 1.4: Catastrophic breakup. Image reproduced from Fig. 4a of [79]. Flow is from right to left. Reprinted from Simpkins and Bales [79] with the permission of Cambridge University Press. © 1972 by Cambridge University Press.

appears to have been widely accepted by the time Pilch and Erdman [66] published their review in 1987. Motivated by nuclear reactor safety issues, the review not only provided a defensible value for We_{cr}, but also included correlations for velocity histories, total breakup times, and drag coefficients. An improved maximum stable fragment diameter (as compared to the conventional estimate based solely on We_{cr}) was derived by accounting for drop fragment size reduction and decreasing relative velocities.

The combined experiments of Hsiang and Faeth [29, 30] spanned a large range of nondimensional parameters: $4 \times 10^{-3} < We < 10^3$, $6 \times 10^{-4} < Oh < 6 \times 10^2$, $3 \times 10^{-2} < Re < 16 \times 10^3$, and $1.15 < \dfrac{\rho_l}{\rho_g} < 12 \times 10^3$. For small Oh, increasing We was observed to result in breakup regimes transitioning through no deformation, nonoscillatory deformation, oscillatory deformation, bag, multimode, and shear. A particularly important transition from dome- to bowl-shaped drops, related to the transition from bag to stripping breakup, was correlated mainly in terms of We and Re [30]. The unsteady drag coefficient evolved from that of a sphere to a thin disk, and scaled primarily with drop deformation; it proved to be insensitive to We, Oh, Re, disturbance type, and density ratio. Finally, unlike drop sizes resulting from bag and multimode regime breakups, final droplet size distributions from stripping breakup were not able to be characterized by a Sauter mean diameter [29].

Recent work by Theofanous et al. [89] studying aerobreakup in rarefied supersonic flows, and subsequent publications [87, 88, 90], has substantially changed the overall understanding of aerobreakup. Instead of the five historically defined breakup regimes, Theofanous et al. [89] proposed a reclassification into two principal breakup regimes: Rayleigh-Taylor piercing (RTP) and shear-induced entrainment (SIE). The RTP regime encompasses the traditional bag and bag-and-stamen regimes for subsonic flows, while SIE is the corresponding mechanism to the shear stripping or sheet thinning models. Theofanous and Li [88] described SIE as a combination of shear-driven radial motion, which results in the flattening, as well as instabilities on the stretched liquid sheet. It thus shares common features with both shear stripping and sheet thinning models. Both SIE and sheet thinning attribute the generation of product droplets to instabilities arising on the accelerated, stretched liquid sheet, while SIE and shear stripping agree on the importance of shear forces (albeit differing on the exact role those shear forces play). Perhaps most importantly, this reclassification argues that the catastrophic breakup regime does not exist. Theofanous and Li [88] contended that limitations of the shadowgraphy visualization technique led to data misinterpretation. "[T]he 'wavy interface' on the frontal area of the drop (in front of the coherent liquid mass), as inferred from shadowgraphs in past work, is a mirage, an artifact created by the projected view of the rather complex flow field that develops with a significant radial component in three dimensions. There are no RT [Rayleigh-Taylor] waves piercing the drop ..." [88]. Using laser-induced fluorescence as their experimental visualization technique, SIE was proposed as the terminal regime for $We > 10^3$.

1.2.1 Instabilities in aerobreakup

The development of instabilities on the surface of a droplet undergoing aerobreakup is typically associated with breakup in the classical bag, stripping, and catastrophic breakup regimes. The actual manifestations of both the Rayleigh-Taylor (RT) and Kelvin-Helmholtz (KH) instabilities during aerobreakup are transient processes that are strongly influenced by the droplet deformation and associated changes in velocity and acceleration. Generally speaking, the region close to the forward stagnation point is subject to RT instability, which plays a key role in the classical bag and catastrophic breakup regimes. The KH instability, on the other hand, manifests in the region closer to the equator where the tangential velocity difference is significant.

1.2.1.1 Surface waves

One of the earliest works to consider surface instabilities was the experimental work of Engel [16], who explored the possibility of surface waves as a source of water mist. Using the theory of waves produced by wind under the effects of surface tension and gravity, comparison was made for the ratio of two wavelengths that are expected from theory and observed in experimental spark pictures. The expected wavelengths were found using

$$s_{\min}^2 = \frac{2\sqrt{(\rho_l - \rho_s)a\sigma}}{\rho_l + \rho_s}, \tag{1.1}$$

$$\lambda_{\min} = 2\pi\sqrt{\frac{\sigma}{a(\rho_l - \rho_s)}}, \tag{1.2}$$

$$\left(\frac{s}{s_{\min}}\right)^2 = \frac{1}{2}\left(\frac{\lambda}{\lambda_{\min}} + \frac{\lambda_{\min}}{\lambda}\right), \tag{1.3}$$

where s is the wave speed, λ is the wavelength, a is the droplet's acceleration, σ is the surface tension coefficient, and ρ_l, ρ_s are, respectively, the post-shock liquid and gas densities. Once $s_{\min}, \lambda_{\min}$ have been determined using experimental or simulation parameters, Eq. (1.3) is used to create a plot of s vs. λ. Since every value of $\left(\frac{s}{s_{\min}}\right)^2 > 1$ in Eq. (1.3) has two solutions of $\frac{\lambda}{\lambda_{\min}}$, the expected or theoretical wavelength ratio can be found given one of the wavelengths (e.g., the coarser wavelength measured from experimental visualizations). Engel's measurements showed fair agreement with the theory, and the breaking of these surface wave crests was partially credited with the observed mist generation.

1.2.1.2 Rayleigh-Taylor instability

The role of RT instability in the classical bag and catastrophic breakup regimes is evidenced by experimental observations of corrugations that appear on the windward faces of deforming droplets. For small $We > We_{cr}$, Joseph et al. [43] found that bag breakup occurred when the wavelength of the fastest growing RT wave, $\Lambda_\perp$, was on the order of the drop diameter. At high $We > 10^4$, RT instability has been proposed as the physical mechanism for catastrophic breakup since the "instability pumps fingers of hot air, heated by the passing shock wave, into the drop. The fingers inflate the drop like a balloon and at the same time bring hot air into contact with all interior parts of the drop. The drop can break explosively like a balloon ..." [43]. Joseph et al.'s analysis was based on two theories of RT instability: an exact viscous theory originally developed by Chandrasekhar [9], and an approximate theory based on viscous potential flow. The exact viscous theory [9] results in the dispersion relation

$$1 - \frac{ak_\perp}{\omega_\perp^2} = -\frac{k_\perp^3 \sigma}{\omega_\perp^2 \rho_l} - \frac{4k_\perp^2}{\omega_\perp}\nu_l + \frac{4k_\perp^3}{\omega_\perp^2}\nu_l^2 \left(\sqrt{k_\perp^2 + \frac{\omega_\perp}{\nu_l}} - k_\perp \right), \tag{1.4}$$

while the approximate viscous potential theory gives

$$1 = \frac{ak_\perp}{\omega_\perp^2} \frac{\rho_l - \rho_g}{\rho_l + \rho_g} - \frac{k_\perp^3 \sigma}{\omega_\perp^2 (\rho_l + \rho_g)} - \frac{2k_\perp^2}{\omega_\perp} \frac{\mu_l + \mu_g}{\rho_l + \rho_g}, \tag{1.5}$$

where k is the wavenumber, ω is the wave growth rate, σ is surface tension coefficient, and μ, ν are, respectively, the dynamic and kinematic viscosities. The subscripted "l, g" refer, respectively, to the liquid and gas phases, and the "$\perp$" subscript denotes association with the RT instability. Assuming that the most dangerous wave was the one with maximum growth rate, Joseph et al. [43] made comparisons between the theoretically predicted wavelengths and measurements made from experimental visualizations of aerobreakup behind $M_s = 2, 3$ shock waves.

The dispersion relation from the exact viscous theory, Eq. (1.4), was also later used by Theofanous et al. [89] who noted that "[w]hen the number of waves is small, we can see that the visual images support the predictions quantitatively. At higher Weber numbers, the quantitative measure in the images is lost, but the gradual transition to smaller and small mixing length scales, in agreement with prediction is unmistakenable[*sic*]. ...” The later review of Theofanous [87] used another RT dispersion relation derived from the work of Mikaelian [62]. Written here in an expanded form, the analysis for RT instability in a fluid of finite thickness results in the dispersion relation

$$\omega_\perp \left(\frac{\nu_l}{a^2}\right)^{\frac{1}{3}} = -k_\perp^2 \left(\frac{\nu^2}{a}\right)^{\frac{2}{3}} + \sqrt{-\frac{k_\perp \left(\frac{\nu^2}{a}\right)^{\frac{1}{3}} \left(\tanh(L_d k_\perp) k_\perp^2 \nu^2 \sigma \rho_l - k_\perp^3 \nu^2 \mu_l^2 - \tanh(L_d k_\perp) a \mu_l^2\right)}{a \mu_l^2}}, \tag{1.6}$$

where $\nu = \dfrac{\mu_l + \mu_g}{\rho_l + \rho_g}$ is the mixture kinematic viscosity, a is the drop acceleration, and L_d is the thickness of the deformed droplet. Equation (1.6) showed good agreement with available experimental results in the RTP regime. For large We, however, Theofanous and Li [88] did not observe the classical catastrophic breakup regime where “fingers of hot air” penetrated the drop and led to explosive breakup. Instead, they observed “a mirror-smooth, central area ... of rather significant lateral extent ... that persists, while an outwardly directed flow with a significant radial component, emanating from the periphery of this frontal region, gives rise to the drop mass redistribution into an elongated, relatively thin, highly fragmented structure. ... We [Theofanous and Li] conjecture that the key physics for the remarkably smooth, central region is the stability of the stagnation flow so created ...” [88]. Thus, as mentioned in Section 1.2, they argued against the existence of the classical catastrophic breakup regime.

1.2.1.3 Kelvin-Helmholtz instability

The KH instability, unlike RT instability, does not manifest across the entire upstream side of the deforming droplet. In fact, Joseph et al. [43] asserted that “since the tangential velocity is zero at the stagnation point and small near the stagnation point, the Kelvin-Helmholtz instability may not interact too strongly with the Rayleigh-Taylor instability.” Away from the forward pole, however, Theofanous and Li [88] experimentally observed initial corrugations of the KH instability in the region approaching the droplet’s equator. Though no comparisons were made between theory and experiment, it was proposed that the KH instability, along with other contributing factors such as turbulent mixing, partially controlled the mass loss rate during breakup [87]. More recently, the numerical work of Jalaal and Mehravaran [39] noted the development of KH waves generated at the droplet equator, which grew to form ligaments. It was also observed that at lower Weber numbers, surface tension seemed to damp the KH instability. In order to compare their numerical results with theory, Jalaal and Mehravaran [39] used various analytical dispersion relations to find the most unstable wave. We proceed by detailing the various theories used by Jalaal and Mehravaran [39]. In the following analysis, we reference the original works cited in [39], as we could not rederive the equations in Jalaal and Mehravaran [39].

We begin with the dispersion relation for the idealized KH problem assuming potential flow, and negligible vorticity layer thickness, droplet velocity, and gravity effects. The dispersion relation in the KH limit [9, 56] is given by

$$\omega_{\|} = k_{\|}\frac{\rho_l u_l + \rho_g u_g}{\rho_l + \rho_g} \pm i\frac{k_{\|}}{\rho_l + \rho_g}\sqrt{\rho_l\rho_g W^2 - (\rho_l + \rho_g)\sigma k_{\|}}, \tag{1.7}$$

where $W = |u_g - u_l|$ is the relative velocity between the phases, and the "$\|$" subscript denotes association with the KH instability. For negligible droplet velocity, $u_l \ll u_g$, and large density ratios, $\rho_g \ll \rho_l$, the wavenumber associated with the fastest growing wave, $K_{\|}$, and its group velocity, $\varpi_{\|}$, are

$$K_{\|} = \frac{2}{3}\frac{\rho_g u_g^2}{\sigma}, \qquad \varpi_{\|} = u_l + \frac{\rho_g}{\rho_l}u_g. \tag{1.8}$$

Relaxing the assumptions to allow for a nonzero vorticity layer, Marmottant and Villermaux [56] obtained a dispersion relation assuming linear boundary layer velocity profiles (see Fig. 1.5). Known as the Rayleigh limit, the dispersion relation [56] is given as

$$\exp(-2k_{\|}^*) = \left(1-2\left(\omega_{\|}^* + k_{\|}^*\frac{\zeta}{\zeta-1}\right)\right)\frac{1+(\xi+1)\left(\omega_{\|}^* + \frac{k_{\|}^*}{\zeta-1}\right) - \frac{{k^*}^3}{We_{\delta_g}}\left(\omega_{\|}^* + \frac{k_{\|}^*}{\zeta-1}\right)^{-1}}{1+(\xi-1)\left(\omega_{\|}^* + \frac{k_{\|}^*}{\zeta-1}\right) - \frac{{k^*}^3}{We_{\delta_g}}\left(\omega_{\|}^* + \frac{k_{\|}^*}{\zeta-1}\right)^{-1}}, \tag{1.9}$$

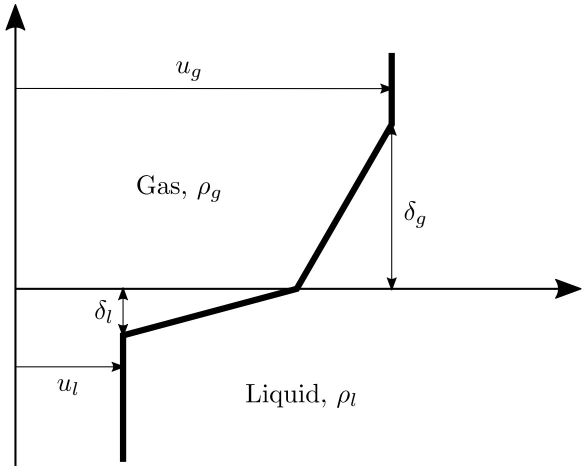

Figure 1.5: Linear velocity profiles used in the KH instability analysis. Adapted from Fig. 20 of [56].

where

$$k_\parallel^* = k_\parallel \delta_g, \qquad \omega_\parallel^* = \frac{\omega_\parallel \delta_g}{u_g - u_l}, \tag{1.10}$$

are, respectively, the nondimensionalized wavenumber and growth rate, δ is the boundary layer thickness,

$$\xi = \frac{\rho_l}{\rho_g}, \qquad \zeta = \frac{u_g}{u_l}, \tag{1.11}$$

are, respectively, the liquid-to-gas density ratio and the gas-to-liquid velocity ratio, and

$$We_{\delta_g} = \frac{\rho_g W^2 \delta_g}{\sigma}, \tag{1.12}$$

is the Weber number based on the gas boundary layer thickness, δ_g. From Kim et al. [47], the wavelength of the fastest growing wave from Eq. (1.9) is

$$\Lambda_\parallel = \frac{2\pi\delta_g}{0.8} f(\xi), \tag{1.13}$$

where

$$f(\xi) = \frac{5}{6} - \frac{1}{6\xi} + \frac{\sqrt{5 + 13\xi - 37\xi^2 + 27\xi^3}}{6\sqrt{2}\xi}. \tag{1.14}$$

From Eq. (1.13), we can easily derive

$$K_{\parallel} = \frac{2\pi}{\Lambda_{\parallel}} = \frac{4}{5}\frac{1}{f(\xi)\delta_g}. \tag{1.15}$$

Marmottant and Villermaux [56] also took Eq. (1.9) to the large We limit for a thick vorticity layer to obtain

$$\exp(-2k_{\parallel}^*) = \left(1 - (2\breve{\omega}_{\parallel}^* + k_{\parallel}^*)\right)\frac{1 + \frac{1}{2}(\xi+1)(2\breve{\omega}_{\parallel}^* - k_{\parallel}^*)}{1 + \frac{1}{2}(\xi-1)(2\breve{\omega}_{\parallel}^* - k_{\parallel}^*)}, \tag{1.16}$$

in the reference frame moving at the average velocity, $\frac{u_l + u_g}{2}$, where

$$\breve{\omega}_{\parallel}^* = \omega_{\parallel}^* - 2k_{\parallel}^*\frac{u_g + u_l}{u_g - u_l}, \tag{1.17}$$

and $k_{\parallel}^*, \omega_{\parallel}^*, \xi$ are defined as in Eqs. (1.10) and (1.11). For $u_l \ll u_g$, the most amplified wavenumber from Eq. (1.16) is

$$K_{\parallel} = \frac{3}{2}\frac{1}{\delta_g}\sqrt{\frac{\rho_g}{\rho_l}}. \tag{1.18}$$

The group velocities corresponding to both Eqs. (1.15) and (1.18) are well-approximated by a convection velocity [47, 56]

$$\varpi_{\parallel} = \frac{\sqrt{\rho_l}u_l + \sqrt{\rho_g}u_g}{\sqrt{\rho_l} + \sqrt{\rho_g}}. \tag{1.19}$$

1.2.1.4 Liquid sheet instabilities

As described in Section 1.2, the instability of the thin liquid sheet that is drawn from the droplet's periphery in the sheet thinning model or SIE, is thought to be responsible for the generation of product droplets. Theofanous and Li [88] simply commented that "the multimode interfacial instability on the stretched out yet accelerated sheet developing at the periphery" plays a critical role in SIE. On the other hand, Liu and Reitz [54] described two possible causes for the streamwise ligaments that are formed from the liquid sheet. The first explanation followed from a mass conservation argument: "[a]s the circular flattened edge of the drop is deflected in the direction of the air flow, the distance from its center to its edge periphery is reduced. Under this condition it also follows from mass conservation arguments that the production of folds on the sheet edge in the azimuthal direction is inevitable (e.g., consider a sheet of paper that is crumpled around a ball). . . . [T]he folding of the thin edged-sheet results in the production of the filaments . . . aligned with the flow of air" [54]. The second explanation was that the sheet broke up according to a "stretched streamwise ligament breakup" mechanism first described by Stapper and Samuelsen [82]. For low liquid flow rates of a planar liquid sheet sandwiched between two shear air layers, Stapper and Samuelsen [82] observed the formation and growth of streamwise vortical waves alternating with intermediate thin liquid membranes. The membranes burst first due to the rotation of the streamwise vortices, leaving streamwise ligaments that subsequently broke up.

An alternative mechanism for liquid sheet breakup as it applies to the sheet thinning model or SIE is given by Jalaal and Mehravaran [39], who attribute the breakup to the rise of RT instability waves. This physical mechanism of liquid sheet breakup is conceptually identical to that proposed by Marmottant and Villermaux [56] for breakup of a round liquid jet by coaxial flow of gas. In both scenarios, the KH instability generates axisymmetric waves at the liquid-gas interface. The transient acceleration of these wave crests or rims (in the case of the liquid jet) into the downstream air triggers a RT instability, which produces "transverse azimuthal modulations." Using the analysis of Chandrasekhar [9], the most amplified wavenumber is

$$K_{\perp} = \sqrt{\frac{a(\rho_l - \rho_g)}{3\sigma}}, \tag{1.20}$$

where a is the maximum acceleration of the primary KH wave expressed as

$$a = \mathcal{A}_{\|} \left(2\pi \frac{\varpi_{\|} - u_l}{\Lambda_{\|}} \right)^2, \tag{1.21}$$

and $\mathcal{A}_{\|}, \Lambda_{\|}, \varpi_{\|}$ are, respectively, the appropriate amplitude, wavelength, and group velocity. Kim et al. [47] found good agreement with this theory for their numerical simulations of the primary breakup of a round liquid jet in coaxial flow.

1.3 Contributions and outline

There exists a gap in the current state of droplet aerobreakup knowledge associated with the underlying fundamental flow physics that dictate the experimentally observed phenomena. Put differently, while the state of knowledge can, for example, predict the expected mode of breakup for any set of given flow and liquid conditions, and while it can describe the overall phenomenology associated with the predicted breakup mode, there is little to no knowledge of the fundamental fluid dynamics driving the observed deformation and subsequent droplet breakup. The research efforts considering surface instabilities described in Section 1.2.1 represent progress in this area, but much work has yet to be done. Even with advancements in experimental methods, it is difficult to visualize and quantify the behavior of the gas phase in aerobreakup experiments. Numerical simulations of these flows are thus a valuable means of probing these flow physics to obtain a more complete understanding of these phenomena. This thesis represents the start of an attempt to bridge this gap in the current state of aerobreakup knowledge. Herein, we build upon the computational efforts of Coralic and Colonius [13], and utilize a compressible multicomponent flow solver to numerically investigate this fundamental fluid dynamics problem.

The remainder of this thesis is organized as follows. The essential modeling and numerical methods are first laid out in Chapters 2 to 4. In Chapter 2, we describe the setup of the problem as it relates to previous experimental investigations. The governing equations and physical model for the compressible multicomponent Navier-Stokes equations are then presented, followed by an explanation of the utilized equation of state and applicable fluid mixture properties. The fundamentals of our numerical method are summarized in Chapter 3, beginning with an overview of the flow solver as developed by Coralic and Colonius [13]. We proceed to develop accurate numerical droplet diagnostics, suitable for computation of droplet center-of-mass properties and deformation metrics. This is followed by the documentation of two numerical method issues encountered in the flow solver. Several improvements made to the flow solver are described in Chapter 4. Namely, these developments include a model to capture capillary effects in the diffuse interface framework of our flow solver, the additional capability of fully 3D simulations in cylindrical coordinates, and various code stability improvements. With the simulation framework thus established, we proceed to present numerical results in Chapters 5 and 6. While 3D simulations of aerobreakup were always the ultimate objective of this thesis project, exploratory 2D simulations, documented in Chapter 5, were initially performed to discover what could be learned from the aerobreakup of water cylinders. Using the inviscid governing equations, numerical results from a parametric study varying the incident shock strength are compared with available experimental data. Characterizations of the droplet's unsteady acceleration and drag properties are also presented. Additionally, results from a series of viscous simulations are used for an estimation of numerical viscosity, and to quantitatively test the boundary layer stripping model of Ranger and Nicholls [69]. Using the newly implemented cylindrical coordinate system, we present in Chapter 6 the results of a fully 3D nonaxisymmetric simulation of droplet aerobreakup with compressible fluids of large density ratio. Following qualitative experimental comparisons, we give the first detailed description of stripping aerobreakup phenomena with an emphasis on the underlying flow physics. This description is further augmented with analyses of various observed surface instabilities. Our 3D numerical results not only contribute to the discussion of the terminal breakup regime (SIE vs. catastrophic), but also elucidate the instabilities associated with the liquid sheet that is drawn from the droplet periphery. Lastly, concluding remarks and suggestions for future work are made in Chapter 7.

Chapter 2

Physical model

2.1 Problem description

Historically speaking, the problem of aerobreakup has been studied experimentally using various apparatus such as shock tubes [6, 14, 69, 70, 79, 89], free-fall towers [30], and wind tunnels (or other continuous air flow devices) [17, 38, 53, 54, 99, 100]. Of these options, shock tubes have been the workhorse responsible for generating large relative velocities between the gas and the liquid. Normal shock waves, in and of themselves, have little effect on the droplet. However, they have proven to be a reliable and repeatable technique to generate a high-speed flow around the droplet, which is responsible for the deformation and disintegration [22, 43, 69]. By varying the strength of the incident shock, the relative velocity, and thus the We, is easily controlled. Using pressure sensors located at various streamwise locations in the shock tube, droplet injection and subsequent arrival of the free-falling droplet at the middle of the test section can be timed to coincide with the arrival of the shock wave. Various droplet injection techniques exist in the literature with the earliest works using hypodermic needles [43, 79] or oscillating thin liquid jets at the Rayleigh instability frequency [69, 97, 98]. More recently, advanced drop generators [6, 17, 44, 89] have been utilized improving the uniformity of the generated droplets. In our numerical study of aerobreakup, we simplify the experimental shock tube setup into an idealized problem described in the following section.

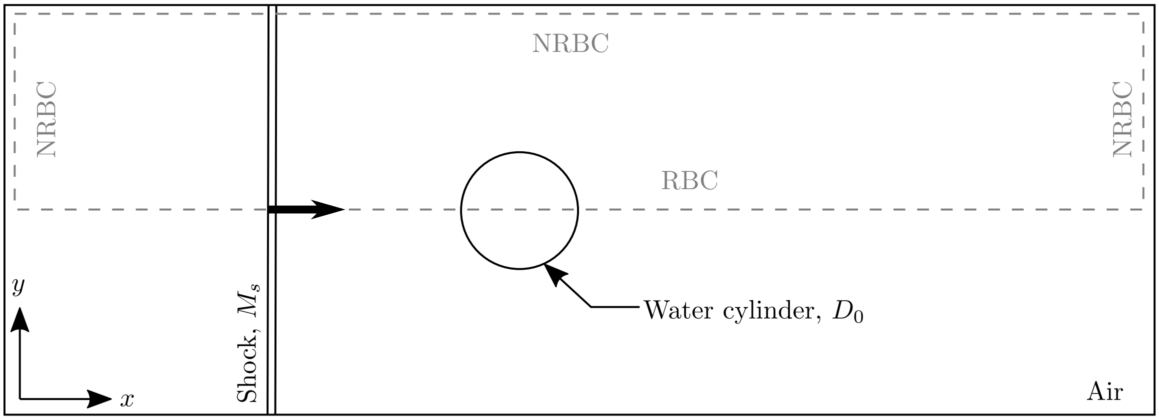

Figure 2.1: Schematic of the 2D initial condition and computational domain (dashed) for the aerobreakup of a water cylinder in a shock tube.

2.2 Idealized problem

In this thesis, results are presented for numerical simulations of the aerobreakup of a water droplet in the flow behind a normal shock wave. The problem is studied in both 2D Cartesian coordinates (Chapter 5) and 3D cylindrical coordinates (Chapter 6). In the idealized problem, we have simplified the actual experimental shock tube setup in several ways. Firstly, our simulations are not confined by rigid walls, i.e., the shock tube test section has been infinitely expanded. Secondly, we initiate the incident shock as a discontinuity in fluid properties. We make no attempt to simulate the actual creation of a shock wave with driver and driven shock tube sections. Finally, our water droplet is initialized to simply exist at rest in the computational domain. In reality, the process of droplet injection in experiments imparts an initial velocity to the droplet in the direction perpendicular to shock propagation. Depending on the experimental setup and the quality of the droplet injection process, the droplet may also experience small oscillations or deformations of its interface, such that the incident shock interacts with a nonspherical droplet. Both the initial perpendicular velocity and interface imperfections are ignored in our simulations. The schematic of the initial condition and computational domain for the 2D Cartesian aerobreakup problem is shown in Fig. 2.1. In the schematic, the shock wave of strength M_s (modeled as a step discontinuity in fluid properties) is traveling in air towards the water droplet, which is initialized as a smeared circular interface of diameter D_0 on the Cartesian grid. The droplet and the ambient air downstream of the shock

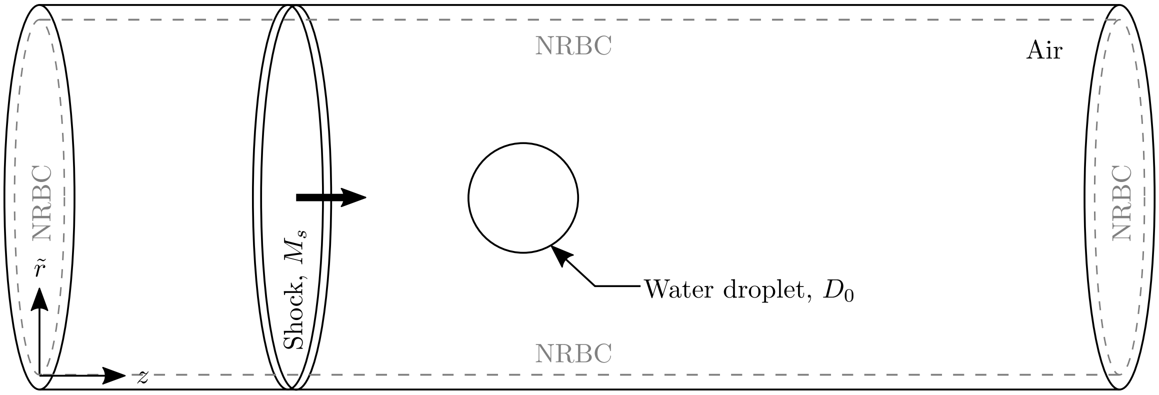

Figure 2.2: Schematic of the 3D initial condition and computational domain (dashed) for the aerobreakup of a water droplet in a shock tube.

are initialized at rest. A reflective boundary condition (RBC) is used to describe the symmetry of the problem across the x-axis, while nonreflective boundary conditions (NRBC) effectively extend the surrounding air to infinity. Further modeling and numerical considerations are discussed in Section 2.3 and Chapter 3, respectively. The schematic of the initial condition and computational domain for the 3D cylindrical aerobreakup problem is shown in Fig. 2.2. In cylindrical coordinates, the entire 3D flow field is simulated with no enforced symmetries in the geometry of the problem. The NRBCs, once again, extend the surrounding air to infinity, and the water drop is initialized as a smeared spherical interface. Further modeling and numerical considerations are discussed in Sections 2.3 and 4.2 and Chapter 3.

We note here that the initialization of the shock wave as a step discontinuity in the simulations results in a well-known "startup" error that appears as two spurious small-amplitude waves. One of these waves is an acoustic wave that travels upstream at speed $u_s - c_s$, where u, c are, respectively, the velocity and sound speed, and the subscripted "s" indicates a post-shock property. The second is an entropy wave that travels downstream at the fluid velocity, u_s. This startup error is frequently observed when an exact discontinuity is initialized, and an explanation of its origin can be found in LeVeque [51]. The upstream-traveling acoustic wave is of no concern since it does not interfere with the aerobreakup of the liquid droplet. The downstream-traveling entropy wave does traverse the droplet behind the incident shock, but because it is so weak compared to the actual shock wave, its effect on the overall breakup physics is insignificant. Numerical tests explicitly removing these startup error waves confirmed the triviality of this interaction.

2.3 Governing equations

2.3.1 Five-equation model with viscous effects

The flows of interest are governed by the compressible multicomponent Navier-Stokes equations. In addition to being compressible, each fluid is considered immiscible and does not undergo phase change. In the absence of mass transfer and surface tension, material interfaces are simply advected by the local flow velocity. For a system of two fluids, this gives rise to a five-equation model, first introduced in its inviscid form by Allaire et al. [2], and subsequently extended to viscous fluids by Perigaud and Saurel [65]. The five-equation model, Eq. (2.1), consists of individual continuity equations for each of the fluids, Eqs. (2.1a) and (2.1b), mixture momentum, Eq. (2.1c), and energy, Eq. (2.1d), equations, and a transport equation for one of the fluid volume fractions, Eq. (2.1e), to identify the material interface.

$$\frac{\partial(\alpha_1\rho_1)}{\partial t} + \nabla\cdot(\alpha_1\rho_1\mathbf{u}) = 0, \tag{2.1a}$$

$$\frac{\partial(\alpha_2\rho_2)}{\partial t} + \nabla\cdot(\alpha_2\rho_2\mathbf{u}) = 0, \tag{2.1b}$$

$$\frac{\partial(\rho\mathbf{u})}{\partial t} + \nabla\cdot(\rho\mathbf{u}\otimes\mathbf{u} + p\mathbf{I} - \mathbf{T}_\mu) = \mathbf{0}, \tag{2.1c}$$

$$\frac{\partial E}{\partial t} + \nabla\cdot\big((E+p)\mathbf{u} - \mathbf{T}_\mu\cdot\mathbf{u}\big) = 0, \tag{2.1d}$$

$$\frac{\partial\alpha_1}{\partial t} + \mathbf{u}\cdot\nabla\alpha_1 = 0, \tag{2.1e}$$

where ρ is the density, α is the volume fraction, $\mathbf{u}$ is the velocity vector, p is the pressure, E is the total energy defined as $E = \rho\varepsilon + \frac{1}{2}\rho\|\mathbf{u}\|^2$, $\mathbf{T}_\mu$ is the viscous stress tensor, ε is the specific internal energy, and the subscripted variables refer to quantities that are specific to individual fluids. The viscous stress tensor, $\mathbf{T}_\mu$, is defined as

$$\mathbf{T}_\mu = 2\mu\left(\mathbf{D} - \frac{1}{3}(\nabla\cdot\mathbf{u})\mathbf{I}\right) + \mu_v(\nabla\cdot\mathbf{u})\mathbf{I}, \tag{2.2}$$

where μ and μ_v are, respectively, the dynamic and bulk viscosities, and

$$\mathbf{D} = \frac{1}{2}\Big(\nabla\mathbf{u} + (\nabla\mathbf{u})^T\Big), \tag{2.3}$$

is the deformation rate tensor. The five-equation model is easily extended to systems with more than two fluids; the governing equations, Eq. (2.1), are simply supplemented with additional continuity equations and volume fraction transport equations. Dynamic and bulk viscosity[1] [45, 75] values at normal temperature and pressure (NTP) for the fluids of interest in this thesis are shown in Table 2.1.

Though other models exist to describe compressible multicomponent flows, the chosen five-equation model possesses several key characteristics. Firstly, the compressible Navier-Stokes equations are cast in conservative form; as such, they conserve the mass of individual fluids, as well as the total momentum and energy. The conservation of mass for each fluid is a distinct advantage over other models, which only conserve total mass and typically result in mass transfer between supposedly immiscible fluids. Furthermore, the choices for both the form of the transport equation and the transported quantity are purposeful. The quasi-conservative form of Eq. (2.1e) is necessary for oscillation-free behavior at material interfaces, while the choice to advect volume fractions, instead of, e.g., an equation of state parameter, decouples the model from the choice of equation of state.

2.3.2 Stiffened gas equation of state

The five-equation model of Section 2.3.1 is closed with the specification of an appropriate equation of state (EOS) that relates the fluid densities, pressures, and internal energies. The stiffened gas EOS [23], which has been widely utilized in compressible multicomponent flow simulations [2, 65, 93], is used in our flow solver to model both gases and liquids.

$$p = (\gamma - 1)\rho\varepsilon - \gamma\pi_\infty, \tag{2.4}$$

---

[1] $\mu_v = 0.57\mu$ for air [75]; $\mu_v = 2\mu/3 + \mu'$ for water using values from Table IV of [45] at NTP.

Fluid	ρ [kg/m^3]	c [m/s]	μ [Pa·s]	μ_v [Pa·s]	γ	π_∞ [Pa]
Air	1.204	343	1.80×10^{-5}	1.03×10^{-5}	1.40	0
Water	1000	1450	1.00×10^{-3}	4.10×10^{-3}	6.12	3.43×10^{8}

Table 2.1: Properties of air and water at NTP.

where γ and π_∞ are fitting parameters that are empirically determined from fluid shock Hugoniot data. The consistent EOS sound speed is calculated as

$$c = \sqrt{\frac{\gamma(p + \pi_\infty)}{\rho}}. \tag{2.5}$$

Given that the fluids being modeled are considered to be immiscible, each fluid in the solver individually obeys the stiffened gas EOS. The properties for the fluids of interest in this work, air and water, are tabulated in Table 2.1. For all numerical results presented in this thesis, the values in Table 2.1 are applicable for their respective fluids, unless explicitly stated otherwise. For air, $\pi_\infty = 0\,\text{Pa}$, and the stiffened gas EOS reduces to the ideal gas law, with γ as the specific heat ratio. The fitting parameters for water are based on the shock Hugoniot data of Gojani et al. [18] following the fitting procedure described in Johnsen [40].

2.3.3 Mixture relationships

Within the diffuse interface region (see Section 3.1.1), mixture rules must be specified for the properties of fluid mixtures. These mixture regions are an artifact of numerical diffusion, and are not a product of mixing on a molecular level. For a system of two fluids, expressions of the mixture volume fraction, density, and internal energy are commonly defined as

$$1 = \alpha_1 + \alpha_2, \tag{2.6}$$

$$\rho = \alpha_1\rho_1 + \alpha_2\rho_2, \tag{2.7}$$

$$\rho\varepsilon = \alpha_1\rho_1\varepsilon_1 + \alpha_2\rho_2\varepsilon_2. \tag{2.8}$$

Following previous work in the literature, we define the following mixture rules for two functions of the stiffened gas EOS fitting parameters [2]

$$\Gamma = \alpha_1 \Gamma_1 + \alpha_2 \Gamma_2, \quad \Gamma = \frac{1}{\gamma - 1}, \tag{2.9}$$

$$\Pi_\infty = \alpha_1 \Pi_{\infty,1} + \alpha_2 \Pi_{\infty,2}, \quad \Pi_\infty = \frac{\gamma \pi_\infty}{\gamma - 1}. \tag{2.10}$$

Following Perigaud and Saurel [65], the mixture viscosities are defined as

$$\mu = \alpha_1 \mu_1 + \alpha_2 \mu_2, \tag{2.11}$$

$$\mu_v = \alpha_1 \mu_{v,1} + \alpha_2 \mu_{v,2}. \tag{2.12}$$

The extension to N fluids is straightforward, as all of the above mixture properties are defined as linear combinations of the properties of the pure fluids composing the mixture.

2.3.4 Nondimensionalization conventions

In this study of aerobreakup, the five-equation model, Eq. (2.1), is solved in dimensionless form. Unless specified otherwise, nondimensionalization of the variables is done using the initial droplet diameter, D_0, and post-shock gas velocity, u_s, pressure, p_s, and density, ρ_s. The resulting change in variables is

$$t^* = t \frac{u_s}{D_0} \sqrt{\frac{\rho_s}{\rho_l}}, \qquad \mathbf{x}^* = \frac{\mathbf{x}}{D_0}, \qquad \rho^* = \frac{\rho}{\rho_s}, \qquad \mathbf{u}^* = \frac{\mathbf{u}}{u_s}, \qquad p^* = \frac{p}{p_s}, \tag{2.13}$$

where the superscripted asterisk denotes a nondimensional quantity. It should be noted that much of the literature denotes ρ_s, u_s, p_s as ρ_g, u_g, p_g; the notation in this work will attempt to clearly make the distinction between these as needed. The additional density ratio in the nondimensionalization of time results in a nondimensional breakup time characteristic of breakup by Rayleigh-Taylor or Kelvin-Helmholtz instabilities [66, 69, 79]. Additionally, for all aerobreakup results presented in this thesis, $t^* = 0$ corresponds to the time instant at which the incident shock reaches the leading edge of the droplet. Following the standard definitions found in the aerobreakup literature, the nondimensional Weber, Reynolds, and Ohnesorge numbers are defined as

$$We = \frac{\rho_s u_s^2 D_0}{\sigma}, \qquad Re = \frac{\rho_s u_s D_0}{\mu_g}, \qquad Oh = \frac{\mu_l}{\sqrt{\rho_l D_0 \sigma}}, \tag{2.14}$$

unless specified otherwise.

Chapter 3

Numerical method

3.1 Overview of the Multicomponent Flow Code

The Multicomponent Flow Code (MFC) is a research flow solver capable of solving the compressible Navier-Stokes equations for multicomponent flows. The numerical method is based on the work of Johnsen and Colonius [41], who developed the method to be both shock- and interface-capturing. Previous improvements to the original work extended the flow solver to 3D Cartesian coordinates, added nonuniform grid capabilities, and implemented a model to capture the effects of molecular viscosity [13]. Since its development, the flow solver has been used to investigate nonspherical bubble collapse [40, 42], and the shock-induced collapse of bubbles inside deformable vessels [12]. Rigorous verification of the algorithm via benchmark test cases [13], as well as parallel performance metrics of MFC [11], have previously been documented, and are not reproduced here. Instead, the following sections will present a high-level overview of the numerical algorithm, while omitting details and nuances that can be found in the previously referenced works.

3.1.1 Interface-capturing scheme

The numerical simulation of material interfaces in the multicomponent flows of interest is made possible by the volume of fluid (VOF) method, which belongs to the broader class of interface-capturing schemes. In contrast to interface-tracking schemes (e.g., classical level set methods), discrete conservation of mass, momentum, and energy in interface-capturing schemes is straightforward to enforce provided the equations are solved in conservative form. Furthermore, interface-capturing schemes are generally more efficient than their interface-tracking counterparts. A common characteristic of interface-capturing schemes (including the VOF method used in MFC) is the relaxation of the natural sharpness of material discontinuities. Instead, the interfaces are allowed to numerically diffuse resulting in an interface region of small, but finite, thickness. As a consequence of the numerical diffusion, unphysical mixtures arise in the diffuse interface region during computation. These unphysical mixtures, if not treated in a manner consistent with the governing equations and thermodynamics, can lead to the generation of spurious oscillations. Fortunately, methods to consistently treat these unphysical mixtures are well-understood [41], and the appropriate mixture fluid properties are calculated using the expressions in Section 2.3.3. It should be noted that for numerical stability purposes, material interfaces are not initialized as sharp discontinuities, but are smeared over a few grid cells. Based on previous results [11, 40], this artificial initial smearing has negligible impact on the computation.

3.1.2 Spatial and temporal discretizations

The five-equation model with viscous effects presented in Section 2.3.1 is spatially-discretized on a Cartesian grid in the following conservative form:

$$\frac{\partial \mathbf{q}}{\partial t} + \frac{\partial \mathbf{f}^a(\mathbf{q})}{\partial x} + \frac{\partial \mathbf{g}^a(\mathbf{q})}{\partial y} + \frac{\partial \mathbf{h}^a(\mathbf{q})}{\partial z} = \frac{\partial \mathbf{f}^d(\mathbf{q})}{\partial x} + \frac{\partial \mathbf{g}^d(\mathbf{q})}{\partial y} + \frac{\partial \mathbf{h}^d(\mathbf{q})}{\partial z} + \mathbf{s}^a(\mathbf{q}), \tag{3.1}$$

where $\mathbf{q}$ is the vector of conservative variables, $\mathbf{f}(\mathbf{q}), \mathbf{g}(\mathbf{q})$, and $\mathbf{h}(\mathbf{q})$ are flux vectors, $\mathbf{s}(\mathbf{q})$ is the source term vector, and the superscripted "a" and "d" denote, respectively, advective and diffusive fluxes (see details in Appendix A.1). The transport equation for the volume fraction in Eq. (3.1) is rewritten from Eq. (2.1e) as

$$\frac{\partial \alpha_1}{\partial t} + \nabla \cdot (\alpha_1 \mathbf{u}) = \alpha_1 \nabla \cdot \mathbf{u}. \tag{3.2}$$

Though Eqs. (2.1e) and (3.2) are mathematically equivalent, the formulation in Eq. (3.2) is ultimately necessary to adapt the Riemann solver to the advection equation [41]. Using a finite-volume framework, Eq. (3.1) is evolved in time using a Godunov-type scheme. A formally third-order weighted essentially nonoscillatory (WENO) scheme is used to reconstruct the cell center average values to the cell boundaries, where the approximate Harten-Lax-van Leer-contact (HLLC) Riemann solver [94] is used to determine the intercell fluxes. While the numerical scheme is formally third-order accurate, it is well known that all shock-capturing schemes deteriorate to first-order accuracy near discontinuities such as material interfaces and shock waves.

Finally, the system of equations is temporally integrated using a third-order total variation diminishing (TVD) Runge-Kutta scheme. Generally speaking, the numerical scheme is stable provided an appropriate time step [11] is chosen that satisfies

$$\Delta t = \mathcal{C} \cdot \min_{i,j,k} \left(\frac{\Delta x_i}{|u_{i,j,k}| + c_{i,j,k}}, \frac{\Delta y_j}{|v_{i,j,k}| + c_{i,j,k}}, \frac{\Delta z_k}{|w_{i,j,k}| + c_{i,j,k}} \right), \quad 0 < \mathcal{C} \leq \frac{1}{N}, \tag{3.3}$$

for the Courant-Friedrichs-Lewy (CFL) number, $\mathcal{C}$, and

$$\Delta t = \mathcal{D} \cdot \min_{i,j,k} \left(\frac{\Delta x_i^2}{\nu_{i,j,k}}, \frac{\Delta y_j^2}{\nu_{i,j,k}}, \frac{\Delta z_k^2}{\nu_{i,j,k}} \right), \quad 0 < \mathcal{D} \leq \frac{1}{2N}, \tag{3.4}$$

for the diffusion number, $\mathcal{D}$, where N is the dimensionality of the simulation and $\nu = \dfrac{\mu}{\rho}$ is the kinematic viscosity. If capillary effects are included in the model (as detailed in Section 4.1), yet another stability constraint on the maximum allowable time step is introduced. Following Brackbill et al. [8], capillary wave propagation is resolved when the time step satisfies

$$\Delta t < \sqrt{\frac{(\rho_1 + \rho_2) \min\limits_{i,j,k} \left(\Delta x_i^3, \Delta y_j^3, \Delta z_k^3 \right)}{4\pi\sigma}}, \tag{3.5}$$

where ρ_1 and ρ_2 are the fluid densities on either side of the material interface, and σ is the surface tension coefficient. Further details on the stability of the numerical scheme, as well as details of the reconstruction process and the time marching scheme can be found in the work of Coralic [11].

3.1.3 Numerical viscosity and breakup mechanism

The absence of molecular viscosity and surface tension modeling in the simulations of Section 5.3 and Chapter 6 has important consequences for the discussion and interpretation of the numerical results. The following comments also partially apply to the results of Section 5.4, which include molecular viscosity modeling, but still neglect surface tension modeling.

In the absence of molecular viscosity modeling, it is important to note that, given the shock- and interface-capturing nature of the numerical method, numerical viscosity is present in all simulation results. The magnitude of the numerical viscosity is dependent on the spatial resolution used in the simulations, and an attempt is made to bound this numerical viscosity in Section 5.4.1 for a nominal spatial resolution of 100 cells per original droplet diameter. Within the computational fluid dynamics community, it is generally understood that so-called “inviscid” simulations, i.e., those done without molecular viscosity modeling, using shock- and interface-capturing schemes, inherently include numerical viscosity effects. A consequence of the resolution-dependent numerical viscosity magnitude is that traditional grid convergence or grid independence of the numerical results cannot be obtained in these so-called “inviscid” simulations. Without the presence of molecular viscosity to regularize the smallest scales in the simulations, increasingly small scales are captured as the grid resolution is refined. The spatial resolution chosen for the numerical results presented in this thesis is selected for its ability to capture the salient flow features of interest without being computationally cumbersome (see details in Appendix D.1). In the remainder of this thesis, numerical results that are referred to as being “inviscid” should be understood by the reader to mean results that do not include explicit molecular viscosity modeling.

In the absence of surface tension modeling, there does not exist a numerical mechanism that approximates capillary effects, i.e., there is no capillary counterpart to numerical viscosity. Without such a numerical mechanism, and without using an explicit capillary model, we do not capture the *ultimate* capillary-driven breakup mechanism of a droplet undergoing aerobreakup. Instead, the actual mechanism of breakup in the numerical results is modeled in terms of diffusion effects, i.e., breakup occurs as a consequence of numerical diffusion and finite spatial resolution. Specifically, in the discussion of the thin liquid sheet that is drawn from the droplet's equator in Section 6.3.1, it is crucial to remember that, although we are able to discuss the various sheet instabilities (see Sections 1.2.1.4 and 6.3.4), it is capillary effects that are, ultimately, responsible for the sheet's physical disintegration.

In light of these clarifications and caveats on numerical viscosity and the mechanism of breakup in the numerical results, the results and conclusions presented herein should be treated as provisional. At the same time, the qualitative and quantitative agreement we are able to obtain in our experimental comparisons (see Sections 5.3.2 and 6.3.2) provide confidence that the results are a fair representation of reality, even in the absence of these physical effects. The definitive quantification of the errors incurred by neglecting viscous and capillary effects in our simulations is dependent upon future work that quantifies these effects. Ultimately, though, it is believed that the results presented herein are representative of aerobreakup phenomena for large Weber and Reynolds number regimes.

3.2 Droplet diagnostics

3.2.1 Droplet size

Any type of analysis on the droplet deformation during aerobreakup relies on accurate measurements of the droplet's size. Unlike experimental studies of aerobreakup where measurement accuracy is strongly dependent on the quality of experimental visualization techniques, numerical simulations lend themselves to accurate measurements with relative ease. Given that our VOF numerical method involves a diffuse interface that is smeared across a few grid cells, however, a threshold liquid volume fraction must be defined to provide a nominal interface location. Using this approach, a coherent droplet body is comprised of all grid cells with $\alpha_l \geq \alpha_{cr}$, where α_{cr} is the liquid volume fraction threshold. For comparison with experimental investigations, it is unclear what value α_{cr} should take to best match the numerical and experimental data (if such a value exists). Therefore, in any experimental comparison shown in this thesis, a range for α_{cr} is specified in an attempt to bound the experimental data. Though this approach of showing a range of α_{cr} can, in some cases, result in

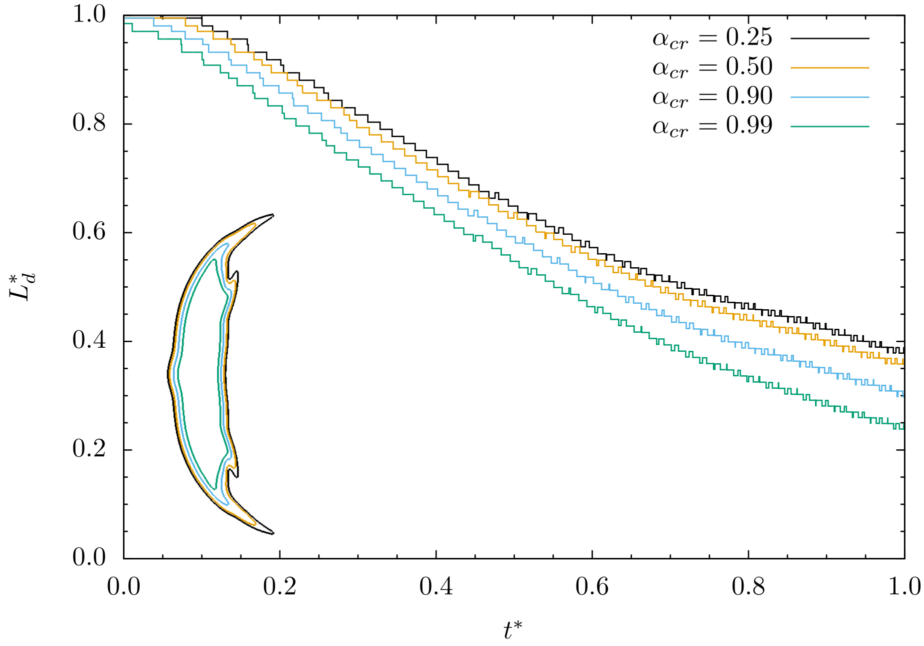

Figure 3.1: Centerline width, L_d^*, of a deforming water droplet for various α_{cr}. The inset contour plot shows the droplet boundary as defined by the values of α_{cr} at $t^* = 0.817$.

a wide spread, there is, unfortunately, no systematic way to rigorously define a more accurate value of α_{cr}. Furthermore, this spread is consistent with the uncertainties that exist in the experimental measurements regarding the specification of the droplet's boundary.

The size of a deformed droplet can be quantified in various ways. Historically, measurements from 2D experimental visualizations have included the drop's centerline width, L_d, deformed diameter, D_d, and coherent body area, A_d. The 3D counterparts of the latter two are, respectively, the drop's projected frontal area, S_d, and coherent body volume, V_d. Consider, for now, a 3D Cartesian simulation of aerobreakup where the streamwise direction is aligned with the x-axis, and the droplet is centered on the origin. The numerical measurement of L_d, for a given α_{cr}, is obtained by finding the difference of the maximum and minimum cell x-boundary locations for cells that satisfy $y, z = 0$ and $\alpha_l \geq \alpha_{cr}$. The threshold liquid volume fraction approach is demonstrated in Fig. 3.1 where we have plotted the centerline width for four distinct values of α_{cr} that range between $\alpha_{cr} = 0.25$ and $\alpha_{cr} = 0.99$. It is clear from Fig. 3.1 that distinct choices of α_{cr} result in slight variations of numerical droplet size. In a manner similar to the determination of L_d, the deformed diameters, D_d, are measured independently in both transverse directions by finding the difference of the maximum and minimum cell y- and z-boundary locations for cells that satisfy $\alpha_l \geq \alpha_{cr}$ (with no restriction on x-position). The drop's coherent body volume, V_d, or its 2D counterpart, A_d, is found using

$$V_d = \int_{\Omega'} 1 \, \mathrm{d}V, \tag{3.6}$$

where Ω' are all grid cells in the computational domain, Ω, for which $\alpha_l \geq \alpha_{cr}$. Although these measurements are only accurate to the nearest grid cell, we find they satisfactorily describe the deformation during the early stages of aerobreakup when the droplet remains a single coherent body. Finally, in order to find the projected frontal area, S_d, in 3D simulations of aerobreakup, we assume that the drop's projected shape is that of a circle whose diameter is D_d. Though this may seem like a crude approximation of S_d, visualizations of isosurfaces of $\alpha_l = \alpha_{cr}$ reveal that the assumption is not far from reality. Furthermore, interface reconstruction using piecewise linear interface calculation (PLIC) methods shows that this assumption gives reasonable quantitative results.

3.2.1.1 Verification using PLIC

Using the PLIC method detailed in Appendix B, we test our assumption of a circular S_d for 3D simulations of aerobreakup in Cartesian coordinates. Given a user-specified isovalue of α_l or α_g, MFC first flags the grid cells in the computational domain that should contribute to the overall PLIC reconstruction. Since we have a diffuse interface method, this step is necessary to ensure that, to the best possible extent, the PLIC reconstruction does not generate concentric interface layers that errantly result in excessive areas (both projected and surface). This flagging is done using a combination of the local interface normal, $\mathbf{n}$, and the volume fractions in the neighboring cells. Once these outer grid cells are flagged, the plane constant, η, is found in each cell by solving the inverse problem given $V = \alpha V_0$ (see details in Appendix B.1). Their contribution to the reconstructed interface surface area is subsequently calculated using Eq. (B.22). In general, the geometrical definition of projected area, A_{proj}, is given by

$$A_{\text{proj}} = \int_A \cos\beta \, \mathrm{d}A, \tag{3.7}$$

where A is the original area, and β is the angle between the normal of A and the normal of the arbitrary plane onto which the projection is done. For the 3D Cartesian simulation where the streamwise direction is aligned with the x-axis, the projected area of the reconstructed PLIC interface is then

$$A_{\text{proj}} = \int_A \hat{\mathbf{n}} \cdot \hat{\boldsymbol{\imath}} \, \mathrm{d}A = \int_A n_x \, \mathrm{d}A, \tag{3.8}$$

where the integrated area is the surface area of the PLIC interface, and the local interface normal has been normalized. Equation (3.8), however, is not quite the correct expression for S_d. Consider the case of a cubic interface with sides of length L. The correct projected frontal area is $S_d = L^2$, while Eq. (3.8) will give $A_{\text{proj}} = 0$. The correct expression for S_d is thus

$$S_d = \int_{A'} n_x \, \mathrm{d}A', \tag{3.9}$$

where A' is the *partial* surface area for which $\hat{\mathbf{n}} \cdot \hat{\boldsymbol{\imath}} > 0$.

We begin by plotting in Fig. 3.2 the surface area time history of a deforming drop in the flow behind a $M_S = 1.47$ shock using PLIC reconstructions. The surface area has been normalized by $A_0 = 4\pi R_0^2$, where R_0 is the initial radius. Since the interface is diffuse, using the interface normals computed for the gas and liquid will result in slightly different results, i.e., PLIC$_g$ and PLIC$_l$. This surface area time history is compared to a curve generated by the open source visualization software, VisIt, developed at Lawrence Livermore National Laboratory. After plotting the isosurface of a particular variable, in this case $\alpha_l = 0.5$, VisIt has a built-in operator to calculate the surface area of the isosurface; this is taken as the reference curve. From Fig. 3.2, we see good agreement for all plotted curves. The projected frontal area, S_d, normalized by $S_0 = \pi R_0^2$, is plotted in Fig. 3.3 using Eq. (3.9) for the PLIC reconstructions and the corresponding built-in VisIt operator. Two additional

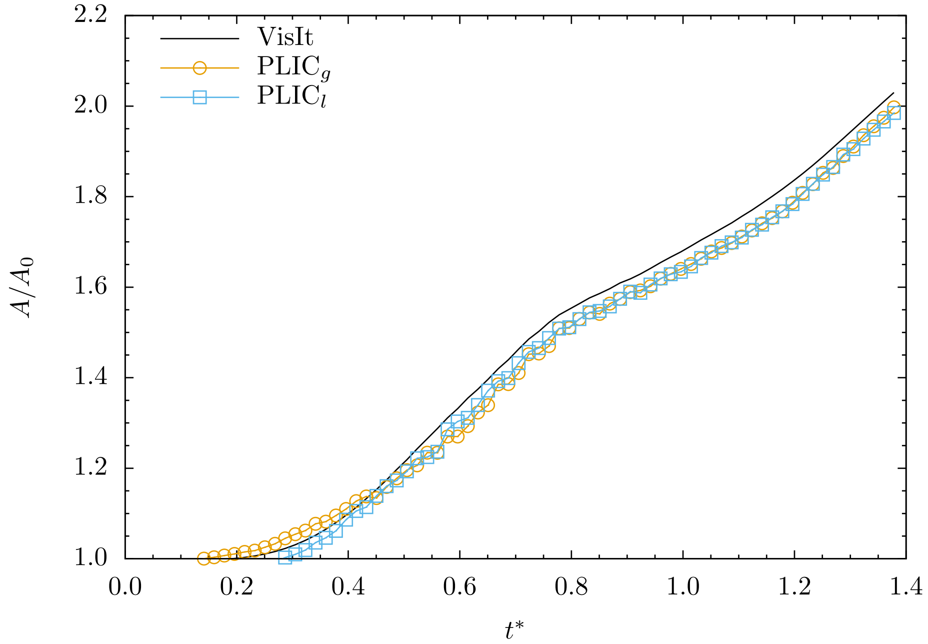

Figure 3.2: Normalized surface area, A/A_0, of a droplet in the flow behind a Mach 1.47 shock wave using an isovalue of $\alpha_l = 0.5$.

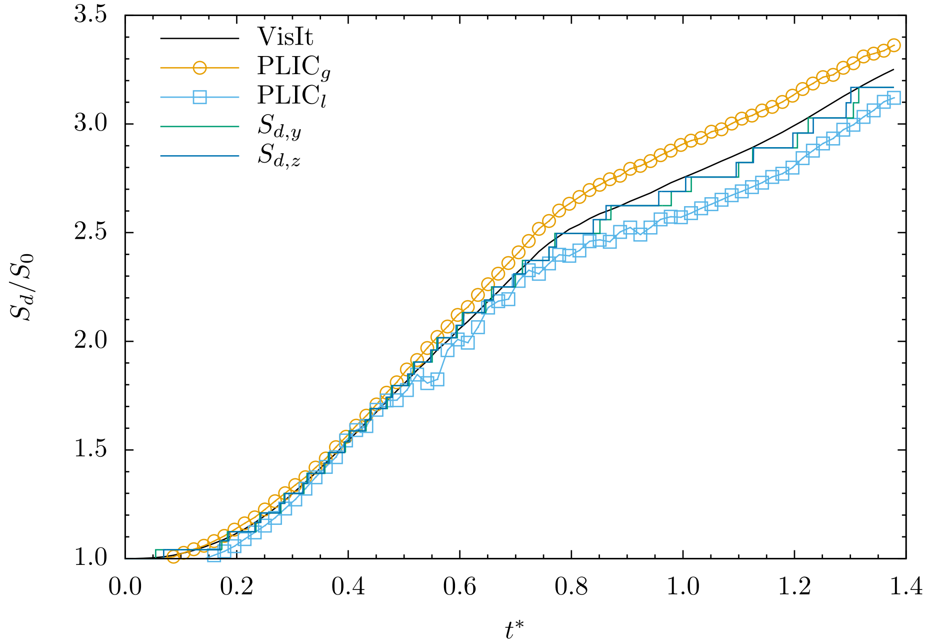

Figure 3.3: Normalized projected frontal area, S_d/S_0, of a droplet in the flow behind a Mach 1.47 shock wave using an isovalue of $\alpha_l = 0.5$.

curves labeled $S_{d,y}$ and $S_{d,z}$ are calculated from the deformed diameter in both transverse directions, $D_{d,y}, D_{d,z}$, assuming the projected frontal area is a circle, i.e., $S_d = \pi R_d^2$. A few observations can be made from Fig. 3.3. Firstly, the curves computed from $D_{d,y}, D_{d,z}$, i.e., those labeled, $S_{d,y}, S_{d,z}$ track the reference VisIt curve better than both PLIC reconstructions, especially at later times. Though the PLIC method could potentially be improved by, e.g., fine-tuning the flagging of outer grid cells, there will always remain some residual error associated with the diffuse interface and the piecewise linear reconstruction. In contrast, the largest error in the $S_{d,y}, S_{d,z}$ curves is a result of approximating to the nearest cell boundary location — an error that would disappear in the limit of infinite resolution. Furthermore, if the PLIC method was improved, it would be relatively expensive to compute at every time step, whereas finding D_d at every time step is straightforward (the discrete data points for the PLIC curves in Figs. 3.2 and 3.3 are plotted at 500 time step intervals). Given the relative simplicity and ease of finding S_d from D_d, and the availability of S_d at every time step (which will become important when used in drag coefficient calculations, for example), we adopt the threshold liquid volume fraction approach for our diagnostics of droplet size.

3.2.2 Droplet center-of-mass calculations

Numerous investigations of droplet aerobreakup have attempted to quantify or characterize the droplet's unsteady drag coefficient, which is a key parameter often used in secondary atomization models. The accurate calculation of the droplet's center-of-mass acceleration is a necessary step towards estimating the drop's unsteady drag. Thus, experimental studies have often extracted acceleration data by differentiating a polynomial fit of the drop's trajectory. The measurement of the drop's drift from the forward stagnation point is often a necessary simplification for extracting meaningful data from photographic evidence, and has been used in previous experimental work [16, 79]. However, acceleration calculations following this methodology are subject to additional error since the drift of the droplet front does not accurately represent the center-of-mass drift. It has previously been shown that the leading-edge drift first overestimates, then underestimates, the center-of-mass drift [87], and this trend is borne out in our numerical results (see Section 5.3.3.1).

Consequently, we compute the deforming droplet's the center-of-mass location, $\mathbf{x}_c$, using

$$\mathbf{x}_c = \frac{\int_\Omega \alpha_l \rho_l \mathbf{x} \, \mathrm{d}V}{\int_\Omega \alpha_l \rho_l \, \mathrm{d}V}, \tag{3.10}$$

where the integrated volume (area in 2D) is that of the entire computational domain, Ω. The liquid partial density, $\alpha_l \rho_l$, in Eq. (3.10) is then the parameter that restricts the integration to cells with nonzero liquid volume fractions.

Once the center-of-mass location is calculated, a few options exist for calculating the velocity and acceleration. Perhaps the simplest method is to differentiate the discrete displacement data using finite-difference approximations. However, this introduces significant noise error into the calculations, and makes it difficult to determine which oscillations (particularly in the acceleration and drag histories) are physical and which are noise-driven. Following the experiments, we could use a polynomial fit to the drift data, and then differentiate the fitted curve to obtain velocity and acceleration curves. Although preferable over the finite-difference method, this strategy also has its drawbacks. Experimental data have shown that the drift history of the droplets is well-approximated by a quadratic polynomial. Fitting the drift data with a quadratic (or even cubic) polynomial then restricts the acceleration to, at best, a linear function. Of course, higher order polynomial fits are possible, but they are still unable to capture the high-frequency oscillations that end up characterizing the acceleration. Taking advantage of the type of quantitative analysis allowed by numerical simulations, we derive integral expressions for the center-of-mass velocity, $\mathbf{u}_c$, and acceleration, $\mathbf{a}_c$, which minimize unnecessary noise error in the calculations and allow us to obtain accurate time histories. However, they are only valid while the liquid mass, m_l, in the domain remains a constant. Once liquid mass flux through the domain boundaries is nonzero, Eqs. (3.12) and (3.15) do not hold, and we terminate their calculation.

3.2.2.1 Center-of-mass velocity

Taking a time derivative of Eq. (3.10), we obtain the following expression (derivation details shown in Appendix C.1):

$$\frac{\mathrm{d}\mathbf{x}_c}{\mathrm{d}t} = \frac{\int_\Omega \alpha_l \rho_l \mathbf{u}\,\mathrm{d}V}{\int_\Omega \alpha_l \rho_l\,\mathrm{d}V} - \frac{1}{m_l}\int_\Omega \mathbf{x}\alpha_l\rho_l(\mathbf{u}\cdot\hat{\mathbf{n}})\,\mathrm{d}A - \frac{\mathbf{x}_c}{m_l}\frac{\mathrm{d}m_l}{\mathrm{d}t}. \tag{3.11}$$

Given that our numerical method is fully conservative, we can immediately drop the last term in Eq. (3.11) since $\frac{\mathrm{d}m_l}{\mathrm{d}t} = 0$. Furthermore, given a sufficiently large computational domain, the mass flux across the volume boundaries remains zero for a significant portion of the simulation time. Therefore, under the assumption of constant liquid mass in the computational domain, i.e., no mass flux through the domain boundaries, the drop's center-of-mass velocity simplifies to

$$\mathbf{u}_c = \frac{\mathrm{d}\mathbf{x}_c}{\mathrm{d}t} = \frac{\int_\Omega \alpha_l \rho_l \mathbf{u}\,\mathrm{d}V}{\int_\Omega \alpha_l \rho_l\,\mathrm{d}V}. \tag{3.12}$$

3.2.2.2 Center-of-mass acceleration

The drop's center-of-mass acceleration is similarly derived by taking the second derivative in time of Eq. (3.10) (details shown in Appendix C.2). Under the same constant mass assumption as in Section 3.2.2.1, the general expression,

$$\begin{aligned}\frac{\mathrm{d}^2\mathbf{x}_c}{\mathrm{d}t^2} = \frac{\int_\Omega \alpha_l \rho_l \mathbf{a}\,\mathrm{d}V}{\int_\Omega \alpha_l \rho_l\,\mathrm{d}V} - \frac{1}{m_l}\left(\int_\Omega \alpha_l\rho_l\mathbf{u}(\mathbf{u}\cdot\hat{\mathbf{n}})\,\mathrm{d}A + \frac{\mathrm{d}}{\mathrm{d}t}\int_\Omega \mathbf{x}\alpha_l\rho_l(\mathbf{u}\cdot\hat{\mathbf{n}})\,\mathrm{d}A\right) \\ - \frac{2}{m_l^2}\frac{\mathrm{d}m_l}{\mathrm{d}t}\left(\int_\Omega \alpha_l\rho_l\mathbf{u}\,\mathrm{d}V - \int_\Omega \mathbf{x}\alpha_l\rho_l(\mathbf{u}\cdot\hat{\mathbf{n}})\,\mathrm{d}A\right) + \frac{2\mathbf{x}_c}{m_l^2}\left(\frac{\mathrm{d}m_l}{\mathrm{d}t}\right)^2 - \frac{\mathbf{x}_c}{m_l}\frac{\mathrm{d}^2 m_l}{\mathrm{d}t^2},\end{aligned} \tag{3.13}$$

simplifies to

$$\mathbf{a}_c = \frac{\mathrm{d}^2\mathbf{x}_c}{\mathrm{d}t^2} = \frac{\int_\Omega \alpha_l \rho_l \mathbf{a}\,\mathrm{d}V}{\int_\Omega \alpha_l \rho_l\,\mathrm{d}V}. \tag{3.14}$$

From the derivation in Appendix C.2, it is obvious that Eq. (3.14) is equivalent to writing

$$\mathbf{a}_c = \frac{\mathrm{d}^2\mathbf{x}_c}{\mathrm{d}t^2} = \frac{\int_\Omega \frac{\partial}{\partial t}(\alpha_l \rho_l \mathbf{u})\,\mathrm{d}V}{\int_\Omega \alpha_l \rho_l\,\mathrm{d}V}. \tag{3.15}$$

From a computational standpoint, however, it is preferable to use Eq. (3.15) since its discrete formulation involves only a finite-difference approximation in time, whereas Eq. (3.14) requires finite-difference approximations in both time and space.

3.3 Known numerical method issues

3.3.1 Spurious interface oscillations

The spurious interface oscillations described in this section were unexpectedly encountered when a visiting scholar used MFC to simulate the impingement of a water droplet onto a rigid wall. The 2D problem is set up as follows: a stationary drop of water is initialized in a static air field and is set a specified distance away from a rigid wall comprised of a stiff fluid. At the start of the simulation, the rigid wall, which has a constant velocity, moves towards the droplet and eventually collides with the drop. Since the wall is impulsively started at the beginning of the simulation, and since MFC is a compressible solver, the wall generates a shock ahead of it that travels faster than the wall, and hits the drop first. Because of the impedance mismatch between the air and the water, the shock is partially transmitted and reflected. The transmitted shock begins to bounce within the drop, while the reflected shock travels back towards the rigid wall and collides with the moving interface. It is this shock-moving-interface interaction that generates large spurious oscillations that travel into the fluid of the rigid wall. The transmitted wave that is moving within the droplet does not generate these spurious oscillations.

In order to study these spurious oscillations, we simplify the 2D problem into a simple 1D problem of a shock interacting with a moving contact discontinuity. Firstly, the stiffness, π_∞, of the involved fluids is observed to have a significant effect on these oscillations, as a shock collision with a moving interface between two gases (different densities and ratios of specific heats) does not generate these spurious waves. Figure 3.4 shows the results of a Mach 1.21 shock in air colliding with a traveling air-benzene interface. The simulation is computed using 10^3 grid cells, and benzene gas is modeled using $(\rho, \gamma, \pi_\infty)_{\text{benzene}} = (3.486\,\text{kg/m}^3, 1.12, 0\,\text{Pa})$. At $t = 1.38\,\text{ms}$, transmitted and reflected shocks can

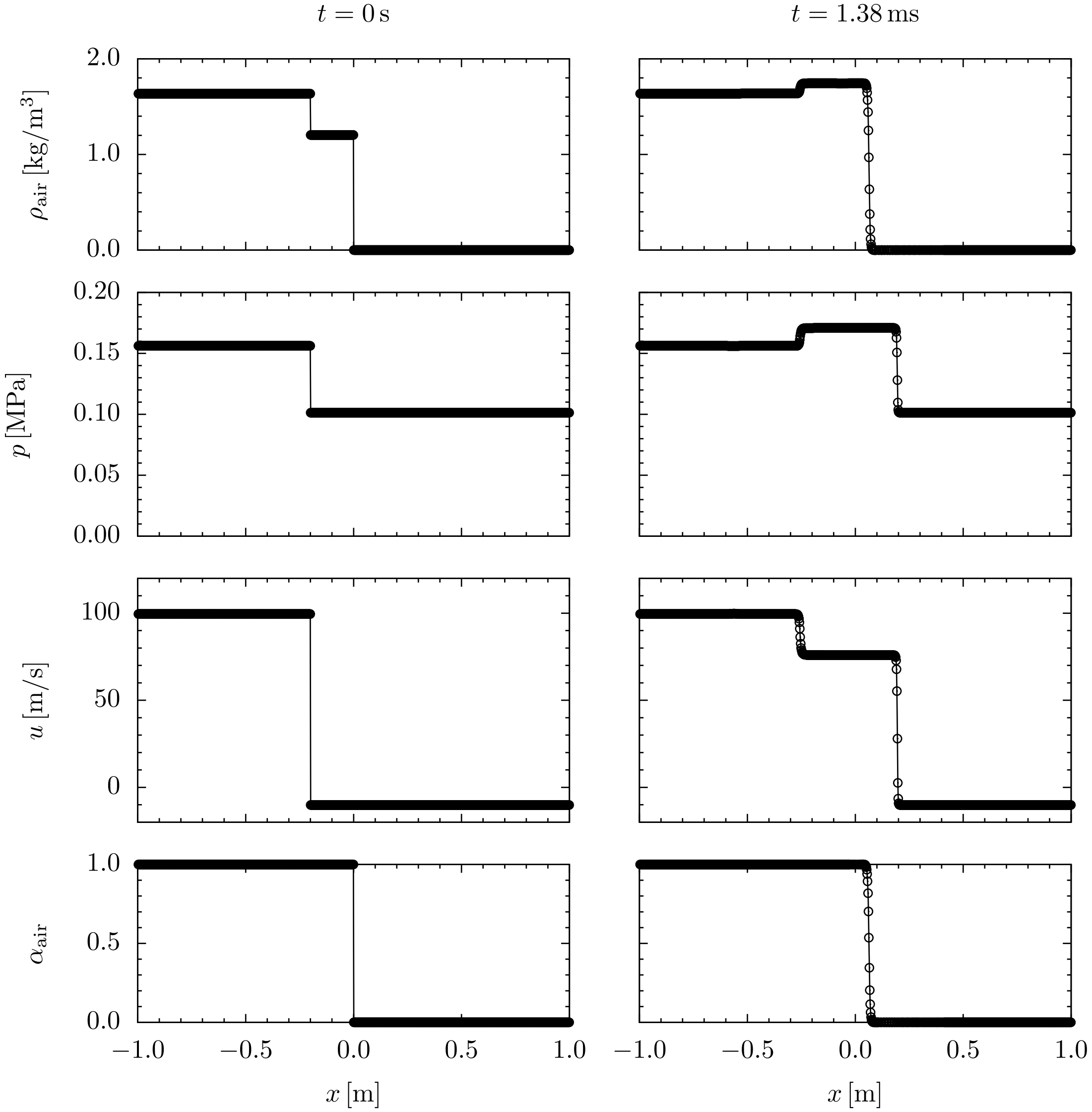

Figure 3.4: Mach 1.21 shock in air colliding with a traveling air-benzene interface. Plots of pressure, velocity, and air density and volume fraction are shown at two times.

be seen propagating, respectively, into the benzene and air. No spurious oscillations are generated in either fluid. The same, however, cannot be said for the case of the same shock in air interacting with a traveling air-water interface (shown in Fig. 3.5). From the pressure plot at $t = 0.62\,\mathrm{ms}$, spurious oscillations of large amplitude can be seen traveling into the liquid phase, $0 \leq x \leq 1$. The presence of these spurious oscillations is unexpected since the collision of a shock with a *stationary* air-water interface does *not* exhibit the same problematic behavior (shown in Fig. 3.6). After much testing, we find that these oscillations arise whenever a shock collides with a gas-liquid or gas-solid interface moving at an appreciable velocity (if the wall is moving with a small enough velocity, the oscillations are not observed, though they may just be small in amplitude).

To date, the only solution we have found for these spurious oscillations is to move from third-order to first-order WENO reconstructions. First-order WENO is known to be explicitly TVD, and is able to successfully suppress all oscillations. We repeat the simulation of Fig. 3.5, now with first-order WENO reconstructions, to obtain the results shown in Fig. 3.7. Though the first-order WENO reconstructions are able to suppress the spurious oscillations, it is clearly seen from Fig. 3.7 that discontinuities in the solution are excessively smeared (this is especially true for the transmitted and reflected shocks visible in the pressure and velocity plots). Using the flux limiters available in MFC (see Section 4.3.2 for details), we find that applying flux limiting to third-order WENO reconstructions is also somewhat successful in suppressing these spurious oscillations (flux-limited higher-order WENO schemes are *not strictly TVD*). The van Albada flux limiter, Eq. (4.42), was found to work well for this particular problem (results shown in Fig. 3.8). Although oscillations are still visible in the pressure plot at $t = 0.62\,\mathrm{ms}$, they are much smaller in amplitude than those seen in Fig. 3.5, and the excessive diffusion from using first-order WENO reconstructions is avoided. The origin of these spurious oscillations is, as of yet, undiagnosed. However, in simulations of aerobreakup, which are the main focus of this thesis, this issue is irrelevant. It is documented here for completeness' sake, and further investigation will be necessary to correct such behavior in MFC.

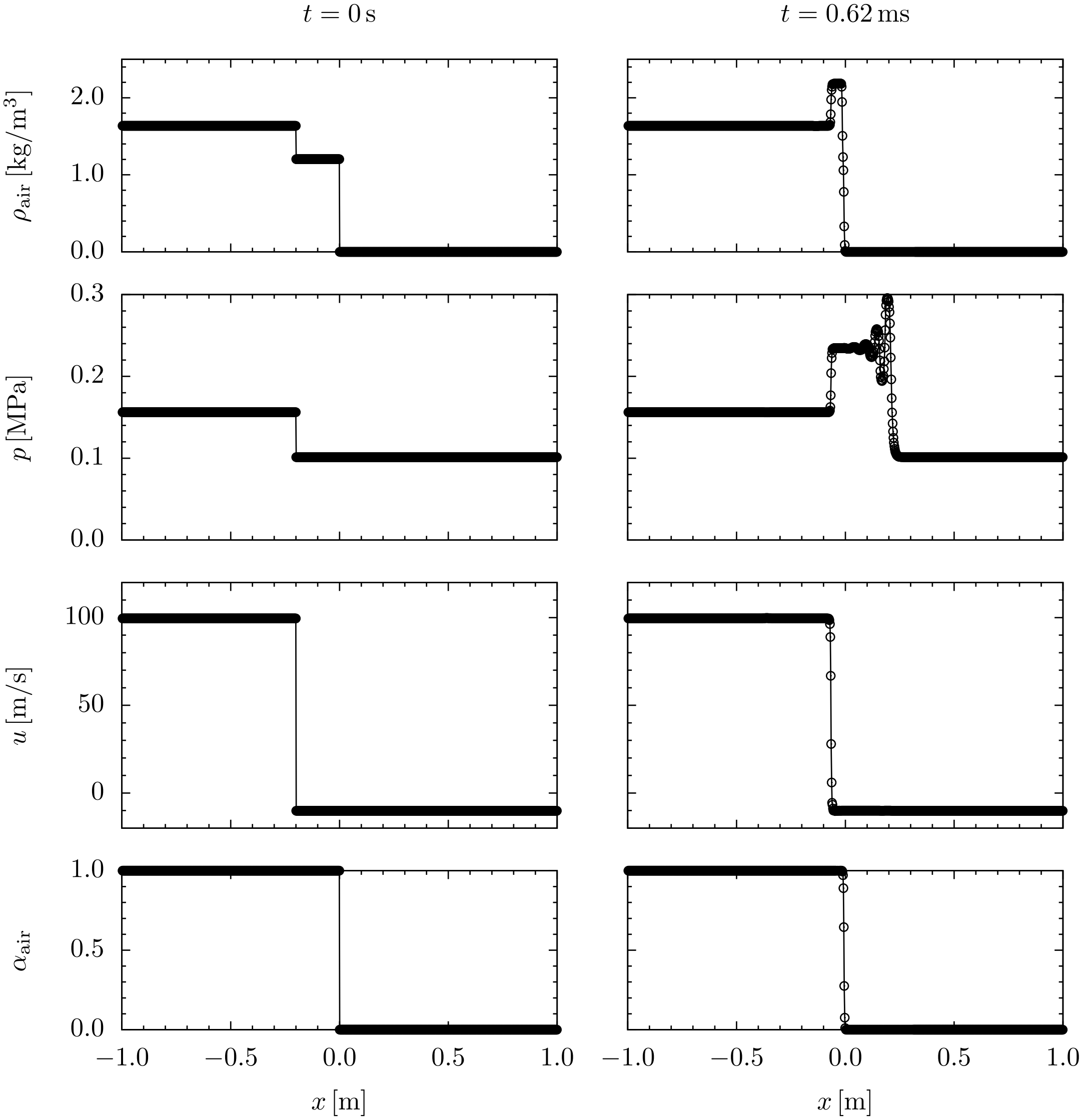

Figure 3.5: Mach 1.21 shock in air colliding with a traveling air-water interface. Plots of pressure, velocity, and air density and volume fraction are shown at two times.

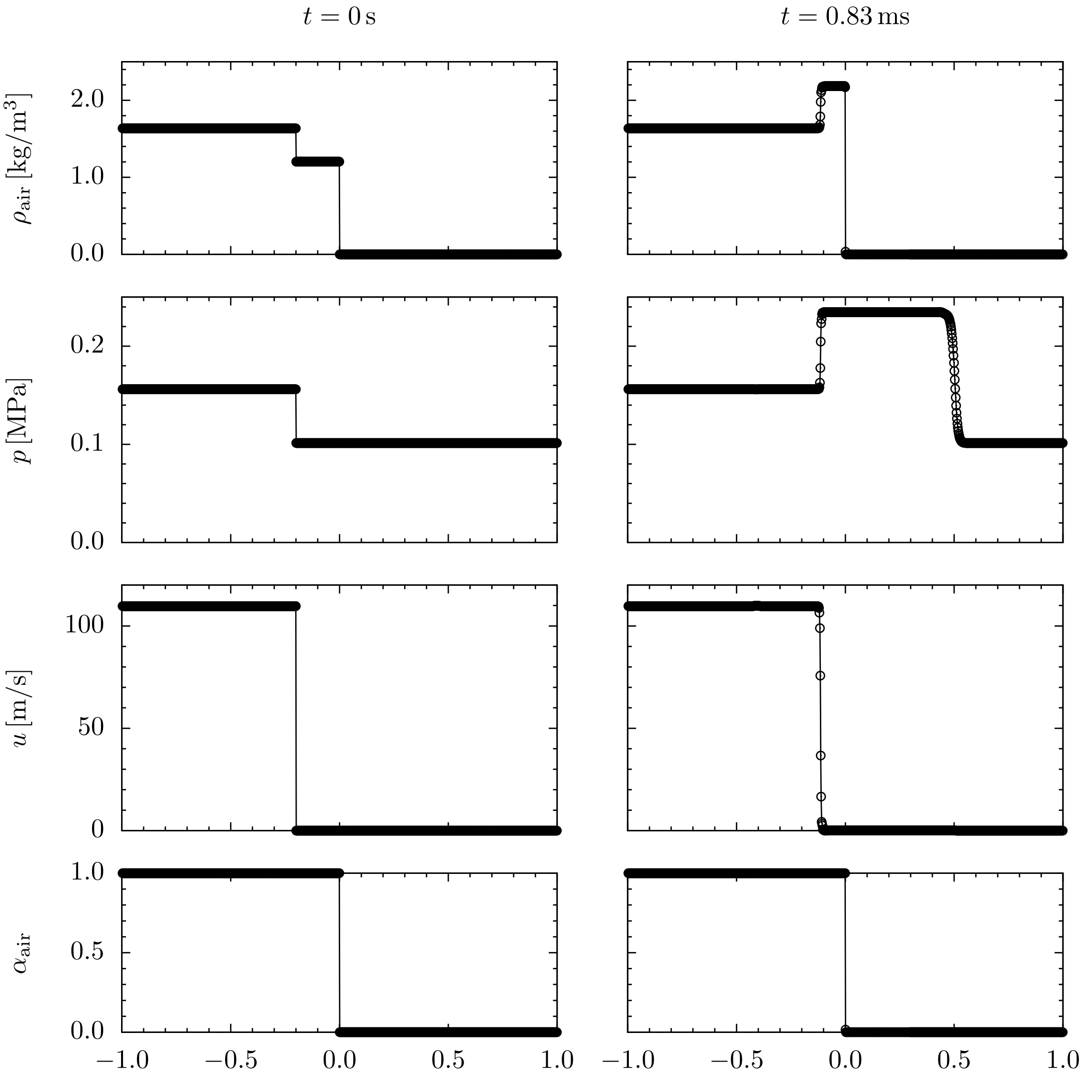

Figure 3.6: Mach 1.21 shock in air colliding with a stationary air-water interface. Plots of pressure, velocity, and air density and volume fraction are shown at two times.

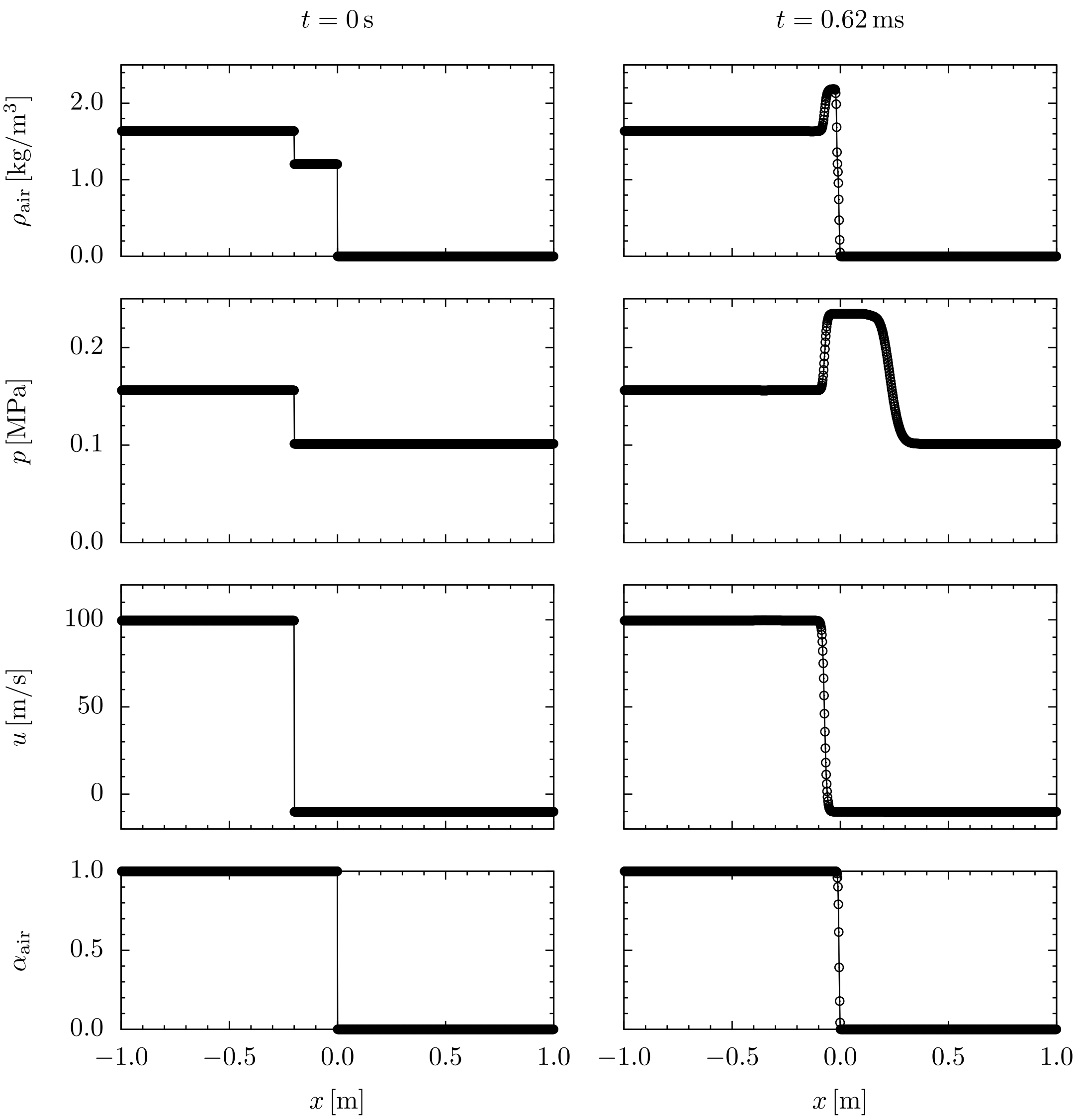

Figure 3.7: Mach 1.21 shock in air colliding with a traveling air-water interface using first-order WENO reconstructions. Plots of pressure, velocity, and air density and volume fraction are shown at two times.

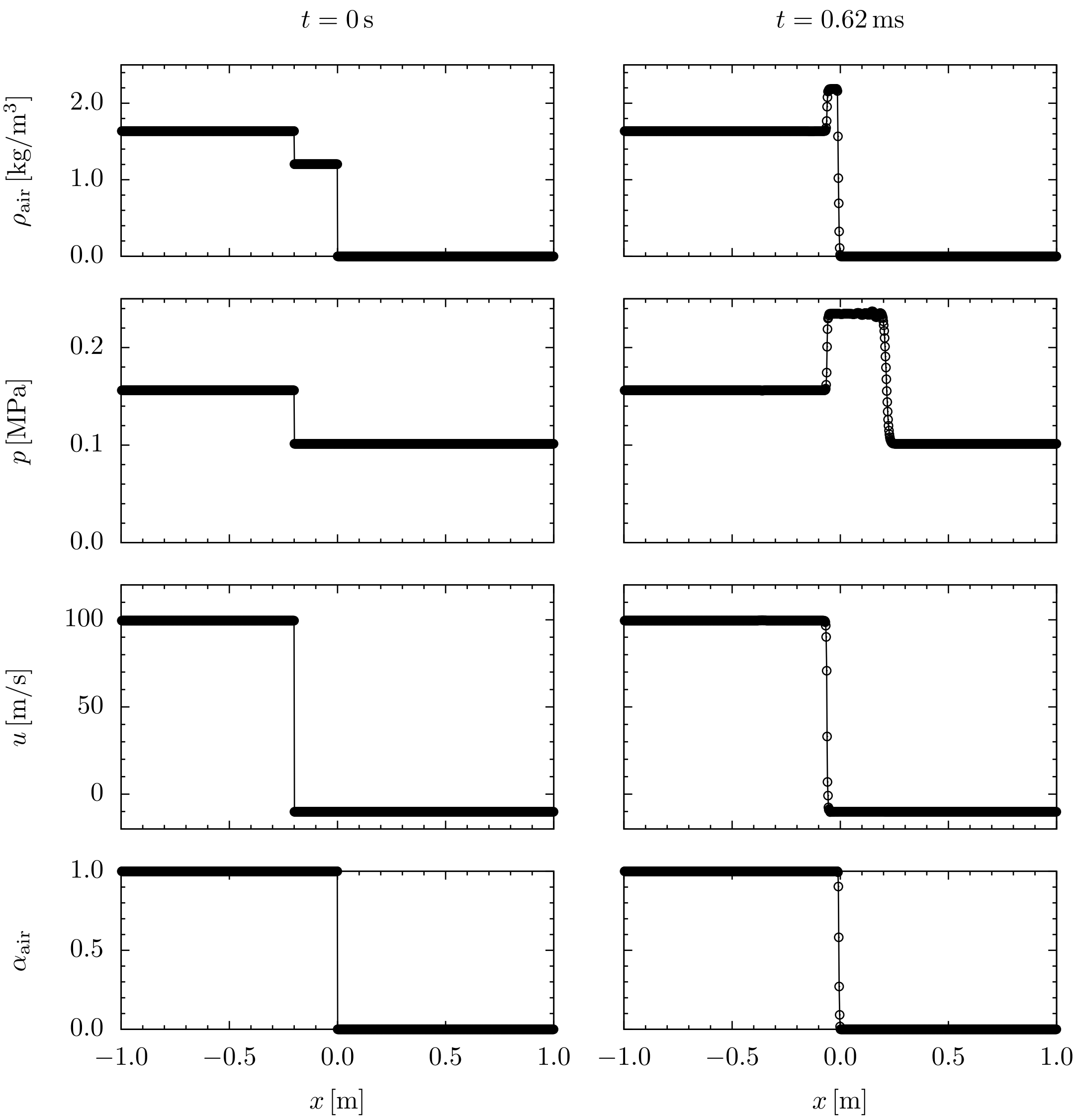

Figure 3.8: Mach 1.21 shock in air colliding with a traveling air-water interface using flux-limited third-order WENO reconstructions. Plots of pressure, velocity, and air density and volume fraction are shown at two times.

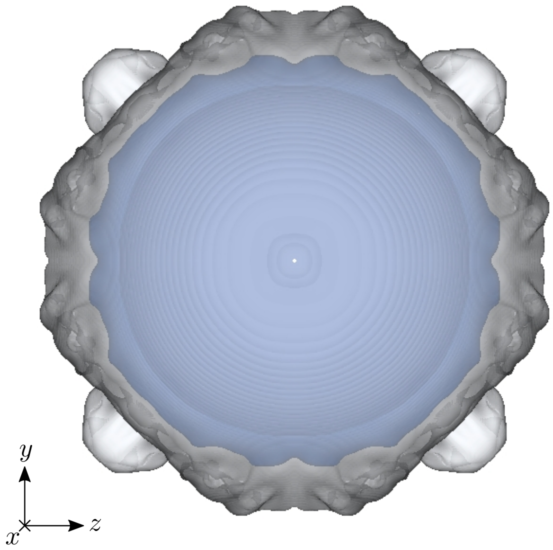

Figure 3.9: Translucent isosurfaces of the liquid volume fraction showing grid alignment effects in 3D Cartesian coordinates. Depicted isosurface values are $\alpha_l = 0.9, 0.5, 0.01$.

3.3.2 3D grid effects

Preliminary 3D simulations of aerobreakup using Cartesian coordinates revealed yet another challenging numerical issue. Specifically, numerical results from these simulations exhibit grid alignment effects that are resilient and persistent. The earliest 3D simulations had attempted to minimize computational cost by employing RBCs in both crossflow directions. When we visualized isosurfaces of the liquid volume fraction, we noticed that the droplet deformation was suspiciously aligned with the Cartesian axes, and resembled either a square or an octagon (see Fig. 3.9). Subsequent removal of the RBCs and simulation of the entire 3D flow field accomplished little in mitigating these grid alignment effects.

The unphysical nature of these grid effects are confirmed by two observations made during our investigation of this issue. Firstly, all simulations in our investigation of this numerical issue exhibit flow features that have four- or eight-fold symmetry. Not once do we observe features of n-fold symmetry, where n is some integer other than four or eight. Furthermore, these four- and eight-fold features are always aligned exactly with the Cartesian coordinate axes, or oriented at 45° to the axes. Attempts to artificially rotate the entire 3D flow field to some arbitrary angle with respect

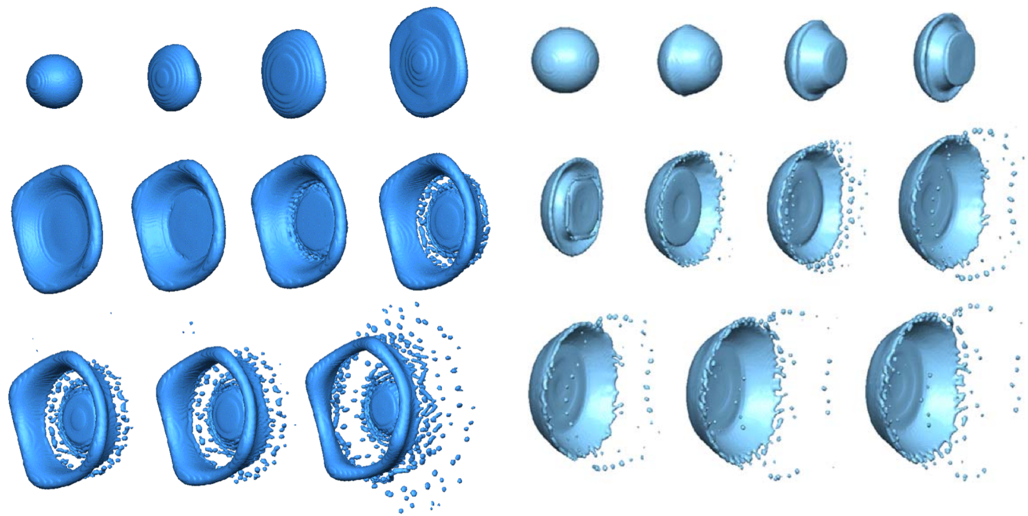

(a) Bag breakup

(b) Shear breakup

Figure 3.10: Grid alignment effects in reproduced Figs. 19 and 20 of [46].

to the Cartesian axes result in an unphysical swirling motion as the numerical method attempts to realign the flow field with the coordinate axes.

A literature search of other numerical investigations of 3D aerobreakup using Cartesian coordinates reveals that these grid alignment effects are not isolated to MFC. In what is referred to as "the most accurate study performed to date" [20], Khosla et al. [46] used the VOF method to investigate the aerobreakup of an ethanol drop in air. However, visualizations of their numerical results (reproduced in Fig. 3.10) reveal grid alignment effects that are not addressed by the authors. More recently, the work of Jalaal and Mehravaran [39] used an open-source code, Gerris, with adaptive mesh refinement (AMR) capabilities to study the initiation and growth of instabilities over droplets in a gas stream. Grid alignment effects are clearly visible in Fig. 3.11, reproduced from [39], which plots cross-sectional slices of the droplet at various streamwise locations. Once again, the grid effects are altogether ignored by the authors. Our literature search for grid effects in 3D Cartesian simulations resulted in two surprising observations. Firstly, the grid alignment effects seen in MFC and in the other numerical studies of aerobreakup, are not isolated to aerobreakup. In fact, they arise in completely other contexts including, e.g., astrophysics simulations [28]. Secondly, although these grid effects are present and observable in the literature, they are rarely acknowledged or discussed,

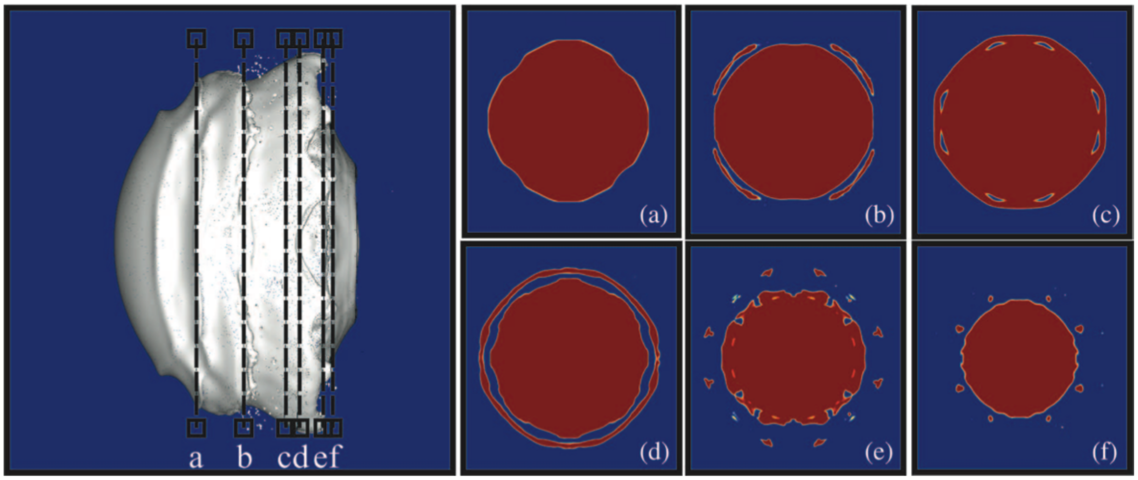

Figure 3.11: Grid alignment effects in reproduced Fig. 16 of [39]. Reprinted from Jalaal and Mehravaran [39] with the permission of AIP Publishing. © 2014 by AIP Publishing LLC.

and a clear solution does not exist. There do exist some unsplit numerical methods that claim to be less susceptible to grid effects, but even they do not claim to have completely solved the issue.

We proceed by documenting, in itemized form, the various fixes we tried to suppress or remove these grid alignment effects. Broadly, these changes are sorted into two categories: initialization changes and numerical method changes. We note upfront that *all of the following attempts to fix this grid effect issue were unsuccessful*, which ultimately resulted in the implementation of 3D cylindrical coordinates in MFC (see Section 4.2). Attempted initialization changes included:

- shifting the center of the droplet such that it did not coincide with a grid cell center, cell boundary, or cell vertex,
- increasing the stiffness of the droplet fluid to approximate flow past a solid sphere,
- adding random small-amplitude perturbations to both the ambient gas and the droplet surface,
- modifying the initial artificial smearing of the spherical interface onto the Cartesian grid,
- and orienting the streamwise flow direction such that it did not align with a coordinate axis.

Not only were these grid effects observable after slight modifications of the initial condition (IC) of the aerobreakup problem, but we could also observe them in an entirely different problem, specifically, the simulation of the free-field pressure-driven collapse of a bubble. After an initial collapse period driven by higher ambient pressure, the bubble reaches a minimum radius and then rebounds when the pressure inside grows sufficiently large. The initial collapse of a circular bubble on a 2D Cartesian grid does not exhibit any grid effects. However, once the minimum radius is reached, grid effects manifest as the bubble rebounds and radially expands. A representative result for this type of bubble collapse problem is shown in Section 3.3.2.2. Realizing that the grid effects are a more systemic issue, and are not isolated to specific initialization conditions, we progressed to modifying the numerical method. Attempted numerical method changes included:

- increasing both the grid resolution and formal order of accuracy of the numerical scheme,
- including viscous and capillary effects in the physical model to capture additional physics,
- and implementing interface sharpening schemes [77, 78, 93] in the context of our diffuse interface method.

Given the presence of grid alignment effects in the AMR code of Jalaal and Mehravaran [39], it is not at all surprising that increasing the grid resolution and the order of accuracy in our MFC simulations are unsuccessful. Inclusion of capillary effects has negligible impact on the simulations, while viscous effects, for $Re \leq \mathcal{O}(100)$, damps out the unphysical droplet deformation. However, at these low Re, the droplet deformation remains axisymmetric, which is uninteresting from an analysis standpoint, and the grid effects are not entirely suppressed as evidenced by the x-vorticity, ω_x, structures shown in Fig. 3.12. Finally, it was suggested to us by another researcher that the grid alignment effects in MFC are a direct consequence of our VOF diffuse interface method. Following their suggestion, we implemented two distinct interface sharpening methods: the interface regularization method of Tiwari et al. [93], and the anti-diffusion method of Shyue [77]. These methods are briefly explained and summarized in Sections 3.3.2.1 and 3.3.2.2.

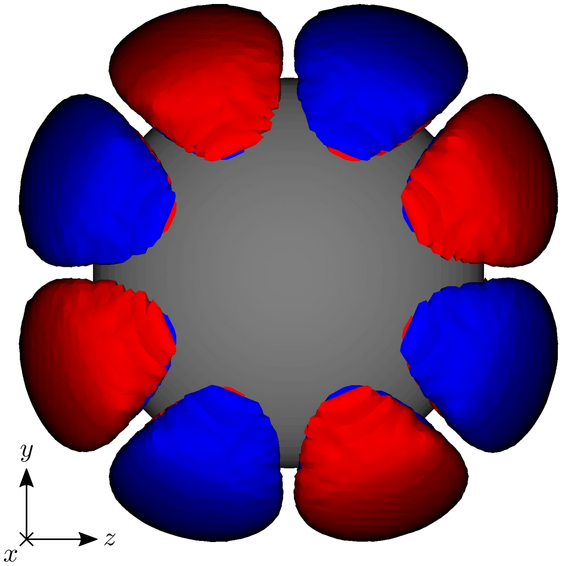

Figure 3.12: Grid-aligned streamwise vorticity structures around a drop ($D_0 = 10\,\mu$m, $Re \approx 270$). The droplet is shown using the $\alpha_l = 0.5$ isosurface (gray), and is surrounded by isosurfaces of positive (red) and negative (blue) x-vorticity, ω_x.

3.3.2.1 Interface regularization method

Following the work of Tiwari et al. [93], we first attempt to sharpen the diffuse interface using regularization terms. Without detailing the full derivation of the model, the final system of equations is reproduced here for completeness. For the stiffened gas EOS, the final reduced system with consistent regularization for two fluids is

$$\frac{\partial(\alpha_1\rho_1)}{\partial t} + \nabla\cdot(\alpha_1\rho_1\mathbf{u}) = \check{\mathcal{R}}_1, \tag{3.16a}$$

$$\frac{\partial(\alpha_2\rho_2)}{\partial t} + \nabla\cdot(\alpha_2\rho_2\mathbf{u}) = \check{\mathcal{R}}_2, \tag{3.16b}$$

$$\frac{\partial(\rho\mathbf{u})}{\partial t} + \nabla\cdot(\rho\mathbf{u}\otimes\mathbf{u}) + \nabla p = \mathbf{u}\check{\mathcal{R}}, \tag{3.16c}$$

$$\frac{\partial E}{\partial t} + \nabla\cdot\big((E+p)\mathbf{u}\big) = \kappa\check{\mathcal{R}} + \big(p(\Gamma_1-\Gamma_2) + (\Pi_{\infty,1}-\Pi_{\infty,2})\big)\mathcal{R}, \tag{3.16d}$$

$$\frac{\partial\alpha_1}{\partial t} + \mathbf{u}\cdot\nabla\alpha_1 = \alpha_1\alpha_2\frac{\rho_2c_2^2-\rho_1c_1^2}{\alpha_1\rho_2c_2^2+\alpha_2\rho_1c_1^2}\nabla\cdot\mathbf{u} + \mathcal{R}. \tag{3.16e}$$

For this model, the appropriate mixture sound speed is calculated as

$$\frac{1}{\rho c^2} = \frac{\alpha_1}{\rho_1c_1^2} + \frac{\alpha_2}{\rho_2c_2^2}, \tag{3.17}$$

where the individual fluid sound speeds are found using the EOS sound speed, Eq. (2.5). κ is the kinetic energy calculated as

$$\kappa = \frac{1}{2}\|\mathbf{u}\|^2, \tag{3.18}$$

and $\mathcal{R}, \check{\mathcal{R}}_1, \check{\mathcal{R}}_2$, and $\check{\mathcal{R}}$ are the so-called regularization terms, which are defined as follows:

$$\mathcal{R} = \mathcal{L}(\alpha_1)\mathcal{U}_0\hat{\mathbf{n}} \cdot \nabla\big(\epsilon\|\nabla\alpha_1\| - \alpha_1(1-\alpha_1)\big), \tag{3.19a}$$

$$\check{\mathcal{R}}_1 = \rho_1\mathcal{R} \approx \mathcal{L}(\alpha_1)\mathcal{U}_0\hat{\mathbf{n}} \cdot \Big(\nabla\big(\epsilon\hat{\mathbf{n}} \cdot \nabla(\alpha_1\rho_1)\big) - (1-2\alpha_1)\nabla(\alpha_1\rho_1)\Big), \tag{3.19b}$$

$$\check{\mathcal{R}}_2 = -\rho_2\mathcal{R} \approx \mathcal{L}(\alpha_1)\mathcal{U}_0\hat{\mathbf{n}} \cdot \Big(\nabla\big(\epsilon\hat{\mathbf{n}} \cdot \nabla(\alpha_2\rho_2)\big) - (1-2\alpha_1)\nabla(\alpha_2\rho_2)\Big), \tag{3.19c}$$

$$\check{\mathcal{R}} = \check{\mathcal{R}}_1 + \check{\mathcal{R}}_2. \tag{3.19d}$$

ϵ, which is a parameter explicitly controlled by the user, is on the order of the grid spacing and defines the interface thickness. The interface normal

$$\hat{\mathbf{n}} = \frac{\nabla\alpha_1}{\|\nabla\alpha_1\|}, \tag{3.20}$$

directs the operation across the interface,

$$\mathcal{L}(\alpha_1) = \begin{cases} 1 & \text{for } 10^{-6} < \alpha_1 < 1 - 10^{-6}, \\ 0 & \text{otherwise,} \end{cases} \tag{3.21}$$

and $\mathcal{U}_0$, which represents the characteristic regularization rate, is defined as

$$\mathcal{U}_0 = \|\mathbf{u}_I\|_{\max} = \frac{\big(\alpha_1(1-\alpha_1)\|\mathbf{u}\|\big)_{\max}}{\big(\alpha_1(1-\alpha_1)\big)_{\max}} = 4\big(\alpha_1(1-\alpha_1)\|\mathbf{u}\|\big)_{\max}, \tag{3.22}$$

where $\|\mathbf{u}_I\|_{\max}$ is the maximum value taken over the entire computational domain.

No results are shown here for the interface regularization method for several reasons. From our testing of the model, numerical results are strongly dependent on the choice of model parameter ϵ, which is user-defined and must be tuned for individual problems. There does not seem to be any sort of guidelines for the choice of ϵ. Further complicating matters, we find that overall code stability is sensitive to the choice of ϵ, resulting, more often than not, in abrupt termination of the code. Since ϵ is intimately tied to both model behavior and code stability, a choice of ϵ for a given simulation made from stability considerations may result in undesirable model behavior. Because of the ambiguity in the choice of the model parameter ϵ, and the severe degradation of code stability, the interface regularization method is determined to be unsuitable for our needs.

3.3.2.2 Anti-diffusion method

We next consider an anti-diffusion method for sharpening interfaces adapted from the work of Shyue [77] and Shyue and Xiao [78]. The equations for a system of two fluids is shown below. Notations have been slightly changed from the original to clarify parallels between this anti-diffusion method and the interface regularization method of Tiwari et al. [93].

$$\frac{\partial(\alpha_1\rho_1)}{\partial t} + \nabla\cdot(\alpha_1\rho_1\mathbf{u}) = -\mathcal{L}\mathcal{U}_0\nabla\cdot\big(\mathcal{D}\nabla(\alpha_1\rho_1)\big), \tag{3.23a}$$

$$\frac{\partial(\alpha_2\rho_2)}{\partial t} + \nabla\cdot(\alpha_2\rho_2\mathbf{u}) = -\mathcal{L}\mathcal{U}_0\nabla\cdot\big(\mathcal{D}\nabla(\alpha_2\rho_2)\big), \tag{3.23b}$$

$$\frac{\partial(\rho\mathbf{u})}{\partial t} + \nabla\cdot(\rho\mathbf{u}\otimes\mathbf{u}) + \nabla p = -\mathcal{L}\mathcal{U}_0\mathbf{u}\nabla\cdot(\mathcal{D}\nabla\rho), \tag{3.23c}$$

$$\frac{\partial E}{\partial t} + \nabla\cdot\big((E+p)\mathbf{u}\big) = -\mathcal{L}\mathcal{U}_0\big(\kappa\nabla\cdot(\mathcal{D}\nabla\rho) + (\rho_1\varepsilon_1 - \rho_2\varepsilon_2)\nabla\cdot(\mathcal{D}\nabla\alpha_1)\big), \tag{3.23d}$$

$$\frac{\partial\alpha_1}{\partial t} + \mathbf{u}\cdot\nabla\alpha_1 = -\mathcal{L}\mathcal{U}_0\nabla\cdot(\mathcal{D}\nabla\alpha_1), \tag{3.23e}$$

where $\mathcal{L}$,$\mathcal{U}_0$ and κ are, respectively, the interface-locating function, Eq. (3.21), the characteristic regularization rate, Eq. (3.22), and the kinetic energy, Eq. (3.18). ε is the specific internal energy computed from the equation of state. $\mathcal{D} = \|\mathbf{u}\|$ serves as the diffusion coefficient, which is set as the magnitude of the local velocity field. The gradients on the right-hand side (RHS) of Eq. (3.23) are calculated using a minmod function [80]. The algorithm to solve Eq. (3.23) consists of a two-step method. The homogeneous system is first solved using the numerical framework described in Chapter 3. An inner time step is then taken (the second step of the two-step algorithm) that solves the system with the anti-diffusive source terms using a straightforward Euler method. In practice, one or two iterations of the inner time step are sufficient for interface sharpening purposes [77]. For stability, the size of the inner time step, $\Delta\tau$, is restricted by

$$\Delta\tau \leq \min\left(\Delta t, \frac{\min(\Delta x^2, \Delta y^2, \Delta z^2)}{2N\mathcal{D}_{\max}}\right), \tag{3.24}$$

where N is the dimensionality of the simulation, and $\mathcal{D}_{\max}$ is the maximum value of $\mathcal{D}$ taken over the entire computational domain [78].

We test the interface sharpening capability of the anti-diffusion method by simulating the 2D free-field pressure-driven collapse of a bubble. A stationary air bubble of diameter D_0 is initialized in water ($\rho_l = 1009.37\,\mathrm{kg/m^3}$). The pressure inside the bubble is $p_g = 1\,\mathrm{atm}$, while the water is at $p_l = 200\,\mathrm{atm}$. RBCs are employed in both directions such that only a quarter of the bubble is simulated. The effective computational domain is $\Omega = [-5D_0, 5D_0] \times [-5D_0, 5D_0]$ such that boundary effects do not influence the bubble collapse physics. For the quarter domain, 300 grid cells are used in each direction (the grid is stretched towards the far field) with a near-field resolution of 200 cells per original bubble diameter. Because of the large pressure ratio across the interface, the bubble initially collapses. A minimum bubble radius is reached when the rising pressure inside the bubble becomes greater than the ambient pressure; this initiates the bubble rebound and subsequent expansion. During the collapse phase of the bubble, no grid alignment effects are observed, i.e., the initially circular bubble interface retains its circular shape as the bubble collapses. However, once the minimum radius is reached, and the bubble begins to rebound, grid alignment effects are observed in the shape of the expanding bubble interface. Figure 3.13 plots the liquid volume fraction, α_l, at a time instant during the rebound of the bubble when grid alignment effects are clearly visible in the interface shape. Unfortunately, although the anti-diffusion method succeeds in its interface sharpening role, the sharpened interface does little to mitigate the grid alignment effects that we are primarily concerned with.

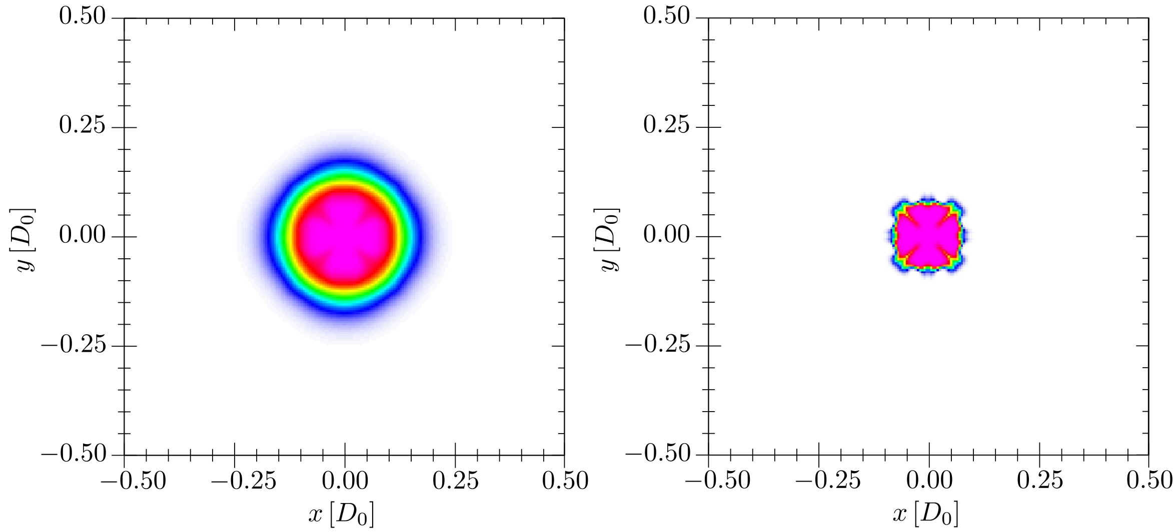

Figure 3.13: Grid alignment effects in the rebound of a free-field pressure-driven bubble collapse. Filled contours of α_l are plotted for simulations with (right) and without (left) anti-diffusion interface sharpening.

3.4 Summary

In this chapter, we present a high-level overview of the numerical method as implemented in the MFC flow solver. The VOF method is the interface-capturing scheme of choice, and the governing equations are spatially discretized onto a Cartesian grid. Within a finite-volume framework, WENO reconstructions and the HLLC approximate Riemann solver are used in a Godunov-type method. Temporal integration is accomplished using a TVD Runge-Kutta time-marching scheme. Clarifications are made on numerical viscosity and breakup mechanism in the absence of molecular viscosity and surface tension modeling. Additional details of the numerical method are available in the references provided herein. Numerical droplet diagnostics, used to quantify metrics of droplet deformation and behavior, are derived and explained. To define a nominal interface location, the threshold liquid volume fraction approach is adopted. Accurate integral expressions for the droplet's center-of-mass displacement, velocity, and acceleration are derived. Finally, two challenging numerical issues associated with MFC are documented along with attempted solutions. The first numerical issue, though not directly applicable to simulations in this thesis, is associated with spurious oscillations that occur when a shock interacts with an interface moving at an appreciable velocity. Flux limiting is shown to mitigate these oscillations, but their exact origin and a rigorous solution remain unclear. The second numerical issue, associated with grid effects in 3D Cartesian simulations, is documented and serves as the primary motivator for the implementation of cylindrical coordinates in Chapter 4.

Chapter 4

Improvements to MFC

4.1 Surface tension model implementation

4.1.1 Motivation and overview

The inclusion of capillary effects into the five-equation model of Section 2.3.1 is primarily motivated by the desire to more accurately model liquid-gas interface dynamics. The importance of the Weber number in classifying the various regimes of breakup indicates the significant role that surface tension plays in the breakup physics. Specifically, in the regime of stripping breakup, capillary forces are responsible for the breakup of the liquid sheet that is stripped off the periphery of the droplet. For simulations of other compressible, multicomponent flows, e.g., the cavitation and collapse of both individual bubbles and bubble clouds, surface tension also plays a key role in properly modeling the complicated interface physics. In this section, we describe the model that has been implemented in MFC to capture capillary effects in Cartesian coordinates. A conservative formulation of the model, detailed in Section 4.1.2, is reproduced from the work of Perigaud and Saurel [65]. Unfortunately, all attempts to render this formulation free of spurious oscillations have been unsuccessful. Consequently, Section 4.1.3 describes a nonconservative formulation that has been verified and is oscillation-free. A brief explanation on the calculation of the interface normals and surface curvatures is included in Section 4.1.4, while verification of the model via Laplace pressure and oscillating ellipse test cases are shown in Section 4.1.5.

4.1.2 Conservative formulation

The following conservative formulation of a model for surface tension was validated by the original authors [65] through various test cases, but an analysis of the presence of parasitic currents in the model was not performed. The authors stated that, in their experience, the parasitic currents are always sufficiently small to preserve the validity of their results, and never lead to computational failure. Unfortunately, we did not find this to be the case. All of the test cases we tried using the conservative formulation suffered from large spurious oscillations that destroyed the integrity of the simulation, and often led to computational failure. Our inability to successfully implement this conservative formulation is what ultimately drove us to the nonconservative formulation of Section 4.1.3. Despite the model's shortcomings, we include here a description of the conservative formulation for the sake of completeness.

Following the work of Perigaud and Saurel [65], a compressible two-phase flow model with surface tension effects can be written as

$$\frac{\partial(\alpha_1\rho_1)}{\partial t} + \nabla\cdot(\alpha_1\rho_1\mathbf{u}) = 0, \tag{4.1a}$$

$$\frac{\partial(\alpha_2\rho_2)}{\partial t} + \nabla\cdot(\alpha_2\rho_2\mathbf{u}) = 0, \tag{4.1b}$$

$$\frac{\partial(\rho\mathbf{u})}{\partial t} + \nabla\cdot(\rho\mathbf{u}\otimes\mathbf{u} + p\mathbf{I} - \mathbf{T}_\sigma) = \mathbf{0}, \tag{4.1c}$$

$$\frac{\partial\mathcal{E}}{\partial t} + \nabla\cdot\big((\mathcal{E}+p)\mathbf{u} - \mathbf{T}_\sigma\cdot\mathbf{u}\big) = 0, \tag{4.1d}$$

$$\frac{\partial\alpha_1}{\partial t} + \mathbf{u}\cdot\nabla\alpha_1 = 0. \tag{4.1e}$$

This is reminiscent of the viscous five-equation model, Eq. (2.1), where viscous effects have now been replaced by capillary effects. The capillary stress tensor, $\mathbf{T}_\sigma$, defined as

$$\mathbf{T}_\sigma = \sigma\left(\|\mathbf{m}\|\mathbf{I} - \frac{\mathbf{m}\otimes\mathbf{m}}{\|\mathbf{m}\|}\right), \tag{4.2}$$

is written such that the surface force of Brackbill et al. [8] may be written as

$$F_{sv} = \nabla \cdot \mathbf{T}_{\sigma}. \tag{4.3}$$

According to Brackbill et al. [8], the surface force, F_{sv}, is equivalent to

$$F_{sv} = \sigma\kappa \frac{\nabla\psi}{[\psi]}, \tag{4.4}$$

where σ is the surface tension coefficient, κ is the surface curvature, ψ denotes a color function that locates the interface, and $[\psi]$ is the color function jump across the interface. In a VOF framework, the liquid volume fraction fulfills all the necessary requirements of the color function. Namely, it remains constant in each fluid except in a small neighborhood of the interface, is always oriented toward the heaviest fluid, and is continuously differentiable. For conciseness, we define

$$\mathbf{m} = \nabla\alpha_l, \tag{4.5}$$

and note that $[\psi] = 1$ for an interface separating pure fluids. Finally, the conserved variable in the energy equation, Eq. (4.1d), is the mixture total energy defined as

$$\mathcal{E} = E + \sigma\|\mathbf{m}\|, \tag{4.6}$$

where $\sigma\|\mathbf{m}\|$ is the capillary potential energy.

4.1.3 Nonconservative formulation

Perigaud and Saurel [65] note that if the energy equation is expanded, the conservative model, Eq. (4.1), can be written in the following nonconservative form:

$$\frac{\partial(\alpha_1\rho_1)}{\partial t} + \nabla\cdot(\alpha_1\rho_1\mathbf{u}) = 0, \tag{4.7a}$$

$$\frac{\partial(\alpha_2\rho_2)}{\partial t} + \nabla\cdot(\alpha_2\rho_2\mathbf{u}) = 0, \tag{4.7b}$$

$$\frac{\partial(\rho\mathbf{u})}{\partial t} + \nabla\cdot(\rho\mathbf{u}\otimes\mathbf{u} + p\mathbf{I}) = -\sigma\kappa\nabla\alpha_1, \tag{4.7c}$$

$$\frac{\partial E}{\partial t} + \nabla\cdot\big((E+p)\mathbf{u}\big) = -\sigma\kappa\left(\mathbf{u}\cdot\nabla\alpha_1\right), \tag{4.7d}$$

$$\frac{\partial \alpha_1}{\partial t} + \mathbf{u}\cdot\nabla\alpha_1 = 0. \tag{4.7e}$$

This nonconservative formulation has removed the capillary stress tensor, and replaced it with relatively simple source terms on the RHS of the momentum and energy equations. These source terms, much like the surface force [8], are composed of the surface tension coefficient, σ, surface curvature, κ, and volume fraction gradient. Since the model is nonconservative, an estimate of the error in discrete conservation is included in the verification.

4.1.4 Calculation of interface normals and surface curvature

The conventional method of calculating the interface normal in a VOF framework is to compute the normalized gradient of the volume fraction, Eq. (3.20), using simple finite-difference approximations. For a diffuse interface method, the calculation of the surface curvature is not as straightforward. Brackbill et al. [8] derived the surface curvature as

$$\kappa = -\nabla\cdot\hat{\mathbf{n}}, \tag{4.8}$$

where $\hat{\mathbf{n}}$ is the normalized gradient of the color function, ψ. They also noted that Eq. (4.8) could be written as

$$\kappa = \frac{1}{\|\mathbf{n}\|}\left(\left(\frac{\mathbf{n}}{\|\mathbf{n}\|}\cdot\nabla\right)\|\mathbf{n}\| - (\nabla\cdot\mathbf{n})\right), \tag{4.9}$$

which was claimed to give better results in practice due to the principal contributions coming from the center of the transition region of ψ. As mentioned in Section 4.1.2, the liquid volume fraction fulfills the necessary requirements to serve as the color function. After trying both Eqs. (4.8) and (4.9) in MFC, we found that these formulations resulted in noisy surface curvature fields that adversely impacted our surface tension model. Consequently, we decided to calculate the interface curvature using a third-order, least squares polynomial fit of the local volume fraction field [15]. Originally developed for level set methods where it was applied to the entire level set field, the least squares fitting procedure of Della Rocca and Blanquart [15] (including their modified polynomial stencils) provides sufficiently smooth interface normal and curvature fields.

4.1.5 Verification and convergence

We proceed to verify our capillary model, Eq. (4.7), using two benchmark test cases: the Laplace pressure jump, and oscillations of a deformed droplet. Discrete momentum conservation errors arising from the nonconservative formulation are checked, and are confirmed to remain small.

4.1.5.1 Laplace pressure jump

The surface tension of a curved material interface between a liquid and a gas supports a pressure difference across the interface known as the Laplace pressure, which for a general curved interface in 3D [65] is

$$\Delta p = \sigma(\kappa_1 + \kappa_2), \tag{4.10}$$

where κ_1 and κ_2 are the main local interface curvatures. In 2D, the Laplace pressure for an infinite cylinder (also called an “equilibrium rod” [8]) is

$$\Delta p = \sigma\kappa = \frac{\sigma}{R}, \tag{4.11}$$

where R is the radius of the cylinder. If a capillary model is wholly successful, one should be able to hold the Laplace pressure jump across an interface without generating any spurious velocity currents. In practice, however, this is a demanding test case, and most capillary models will generate small velocity currents near the material interface.

N	N_d	L_2
100	68	5.53×10^{-6}
200	936	1.25×10^{-6}
400	5592	0.31×10^{-6}

Table 4.1: Convergence results for Laplace pressure jump test case.

We consider a 2D water droplet of diameter $D_0 = 10\,\mu$m surrounded by quiescent air at atmospheric pressure, $p_\infty = 101325\,$Pa. From Eq. (4.11), the Laplace pressure jump is $\Delta p = 14572\,$Pa, since the surface tension coefficient between air and water is $\sigma = 0.07286\,$N/m. The computational domain extends $1.5D_0$ out in either direction such that $\Omega = [-2D_0, 2D_0] \times [-2D_0, 2D_0]$, and terminates with periodic boundary conditions (BCs). Using uniform grids with spatial resolutions of $N = 100, 200, 400$ cells in each direction, we compute root-mean-square (RMS) errors [8] at a physical time of approximately $t = 2.76\,\mu$s (this physical time corresponds to 2×10^5 time steps for the finest resolution case running at $\mathcal{C} \approx 0.2$). The L_2-norm is computed as

$$L_2 = \left(\frac{\sum_{i,j=1}^{N_d} \left((p_{i,j} - p_\infty) - \Delta p \right)^2}{N_d \cdot (\Delta p)^2} \right)^{1/2}, \tag{4.12}$$

where N_d is the number of cells lying within the drop as defined by $\alpha_l \geq 0.98$. The results are tabulated in Table 4.1, and the convergence plot is shown as Fig. 4.1. Our capillary model is seen to be mesh convergent, with an approximately second-order convergence rate. Since we are using a nonconservative model for surface tension, Eq. (4.7), we proceed to check the resultant errors in the discrete conservation of the momentum equations to make sure they remain small. Since the simulations were initialized at rest, all momenta in the computational domain are a consequence of the source term used to model capillary effects. Figure 4.2 shows the total momenta for all three resolutions integrated over the computational domain as

$$\mathbf{p}_\Omega = \int_\Omega \mathbf{p}\, \mathrm{d}A, \tag{4.13}$$

where $\mathbf{p}$ is the momentum vector. Recalling that most capillary models will generate small spurious

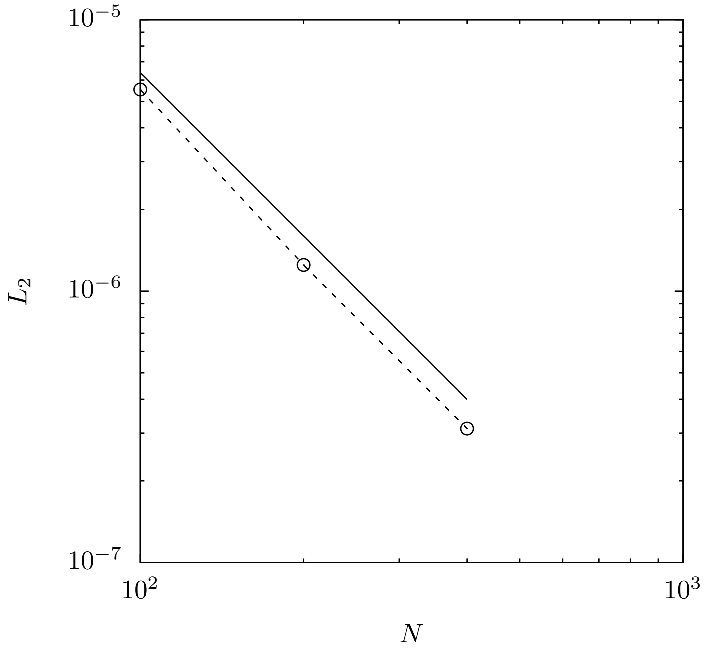

Figure 4.1: Grid convergence of the L_2-norm for the Laplace pressure jump test case. A reference slope for second-order convergence (continuous) is included.

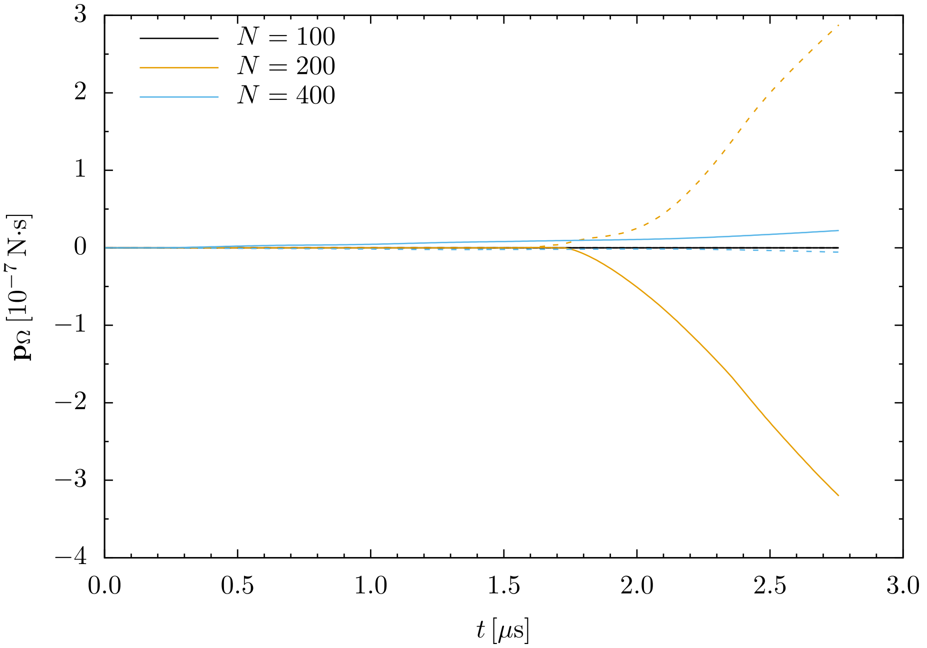

Figure 4.2: Discrete momentum conservation errors in the x-coordinate (continuous) and y-coordinate (dashed) for the Laplace pressure jump test case.

velocity currents near the interface where the mixture density is relatively large, the values of $\mathbf{p}_\Omega$ shown in Fig. 4.2 are considered to be acceptable, and are not cause for concern.

4.1.5.2 Oscillation of elliptical interface

The oscillations of a deformed droplet under the effects of surface tension are a useful test of a model's ability to capture the dynamical effects of capillary forces. Consider an interface at rest, initialized in 2D as an oblate ellipse. Initially, all the energy in the system exists as capillary potential energy arising from the large deformations of the interface. When the simulation is started, capillary forces attempt to restore the interface to a state of equilibrium, i.e., a perfect circle. As capillary potential energy is converted into kinetic energy, the interface is set into motion. The interface is successfully restored to its equilibrium state for a brief instant; however, the kinetic energy at this point is too large for the interface to remain at equilibrium. Therefore, the interface continues to deform into a prolate ellipse, converting the kinetic energy back into capillary potential energy. Once all the kinetic energy is gone, capillary potential energy, once again, forces the interface to deform back through the equilibrium state into its initial state of an oblate ellipse. Thus, the observed oscillations of a deformed droplet are the consequence of energy transfer between kinetic energy and capillary potential energy. The period of these oscillations is defined as the time required for the deformed droplet to return to its original state, and thus corresponds to two cycles of kinetic energy. We can calculate the theoretical period of oscillation [65] as

$$T = 2\pi\sqrt{\frac{(\rho_1 + \rho_2)R_0^3}{6\sigma}}, \tag{4.14}$$

where ρ_1 and ρ_2 are the fluid densities on either side of the material interface, and R_0 is an equivalent equilibrium radius.

For our test case, we consider a 2D liquid droplet initialized as an ellipse whose shape is given by

$$\frac{x^2}{1.25} + \frac{y^2}{0.8} = 1, \tag{4.15}$$

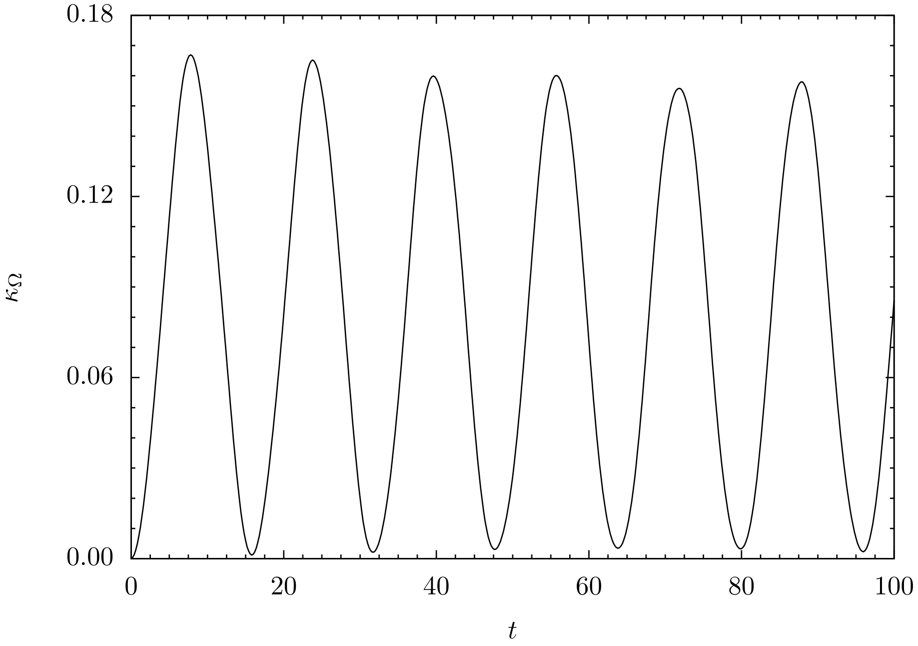

Figure 4.3: Kinetic energy of an oscillating elliptical droplet due to capillary forces.

such that the equivalent equilibrium radius (based on area) is $R_0 = 1$. The static droplet is surrounded by quiescent gas, which fills the rest of the computational domain, $\Omega = [-2, 2] \times [-2, 2]$. Periodic BCs are employed in all directions. Following Shukla [76], we take the nondimensional gas and liquid properties to be $(\rho, \gamma, \pi_\infty)_g = (1, 1.4, 0)$ and $(\rho, \gamma, \pi_\infty)_l = (100, 4.4, 100)$. The EOS parameters for the liquid have been chosen such that the acoustic time scale, which determines the maximum allowable time step, is not orders of magnitude smaller than the time period of oscillation. The surface tension coefficient between these two fluids is $\sigma = 0.72$. Initial pressures for the gas and liquid are, respectively, $p_g = 1$ and $p_l = 1.72$. With these fluid parameters, we calculate the theoretical period of oscillation to be $T = 30.38$ in nondimensional time units. Using a uniform grid with a spatial resolution of $N = 200$ cells in each direction, we simulate the oscillating droplet for approximately three periods. Figure 4.3 shows the total kinetic energy in the computational domain calculated as

$$\kappa_\Omega = \frac{1}{2} \int_\Omega \rho \|\mathbf{u}\|^2 \, \mathrm{d}A. \tag{4.16}$$

Recalling that a droplet oscillation period corresponds to two cycles of kinetic energy, we calculate the

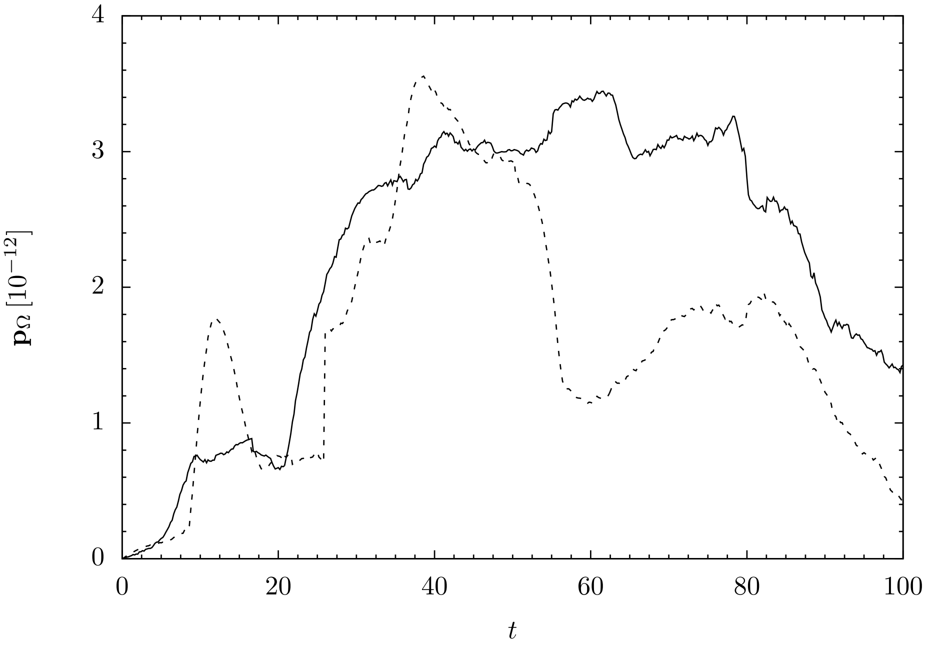

Figure 4.4: Discrete momentum conservation errors in the x-coordinate (continuous) and y-coordinate (dashed) for the oscillating elliptical interface test case.

numerical period of oscillation to be, on average, $T = 32$, which compares well with the theoretical value. The amplitude of the oscillations is seen to slowly decrease with time, which is attributed to the numerical dissipation present in the numerical scheme. We, again, check the discrete conservation errors in the momentum equations by calculating $\mathbf{p}_\Omega$, Eq. (4.13), which is plotted in Fig. 4.4. For this test case, the discrete conservation errors remain on the order of machine precision.

4.2 Cylindrical coordinates implementation

4.2.1 Motivation and overview

Motivated by the grid effects seen in the 3D Cartesian coordinates simulations (described in Section 3.3.2), MFC has been expanded to allow for 3D simulations in cylindrical coordinates. Despite the challenges associated with solving the governing equations on a cylindrical grid, the grid geometry itself provides a more natural representation of the geometry of the physical aerobreakup problem.

Generally, numerical methods associated with flow solvers using cylindrical coordinates must overcome two difficulties. Firstly, they must have a method of treating the axis singularity that arises as $r \to 0$. Secondly, due to the nature of the cylindrical grid, computational cells with a fixed $\Delta\theta$ decrease in size like $\Delta\theta^2$ as $r \to 0$. This leads to a strict restriction on the CFL condition, that, if not handled appropriately, can make numerical simulations prohibitively expensive. The remainder of this section is organized as follows. Section 4.2.2 first details how the governing equations are spatially discretized in cylindrical coordinates. The calculations of the diffusive fluxes and source terms are explained in Section 4.2.3. Sections 4.2.4 and 4.2.5 then describe the methods we use to overcome the aforementioned challenges of the axis singularity and time step restriction. Finally, convergence of the method is shown in Section 4.2.6.

4.2.2 Spatial discretization

Reminiscent of the spatial discretization in Cartesian coordinates shown in Eq. (3.1), the five-equation model with viscous effects of Section 2.3.1 is discretized onto a cylindrical grid in the following conservative form:

$$\frac{\partial \mathbf{q}}{\partial t} + \frac{\partial \mathbf{f}^a(\mathbf{q})}{\partial z} + \frac{\partial \mathbf{g}^a(\mathbf{q})}{\partial r} + \frac{\partial \mathbf{h}^a(\mathbf{q})}{\partial \theta} = \frac{\partial \mathbf{f}^d(\mathbf{q})}{\partial z} + \frac{\partial \mathbf{g}^d(\mathbf{q})}{\partial r} + \frac{\partial \mathbf{h}^d(\mathbf{q})}{\partial \theta} + \mathbf{s}^a(\mathbf{q}) + \mathbf{s}^d(\mathbf{q}), \tag{4.17}$$

where $\mathbf{q}$ is the vector of conservative variables, $\mathbf{f}(\mathbf{q}), \mathbf{g}(\mathbf{q})$, and $\mathbf{h}(\mathbf{q})$ are flux vectors, $\mathbf{s}(\mathbf{q})$ are source term vectors, and the superscripted "a" and "d" again denote, respectively, advective and diffusive fluxes (see details in Appendix A.2). Equations (3.1) and (4.17) are intentionally similar. The primary difference between the two equations lies in the source term vectors, $\mathbf{s}(\mathbf{q})$. In Cartesian coordinates, $\mathbf{s}^a(\mathbf{q})$ has only one nonzero element for the volume fraction transport equation (see Eq. (A.4)), which is necessary to adapt Eq. (2.1e) to the Riemann solver. In cylindrical coordinates, the divergence operator on an arbitrary vector, $\mathbf{v} = (v_z, v_r, v_\theta)^T$, is

$$\nabla \cdot \mathbf{v} = \frac{\partial v_z}{\partial z} + \frac{\partial v_r}{\partial r} + \frac{v_r}{r} + \frac{1}{r}\frac{\partial v_\theta}{\partial \theta}. \tag{4.18}$$

Following Johnsen [40], our approach, then, in implementing cylindrical coordinates into MFC, is to move all the $\frac{v_r}{r}$ terms to the RHS as geometrical source terms in $\mathbf{s}(\mathbf{q})$. This results in the advective and diffusive source term vectors shown in Eq. (A.9). By discretizing the governing equations in this manner, the source terms account for all cylindrical geometry effects, and the left-hand side (LHS) can effectively be treated as if one were working in Cartesian coordinates.

The reconstruction of the state variables from the cell center to the cell boundaries is performed using the same third-order WENO scheme used in Cartesian coordinates. Using the Cartesian WENO weights and polynomials, formal order of accuracy is retained in the axial and radial coordinates, while not guaranteed in the azimuthal coordinate. Though derivations of WENO weights and polynomials for curvilinear coordinate systems exist within the literature [52, 61, 96], they each suffer from various issues that make them unsuitable for our purposes. The work of Li [52] derived a second-order WENO scheme in a finite-difference framework, but the method added such complexity and cost to the simulation that the author questioned whether the additional effort was worth the investment for such low order of accuracy. Wang and Johnsen [96] recently proposed a high-order accurate and conservative scheme, but assumed cylindrical/spherical symmetry, and their method suffered from stability issues. Finally, the recent work of Mignone [61] proposed a reconstruction scheme for finite-volume methods in cylindrical and spherical coordinates; the complexity of this scheme, however, made it undesirable for us to implement. Recalling that our shock-capturing scheme already deteriorates to first-order accuracy near discontinuities, the loss of accuracy in the azimuthal coordinate is not catastrophic as long as the overall convergence of the method remains at least first-order. The convergence studies shown in Section 4.2.6 show that using the Cartesian WENO weights and polynomials in our cylindrical coordinate simulations do not lead to total loss of convergence, and we are able to recover the second-order accuracy that we expect from other aspects of our numerical method in the absence of discontinuities. Since the cylindrical coordinate system is an orthogonal coordinate system, no modifications to the Riemann solvers are necessary to compute the intercell fluxes.

4.2.3 Diffusive fluxes and source terms

The algorithm to compute the diffusive fluxes, $\mathbf{f}^d(\mathbf{q})$, and source terms, $\mathbf{s}^d(\mathbf{q})$, in cylindrical coordinates is altered from that for Cartesian coordinates (detailed in [13]). Within the Cartesian framework, the velocity gradient at the cell boundaries, required to calculate the diffusive fluxes, is reconstructed from the cell center velocity gradient using a WENO scheme. For cylindrical coordinates, the velocity, in addition to the velocity gradient, is required at the cell boundaries. However, instead of using WENO to reconstruct the cell center values to the cell boundaries, we employ a series of finite-difference approximations and averaging procedures to obtain the necessary building blocks to construct $\mathbf{f}^d(\mathbf{q})$ and $\mathbf{s}^d(\mathbf{q})$.

Firstly, the velocities at the cell boundaries are obtained by averaging the cell center values on either side of the cell face:

$$\mathbf{u}_{i+1/2,j,k} = \frac{1}{2}(\mathbf{u}_{i,j,k} + \mathbf{u}_{i+1,j,k}), \tag{4.19a}$$

$$\mathbf{u}_{i,j+1/2,k} = \frac{1}{2}(\mathbf{u}_{i,j,k} + \mathbf{u}_{i,j+1,k}), \tag{4.19b}$$

$$\mathbf{u}_{i,j,k+1/2} = \frac{1}{2}(\mathbf{u}_{i,j,k} + \mathbf{u}_{i,j,k+1}), \tag{4.19c}$$

where i, j, k are, respectively, indices in the axial, radial, and azimuthal coordinates. A second-order finite-difference approximation is then used to compute the component of the velocity gradient normal to each cell face:

$$\left.\frac{\partial \mathbf{u}}{\partial \mathbf{x}_i}\right|_{i+1/2,j,k} = \frac{\mathbf{u}_{i+1,j,k} - \mathbf{u}_{i,j,k}}{\mathbf{x}_{i+1,j,k} - \mathbf{x}_{i,j,k}}, \tag{4.20a}$$

$$\left.\frac{\partial \mathbf{u}}{\partial \mathbf{x}_j}\right|_{i,j+1/2,k} = \frac{\mathbf{u}_{i,j+1,k} - \mathbf{u}_{i,j,k}}{\mathbf{x}_{i,j+1,k} - \mathbf{x}_{i,j,k}}, \tag{4.20b}$$

$$\left.\frac{\partial \mathbf{u}}{\partial \mathbf{x}_k}\right|_{i,j,k+1/2} = \frac{\mathbf{u}_{i,j,k+1} - \mathbf{u}_{i,j,k}}{\mathbf{x}_{i,j,k+1} - \mathbf{x}_{i,j,k}}. \tag{4.20c}$$

Finally, the known velocity gradient components are appropriately averaged to obtain the remaining velocity gradient components:

$$\left.\frac{\partial \mathbf{u}}{\partial \mathbf{x}_i}\right|_{i,j+1/2,k} = \frac{1}{4}\left(\left.\frac{\partial \mathbf{u}}{\partial \mathbf{x}_i}\right|_{i+1/2,j,k} + \left.\frac{\partial \mathbf{u}}{\partial \mathbf{x}_i}\right|_{i-1/2,j,k} + \left.\frac{\partial \mathbf{u}}{\partial \mathbf{x}_i}\right|_{i+1/2,j+1,k} + \left.\frac{\partial \mathbf{u}}{\partial \mathbf{x}_i}\right|_{i-1/2,j+1,k} \right), \quad (4.21a)$$

$$\left.\frac{\partial \mathbf{u}}{\partial \mathbf{x}_i}\right|_{i,j,k+1/2} = \frac{1}{4}\left(\left.\frac{\partial \mathbf{u}}{\partial \mathbf{x}_i}\right|_{i+1/2,j,k} + \left.\frac{\partial \mathbf{u}}{\partial \mathbf{x}_i}\right|_{i-1/2,j,k} + \left.\frac{\partial \mathbf{u}}{\partial \mathbf{x}_i}\right|_{i+1/2,j,k+1} + \left.\frac{\partial \mathbf{u}}{\partial \mathbf{x}_i}\right|_{i-1/2,j,k+1} \right), \quad (4.21b)$$

$$\left.\frac{\partial \mathbf{u}}{\partial \mathbf{x}_j}\right|_{i+1/2,j,k} = \frac{1}{4}\left(\left.\frac{\partial \mathbf{u}}{\partial \mathbf{x}_j}\right|_{i,j+1/2,k} + \left.\frac{\partial \mathbf{u}}{\partial \mathbf{x}_j}\right|_{i,j-1/2,k} + \left.\frac{\partial \mathbf{u}}{\partial \mathbf{x}_j}\right|_{i+1,j+1/2,k} + \left.\frac{\partial \mathbf{u}}{\partial \mathbf{x}_j}\right|_{i+1,j-1/2,k} \right), \quad (4.21c)$$

$$\left.\frac{\partial \mathbf{u}}{\partial \mathbf{x}_j}\right|_{i,j,k+1/2} = \frac{1}{4}\left(\left.\frac{\partial \mathbf{u}}{\partial \mathbf{x}_j}\right|_{i,j+1/2,k} + \left.\frac{\partial \mathbf{u}}{\partial \mathbf{x}_j}\right|_{i,j-1/2,k} + \left.\frac{\partial \mathbf{u}}{\partial \mathbf{x}_j}\right|_{i,j+1/2,k+1} + \left.\frac{\partial \mathbf{u}}{\partial \mathbf{x}_j}\right|_{i,j-1/2,k+1} \right), \quad (4.21d)$$

$$\left.\frac{\partial \mathbf{u}}{\partial \mathbf{x}_k}\right|_{i+1/2,j,k} = \frac{1}{4}\left(\left.\frac{\partial \mathbf{u}}{\partial \mathbf{x}_k}\right|_{i,j,k+1/2} + \left.\frac{\partial \mathbf{u}}{\partial \mathbf{x}_k}\right|_{i,j,k-1/2} + \left.\frac{\partial \mathbf{u}}{\partial \mathbf{x}_k}\right|_{i+1,j,k+1/2} + \left.\frac{\partial \mathbf{u}}{\partial \mathbf{x}_k}\right|_{i+1,j,k-1/2} \right), \quad (4.21e)$$

$$\left.\frac{\partial \mathbf{u}}{\partial \mathbf{x}_k}\right|_{i,j+1/2,k} = \frac{1}{4}\left(\left.\frac{\partial \mathbf{u}}{\partial \mathbf{x}_k}\right|_{i,j,k+1/2} + \left.\frac{\partial \mathbf{u}}{\partial \mathbf{x}_k}\right|_{i,j,k-1/2} + \left.\frac{\partial \mathbf{u}}{\partial \mathbf{x}_k}\right|_{i,j+1,k+1/2} + \left.\frac{\partial \mathbf{u}}{\partial \mathbf{x}_k}\right|_{i,j+1,k-1/2} \right). \quad (4.21f)$$

Thus, all the necessary building blocks to construct $\mathbf{f}^d(\mathbf{q})$ and $\mathbf{s}^d(\mathbf{q})$ are obtained. Using this method of finite-difference approximations and averages, we ensure that the stencils used to construct the diffusive fluxes and source terms remain symmetric, which is consistent with the elliptical nature of the viscous terms in the Navier-Stokes equations.

4.2.4 Treatment of axis singularity

A primary challenge of implementing numerical methods in cylindrical coordinates is finding appropriate methods to treat the singularity that arises at the axis as $r \to 0$. For finite-difference and pseudo-spectral schemes, Mohseni and Colonius [63] proposed an approach that can be summarized as follows:

1. A new radial coordinate is defined over both positive and negative radius as

$$\tilde{r}(r,\theta) = \begin{cases} r & \text{if } 0 \leq \theta < \pi, \\ -r & \text{if } \pi \leq \theta < 2\pi. \end{cases} \quad (4.22)$$

2. Radial differentiation is performed in the new coordinate, $\tilde{r}$, on a set of nodes that avoids the

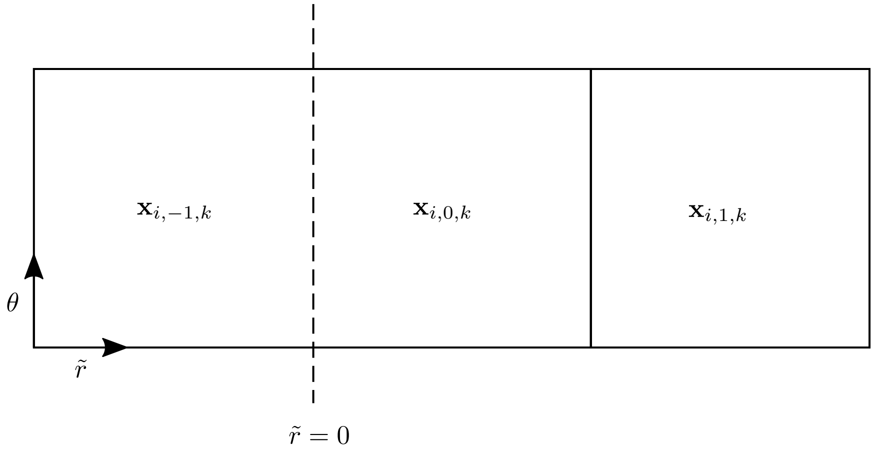

Figure 4.5: Schematic of grid cells near the axis (denoted by dashed line) in cylindrical coordinates.

singularity. For finite-difference schemes, such a set of nodes (for a uniform grid) is

$$r_n = \frac{(2n+1)\Delta r}{2}, \quad n = 0, 1, 2, \ldots. \tag{4.23}$$

3. To appropriately transform scalar and vector quantities from the r-coordinate to the $\tilde{r}$-coordinate when computing radial derivatives, the following rule holds: when $0 \leq \theta < \pi$, all quantities are the same in both coordinates. For $\pi \leq \theta < 2\pi$, any polar components, $\mathbf{v}_r$ and $\mathbf{v}_\theta$, of a vector quantity, $\mathbf{v}$, radial derivative, or r are multiplied by -1.

In a finite-difference scheme, radial differentiation across the axis can be simplified by avoiding a node at the singularity. However, in a finite-volume scheme, one must choose to place the singularity at either a cell boundary or cell center. Neither option is ideal, as, in a finite-volume scheme, both cell center and cell boundary values are constantly utilized. We choose to place the axis singularity at a cell boundary (shown in Fig. 4.5) such that $\frac{1}{r}$ for the cell centers directly adjacent to the axis, $\mathbf{x}_{i,0,k}$, are well defined. For the correct treatment of the axis in cylindrical coordinates, an axis boundary condition has been created to adapt the method of Mohseni and Colonius [63] to the finite-volume framework of MFC. The axis boundary condition requires that the number of grid cells in the azimuthal coordinate is an even number, such that the conservative variables in cells $\mathbf{x}_{i,-1,k}, \mathbf{x}_{i,-2,k}, \ldots$ for any θ can be derived from the conservative variables of the cells $\mathbf{x}_{i,0,k}, \mathbf{x}_{i,1,k}, \ldots$

at $\theta \pm \pi$. Using the transformation rule [63], the conservative variables for cells $\mathbf{x}_{i,-1,k}, \mathbf{x}_{i,-2,k}, \ldots$ are populated as

$$\mathbf{q}_{i,-j,k} = \mathbf{v}_{i,j-1,k}, \quad j = 1, 2, \ldots, N, \tag{4.24}$$

where $\mathbf{v} = (\alpha_1\rho_1, \alpha_2\rho_2, \rho u_z, -\rho u_r, -\rho u_\theta, E, \alpha_1)^T$, and N is the number of grid cells in the buffer region.

Given the location of the axis, the $\frac{1}{r}$ terms that lie on the cell faces $\mathbf{x}_{i,-1/2,k}$ must be appropriately handled to avoid the singularity. Looking at the equations in Appendix A.2, $\frac{1}{r}$ appears in $\mathbf{g}^d(\mathbf{q}), \mathbf{h}^a(\mathbf{q}), \mathbf{h}^d(\mathbf{q}), \mathbf{s}^a(\mathbf{q})$ and $\mathbf{s}^d(\mathbf{q})$. Remembering that $\mathbf{h}^a(\mathbf{q})$ and $\mathbf{h}^d(\mathbf{q})$ are evaluated on the cell faces normal to the azimuthal coordinate ($\mathbf{x}_{i,j,k\pm1/2}$), we can see that these fluxes require no special treatment since $\frac{1}{r}$ is evaluated at the cell center radius, which we have chosen to be well defined for all cells. The advective source term vector, $\mathbf{s}^a(\mathbf{q})$, which is evaluated as the average of the cell face values, also does not require special treatment since the $\frac{1}{r}$ is again evaluated at the cell center. This leaves the diffusive source term vector, $\mathbf{s}^d(\mathbf{q})$, and radial flux vector, $\mathbf{g}^d(\mathbf{q})$. $\frac{1}{r}$ appears in various components of the viscous stress tensor, which is typically evaluated at the cell faces. For example, $\mathbf{g}^d(\mathbf{q})$ is evaluated at $\mathbf{x}_{i,j\pm1/2,k}$, and then the divergence theorem is used to compute $\frac{\partial \mathbf{g}^d(\mathbf{q})}{\partial r}$ at $\mathbf{x}_{i,j,k}$ for the RHS of Eq. (4.17). $\mathbf{s}^d(\mathbf{q})$ is found by averaging the cell face values to find a cell center value. Since $\frac{1}{r}$ is not defined at the axis, we modify the computation of $\mathbf{g}^d(\mathbf{q})$ and $\mathbf{s}^d(\mathbf{q})$ for the cells directly adjacent to the axis, $\mathbf{x}_{i,0,k}$. To do this, we compute the required viscous stress tensor components at the following cell center locations: $\mathbf{x}_{i,-1,k}, \mathbf{x}_{i,0,k}$ and $\mathbf{x}_{i,1,k}$. The velocities at these cell centers are already known at each time step, and the velocity gradient is calculated using second-order finite-difference approximations:

$$\left.\frac{\partial \mathbf{u}}{\partial \mathbf{x}_i}\right|_{i,j,k} = \frac{\mathbf{u}_{i+1,j,k} - \mathbf{u}_{i-1,j,k}}{\mathbf{x}_{i+1,j,k} - \mathbf{x}_{i-1,j,k}}, \tag{4.25a}$$

$$\left.\frac{\partial \mathbf{u}}{\partial \mathbf{x}_j}\right|_{i,j,k} = \frac{\mathbf{u}_{i,j+1,k} - \mathbf{u}_{i,j-1,k}}{\mathbf{x}_{i,j+1,k} - \mathbf{x}_{i,j-1,k}}, \tag{4.25b}$$

$$\left.\frac{\partial \mathbf{u}}{\partial \mathbf{x}_k}\right|_{i,j,k} = \frac{\mathbf{u}_{i,j,k+1} - \mathbf{u}_{i,j,k-1}}{\mathbf{x}_{i,j,k+1} - \mathbf{x}_{i,j,k-1}}. \tag{4.25c}$$

Once the components of $\mathbf{T}_\mu$ in $\mathbf{g}^d(\mathbf{q})$ and $\mathbf{s}^d(\mathbf{q})$ have been constructed, we immediately have $\mathbf{s}^d(\mathbf{q})\big|_{i,0,k}$, and $\left.\dfrac{\partial \mathbf{g}^d(\mathbf{q})}{\partial r}\right|_{i,0,k}$ is easily computed using a finite-difference approximation:

$$\left.\frac{\partial \mathbf{g}^d(\mathbf{q})}{\partial r}\right|_{i,0,k} = \frac{\mathbf{g}^d(\mathbf{q})\big|_{i,1,k} - \mathbf{g}^d(\mathbf{q})\big|_{i,-1,k}}{\tilde{r}_{i,1,k} - \tilde{r}_{i,-1,k}}. \tag{4.26}$$

In this manner, we avoid all evaluation of $\dfrac{1}{r}$ at the axis, and thus eliminate, for all practical purposes, the singularity that arises from the geometry of cylindrical coordinates.

4.2.5 Spectral filtering in the azimuthal coordinate

An unavoidable characteristic of computational grids in cylindrical coordinates is the large variation of grid cell size in the radial coordinate. Cells at large radial distances from the axis are associated with larger cell volumes, which in a shock-capturing scheme, translates to stronger numerical viscosity effects. The strong numerical diffusion in these far-field cells result in the smearing and weakening of any propagating waves. This effect is, in fact, auspicious for our purposes, since we are not particularly interested in the far-field physics, and simply require that outgoing waves are not reflected back into the domain by the boundaries. On the other hand, the small grid cells in the near field (close to the axis) present a problem for computational stability. Since we are solving the compressible Navier-Stokes equations, the choice of a stable time step is subject to the following condition:

$$\Delta t = \mathcal{C} \cdot \min_{i,j,k} \left(\frac{\Delta z_i}{|u_{z_{i,j,k}}| + c_{i,j,k}}, \frac{\Delta r_j}{|u_{r_{i,j,k}}| + c_{i,j,k}}, \frac{r_{i,j-1/2,k} \Delta \theta_k}{|u_{\theta_{i,j,k}}| + c_{i,j,k}} \right), \quad 0 < \mathcal{C} \leq \frac{1}{3}. \tag{4.27}$$

From Eq. (4.27), it is clear to see that the small arclengths associated with the cells closest to the axis will lead to a severe restriction on the allowable time step. Following an approach found in Mohseni and Colonius [63] and references therein, this restriction on the CFL number can be alleviated by explicitly filtering the results in the azimuthal coordinate.

Since the solution at any time step is periodic in the azimuthal coordinate, it is possible to employ a sharp spectral filter at a particular cutoff wavenumber. At a given radius $r_n = n\Delta r$, the effective mesh spacing in the azimuthal coordinate becomes

$$\Delta \mathbf{x}_\theta = \frac{2\pi n \Delta r}{N_m}, \quad n = 1, 2, \ldots, \tag{4.28}$$

where N_m is the number of modes retained by the spectral filter. Thus, if the number of retained modes at radius r_n is less than or equal to a maximum of $N_m = 2\pi n$, then the CFL constraint will be dictated by Δr. In our implementation of the spectral filter in MFC, the conservative variables in the grid cells closest to the axis (from $\mathbf{x}_{i,0,k}$ out to $\mathbf{x}_{i,5,k}$) are filtered after every Runge-Kutta time stage using the freely available FFTW library. $N_m = 3$ for the rings of grid cells at $\mathbf{x}_{i,0,k}$. The choice of N_m for $n = 0$, and the maximum radius at which to apply the spectral filter is somewhat arbitrary; preliminary testing shows that numerical results are fairly insensitive to changes. The values chosen here appear to work well for the simulations we have run to date. Finally, it should be noted that in order to minimize processor communication costs, a "pencil processor blocking" scheme has been used when partitioning the domain between parallel processors. That is to say, all grid cells at a given radial and axial coordinate are assigned to a single processor, such that no communication between processors is necessary to apply the spectral filter.

4.2.6 Verification and convergence

Unfortunately, there does not exist a simple verification test for the Navier-Stokes equations in the context of cylindrical coordinates. Instead, we proceed to verify our implementation in two parts. Firstly, we verify our algorithm for the inviscid Euler equations by simulating the outward propagation of a spherical pressure wave, for which there exists an analytical solution. We then independently verify the viscous stress tensor using the method of manufactured solutions. In both test cases, we are able to recover approximately second-order convergence rates, which support our claim that using Cartesian WENO weights and polynomials in our implementation of cylindrical coordinates is not catastrophically detrimental to our overall order of accuracy.

4.2.6.1 Spherical pressure pulse

The analytical solution of an outwardly propagating spherical pressure wave is obtained by solving the spherically symmetric radial wave equation

$$\frac{\partial^2 p}{\partial r^2} + \frac{2}{r}\frac{\partial p}{\partial r} = \frac{1}{c^2}\frac{\partial^2 p}{\partial t^2}, \tag{4.29}$$

or alternatively,

$$\frac{\partial^2 (rp)}{\partial t^2} - c^2 \frac{\partial^2 (rp)}{\partial r^2} = 0. \tag{4.30}$$

The general solution to Eq. (4.30) is

$$p(r,t) = \frac{1}{r} f(r+ct) + \frac{1}{r} f(r-ct). \tag{4.31}$$

If we take a narrow pressure pulse as our initial condition, and give it the form

$$p(r) = p_0 e^{-\pi r^2}, \tag{4.32}$$

where p_0 is the amplitude, we can explicitly solve for $f(r \pm ct)$. Doing so, we find that

$$p(r,0) = p_0 e^{-\pi r^2} = \frac{2}{r} f(r), \tag{4.33}$$

which means that

$$f(r) = \frac{r}{2} p_0 e^{-\pi r^2}. \tag{4.34}$$

The analytical solution to our initial value problem (IVP) is then

$$p(r,t) = \frac{p_0}{r}\left(\frac{r+ct}{2} e^{-\pi (r+ct)^2} + \frac{r-ct}{2} e^{-\pi (r-ct)^2}\right). \tag{4.35}$$

Using Eq. (4.32), we initialize a narrow 3D pressure pulse of amplitude $p_0 = 100\,\mathrm{Pa}$ in a quiescent

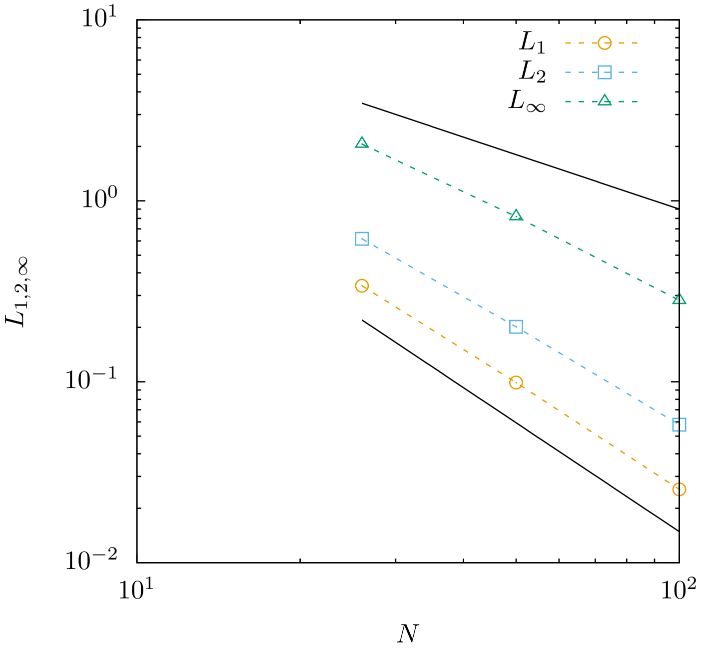

Figure 4.6: Grid convergence of various p-norms for an outwardly propagating spherical pressure wave. Reference slopes for first- and second-order convergence are included (continuous).

gas at atmospheric pressure, $p_\infty = 100\,\mathrm{kPa}$. The gas has density, $\rho_g = 1\,\mathrm{kg/m^3}$, and EOS parameters $\gamma_g = 1.4$ and $\pi_{\infty,g} = 0\,\mathrm{Pa}$. Using spatial resolutions of $(N_z, N_r, N_\theta) = (52, 26, 26), (100, 50, 50)$, and $(200, 100, 100)$ cells, we simulate the spherical pressure wave in the computational domain, $\Omega = [-4, 4] \times [0, 4] \times [0, 2\pi]$. At $t = 0.005\,\mathrm{s}$, we compute various p-norms of the error by comparing the numerical solution to the analytical solution found in Eq. (4.35); these are plotted in Fig. 4.6. Pointwise convergence is observed to be better than first-order accurate, and the L_1- and L_2-norms have approximately second-order convergence.

4.2.6.2 Method of manufactured solutions

We employ the method of manufactured solutions to check convergence of the viscous stress tensor. This is done by initializing an analytical velocity field from which the viscous stress tensor can be calculated. We can then check convergence for the overall viscous contributions to the RHS of the momentum and energy equations after the first time step. Being careful to initialize a physically realizable velocity field, we transform the Cartesian velocity field for Couette flow into cylindrical

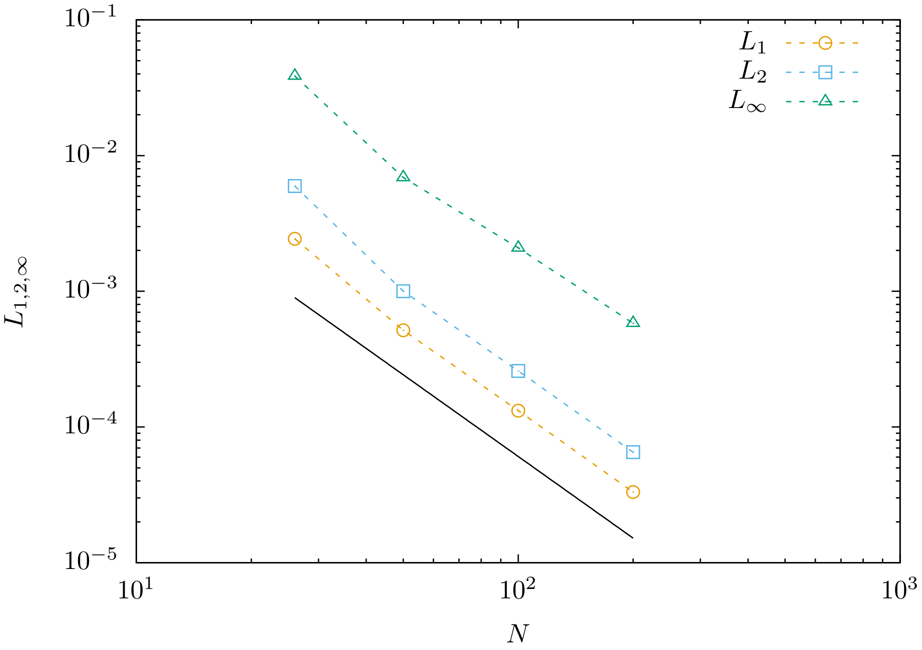

Figure 4.7: Grid convergence of various p-norms for the viscous contribution to the r-momentum equation. A reference slope for second-order convergence (continuous) is included.

coordinates as

$$\begin{pmatrix} u \\ v \\ w \end{pmatrix} = \begin{pmatrix} y \\ 0 \\ 0 \end{pmatrix} \implies \begin{pmatrix} u_z \\ u_r \\ u_\theta \end{pmatrix} = \begin{pmatrix} 0 \\ r\cos\theta\sin\theta \\ -r\sin^2\theta \end{pmatrix}. \tag{4.36}$$

The viscous stress tensor in cylindrical coordinates is then calculated to be:

$$\mathbf{T}_\mu = \begin{pmatrix} 0 & 0 & 0 \\ 0 & 2\mu\cos\theta\sin\theta & \mu(2\cos^2\theta - 1) \\ 0 & \mu(2\cos^2\theta - 1) & -2\mu\cos\theta\sin\theta \end{pmatrix}. \tag{4.37}$$

After going through some simple algebra to calculate the diffusive fluxes, we find that the overall viscous contribution to all momentum equations is identically zero, and the contribution to the energy equation is the constant, μ. For the computational domain $\Omega = [0, 2\pi] \times [0, 2\pi] \times [0, 2\pi]$, we use spatial resolutions of $N = 26, 50, 100$, and 200 cells in each direction. We are then able to compute various p-norms of the error in the viscous contributions to the momentum and energy equations, which are plotted in Figs. 4.7 to 4.9. The error in the viscous contribution to the z-momentum equation for all resolutions is on the order of machine precision; this convergence plot

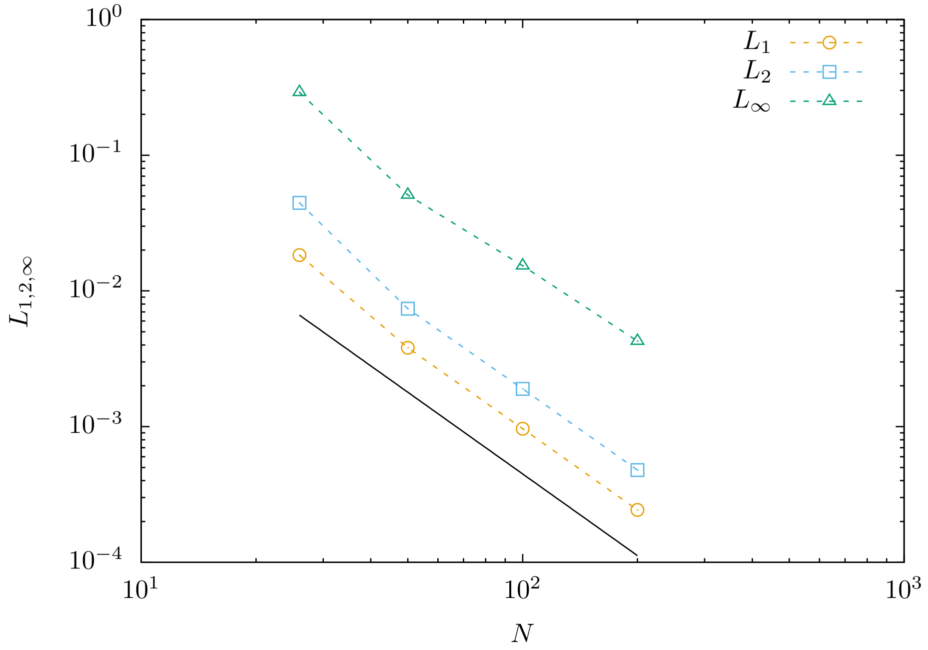

Figure 4.8: Grid convergence of various p-norms for the viscous contribution to the θ-momentum equation. A reference slope for second-order convergence (continuous) is included.

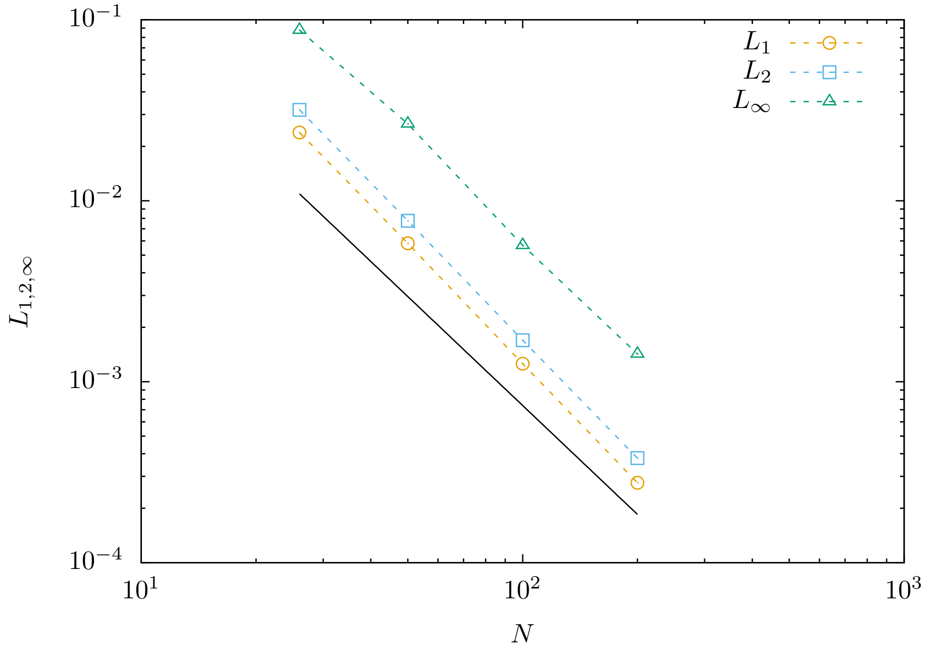

Figure 4.9: Grid convergence of various p-norms for the viscous contribution to the energy equation. A reference slope for second-order convergence (continuous) is included.

is, therefore, not shown since the machine-precision-magnitude p-norms fluctuate so as to create a nonsensical convergence plot. From the reference slopes for second-order convergence, it is clear that we have second-order accuracy for all computed p-norms.

4.3 Code stability improvements

4.3.1 Volume fraction limiting

The volume fractions in our numerical scheme are theoretically bounded between 0 and 1, such that the mixture rule, Eq. (2.6), holds for any number of fluids in the system. However, the numerical method does not explicitly bound the volume fractions to their physical limits. Since we only advect $N-1$ volume fractions for a system of N fluids, the unadvected volume fraction, in fact, may be negative if the sum of the first $N-1$ volume fractions exceeds 1, even if only by a small value. This presents a complication when computing the mixture properties within the diffuse interface region using the mixture rules of Section 2.3.3. With no explicit bounds on the volume fractions, numerical mixture properties are not bounded, as they physically should be, by the corresponding properties of the constituent pure fluids. In the case of multiphase flows, where liquids and gases co-exist in a nonphysical mixture region, these numerical mixture properties may lead to computational failure if, e.g., the sound speed is calculated to be imaginary. To avoid this numerical instability of the flow solver, a volume fraction limiting method is implemented such that only physical volume fraction values are used when computing mixture properties. To accomplish this, all N volume fractions are first limited to their physical bounds, i.e., $0 \leq \alpha_n \leq 1, \quad n = 1, 2, \ldots, N$. Then, all volume fractions are rescaled to ensure that Eq. (2.6) is precisely satisfied, i.e.,

$$\alpha_n = \frac{\alpha_n}{\sum_{m=1}^{N} \alpha_m}, \quad n = 1, 2, \ldots, N. \tag{4.38}$$

The limited volume fractions are then used in the mixture rules to compute the mixture properties. It is important to note that the volume fractions are *only limited when computing mixture properties*;

the volume fractions advected by the transport equations are untouched so as to not interfere with the mass conservation properties of the governing equations.

4.3.2 Flux limiting

With the exception of first-order WENO schemes, numerical methods using WENO reconstructions are not generally TVD. For flows involving the interaction of shock waves and material interfaces, it is possible that WENO is unable to find a smooth stencil, and may reconstruct a variable that a) is outside its physical bounds, b) will be outside its physical bounds once updated, or c) will result in other dependent variables being outside their physical bounds [11]. Because the numerical method is not TVD, stability is not guaranteed in the long-term when evolving a general initial condition, even when the time step restrictions in Section 3.1.2 are met. One method to partially alleviate this issue is to employ flux limiters in the affected regions of the flow. Flux limiters have the unfortunate consequence of increasing the smearing of material interfaces, but may, in some cases, be necessary to maintain stability and prevent abrupt termination of the simulation. It is our experience that this is particularly true when simulated fluids have large values of π_∞ (e.g., when approximating solid material as a stiff fluid). For the initial conditions relevant to the results in this thesis, flux limiters were found to be unnecessary, and so are not utilized. However, they are available as an option to the user, and are documented here for completeness. The full details of the theory and development of flux limiters are not included here, as they have already been extensively documented in the literature (see, e.g., [50, 51]). Instead, we focus here on specific implementation details. We note that the current implementation of flux limiters in MFC does not apply to viscous and capillary modeling terms in the governing equations.

The basic premise of flux limiting schemes is to limit spatial derivatives to realistic values, such that the updated values are physically meaningful. In practice, the flux limiter only operates in regions near discontinuities, and does not affect smooth regions of the flow. Consider, for now, the fluxes in the x-coordinate. The limited flux at a cell boundary, $f^{\text{TVD}}_{i+1/2}$, is constructed from a linear combination of a high-order flux, $f^{\mathrm{HI}}_{i+1/2}$, and a low-order flux, $f^{\mathrm{LO}}_{i+1/2}$, as

$$f^{\mathrm{TVD}}_{i+1/2} = f^{\mathrm{LO}}_{i+1/2} + \phi(\chi_{i+1/2}) \left(f^{\mathrm{HI}}_{i+1/2} - f^{\mathrm{LO}}_{i+1/2} \right), \tag{4.39}$$

where $\phi(\chi)$ is an upwind flux limiter function. The upwind direction is based on the intercell velocity from the Riemann solver, u^{RS}. Using the volume fraction gradient to localize the flux limiters to nonsmooth regions of the flow, we compute the ratio of consecutive volume fraction gradients, χ, at the cell boundary as

$$\chi_{i+1/2} = \begin{cases} \dfrac{\alpha_i - \alpha_{i-1}}{\alpha_{i+1} - \alpha_i} & \text{if } u^{\mathrm{RS}} \geq 0, \\ \dfrac{\alpha_{i+2} - \alpha_{i+1}}{\alpha_{i+1} - \alpha_i} & \text{if } u^{\mathrm{RS}} < 0. \end{cases} \tag{4.40}$$

The flux limiter function, $\phi(\chi)$, is then defined based on the choice of flux limiter. The choice of a flux limiter for a particular problem is typically determined heuristically, as no flux limiter has been shown to work well for all problems. The flux limiter options in MFC are restricted to symmetric flux limiters, which have the desirable property that

$$\frac{\phi(\chi)}{\chi} = \phi\left(\frac{1}{\chi}\right), \tag{4.41}$$

so that limiting actions for forward and backward gradients act in the same way. The flux limiter options are:

$$\phi(\chi) = \begin{cases} \max\big(0, \min(1,\chi)\big) & \text{minmod,} \\ \max\left(0, \min\left(2\chi, \dfrac{1+\chi}{2}, 2\right)\right) & \text{monotonized central,} \\ \dfrac{1.5(\chi^2+\chi)}{\chi^2+\chi+1} & \text{ospre,} \\ \max\big(0, \min(2\chi,1), \min(\chi,2)\big) & \text{superbee,} \\ \max\big(0, \min(\xi\chi,1), \min(\chi,\xi)\big),\ 1 \le \xi \le 2 & \text{Sweby,} \\ \dfrac{\chi^2+\chi}{\chi^2+1} & \text{van Albada,} \\ \dfrac{\chi+|\chi|}{1+|\chi|} & \text{van Leer.} \end{cases} \tag{4.42}$$

Once the flux limiter function at a cell boundary, $\phi(\chi_{i+1/2})$, has been computed using Eqs. (4.40) and (4.42), all that remains is to calculate high-order and low-order fluxes. The high-order flux, $f^{\mathrm{HI}}_{i+1/2}$, is naturally chosen to be the Riemann flux resulting from the WENO-reconstructed cell boundary values. We similarly compute a low-order flux, $f^{\mathrm{LO}}_{i+1/2}$, from the Riemann solver assuming that the cell boundary values are equivalent to the cell center average values on either side of the cell boundary. This is equivalent to using a first-order WENO scheme. Finally, we note that the value of $\phi(\chi_{i+1/2})$, calculated from the volume fraction gradient using Eqs. (4.40) and (4.42), is used for *all equations* in the model. Formulations for the limited fluxes in the remaining two coordinate directions are straightforward, and left to the reader.

4.4 Summary

In this chapter, several improvements made to the MFC flow solver are documented. Firstly, a nonconservative model to capture capillary effects in our diffuse interface framework is successfully implemented and verified using two benchmark test cases. The results of the static Laplace pressure jump and dynamic oscillating ellipse test cases compare well with theoretical results, and convergence of the method is shown. Though currently only implemented in the Cartesian coordinates framework, it is extendable to cylindrical coordinates as long as an appropriate curvature calculation is utilized. Secondly, motivated by the grid effects seen in Chapter 3, the flow solver is adapted to allow for simulations in 3D cylindrical coordinates. Appropriate treatments for the axis singularity, and the CFL stability condition are explained and implemented. In this new spatial discretization, the inviscid equations and the viscous terms are independently verified using the propagation of a spherical pressure pulse and the method of manufactured solutions. Convergence of the governing equations is also shown in the new coordinate system. Finally, overall code stability is improved with the additions of volume fraction and flux limiting.

Chapter 5

Two-dimensional aerobreakup[1]

5.1 Overview

Prior to performing computationally expensive 3D simulations of aerobreakup, exploratory 2D simulations are undertaken to investigate the aerobreakup physics that can be extracted from the breakup of water cylinders. The experiments of Igra and Takayama [33] and related publications [32, 35–37] have already shown that the breakup process of cylinders is qualitatively similar to that of spherical droplets. Our study of 2D aerobreakup, therefore, primarily investigates the effect of incident shock Mach number on the breakup process. We initially focus on the experiments of Igra and Takayama [36] who studied the aerobreakup of water cylinders in the flow behind $M_s = 1.18, 1.30, 1.47, 1.73$ shock waves. Section 5.3.1 provides a qualitative description of the aerobreakup process, while comparisons with available experimental data are shown in Section 5.3.2. In addition to the four experimentally studied M_s, simulations for $M_s = 2.00, 2.50$ are run to investigate the effects of transonic and supersonic post-shock flow velocities. Additional quantitative results of the parametric study are shown in Section 5.3.3.

The approximate Weber and Reynolds numbers, Eq. (2.14), corresponding to the experimental investigations range from 940 to 1.93×10^4 and 3.99×10^4 to 2.376×10^5, respectively. These Weber

---

[1] The work in this chapter has been published in large part in [60]: J. C. Meng and T. Colonius. Numerical simulations of the early stages of high-speed droplet breakup. *Shock Waves*, 25(4):399–414, July 2015. doi: 10.1007/s00193-014-0546-z

and Reynolds numbers suggest that the physical mechanisms of breakup are primarily driven by inertia, and that a reasonable first approximation can be made by neglecting the effects of surface tension and molecular viscosity. Therefore, all simulations in our parametric study solve the inviscid compressible multicomponent Euler equations (albeit, with the caveat of numerical viscosity as discussed in Section 3.1.3). With these simplifications, we do not capture all the physics of the breakup process. For example, the absence of surface tension restricts our capability to simulate the breakup of the thin liquid filaments that are stripped off the edge of the cylinder. However, for the early stages of breakup where the cylinder remains, for the most part, a coherent body, the roles of molecular viscosity and surface tension are expected to be relatively minor compared to that of inertia.

Finally, in addition to our inviscid shock strength parametric study, a series of viscous simulations, with explicit modeling of molecular viscosity, are run for $M_s = 1.50$. These viscous results are subsequently used to investigate the numerical viscosity associated with our computational grid (Section 5.4.1), and to test the boundary layer stripping model of Ranger and Nicholls [69] (Section 5.4.2).

5.2 Simulation parameters

The range of simulated M_s along with relevant density, pressure, and sound speed ratios, and post-shock velocities and Mach numbers in both shock-stationary and shock-moving reference frames are summarized in Table 5.1. All numerical simulations are performed on the computational domain $\Omega = [-6.25D_0, 17D_0] \times [0, 6D_0]$ using a spatial resolution of $(N_x, N_y) = (1200, 600)$ grid cells. Furthermore, the grid is stretched near the boundaries using a hyperbolic tangent function. The most refined portion of the grid is located near the initial position of the cylinder and in the region of the near-field wake. In this region, the nominal grid resolution is $\Delta x^* = \Delta y^* = 0.01$. A schematic of the computational grid is shown in Fig. 5.1. In addition to the limitations imposed by the absence of viscous and capillary effects, our analysis is also restricted to the early stages of breakup since the flow is assumed to be symmetric across the cylinder's centerline. Experimental visualizations

				Shock-stationary		Shock-moving	
M_s	$\rho_s/\rho_{g,0}$	$p_s/p_{g,0}$	$c_s/c_{g,0}$	u_s [m/s]	u_s/c_s	u_s [m/s]	u_s/c_s
1.18	1.307	1.458	1.056	309.8412	0.8549	95.1466	0.2625
1.30	1.516	1.805	1.091	294.3115	0.7860	151.8615	0.4056
1.47	1.811	2.354	1.140	278.5767	0.7120	225.9420	0.5775
1.50	1.862	2.458	1.149	276.4776	0.7011	238.3374	0.6044
1.73	2.247	3.325	1.217	264.3956	0.6330	329.3577	0.7885
2.00	2.667	4.500	1.299	257.4221	0.5774	428.9979	0.9622
2.50	3.333	7.125	1.462	257.4096	0.5130	600.6154	1.1970

Table 5.1: Simulated M_s and relevant normal shock parameters.

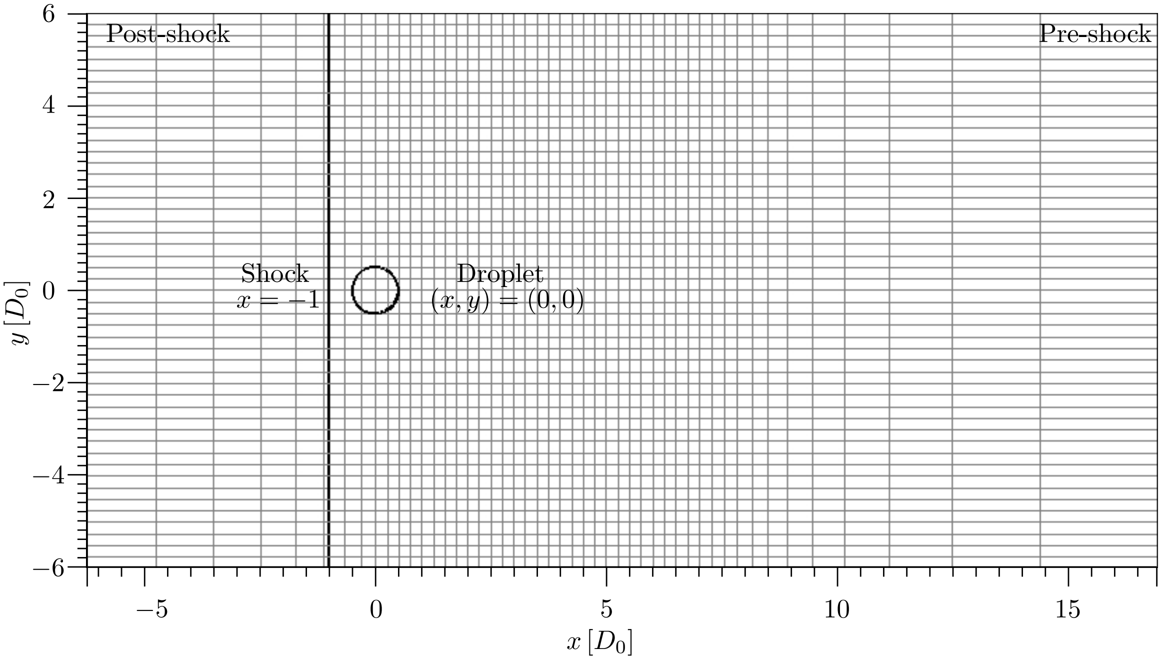

Figure 5.1: Schematic of the nonuniform computational grid at 1:25 of the actual resolution. As a result of the symmetry of the initial condition, only the top half of the displayed computational grid is utilized in the simulation.

of both cylinder and droplet breakup show no significant asymmetries during the early stages of breakup. We employ a RBC along the x-axis, and enforce characteristic NRBCs along the three remaining boundaries. Implemented following Thompson [91, 92], these characteristic BCs do not contaminate the solution through the reflection of outgoing waves. The simulations are run with a constant CFL number of $\mathcal{C} = 0.25$.

As discussed in Section 3.1.3, traditional grid convergence or independence of the computational results cannot be definitively shown in these inviscid calculations; this is a known issue associated with nominally inviscid calculations using shock- and interface-capturing methods.. Without the presence of molecular viscosity to regularize the smallest scales, ever finer flow features are obtained in the simulation as spatial resolution is improved. A grid resolution study for the $M_s = 1.47$ case is performed, which repeats the simulation at half and double the nominal spatial resolution. The finest resolution run, while resolving finer flow features, shows little difference in measurements of cylinder deformation and center-of-mass properties. The details of this study can be found in Appendix D.1. We believe that the present spatial resolution of $(N_x, N_y) = (1200, 600)$ is able to capture the salient features in the flow without being computationally cumbersome.

5.3 Inviscid results

5.3.1 Qualitative description

Across the range of simulated M_s, the qualitative flow features of the aerobreakup process are observed to be similar in nature. In fact, the differences that arise are associated with quantification of relevant length and time scales. Accordingly, in describing the flow physics, we will, in this section, focus solely on the $M_s = 1.47$ case. A time history of the breakup process is shown in Fig. 5.2, where the shock (and subsequent flow) is moving from left to right. The incident shock and the subsequent wave system in the wake of the deforming cylinder are visualized using a numerical

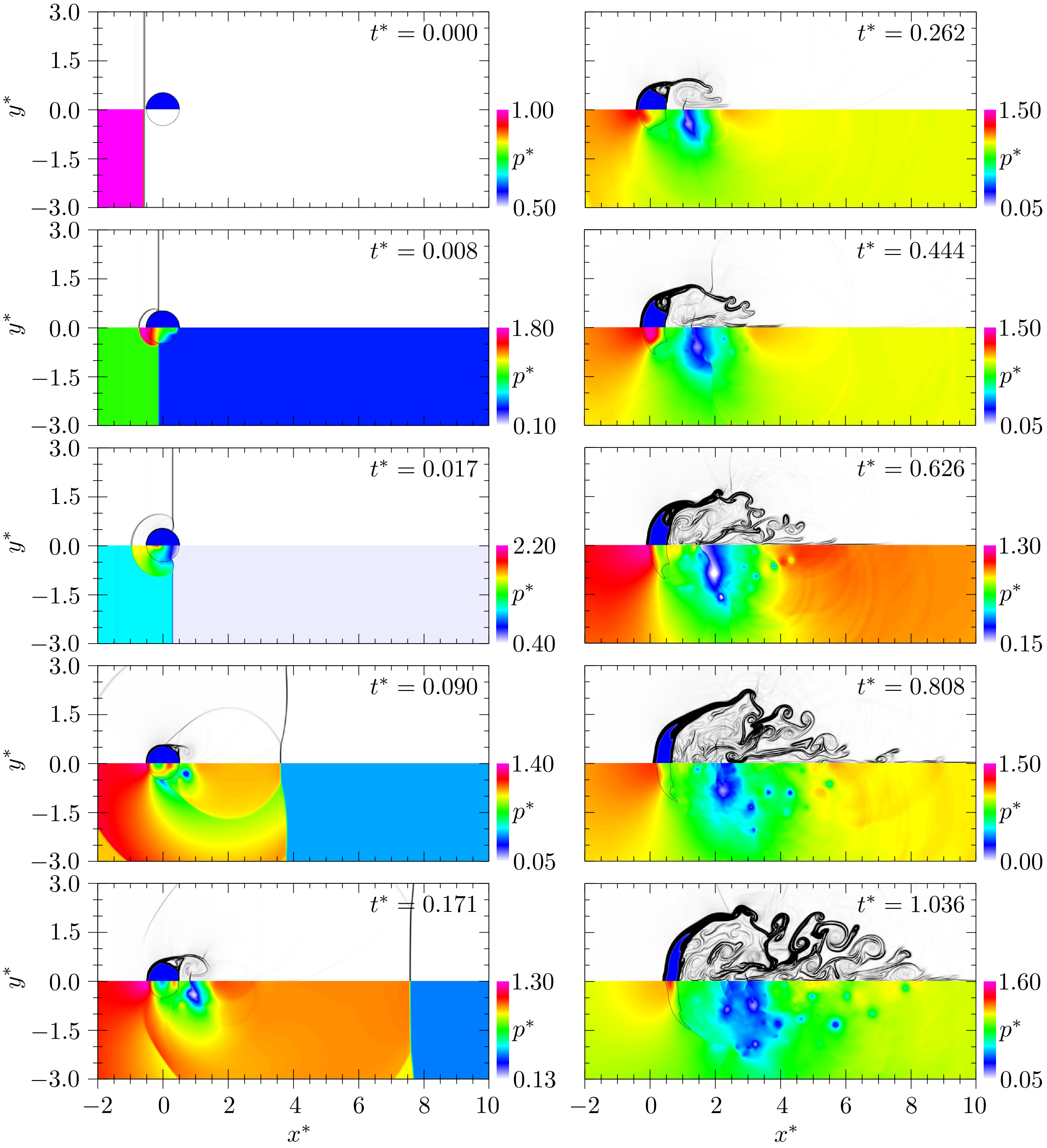

Figure 5.2: Numerical schlieren (top) and filled pressure contours (bottom) of the aerobreakup of a $D_0 = 4.8\,\text{mm}$ cylinder behind a $M_s = 1.47$ shock wave. Isopleths are shown for $\alpha_l \geq 0.5$.

schlieren function[2]. As mentioned in Section 2.1, the actual traversal of the shock wave over the cylinder does little in terms of cylinder deformation. The shock's influence, or lack of it, on the cylinder is attributed to the fact that the time scale of the shock is smaller than the relaxation time of the cylinder [1]. In fact, during early times, the liquid cylinder can be approximated as being rigid. The original shock and reflected wave are seen at $t^* = 0.008$. Behind the reflected wave, there is a high pressure region associated with the forward stagnation point. At a critical angle preceding the equator of the cylinder, the shock reflection transitions from a regular reflection to a Mach reflection shown at $t^* = 0.017$. This transition marks the peak drag experienced by the cylinder, and the corresponding phenomenon has been studied in the literature for rigid cylinders and spheres [83, 85]. The convergence of the Mach stems behind the cylinder results in a secondary wave system ($t^* = 0.090$) that generates high pressures at the rear stagnation point. The nonuniform pressure distribution around the cylinder results in an initial flattening that is reinforced by the pulling of material away from the equator by the surrounding flow. It has been suggested that the early time flattening is independent of viscosity or material type at large Weber numbers [43]. In conjunction with the lateral elongation, tips are observed to form on the cylinder's periphery ($0.171 \leq t^* \leq 0.444$), which are thought to be the onset of the stripping process [10]. These tips are eventually drawn downstream into thin filaments. Though not captured in these simulations (due to the absence of surface tension), the rise of capillary instabilities in these filaments causes them to break up downstream. Behind the cylinder, unsteady vortex shedding from the shear layer near the cylinder periphery drives the formation of a complex wake. Initially, the wake consists of a single large recirculation region, seen in the numerical schlieren contours from $t^* = 0.090$–0.262, and shown in Fig. 5.4. This vortical structure is observed to entrain downstream fluid and transport it upstream to impinge on the back of the cylinder. This upstream jet is shown in Fig. 5.3 and persists for the duration of the simulation. It was originally thought that the jet might be an artifact of

---

[2] Following Quirk and Karni [68], the numerical schlieren function is computed as the exponential of the negative, normalized density gradient.

$$\varphi = \exp\left(-\beta \frac{\|\nabla \rho\|}{\|\nabla \rho\|_{\max}}\right),$$

where β is a scaling parameter that allows simultaneous visualization of waves in both fluids. Following Johnsen [40], $\beta_{\text{air}} = 40$ and $\beta_{\text{water}} = 400$.

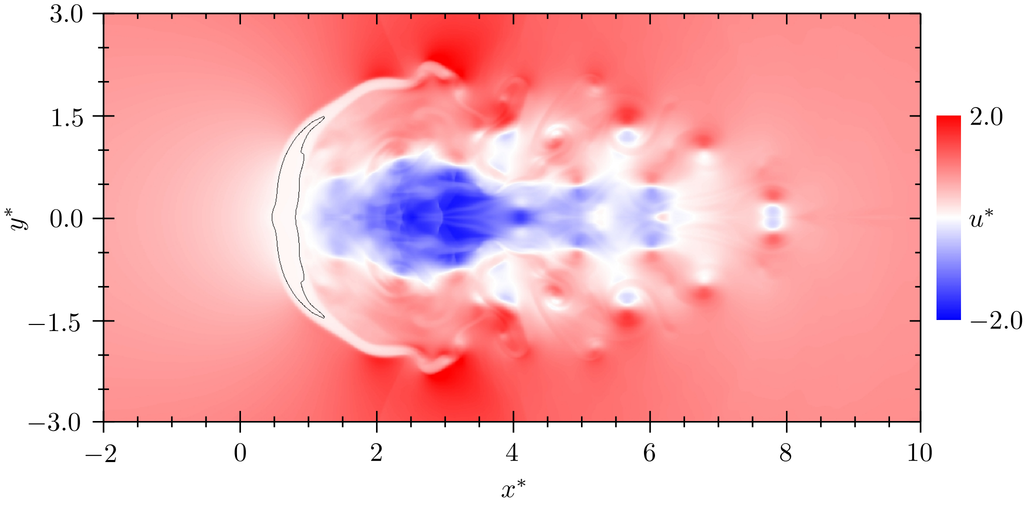

Figure 5.3: Filled contours of streamwise velocity, u^*, showing the persistent upstream jet in the wake of a deforming cylinder at $t^* = 1.036$. The $\alpha_l = 0.5$ isopleth is shown for reference.

assuming transverse symmetry in these 2D simulations. However, it is observed to still exist in our fully 3D results, and so we defer its discussion to Section 6.3.3. As additional vortices are shed from the shear layer, the wake becomes increasingly chaotic. Within the wake, a standing shock can also be observed ($0.171 \leq t^* \leq 0.444$), which is associated with the turning of the locally supersonic flow.

An interesting flow feature is the existence of a recirculation region near the equator of the deforming cylinder. A similar phenomenon, described as "secondary eddies," has been experimentally observed for unsteady flow past an impulsively started rigid cylinder when $Re \gtrsim 500$ [7, 27]. We proceed to describe how this recirculation region is formed. Consider for now the top half of the water cylinder. As the normal shock passes over the hemisphere, negative out-of-plane vorticity, ω_z, is generated by the baroclinic vorticity term, $\frac{1}{\rho^2}\nabla\rho \times \nabla p$, which is transported downstream by the surrounding flow. This stream of negative vorticity is the source of vortex shedding that creates the wake behind the deforming cylinder. Along the back side of the cylinder, the baroclinic term generates another vorticity stream, this time of positive sign. The recirculation region in the cylinder's wake transports this positive vorticity up along the flattened back of the cylinder until it runs perpendicularly into the stream of negative vorticity coming off the front of the cylinder. These two streams of opposite vorticity interact to form the recirculation region seen in Fig. 5.4. The recirculation region is composed of two counter-rotating vortices that are trapped by the two vortic-

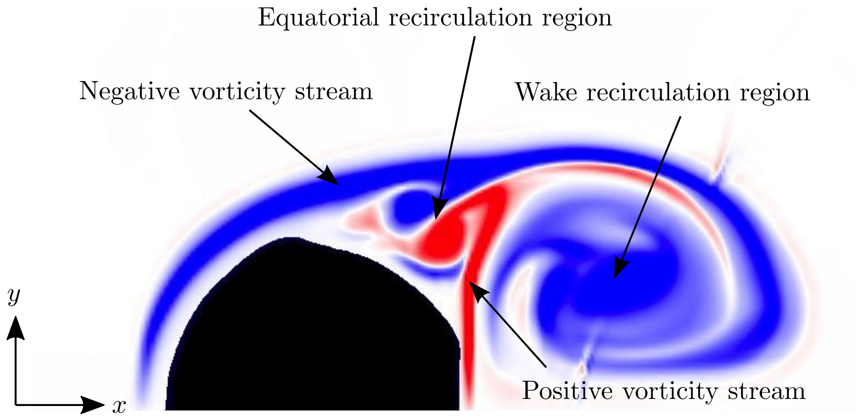

Figure 5.4: Positive (red) and negative (blue) out-of-plane vorticity, ω_z, streams interacting to form a recirculation region at the cylinder equator ($t^* = 0.171$).

ity streams and the cylinder body. It persists through the early deformation times of the cylinder, and appears to contribute to the stripping mechanism at the edge of the cylinder. Engel [16] had postulated that vortices in the wake of the deforming droplet (what we call the wake recirculation region) might contribute to the formation of water mist by “eating away” at the back of the droplet. From the later discussion of our 3D results in Section 6.3.3, we are able to show that this wake recirculation region does, in fact, play a key role in the overall flow physics. For now, though, we note the contributing role of the equatorial recirculation region to the stripping process. In time, as pressure forces further flatten the cylinder, the two vorticity streams are bent parallel to the flow, and the equatorial recirculation region disappears.

In the five-equation model of Section 2.3.1, the standard single-phase vorticity equation, derived by taking the curl of the mixture momentum equation, is valid for the mixture fluid since the mixture continuity equation follows from Eqs. (2.1a), (2.1b) and (2.7). From the vorticity equation, we observe that the generation of vorticity in our simulations can only arise from the baroclinic vorticity term. The density gradient that exists across our diffuse interface couples with the pressure gradient formed by the passage of the incident shock wave and the subsequent flow to generate the vorticity that plays a key role in the flow physics described in this section, and in Section 6.3.3 for the 3D case of a spherical droplet. If we momentarily consider flow past a rigid body, the no-slip boundary condition results in the deposition of a sheet of vorticity at the surface that is

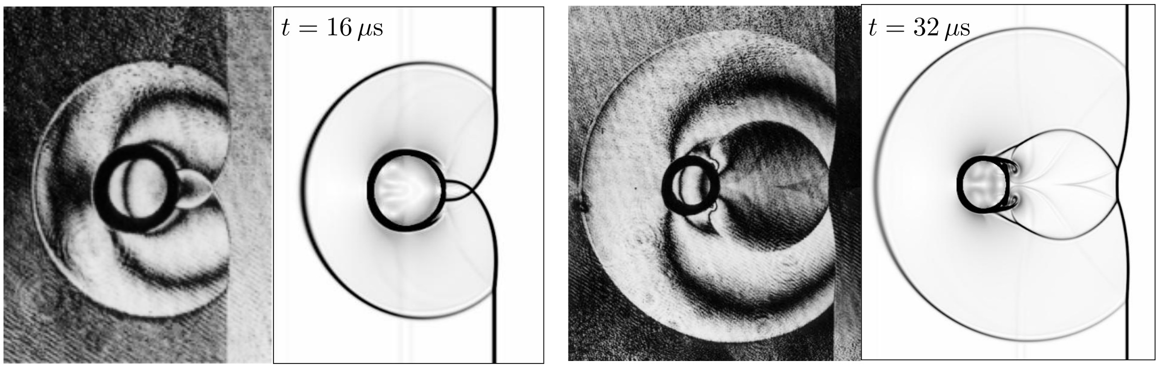

Figure 5.5: Comparison of numerical schlieren images (right) to experimental holographic interferograms (left) from Figs. 6 and 9 of [35]. Note that the values of time have been adjusted from the original work as described in Appendix D.2. Experimental images reprinted from Igra and Takayama [35] with the permission of Springer. © 2001 by Springer-Verlag.

subsequently diffused by viscosity and rolls up at the flow separation point. In the limit of a sharp interface, the appropriate boundary condition that exists at the interface between two modeled fluids would similarly be another vorticity generation mechanism. However, for the diffuse interface that exists in the simulations presented in this thesis, baroclinicity is the only viable mechanism of vorticity generation.

5.3.2 Experimental comparisons

Due to the quality and availability of the experimental visualizations in the literature (see, e.g., Fig. 5.10), qualitative comparisons with our numerical results can only be made at the early times of aerobreakup. Such a comparison is shown in Fig. 5.5 for the passage of a $M_s = 1.47$ shock over a $D_0 = 4.8\,\mathrm{mm}$ cylinder. At these early times in the breakup process, it is hard to make any comparisons regarding the cylinder's deformation. Furthermore, there is some uncertainty regarding the timing of this comparison, which is detailed in Appendix D.2. For now, we can only comment on the primary and secondary wave systems that are generated as the shock interacts with the water cylinder. The primary wave system consists of the incident and reflected shocks, while the secondary wave system is generated when the Mach stems on both sides of the cylinder converge at the rear stagnation point. From Fig. 5.5, we see good agreement between the experimental visualizations and our numerical results.

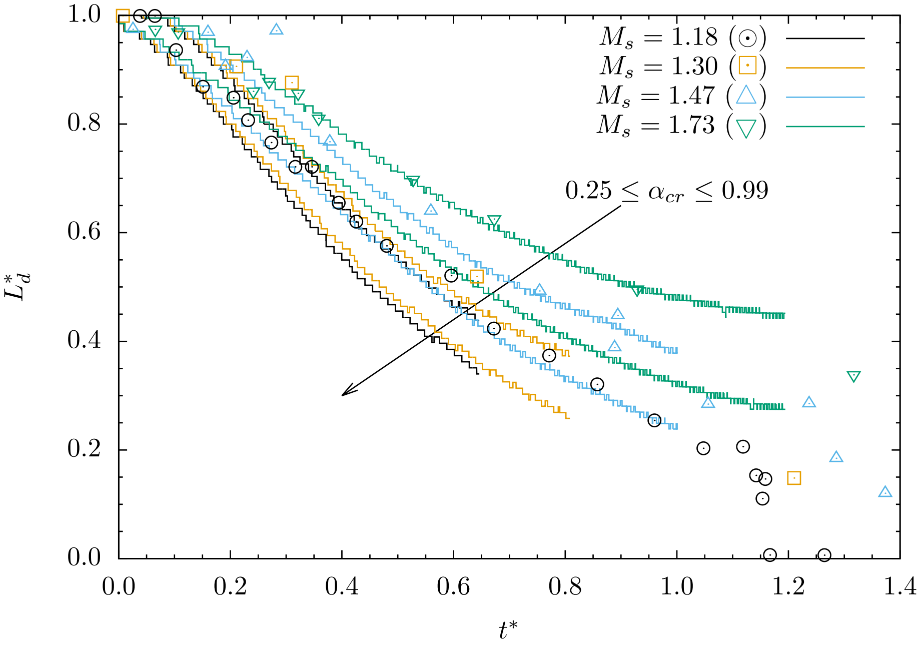

Figure 5.6: Comparison of cylinder centerline width, L_d^*, from Igra and Takayama's experiments (discrete) and our simulations (continuous). The arrow indicates the direction of increasing α_{cr}.

Using holographic interferograms, Igra and Takayama [36] quantified the cylinder's deformation by measuring its spanwise diameter, D_d, centerline width, L_d, and coherent body area, A_d. In the following plots, we compare our numerical results with the experimental measurements for the above deformation metrics. There exists, in our comparison, an inherent uncertainty associated with the methodology or criteria used to define the boundary of the deforming body. The first part of the uncertainty arises from the experimental data itself. From Igra and Takayama's discussion, it is not possible to unambiguously identify the criteria they used to determine the boundaries of the deforming body. Furthermore, they provide limited quantification of the error associated with their measurements of deformation. The second part of the uncertainty arises from our diffuse interface method and the choice of α_{cr} to be used in the threshold liquid volume fraction approach. As explained in Section 3.2.1, a range for α_{cr} is shown in an attempt to bound the experimental data. Figures 5.6 to 5.8 show, respectively, the centerline width, deformed diameter, and coherent body area for the four M_s studied by Igra and Takayama [36]. Additional data is included in Fig. 5.8 from the numerical work of Chen [10], who also simulated the same experiments. After the pas-

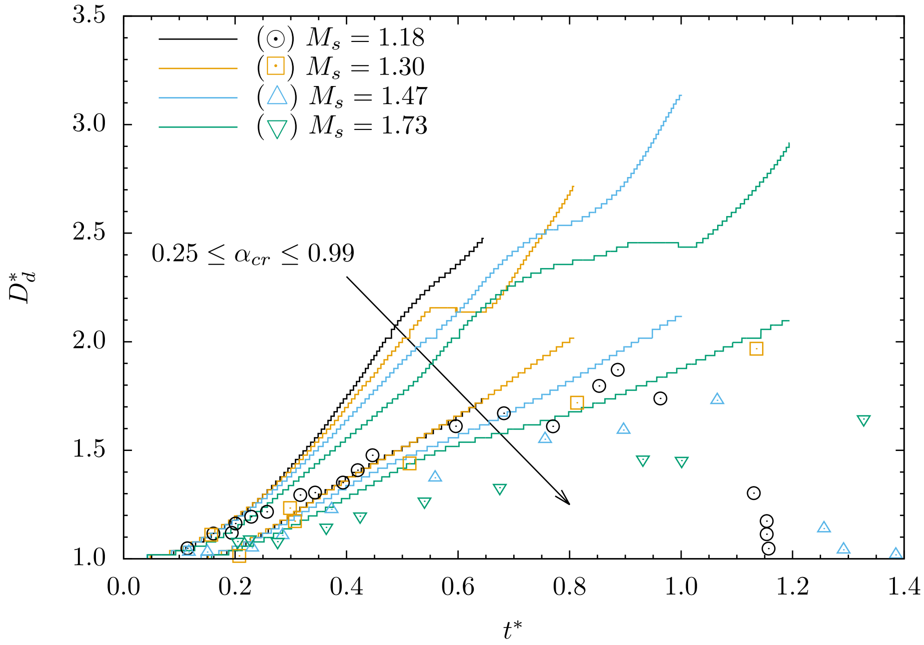

Figure 5.7: Comparison of cylinder deformed diameter, D_d^*, from Igra and Takayama's experiments (discrete) and our simulations (continuous). The arrow indicates the direction of increasing α_{cr}.

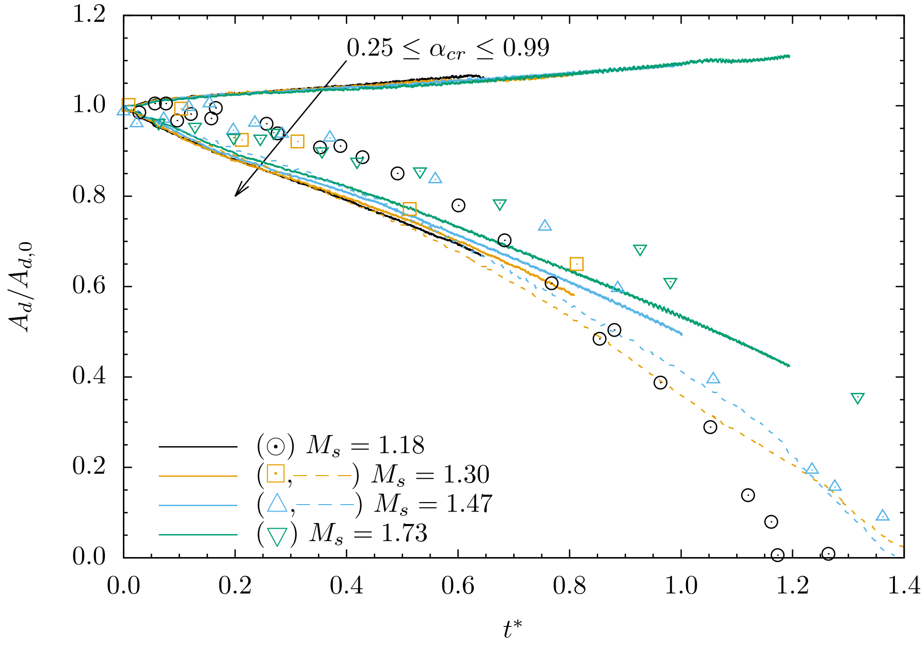

Figure 5.8: Comparison of cylinder coherent body area, $A_d/A_{d,0}$, from Igra and Takayama's experiments (discrete) and our simulations (continuous). The numerical results of Chen [10] (dashed) are shown for $\alpha_{cr} = 0.9$. The arrow indicates the direction of increasing α_{cr}.

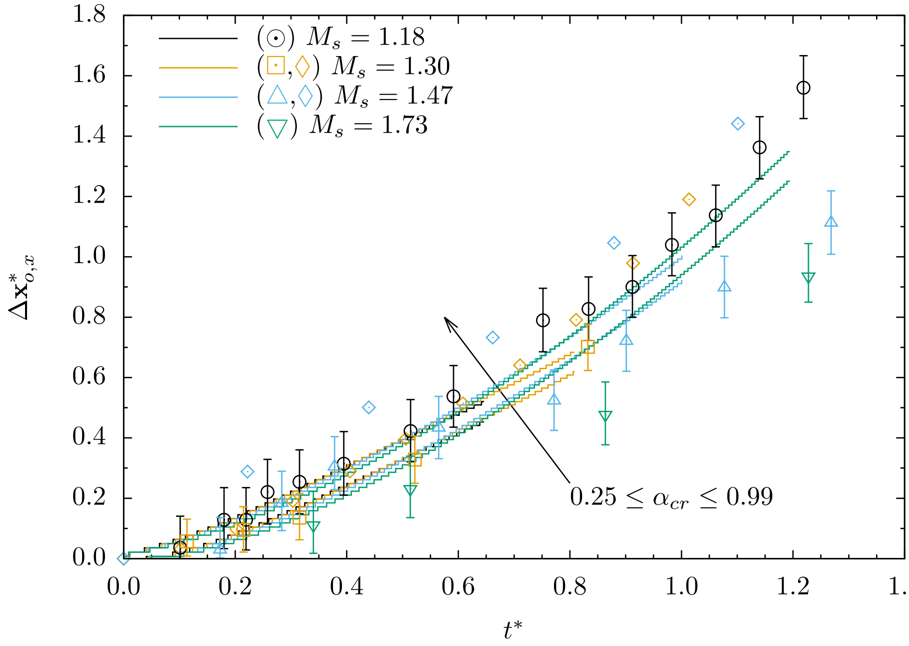

Figure 5.9: Comparison of cylinder leading edge drift, $\Delta\mathbf{x}^*_{o.x}$, from Igra and Takayama's experiments (discrete) and our simulations (continuous). The numerical results of Chen [10] (◊) are shown for $\alpha_{cr} = 0.9$. The arrow indicates the direction of increasing α_{cr}.

sage of the shock wave, the cylinder's deformation is characterized by flattening in the streamwise direction, which is quantified here as an increase in diameter and decrease in centerline width. As material is stripped off the cylinder's periphery by the surrounding high-speed flow, the area of the cylinder monotonically decreases. The cylinder's drift, as measured off the forward stagnation point, is shown in Fig. 5.9. For early times in the breakup ($t^* \leq 0.8$), our numerical results coincide well with the experimental measurements, falling within the error bounds. Our numerical results are also improved over those from Chen [10] for both $M_s = 1.30$ and $M_s = 1.47$. At later times, especially for the higher M_s cases, the comparison deteriorates. Though the exact cause of this is unclear, one possibility is uncertainty in the experimental measurements due to the quality of the experimental visualizations. Figure 5.10 shows a timelapse of the aerobreakup visualized using holographic interferograms, which is reproduced from Igra and Takayama [37]. Though this particular experiment involves two water cylinders, it demonstrates the available experimental visualization quality from which the measurements of Igra and Takayama [36] are made. The above qualitative and quantitative comparisons with experimental data, though not a rigorous validation of our simulations due

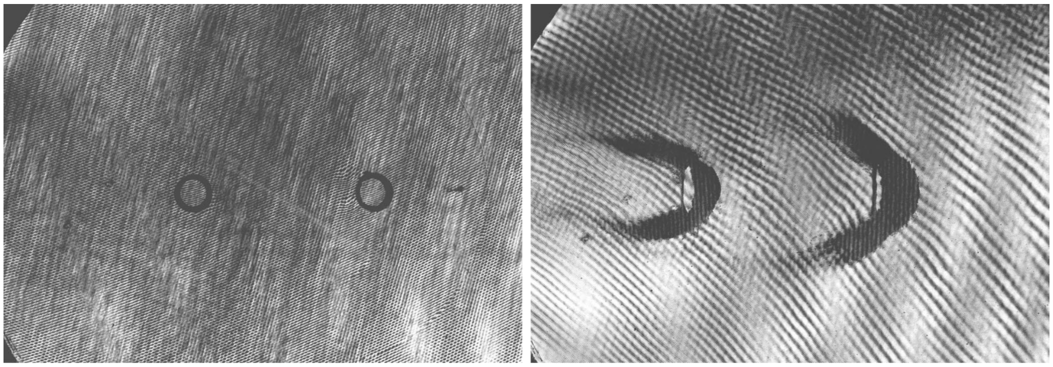

(a) $t = 70\,\mu\text{s}$, $t^* = 0.154$

(e) $t = 560\,\mu\text{s}$, $t^* = 1.231$

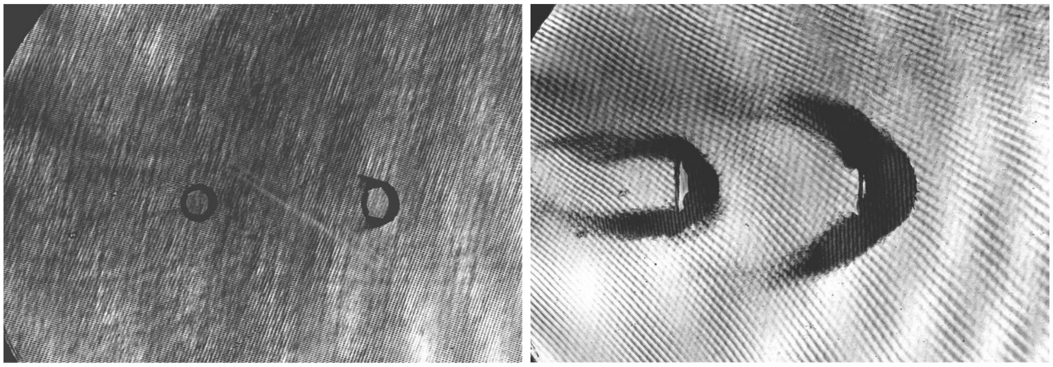

(b) $t = 140\,\mu\text{s}$, $t^* = 0.308$

(f) $t = 700\,\mu\text{s}$, $t^* = 1.539$

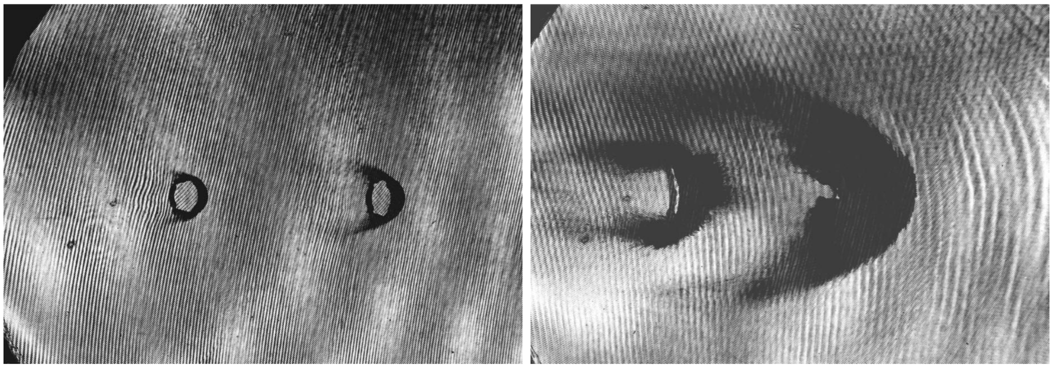

(c) $t = 210\,\mu\text{s}$, $t^* = 0.462$

(g) $t = 910\,\mu\text{s}$, $t^* = 2.000$

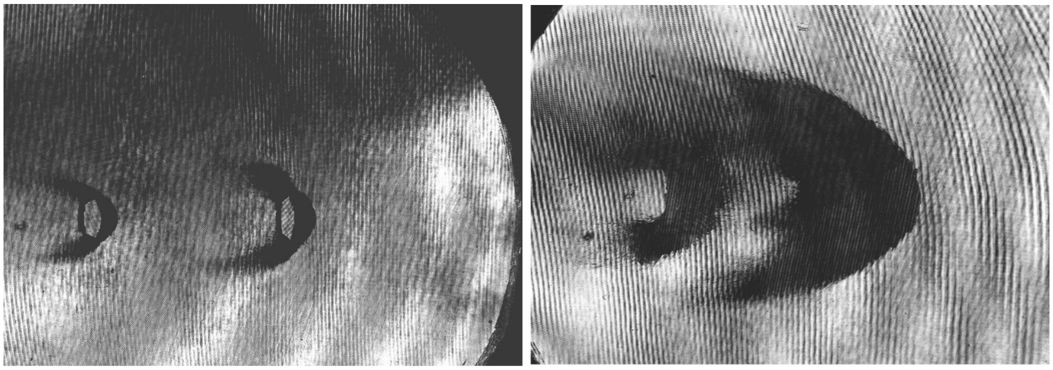

(d) $t = 350\,\mu\text{s}$, $t^* = 0.769$

(h) $t = 1050\,\mu\text{s}$, $t^* = 2.308$

Figure 5.10: Experimental holographic interferograms from Fig. 3 of [37] showing the aerobreakup of two $D_0 = 4.8\,\text{mm}$ water cylinders behind a $M_s = 1.47$ shock wave. Flow is from right to left. Reprinted from Igra and Takayama [37] with the permission of ASME. © 2003 by ASME.

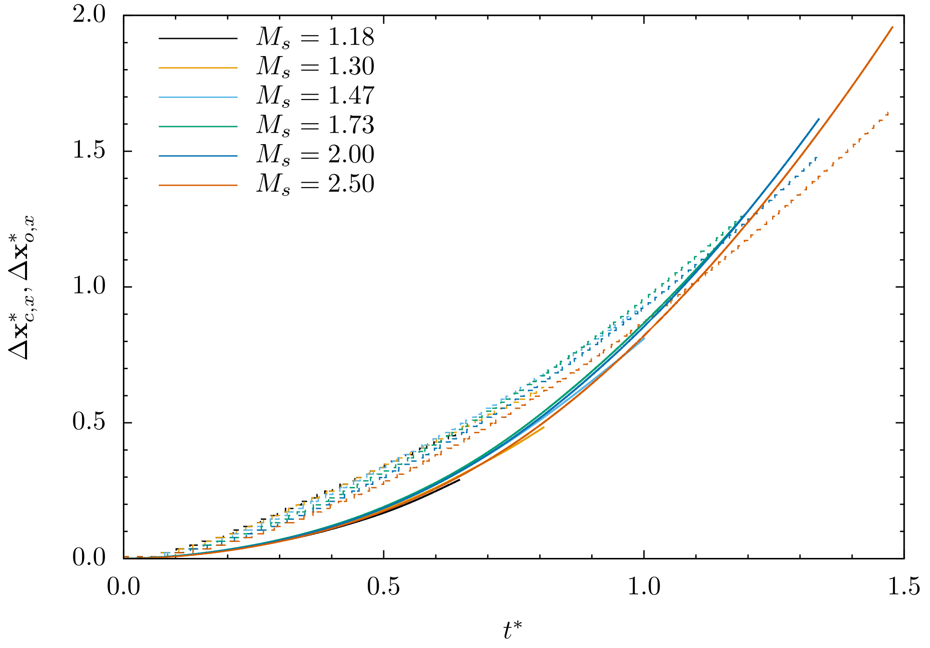

Figure 5.11: Cylinder streamwise drift as measured from the center of mass, $\Delta\mathbf{x}^*_{c,x}$ (continuous), and forward stagnation point, $\Delta\mathbf{x}^*_{o,x}$ (dashed).

to the aforementioned ambiguities, provide confidence in the accuracy of our numerical results.

5.3.3 Integral quantities and metrics

5.3.3.1 Center-of-mass properties

Proceeding to the results of our parametric study, we first examine the cylinder's center-of-mass drift and velocity curves. As noted by Theofanous [87], the stagnation point drift, $\Delta\mathbf{x}^*_{o,x}$, of the cylinder is an inaccurate representation of the center-of-mass drift, $\Delta\mathbf{x}^*_{c,x}$, though the former has often been a necessary simplification for extracting data from experimental visualizations. To evaluate the significance of the error, we compute both the location of the cylinder's center of mass using Eq. (3.10) and its leading edge (using $\alpha_{cr} = 0.50$), and plot both in Fig. 5.11 for the full range of simulated shock Mach numbers. Firstly, the appropriate nondimensionalization of time using the characteristic breakup time, Eq. (2.13), appears to collapse the cylinder trajectories across all simulated M_s. If one were to calculate the cylinder's acceleration from the drift data using finite-difference approximations or polynomial fitting, significant errors will be incurred by using $\Delta\mathbf{x}^*_{o,x}$

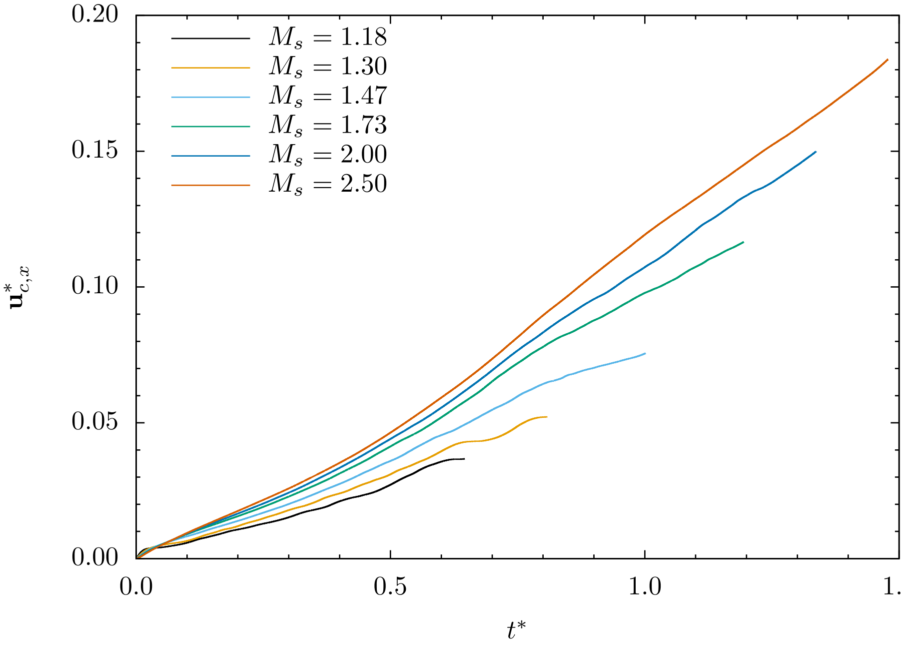

Figure 5.12: Cylinder streamwise center-of-mass velocity, $\mathbf{u}^*_{c,x}$.

instead of $\Delta\mathbf{x}^*_{c,x}$.

The cylinder's streamwise center-of-mass velocity, $\mathbf{u}^*_{c,x}$, computed from Eq. (3.12) and shown in Fig. 5.12, is not terribly interesting. Some cursory observations include a) stronger shocks induce higher cylinder velocities, as expected since u_s increases with M_s in the shock-moving reference frame, b) transition from subsonic to supersonic freestream flow does not appear to significantly alter the motion of the cylinder (also deducible from Fig. 5.11), and c) the noncollapse of the curves suggest an alternate scaling might be necessary.

The unsteady acceleration of a droplet suddenly exposed to a high-speed flow, and specifically, its unsteady drag coefficient, is of interest in many applications. For example, when modeling flows with particle or droplet clouds, the drag coefficient is often the parameter used to model the dynamics of the disperse phase. Attempts to calculate the drag coefficient of a deforming body have often assumed constant acceleration [37, 69, 79]. Indeed, the acceleration data reported by Chen [10] are derived from the drift data under this assumption; we thus do not make comparisons with those results. Despite the ubiquity of this simplification in the literature, our numerical results lead us to believe that this is not an accurate representation of the underlying physics.

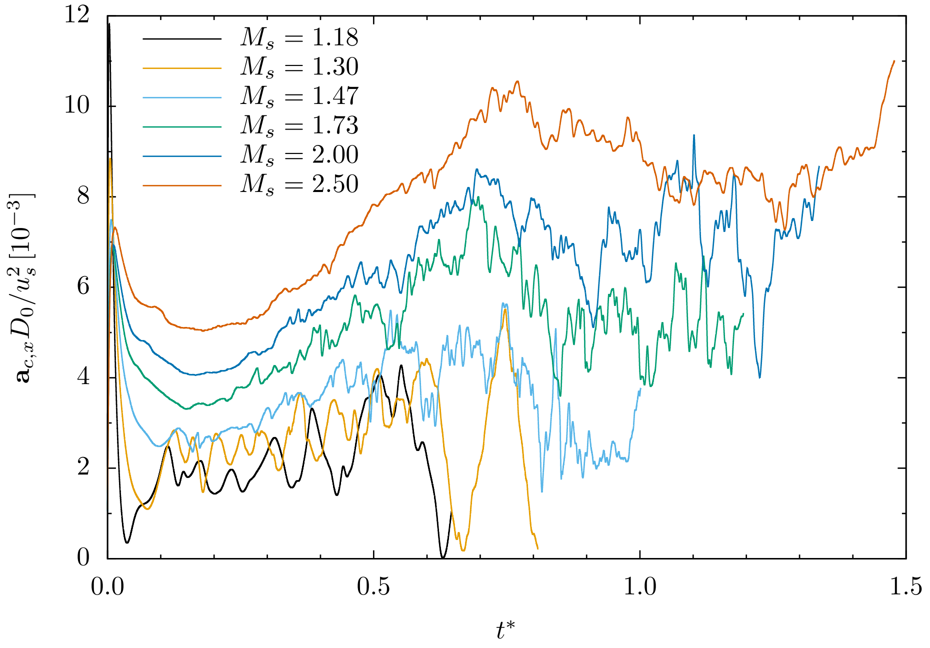

Figure 5.13: Cylinder streamwise center-of-mass acceleration, $\mathbf{a}_{c,x} D_0/u_s^2$.

Using Eq. (3.15), we compute the acceleration in the streamwise direction experienced by the cylinder's center of mass, $\mathbf{a}_{c,x}$. The results are plotted in Fig. 5.13, where acceleration has been nondimensionalized by the original cylinder diameter and post-shock air velocity. The initial spike in acceleration is the passage of the shock wave over the cylinder. As mentioned in Section 5.3.1, the maximum acceleration occurs when the shock reflection on the cylinder's surface transitions from a regular reflection to a Mach reflection. Once the shock has passed, the surrounding high-speed air begins to accelerate the cylinder. The acceleration oscillations, visible in Fig. 5.13, were initially thought to be associated with wake instability. However, replotting Fig. 5.13 using standard convective time units, $\dfrac{tu_s}{D_0}$, (shown in Fig. 5.14) reveals that the oscillations have a higher frequency than the well-known Stouhal number, $St = \dfrac{fD_0}{u_s}$, of 0.2 associated with wake instability behind a rigid sphere or cylinder. Note that the vertical gridlines in Fig. 5.14 (spaced $\dfrac{5D_0}{u_s}$ apart) coincide with the expected period for $St = 0.2$. Instead, these oscillations are perhaps related to the secondary higher-frequency St that is known to be associated with small-scale instabilities from the separation of the shear layer [48, 72].

In the course of our numerical analysis, we find that scaling the nondimensional acceleration by

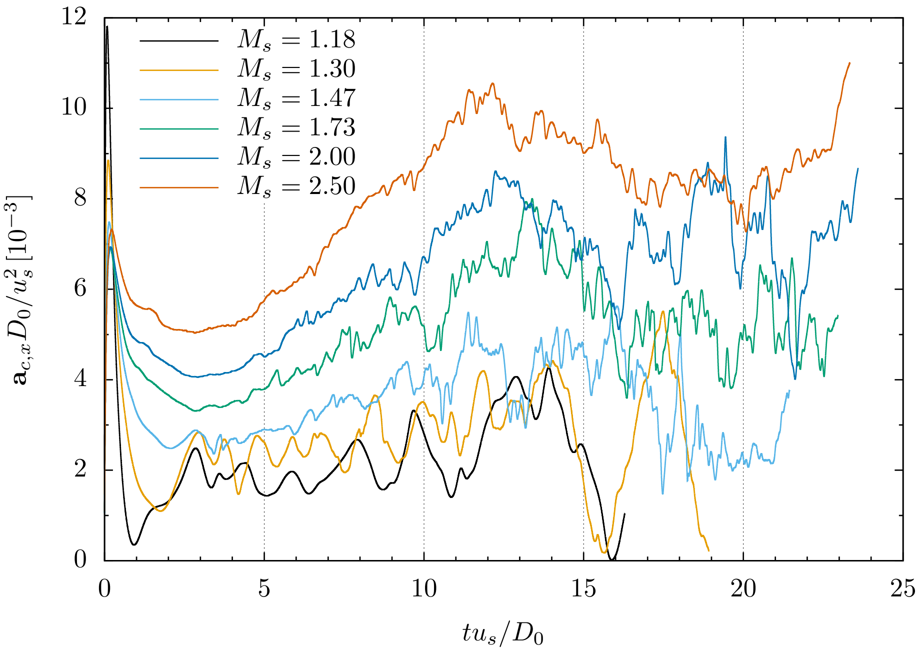

Figure 5.14: Cylinder streamwise center-of-mass acceleration in convective time units.

the pressure ratio across the incident shock wave appears to collapse the acceleration curves across all simulated shock Mach numbers. The rescaled nondimensional acceleration, plotted in Fig. 5.15, is given by

$$\check{\mathbf{a}}_{c,x} = \mathbf{a}_{c,x} \left(\frac{D_0}{u_s^2}\right) \left(\frac{p_{g,0}}{p_s}\right), \tag{5.1}$$

where $\dfrac{p_s}{p_{g,0}}$ is the pressure ratio across the incident shock (see Table 5.1).

5.3.3.2 Drag coefficient

Given our accurate acceleration history for the deforming cylinder, we can proceed to calculate its unsteady drag coefficient. The drag coefficient is defined as

$$C_D = \frac{F_D}{\frac{1}{2}\rho u^2 S} = \frac{m_l \mathbf{a}_{c,x}}{\frac{1}{2}\rho_s W^2 D}, \tag{5.2}$$

where $W = u_s - u_c$, F_D is the drag force, and D is a characteristic diameter. If we take the characteristic diameter to be the original cylinder diameter, $D = D_0$, as has typically been done in the literature, the computed drag coefficients, shown in Fig. 5.16, collapse across the range of

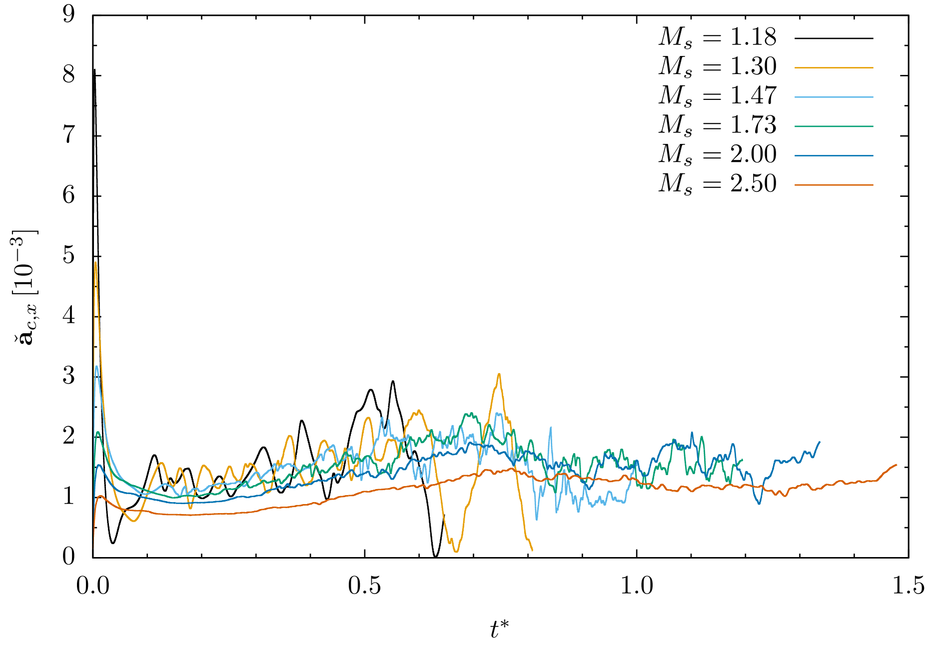

Figure 5.15: Rescaled cylinder streamwise center-of-mass acceleration, $\check{\mathbf{a}}_{c,x}$.

simulated M_s, and all exhibit an upward trend. Though a time-dependent drag coefficient can be used to model the dynamics of particles or droplets, we make an improvement by recognizing that the drag coefficient calculation should account for the changing diameter of the deforming cylinder. Recalculating the drag coefficient using the cylinder's deformed diameter, D_d, we find that the resultant C_D, shown in Fig. 5.17, can be reasonably approximated as a constant over the initial breakup period. It is notable that wave drag (in the case of supersonic post-shock flow) does not significantly alter the drag coefficient (as would be expected in the rigid body case). Not only is this drag coefficient more physically correct than the one based on the original cylinder diameter, it also simplifies the modeling of particle and drop dynamics since it can be approximated as a constant for the early times of breakup.

5.4 Viscous results

Using a $M_s = 1.50$ incident shock, a series of viscous runs, with explicit modeling of molecular viscosity, are performed varying the Reynolds number, Eq. (2.14), from 15 to 5000. Since the

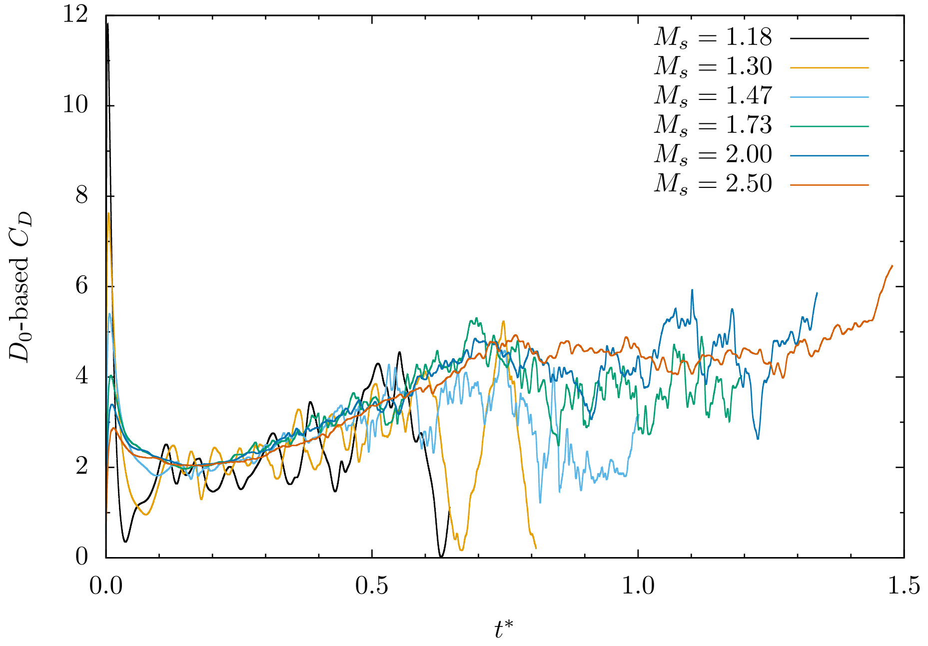

Figure 5.16: Cylinder unsteady drag coefficient, C_D, based on D_0.

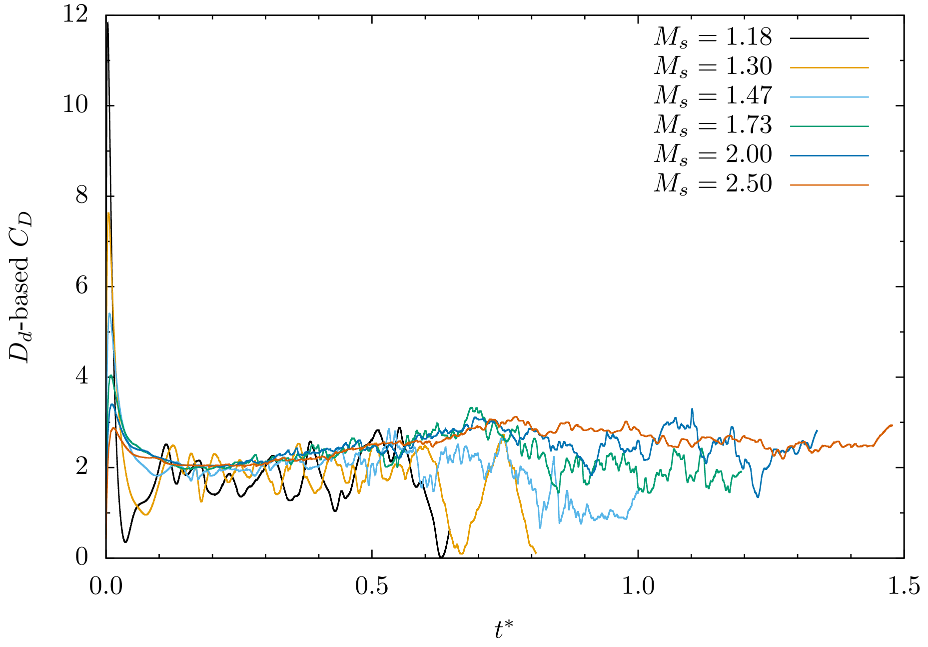

Figure 5.17: Cylinder unsteady drag coefficient, C_D, based on D_d.

D_0 [μm]	Re
0.50	15
2.50	75
5.00	150
16.84	500
50.00	1500
100.00	3000
168.43	5000

Table 5.2: Cylinder diameters and corresponding Re in the flow behind a $M_s = 1.50$ shock wave.

governing equations are solved in dimensionless form, the Reynolds number is varied by changing the physical diameter of the cylinder. However, the same viscous results would have been obtained had we varied the Reynolds number in some other fashion, e.g., holding cylinder diameter constant while varying u_s. The physical cylinder diameters and their corresponding Reynolds numbers, Eq. (2.14), are shown in Table 5.2.

5.4.1 Estimation of numerical viscosity

In the absence of molecular viscosity modeling, the aerobreakup simulations of Section 5.3 are considered to be inviscid. However, since the numerical method is both shock- and interface-capturing, numerical viscosity is present in the simulations, and its magnitude is related to the spatial resolution of the grid. Viscous simulations, i.e., simulations with molecular viscosity, are performed in an attempt to find an approximate lower bound for the apparent Reynolds number corresponding to the numerical viscosity associated with the present $(N_x, N_y) = (1200, 600)$ grid resolution. Our approach to estimating the magnitude of the numerical viscosity involves running a series of viscous simulations, holding grid resolution constant, while successively decreasing Reynolds numbers. At a critical Reynolds number, Re_{cr}, the molecular viscosity becomes sufficiently large to influence the flow physics, and causes a significant deviation from the inviscid simulation results.

Using the nominal $(N_x, N_y) = (1200, 600)$ spatial resolution, a series of simulations varying the Reynolds number from $Re = 15$–5000 are performed for the aerobreakup of a water cylinder behind a $M_s = 1.5$ shock. We begin by looking at metrics of the streamwise, $\Delta\mathbf{x}^*_{d,x}$, and spanwise, $\Delta\mathbf{x}^*_{d,y}$, extents, of the deformed cylinder using $\alpha_{cr} = 0.9$; time histories are shown, respectively, in Figs. 5.18

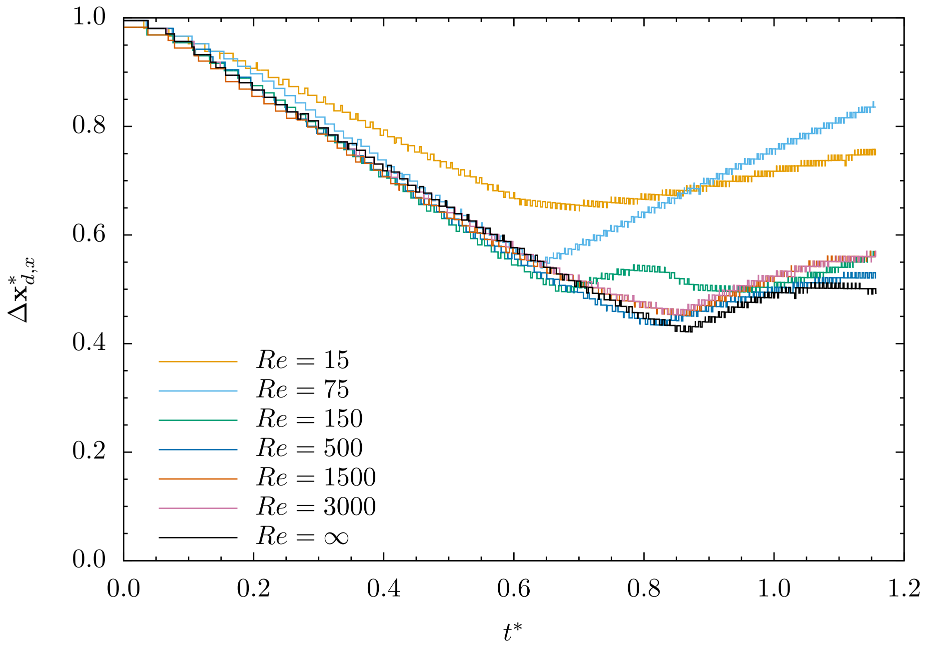

Figure 5.18: Streamwise extents of the deformed cylinder, $\Delta\mathbf{x}^*_{d,x}$, over a range of Re.

and 5.19. For the higher Re simulations ($Re \geq 500$), the plotted results suggest that the molecular viscosity is not yet sufficient to drastically alter the cylinder deformation from the inviscid case. However, as the Re is lowered, the molecular viscosity overcomes the numerical viscosity, and begins to affect the breakup dynamics. This is clearly seen for the $Re \leq 150$ curves in Figs. 5.18 and 5.19. Motivated by the presence of the viscous stress tensor in the energy equation, Eq. (2.1d), we proceed to plot the time histories of the kinetic and total energies integrated over the computational domain (Figs. 5.20 and 5.21, respectively). As the incident shock wave moves through the domain, the energy increases in a linear manner. When the shock exits at approximately $t^* = 0.4$, the energy in the domain begins to slowly decrease due to a net flux of energy out of the domain. In Fig. 5.20, the curves for $Re \geq 500$ match the inviscid curve indicating that the magnitude of the molecular viscosity is less than that of the numerical viscosity, which is responsible for the behavior of the curves. For Reynolds numbers $15 < Re < 150$, the magnitude of the molecular viscosity surpasses that of numerical viscosity, and changes the overall behavior of the curves. In Fig. 5.21, a smaller range of values for the Reynolds number is plotted, but it can be seen that the curves for $Re \geq 500$ are almost indistinguishable from the inviscid curve. Based on these viscous simulations, the apparent

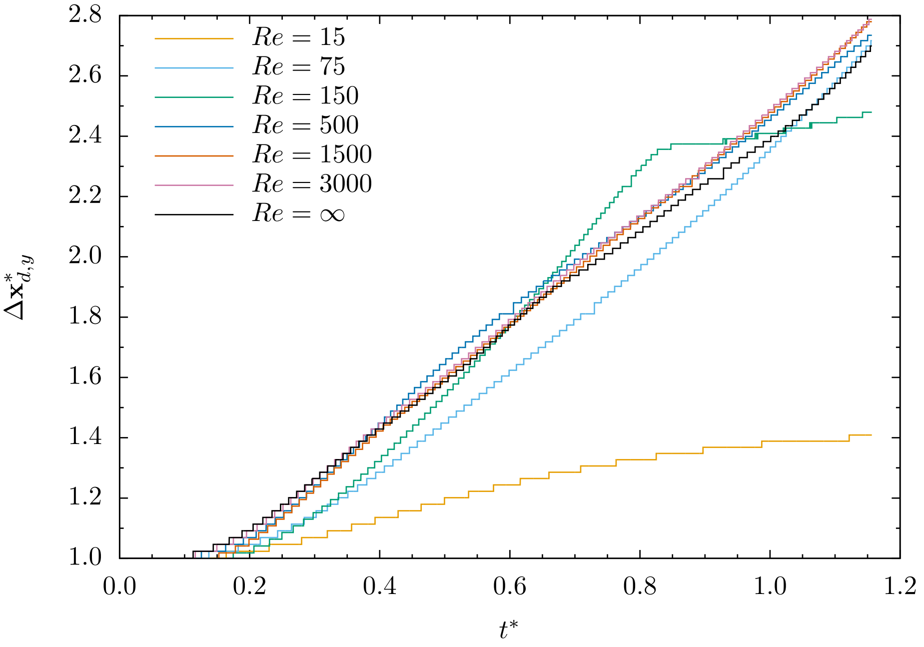

Figure 5.19: Spanwise extents of the deformed cylinder, $\Delta \mathbf{x}^*_{d,y}$, over a range of Re.

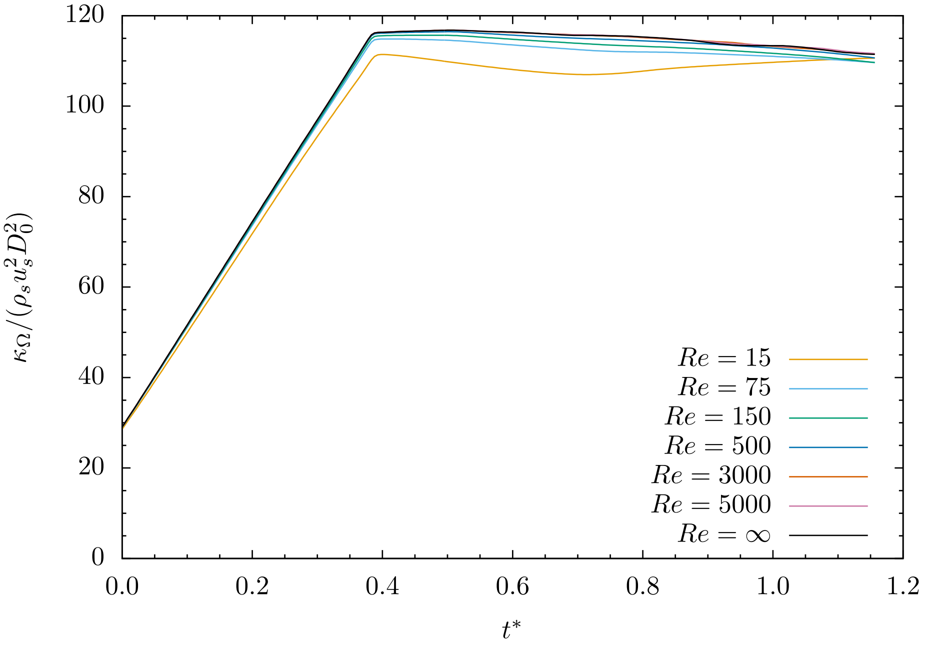

Figure 5.20: Computational domain kinetic energy, κ_Ω, over a range of Re.

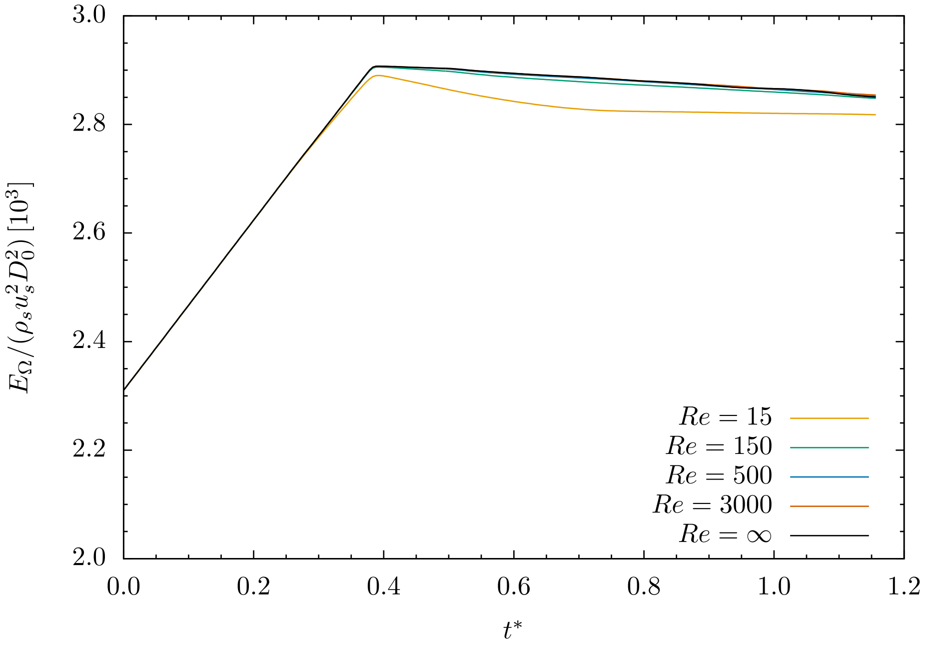

Figure 5.21: Computational domain total energy, E_Ω, over a range of Re.

Reynolds number associated with the numerical viscosity is believed to be no less than $Re_{cr} = 500$ at the level of resolution used in the present results. For a Mach 1.47 shock wave, this corresponds to a physical cylinder diameter of approximately $18\,\mu$m.

5.4.2 Testing the boundary layer stripping model

As briefly discussed in Section 1.2, the boundary layer stripping model of Ranger and Nicholls [69] is one of two theories that exist in the literature to describe the mechanism of mass loss in the stripping regime. Previous works that have argued against this theory include Liu and Reitz [54] who claimed that their experimental results cast considerable doubt on the boundary layer stripping model since cases with similar We and different Re exhibited the same breakup mechanism. Correspondingly, cases with similar Re and different We resulted in different modes of breakup. Thus, they argued that the stripping regime was relatively Re-independent. Their argument, however, is flawed in that Ranger and Nicholls [69] only claimed that Re would affect the *mass stripping rate*, and not the overall breakup mode. Indeed, Ranger and Nicholls state that "[t]he purpose of this study . . . is to establish the influence of various parameters on the *rate of disintegration* [emphasis added] and the time required for breakup to occur." The numerical work of Khosla et al. [46] also claimed to show "substantial evidence" against the boundary layer stripping model, but only qualitatively stated that "[t]echnically . . . we did not observe any 'boundary-layer' shearing. The refinement was fine enough to capture the boundary layer at the Reynolds numbers considered, but it was not the boundary layer that got sheared, but the entire edge itself." Unfortunately, the details of Khosla et al.'s numerical simulations are not provided.

Our viscous simulations of 2D aerobreakup put us in a unique position of being able to quantitatively test the boundary layer stripping model against our numerical results. Assuming steady, incompressible flow and a spherical droplet, Ranger and Nicholls [69] used a simplified analysis, similar to that of Taylor [86], to derive the following expression for the total mass loss as a function of t^*:

$$m_{\text{lost}}(t^*) = \sqrt{\frac{3}{2}\pi^3} \left(\frac{\rho_g \mu_g}{\rho_l \mu_l}\right)^{1/6} \left(\rho_l \nu_l^{1/2} u_s^{-1/2} D_0^{5/2}\right) \int_0^{t^*} \left(\frac{D}{D_0}\right)^{3/2} \left(1 - \frac{u_l}{u_s}\right)^{1/2} \mathrm{d}t^*. \tag{5.3}$$

Note that an arithmetic error in the exponent of the density ratio has been corrected in Eq. (5.3). Since viscous shear forces play a dominant role in the stripping of liquid from the droplet's equator, it is expected from theory that the Reynolds number should strongly affect the mass stripping rate. Specifically, as Reynolds number increases, i.e., viscous forces become less dominant, the rate of mass loss should correspondingly decrease. From our numerical results, we are able to track the mass of the coherent cylinder body using the threshold liquid volume fraction approach. We compute the nondimensional mass of the coherent body, m_d^*, as

$$m_d^* = \frac{1}{\rho_l D_0^2} \int_{\Omega'} \alpha_l \rho_l \, \mathrm{d}A, \tag{5.4}$$

where Ω' is defined as in Eq. (3.6). Results are shown in Fig. 5.22. We see that our viscous simulations do not support the boundary layer stripping model. Firstly, our numerical results indicate that mass loss is independent of Re (at least across an order of magnitude) during the early stages of breakup when the cylinder is well-approximated by a circle. Secondly, at later times, our

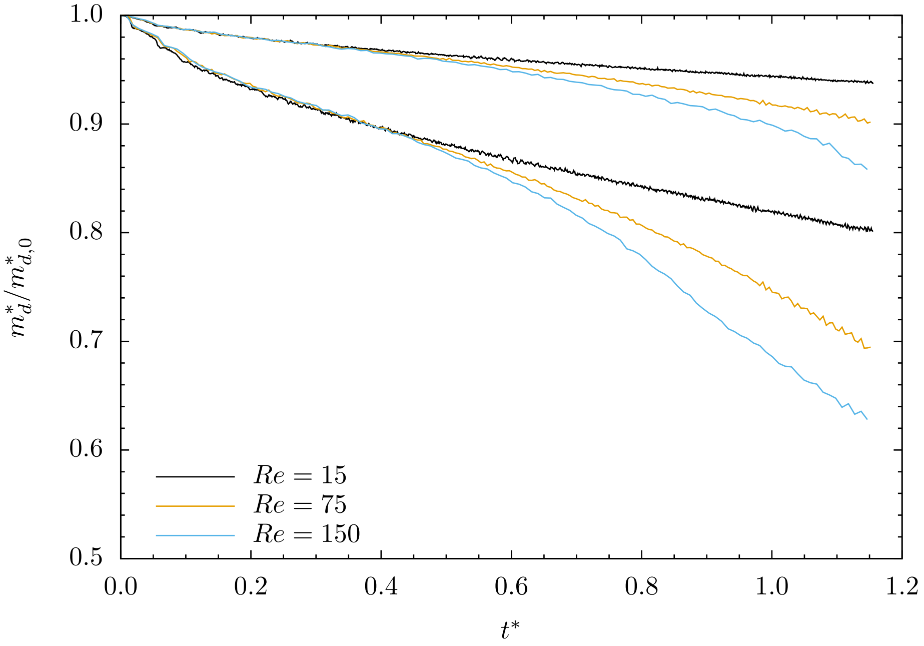

Figure 5.22: Normalized coherent body mass, $m_d^*/m_{d,0}^*$, over a range of Re using a spatial resolution of $(N_x, N_y) = (1200, 600)$. For each Re, two curves are shown corresponding to $\alpha_{cr} = 0.5, 0.9$.

numerical results show the reversal of the theoretically-expected trend of decreasing Re resulting in faster disintegration. While mass loss is always observed to occur at the cylinder periphery in the simulations, visualizations of the cylinder wakes at these three Re reveal differences in the generated flow scales. This scale generation difference also applies to the thin liquid sheet at the cylinder periphery, which is able to stretch and fold at higher Re resulting in increased mass loss rates. This effect becomes more pronounced at later times when the sheet has had sufficient time to develop. Thus, the difference in the mass loss rate as the Re is varied is attributable to the differences in generated flow scales.

5.5 Summary

In this chapter, the 2D aerobreakup of water cylinders in the flow behind normal shock waves in air is simulated. A parametric study varying the incident shock Mach number from $M_s = 1.18$–2.50 is carried out using the inviscid version of the governing equations. A qualitative description of the aerobreakup process is provided with emphasis on several key flow features such as the equatorial recirculation region and the presence of an upstream jet in the wake. While qualitative comparisons with experimental visualizations are limited to early times, quantitative comparisons with experimental data are shown for various metrics of cylinder deformation and displacement. Whilst the cylinder's displacement and velocity histories are fairly well-approximated, respectively, by parabolic and linear curves, the detailed unsteady acceleration imparted to the cylinder is far from constant, as has been erroneously assumed by previous work. When correctly scaled by the nonuniform diameter of the deforming cylinder, the unsteady drag coefficient is reasonably approximated by a constant for a significant portion of the aerobreakup process. The transition from subsonic to supersonic freestream flow does not alter the similarity of the solutions, and wave drag, notably, does not significantly change the unsteady drag coefficient, as would be expected in the case of flow past a rigid body. Using a series of viscous simulations with various Re, an attempt is made to bound the magnitude of the numerical viscosity present in the inviscid simulations. Additionally, these viscous simulations allow for the first quantitative examination of the mass loss rate equation of Ranger and Nicholls [69]. We find that, contrary to the boundary layer stripping theory, our numerical results show Re-independence at early times. Furthermore, the trend at later times for varying Re is reversed from that expected from theory.

Chapter 6

Three-dimensional aerobreakup

6.1 Overview

Given the similarity of observed flow phenomena across the range of M_s from our 2D parametric study, our numerical investigation of 3D aerobreakup consists of a single large-scale simulation believed to be representative of the stripping aerobreakup regime. Using the cylindrical coordinates implementation of Section 4.2, we simulate the full 3D aerobreakup of a water droplet in the flow behind a $M_s = 1.47$ shock wave in air. Relevant shock parameters and post-shock flow conditions can be found in Table 5.1. In light of the strong inertial forces that are, again, expected to dominate the majority of the breakup process, viscous and capillary effects are neglected. In the absence of these effects, the discussion in Section 3.1.3 on numerical viscosity and breakup mechanism is particularly relevant, and should be kept in mind.

The relevant simulation parameters are first laid out in Section 6.2. We then provide a qualitative description of the stripping aerobreakup phenomena in Section 6.3. After a description of the liquid droplet's morphology (Section 6.3.1), we show qualitative comparisons with experimental visualizations (Section 6.3.2) and investigate the gas behavior to shed light on the previously described liquid behavior (Section 6.3.3). A Fourier decomposition of the flow field is performed in Section 6.4 in an attempt to find the most energetic azimuthal modes. Finally, the droplet's center-of-mass properties and brief comments on breakup time are shown in Section 6.5.

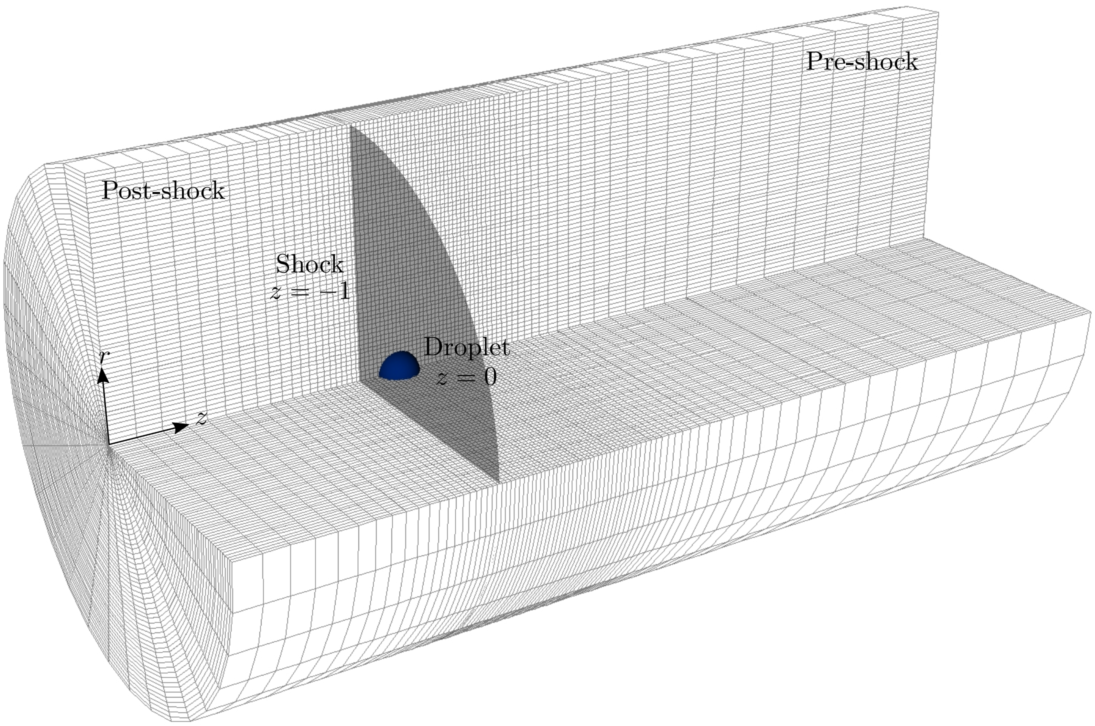

Figure 6.1: Schematic of the nonuniform computational grid at 1:10 of the actual resolution. The grid extends radially outward for $6D_0$, and the axial extents are $-7D_0 \leq z \leq 15.5D_0$.

6.2 Simulation parameters

The simulation is performed on the computational domain $\Omega = [-7D_0, 15.5D_0] \times [0, 6D_0] \times [0, 2\pi]$ using a spatial resolution of $(N_z, N_r, N_\theta) = (800, 600, 320)$ grid cells. The grid is stretched towards the axial boundaries using a hyperbolic tangent function. The most refined portion of the grid is located near the initial position of the droplet and in the region of the near-field wake. In this region, the nominal grid resolution is $\Delta z^* = \Delta r^* = 0.01$. The azimuthal resolution, and correspondingly $\Delta\theta$, are chosen such that the cells near the interface of the spherical droplet are close to regular. Again, traditional grid convergence or independence cannot be shown without the presence of molecular viscosity; the current spatial resolution follows from our grid resolution study in 2D (Appendix D.1) and is believed to capture the salient flow features. A schematic of the computational grid is shown in Fig. 6.1. Unlike the 2D simulations of Chapter 5, no symmetries are enforced or assumed, and the problem setup is completely general. At the boundaries of the computational domain, simple extrapolation BCs are applied such that outgoing waves are not reflected back to contaminate the solution. The simulation is run with a constant CFL number of $\mathcal{C} = 0.2$. Since the IC is axisymmetric, the gas is initially seeded with small random radial and azimuthal velocity perturbations, the largest of which have approximate magnitudes of $\mathcal{O}(10^{-4}u_s)$. These white-noise-type perturbations are generated via the Fortran compiler's intrinsic random number generator, and are applied to both the pre-shock and post-shock gas in the IC.

6.3 Qualitative description

In the following section, we provide a comprehensive qualitative description of the aerobreakup process. We begin by describing in Section 6.3.1 the evolution of the deforming droplet as observed from our simulation with a focus on the behavior of the liquid phase. Experimental visualizations are subsequently reproduced, and similarities in the droplet evolution and morphology are described in Section 6.3.2. The underlying flow physics associated with the gas phase are detailed in Section 6.3.3. Finally, a discussion of surface instabilities is included in Section 6.3.4.

6.3.1 Droplet morphology

Figure 6.2 shows an isometric view of isosurfaces of the liquid volume fraction. A quarter-cut has been removed for easier visualization of the interior isosurfaces, and the images (on each page) are ordered top to bottom, left to right. From Fig. 6.2, we observe that the morphology of the drop is not the typical flattening of a sphere into an ellipsoid with increasing eccentricity. Instead, the deformed sphere initially takes on a muffin-like shape, with the top of the muffin oriented upstream. That is, the upstream side of the droplet remains fairly spherical, but is pushed into the liquid behind it creating the muffin lip. The downstream side of the droplet is quickly compressed into a flat plane and remains so for a significant portion of the breakup. Two liquid sheets are observed during this deformation. The first is the established liquid sheet drawn from the droplet equator, while the second expands from the planar downstream side of the droplet. As the muffin-shaped droplet is compressed en masse, the liquid sheets eventually merge into a single sheet emanating from the droplet periphery. From Fig. 6.3, we see that the present spatial resolution is sufficient to

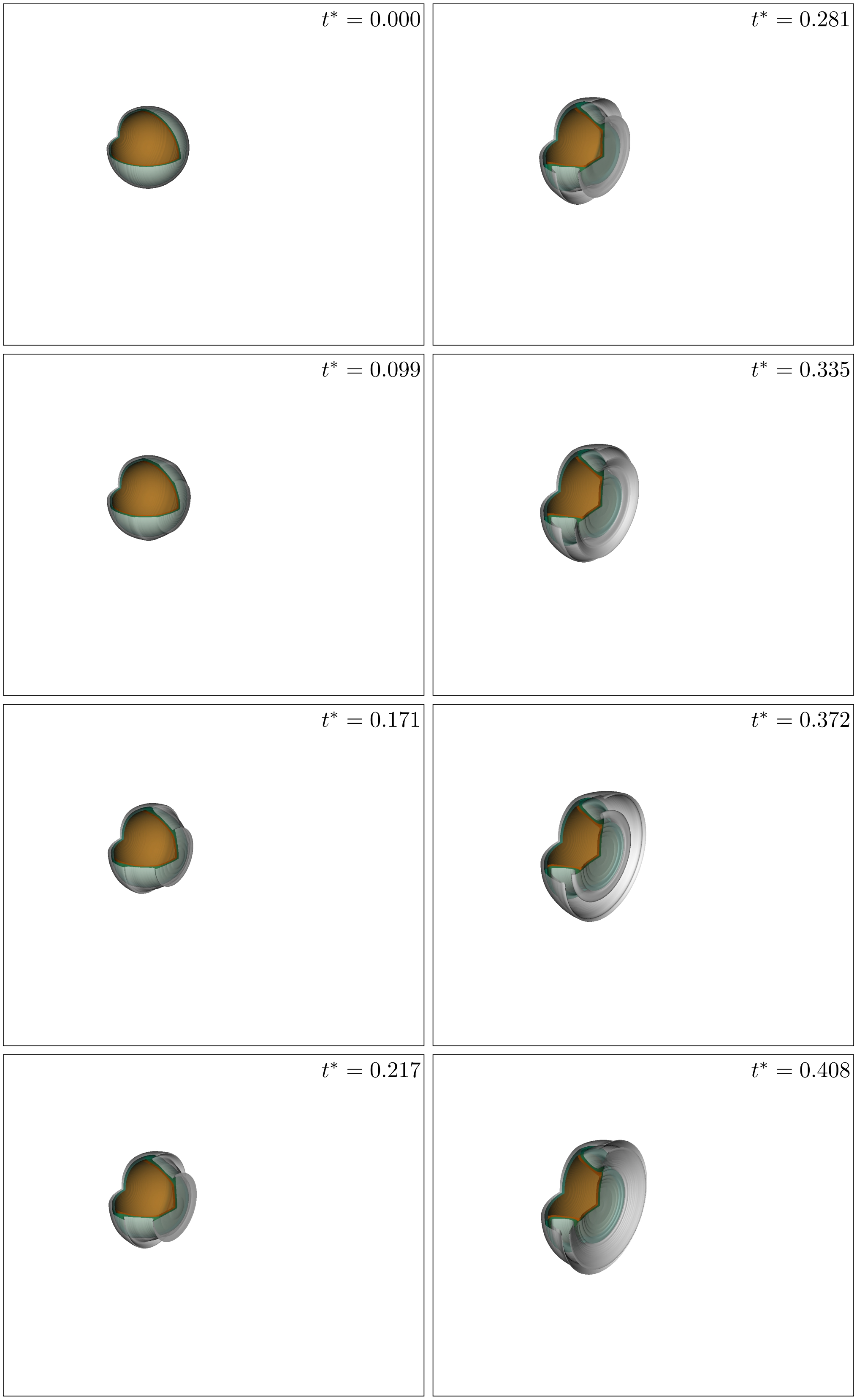

Figure caption on page 115.

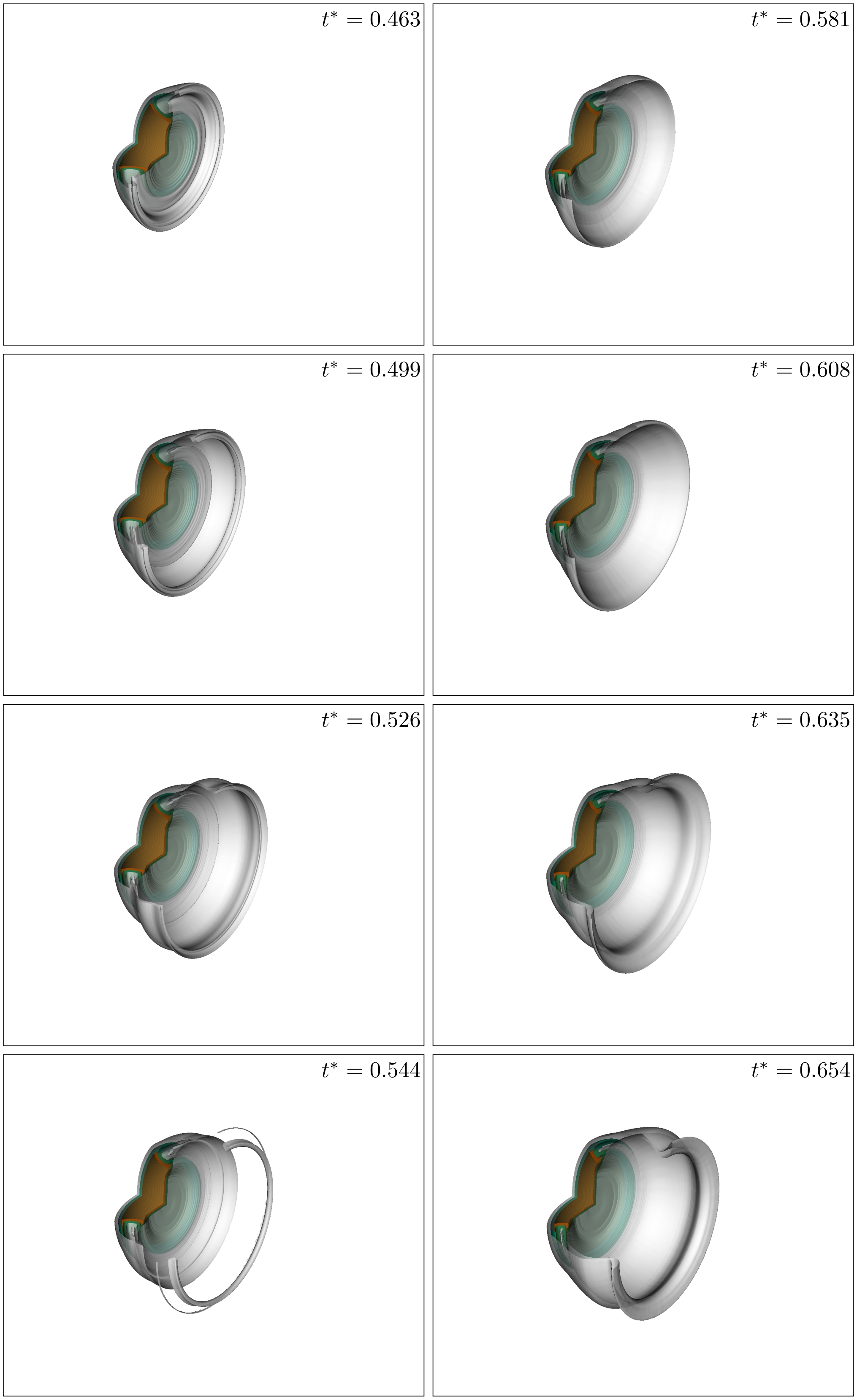

Figure caption on page 115.

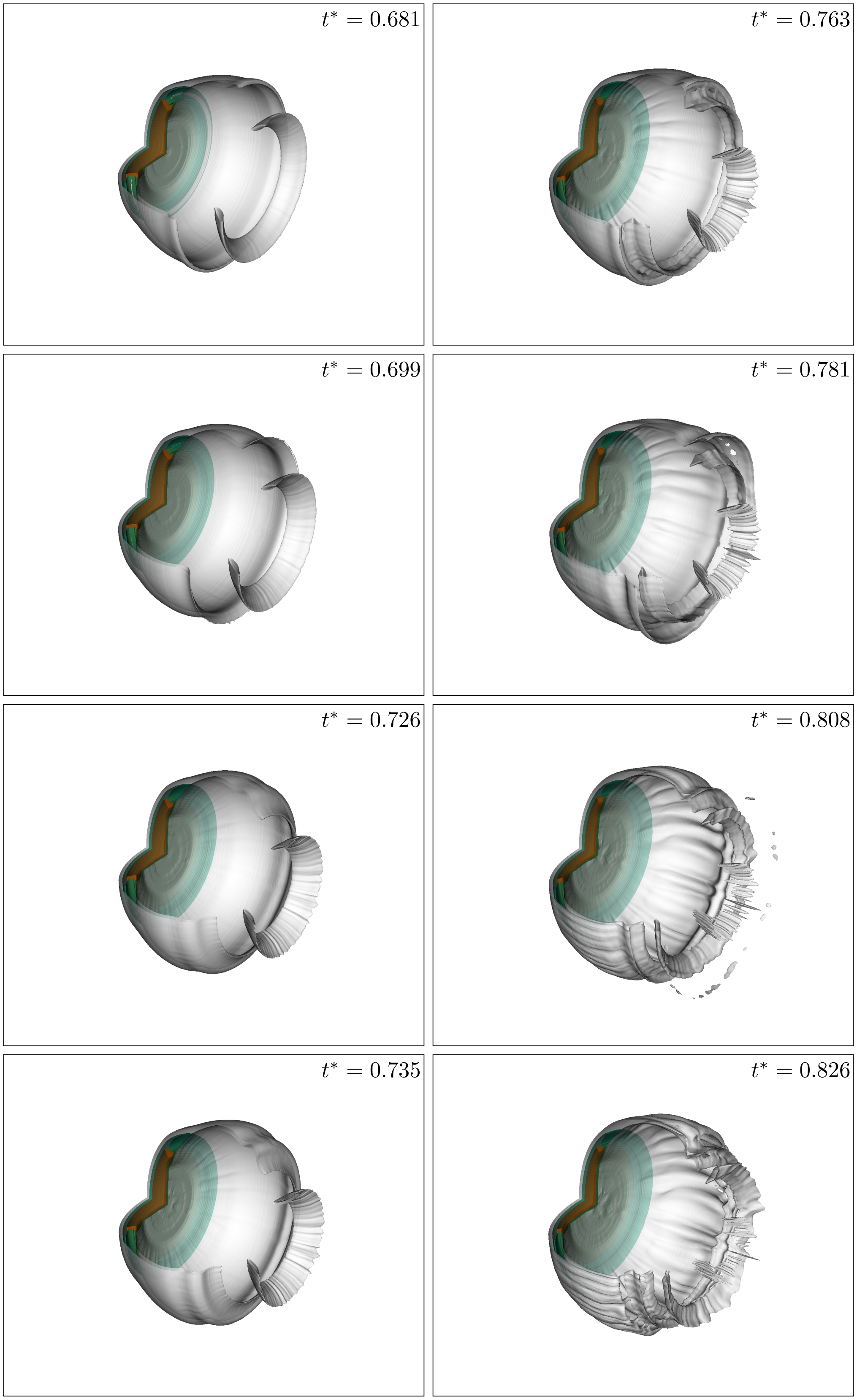

Figure caption on page 115.

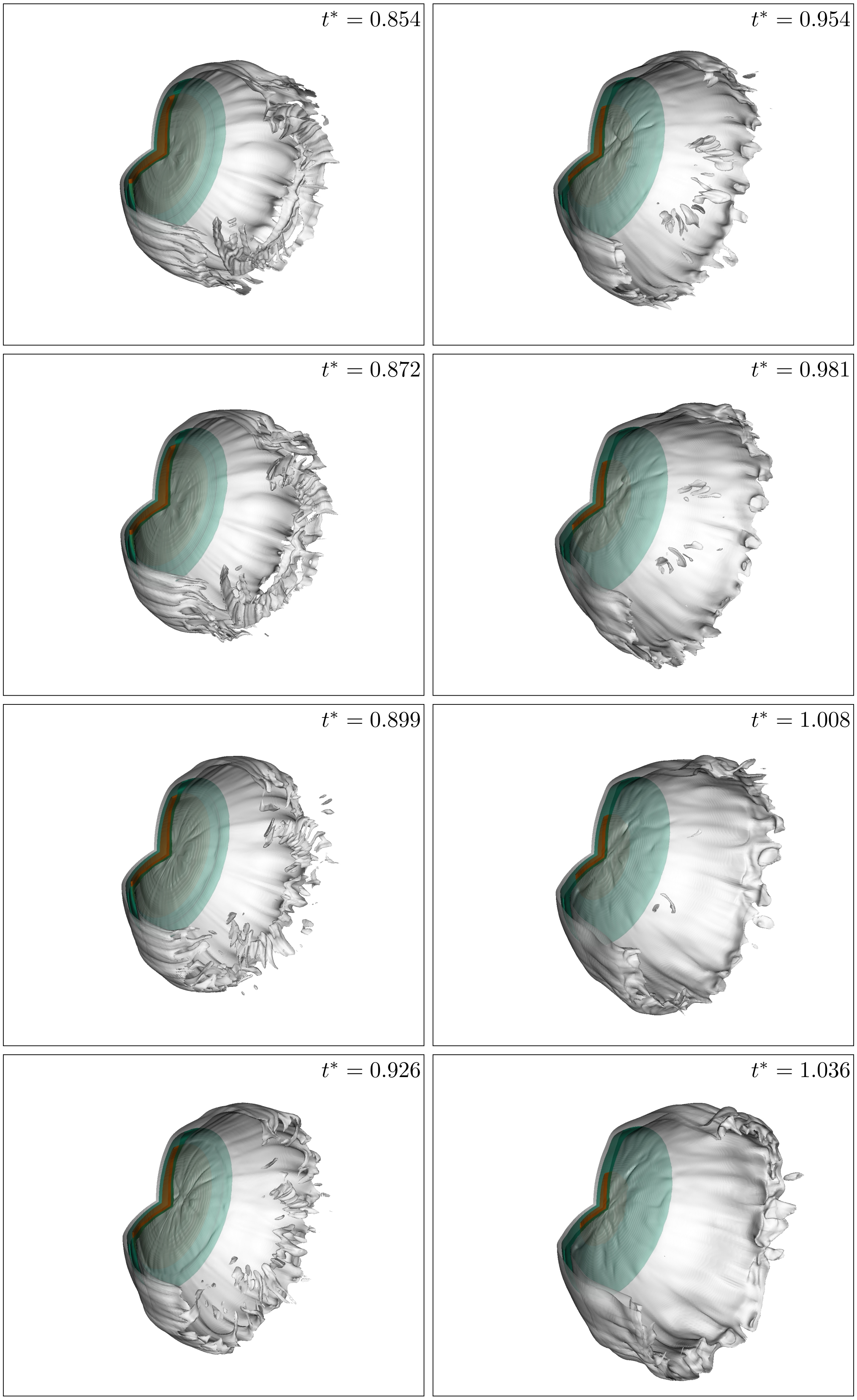

Figure 6.2: Isosurfaces of the liquid volume fraction, $\alpha_l = 0.99, 0.50, 0.01$ (orange, green, white). Flow is from top left to bottom right.

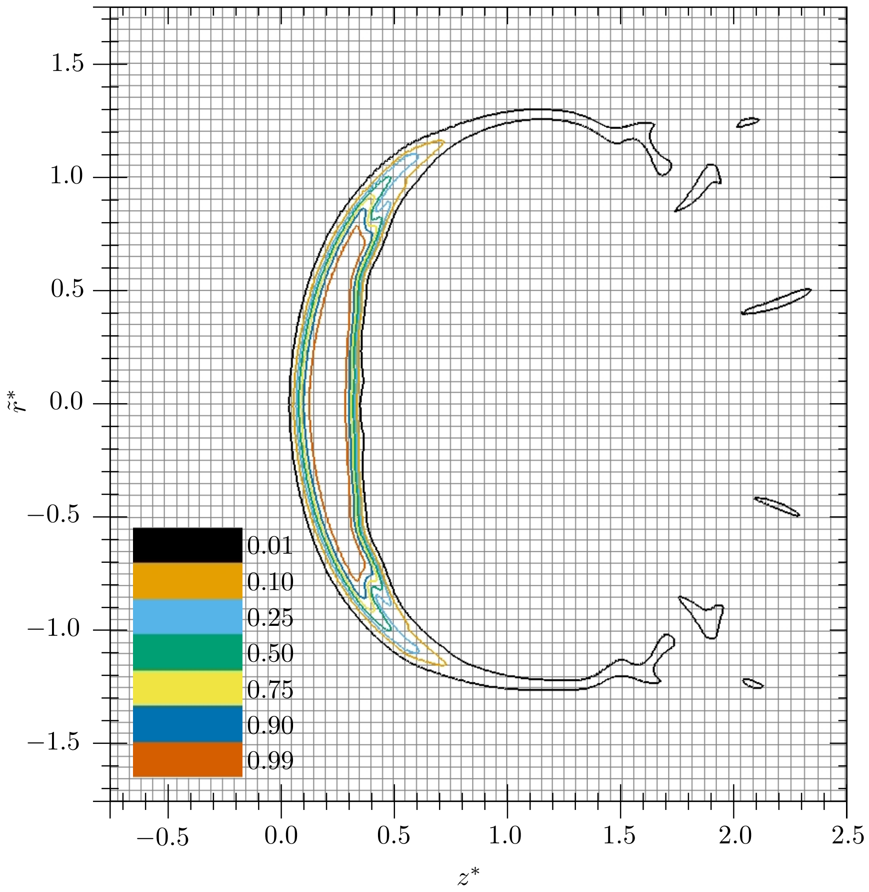

Figure 6.3: Sliced isopleths of α_l at $t^* = 0.799$ shown on the computational grid at 1:5 of the actual resolution.

resolve these liquid sheets, even at late times in the simulation. Since surface tension is not modeled in these results, the disjoint interface is an artifact of numerical diffusion and finite resolution. From the sequence of images in Fig. 6.2, the liquid sheet is observed to radially flap, and the dynamic liquid structure is reminiscent of a swimming jellyfish. Furthermore, this liquid sheet forms an envelope for a large cavity that exists directly behind the flattened drop. Theofanous et al. [90] experimentally observed this phenomenon (see Fig. 6.6) and described it as “a cylindrical ‘curtain’ around an empty space behind the coherent portion of the drop.” In the experiments, the curtain is composed of liquid fragments from the disintegrated liquid sheet. Our simulation, in the absence of surface tension, is unable to capture such a disintegration, though the small α_l-isovalue needed to visualize the sheet is indicative of its primarily gaseous composition. At approximately $t^* = 0.681$, the axisymmetry of the liquid sheet is lost as instabilities arise on the surface in the form of transverse azimuthal modulations as described in Section 1.2.1.4. These instabilities, as they relate to our numerical results, are further discussed in Section 6.3.4. At late times in the breakup process, the larger α_l-isosurfaces show the coherent droplet body as a large thin disk-like shape.

As discussed in Section 3.1.3, the actual physical disintegration mechanism of the thin liquid sheet is driven by capillary forces. In our simulations, however, breakup of the sheet occurs as a consequence of numerical diffusion and finite spatial resolution. In an attempt to quantify how significant capillary effects are in the disintegration of the liquid sheet, we proceed to compute an approximate sheet Weber number as

$$We_{\text{sheet}} = \frac{\rho_l \mathbf{u}_{c,z}^2 \frac{5D_0}{100}}{\sigma}, \tag{6.1}$$

where the length scale of $\dfrac{5D_0}{100}$ is obtained by observing that the sheet is resolved on approximately five grid cells in Fig. 6.3, and the nominal spatial resolution is 100 cells per original droplet diameter. From the numerical viscosity analysis of Section 5.4.1, we can estimate the physical diameter of the droplet to be approximately $18\,\mu$m in the flow behind a $M_s = 1.47$ shock wave. The surface tension coefficient between air and water is $\sigma = 0.07286\,\text{N/m}$, and we take the droplet velocity as the final value of $\mathbf{u}_{c,z} = 12.946\,\text{m/s}$ before Eq. (3.12) is invalid due to mass loss through the domain boundaries. Using these values, the sheet Weber number is approximately $We_{\text{sheet}} = 2.07$. The vast literature on the atomization of both planar and annular liquid sheets exposed to gas flows (e.g., [31, 55, 57, 74, 81] is beyond the scope of this thesis, but capillary effects are expected to play a significant role in the sheet disintegration given the small We_{sheet} value.

6.3.2 Experimental comparisons

For comparison, we look to the experimental visualizations of Theofanous et al. [90] and related publications, e.g., [87–89]. Their images, using shadowgraphy and laser-induced flourescence imaging, are, by far, the clearest images we have found in the literature capturing the aerobreakup process. The experiments shown in this section studied the breakup of water droplets (among other tested liquids) in a helium shock tube. Despite a mismatch in flow conditions and a dearth of timing data, our numerical results show good qualitative agreement with the experimental visualizations of the SIE phenomenology. Figures 6.4 and 6.5 are two timelapses taken of the aerobreakup process for aerobreakup in Mach 0.16 and 0.32 flow (recall that our numerical results are for Mach 0.58 flow). The experimental Reynolds and Weber numbers are $Re = 1.2 \times 10^4$, $We = 210$ for Fig. 6.4, and $Re = 2.2 \times 10^4$, $We = 780$ for Fig. 6.5. These large Reynolds numbers, and Weber numbers that are firmly in the stripping regime allow us to make qualitative comparisons with our numerical results. From Figs. 6.4 and 6.5, which are most comparable to Fig. 6.2, we see the same initial deformation of the droplet into a muffin-like shape. The upstream side of the droplet remains spherical, while the downstream side is flattened into a planar surface. What appears to be a thin liquid sheet coming from the spherical lip is visible in the second to the right column of Fig. 6.4 (the translucent liquid and oblique camera angle make it difficult to determine with certainty), while tips are seen in Fig. 6.5 that quickly disintegrate into a mist that obscures the coherent part of the droplet. At late times in the SIE process, the mist of liquid fragments seen in Fig. 6.6 form a cylindrical curtain around a cavity behind the coherent droplet. For comparison, we show in Fig. 6.7 the right image of Fig. 6.6b next to the liquid sheet as visualized by an isosurface of $\alpha_l = 0.01$. Though these experimental comparisons are not without uncertainty, the overall good qualitative agreement between experimental and numerical results gives us confidence in both the fidelity of our simulation, and in the conclusions that are drawn from our analysis.

6.3.3 Gas behavior

From their experimental results, Liu and Reitz [54] proposed a rough classification of the breakup process into two stages. They experimentally observed the first stage as a pressure-driven shape change of the droplet. This deformation stage, shared amongst multiple breakup regimes, is characterized by a flattening of the droplet in the streamwise direction. This pancaking is a consequence of the nonuniform pressure distribution around the droplet surface. High pressures at the forward and rear stagnation points, as well as low pressures at the equator due to the acceleration of the

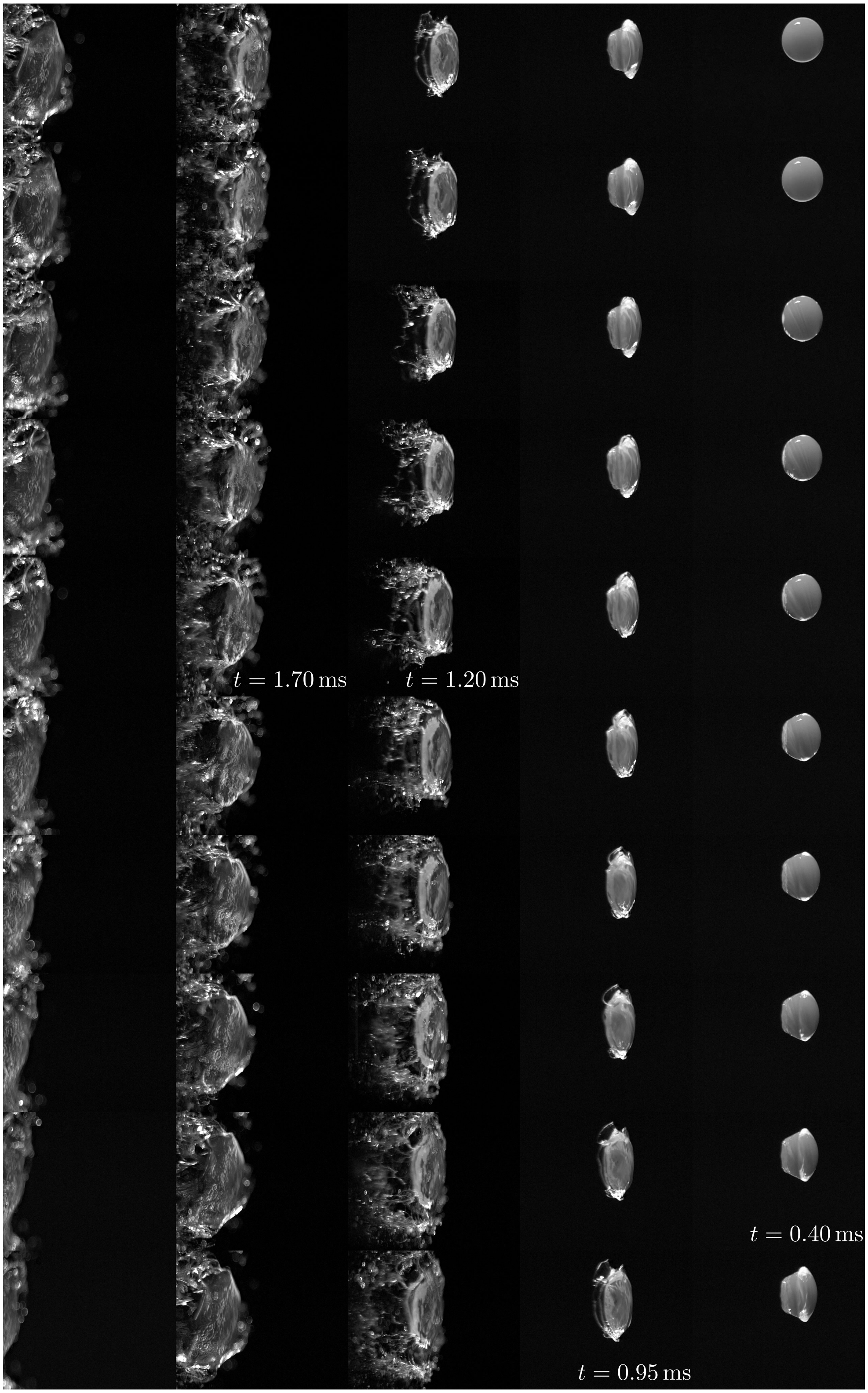

Figure 6.4: Experimental visualization of the aerobreakup of a water droplet in Mach 0.16 flow from Fig. 14 of [90]. Flow is from right to left, and the images are ordered top to bottom, right to left. Limited timing information is available, and is shown on the bottom right of the corresponding frame. Individual frames are reproduced from the video stored online (URL: http://dx.doi.org/10.1063/1.3680867.6). Reprinted from Theofanous et al. [90] with the permission of AIP Publishing. © 2012 by the American Institute of Physics.

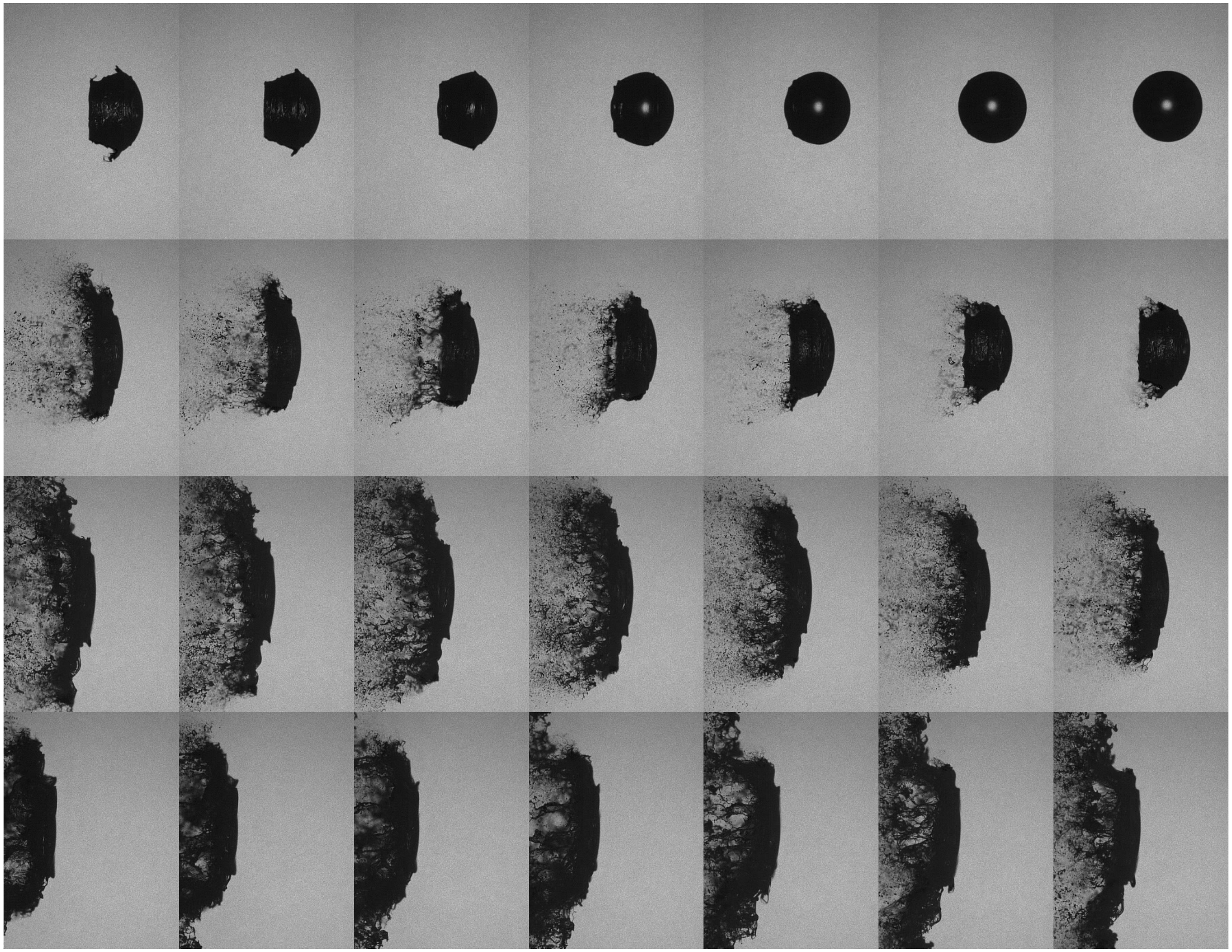

Figure 6.5: Experimental visualization of the aerobreakup of a water droplet in Mach 0.32 flow from Fig. 33b of [90]. Flow is from right to left, and the images are ordered right to left, top to bottom. No timing information is available. Individual frames are reproduced from the video stored online (URL: http://dx.doi.org/10.1063/1.3680867.12). Reprinted from Theofanous et al. [90] with the permission of AIP Publishing. © 2012 by the American Institute of Physics.

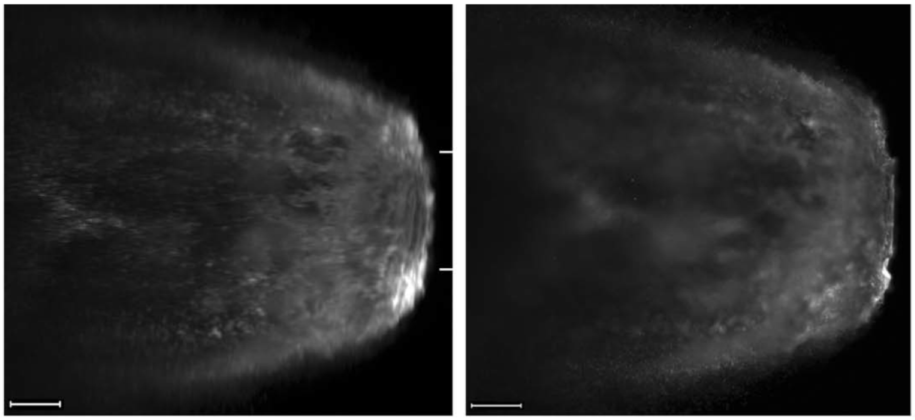

(a) Mach 0.56 flow at $t^* = 0.72$.

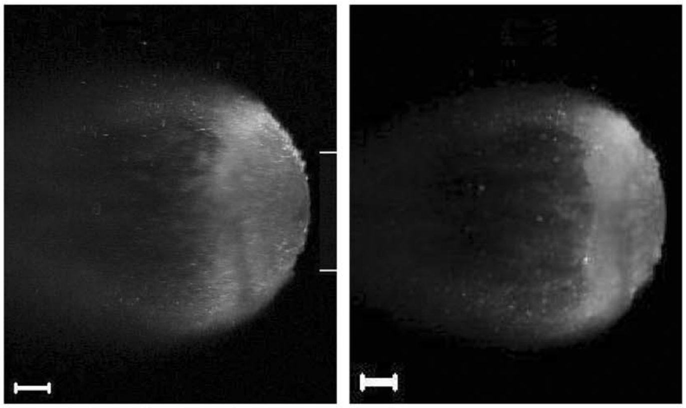

(b) Mach 0.59 flow at $t^* = 0.81$.

Figure 6.6: Experimental visualizations from two camera angles of the aerobreakup of a water droplet showing the advanced stages of SIE from Fig. 17 of [90]. Reprinted from Theofanous et al. [90] with the permission of AIP Publishing. © 2012 by the American Institute of Physics.

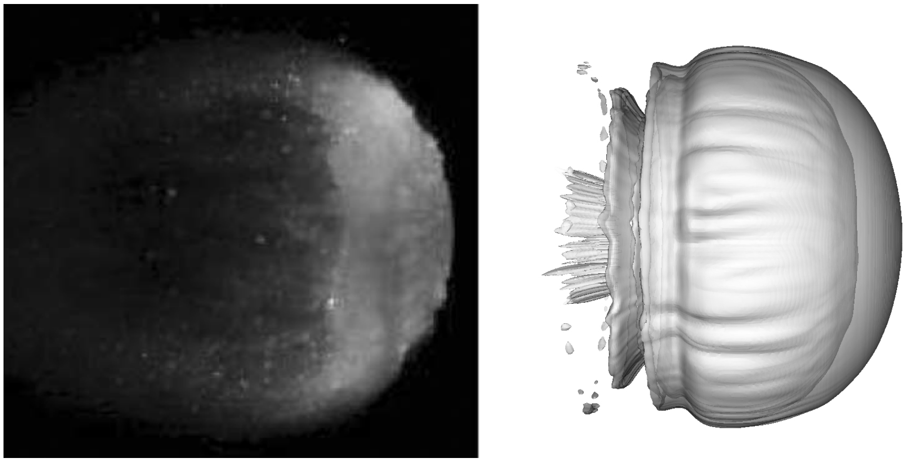

Figure 6.7: Comparison of experimental and numerical liquid "curtains." The experimental image on the left is for Mach 0.59 flow at $t^* = 0.81$ [90], and the numerical image on the right is for Mach 0.5775 flow at $t^* = 0.808$. Experimental image reprinted from Theofanous et al. [90] with the permission of AIP Publishing. © 2012 by the American Institute of Physics.

gas, both contribute to the flattening of the droplet. The second stage, as described by Liu and Reitz [54], is characterized by droplet disintegration and is when the phenomenology diverges for the various breakup regimes. For the stripping regime, they observed the edges of the droplet being drawn out into a thin liquid sheet by drag forces, and the subsequent breakup of the sheet into fine ligaments. Contrary to Liu and Reitz's description of the breakup process as two consecutive stages, our numerical results suggest that the phenomenology of stripping may be better described as the simultaneous flattening and stripping of liquid material. In fact, not only are the flattening and the disintegration processes occurring concurrently throughout the breakup process, they are also intricately connected by the dynamic behavior of the surrounding gas flow.

In order to elucidate why the liquid behaves as it does, we look to the behavior of the surrounding gas flow as visualized in Figs. 6.8 and 6.9 (images are, again, ordered top to bottom, left to right). Figure 6.8 shows 2D slices taken through the center of the droplet, $x^*, y^* = 0$, that are offset for unobstructed viewing of both planes. The vertical plots are colored by velocity magnitude normalized by the post-shock gas velocity, $\|\mathbf{u}\|^*$, while the horizontal plots are colored by pressure, p^*. Isopleths of the numerical schlieren function (defined in Section 5.3.1) reveal the intricate and dynamic flow structures that develop in the wake. The three-dimensionality of the aerobreakup process is well captured in Fig. 6.9, which plots various isosurfaces of azimuthal vorticity, ω_θ. Since the innermost regions of the flow are obstructed from view, slices are again taken through the center of the drop and offset to both sides. The transverse slice, offset upstream of the droplet, is taken at $z^* = 1$.

The incident and reflected shock waves, as well as the secondary wave system generated by the convergence of Mach stems at the rear stagnation point, are visible in the first few snapshots of Fig. 6.8. Much like in the 2D results of Section 5.3.1, the peak drag of the droplet is marked by the transition of the reflected shock from a regular reflection to a Mach reflection at some inclination angle preceding the droplet equator. Promptly after the passage of the incident shock, the flow is accelerated to approximately $1.5u_s$ at the droplet's equator (pink coloring is visible at $t^* = 0.044$ in Fig. 6.8), which is the value expected from potential flow theory for flow past a rigid sphere. In the early stages of droplet deformation, $t^* \leq 0.381$, the transmitted wave that propagates into the

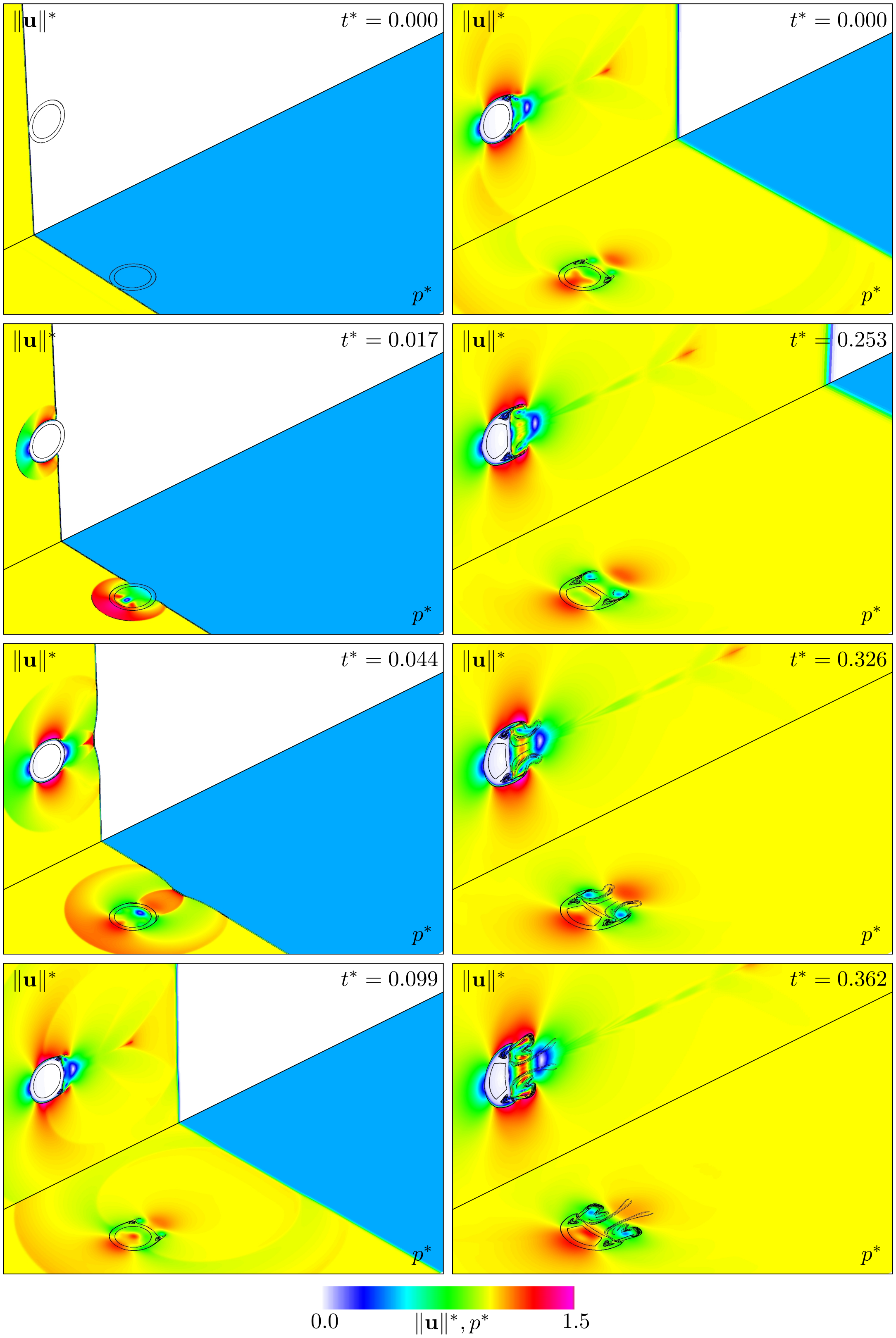

Figure caption on page 125.

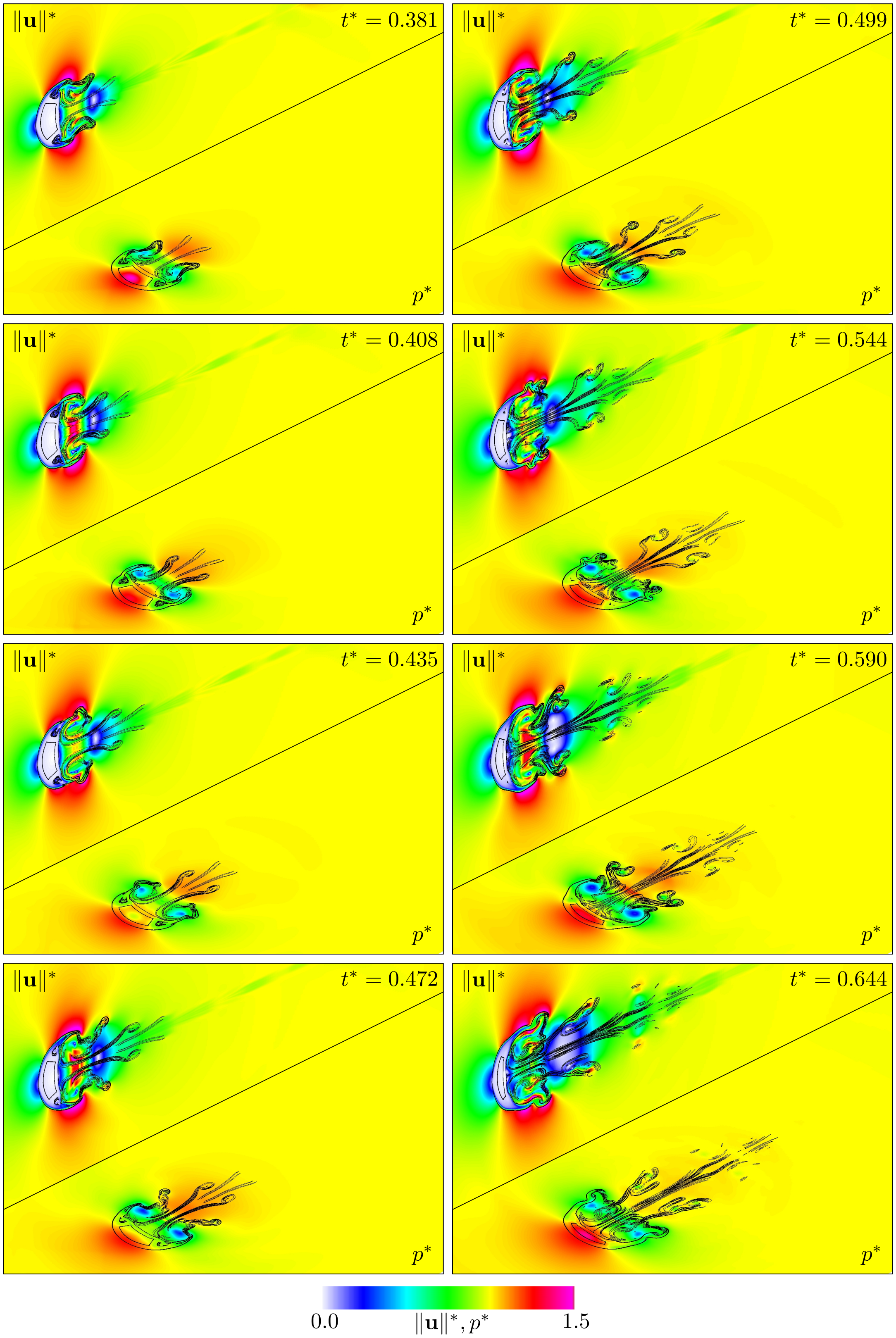

Figure caption on page 125.

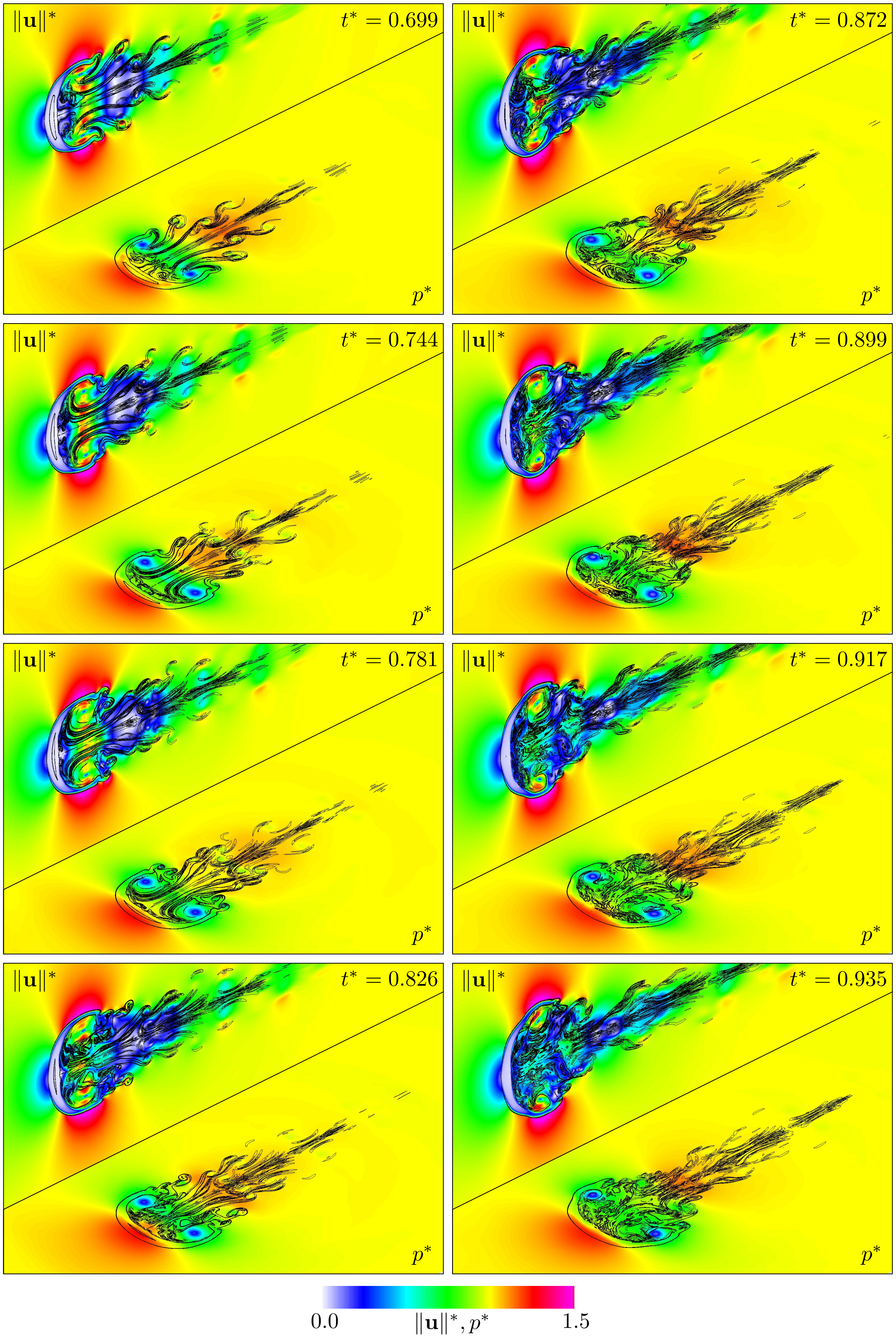

Figure 6.8: Filled contour slices of velocity magnitude, $\|\mathbf{u}\|^*$, and pressure, p^*, and isopleths of the numerical schlieren function. Flow is from bottom left to top right. Offset 2D slices are taken at $x^* = 0, y^* = 0$. The numerical schlieren function is defined as in Section 5.3.1.

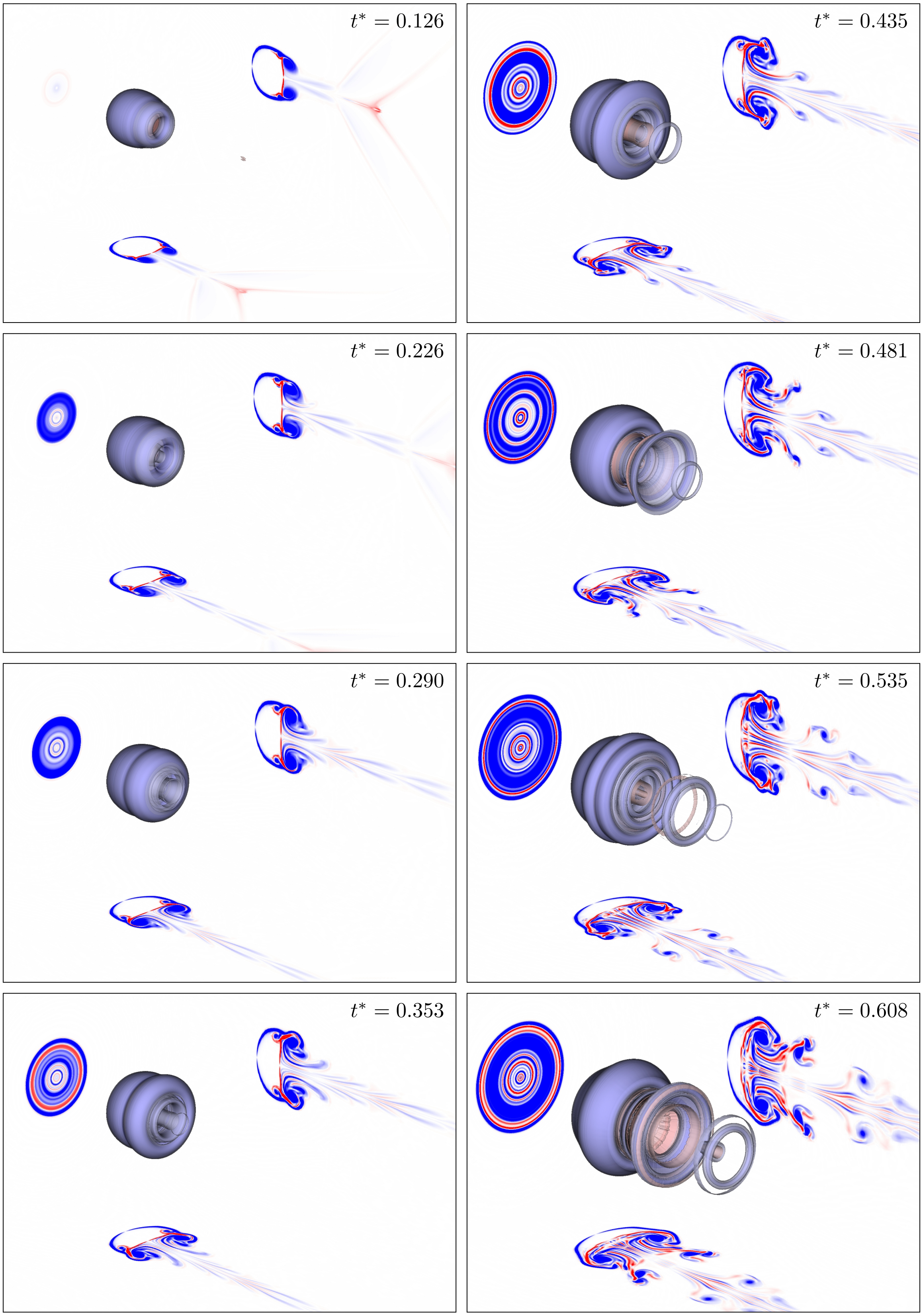

Figure caption on page 128.

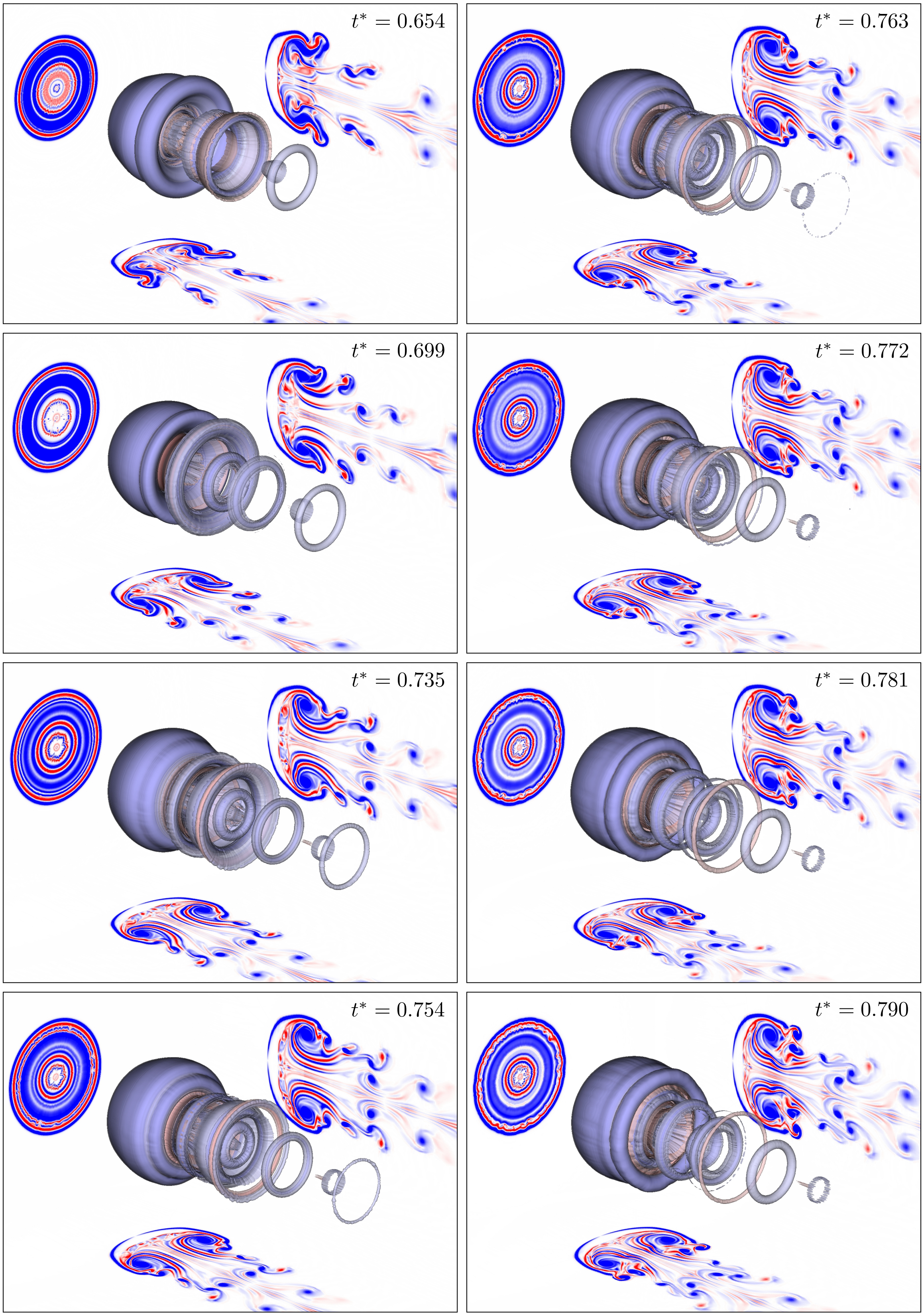

Figure caption on page 128.

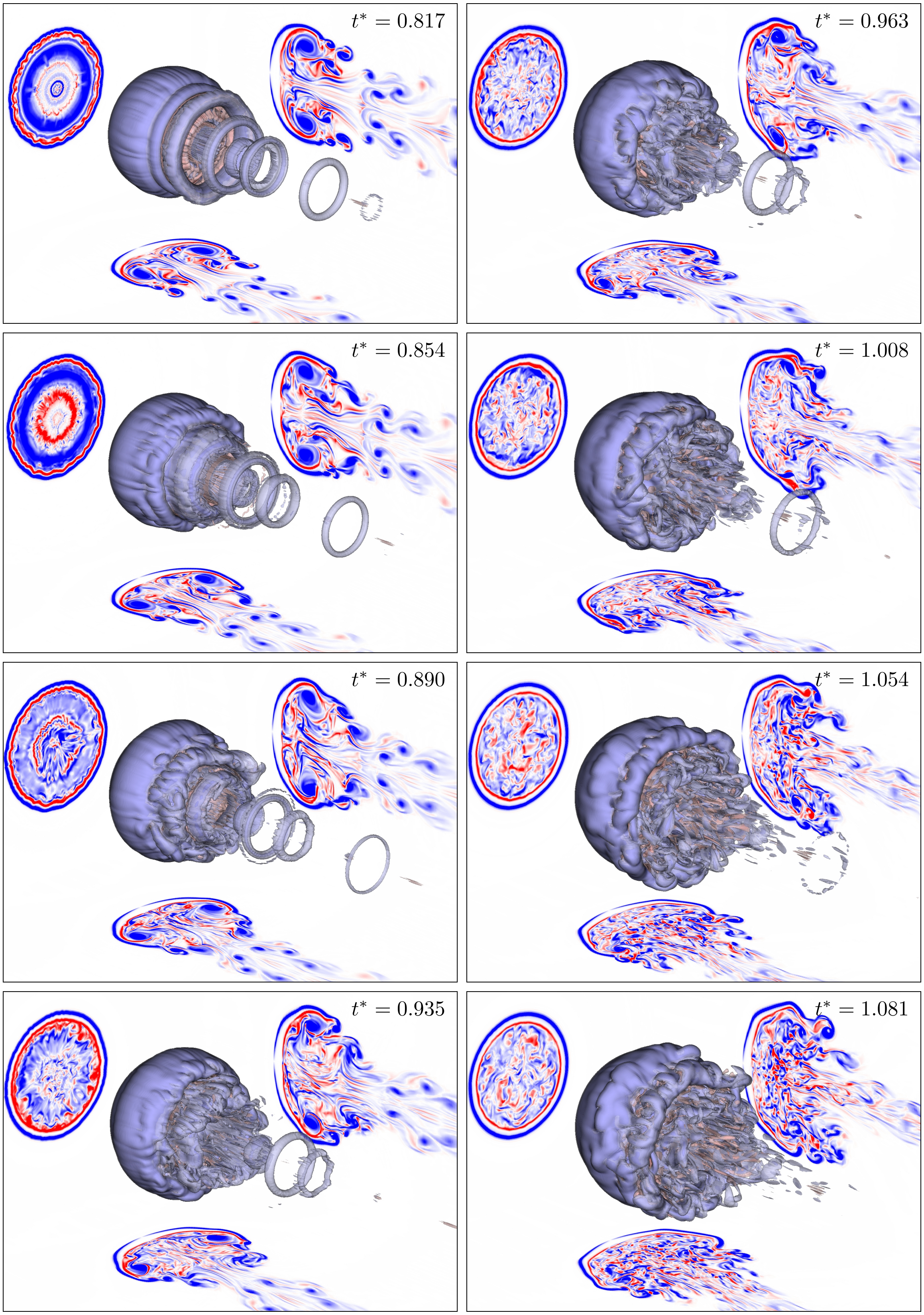

Figure 6.9: Isosurfaces of positive (red) and negative (blue) azimuthal vorticity, ω_θ. Flow is from top left to bottom right. Offset 2D slices are taken at $x^* = 0, y^* = 0, z^* = 1$.

liquid from the incident shock wave is seen in the filled pressure contours to bounce back and forth within the droplet. From our numerical results and the aerobreakup literature, this transmitted wave inside the liquid droplet is not thought to play a significant role in the aerobreakup process. The nonuniform pressure distribution around the droplet, i.e., higher pressures at the forward and rear stagnation points, is the principal mechanism driving droplet deformation. Unlike the case of steady separated flow past a rigid sphere, the pressure at the rear stagnation point remains, during the initial flattening, larger than the pressure at the droplet's equator. The equatorial recirculation region, visible in Fig. 6.9 and discussed for 2D aerobreakup in Section 5.3.1, is formed again by the interaction of two opposite-sign azimuthal vorticity streams generated by baroclinicity. Its location coincides with the sides of the muffin-shaped droplet behind the lip of the spherical upstream droplet surface. This equatorial recirculation region thus serves as a possible explanation for the muffin-like shape of the deformed droplet, and, for the duration of its existence, is at least partially responsible for the liquid sheets that are drawn out from both the spherical lip and the planar back of the droplet. Behind the droplet, the wake recirculation region is quickly established as evidenced by the departure of the flow reversal region (i.e., the white patch in the wake directly behind the droplet where the streamwise velocity changes direction) from the rear stagnation point at $t^* = 0.099$ in Fig. 6.8 (at $t^* = 0.126$ in Fig. 6.9, the wake recirculation region already exists). The flow reversal patch also serves to demarcate the end of the upstream jet that is created in the wake. Other notable flow features visible in Fig. 6.8 include the initiation of two parallel shear layers at the droplet equator. These are observed to persist for the duration of the simulation, and the corresponding KH instability is responsible for the unsteady vortex shedding driving the development of a complicated wake. KH roll-up and subsequent vortex shedding from the shear layers can be seen particularly clearly from the numerical schlieren isopleths at $t^* = 0.435, 0.544, 0.781$ in Fig. 6.8. For clarity, it would be expedient to separately discuss the phenomenology associated with the wake recirculation region, upstream jet, and equatorial shear layers. However, these flow features are so intricately interconnected that such a disjointed discussion would be both incomplete and overly simplistic. Rather, what follows is an attempt at a comprehensive examination and discussion of these flow phenomena.

The formation of the wake recirculation region initiates a strongly coupled, self-sustaining set of flow phenomena that evolve with ever-increasing complexity. The wake recirculation region, created by the stream of negative azimuthal vorticity from the upstream side of the droplet, remains in the near-field wake region. It is perpetually sustained by the same vorticity stream, and entrains the surrounding fluid, which is pulled into an upstream jet that impinges on the rear stagnation point of the droplet. This upstream jet, driven by the recirculation region, preserves high pressure at the rear stagnation point that contributes to both the pancaking of the coherent droplet, as well as the generation of positive vorticity along the back of the droplet. The positive vorticity is transported towards the equator by the recirculation region, and interacts with the negative vorticity stream to create, at early times, the equatorial recirculation region. Some positive vorticity is also transported downstream, forming a parallel stream inside the negative vorticity stream coming from the upstream side of the droplet. The shear flow that is created when the upstream jet impinges on the back of the droplet may also contribute to the liquid sheet that arises from the downstream side. As the equatorial liquid sheet is blown downstream by inertial forces from the surrounding gas flow, shear layers are formed on both sides of the sheet. The gas that is accelerating around the droplet creates shear on the exterior, while the wake recirculation region, that exists inside the cavity enveloped by the sheet, creates shear along the interior. Both the interior and exterior shear layers are visible in Fig. 6.8. As the liquid sheet flaps, generating longitudinal ripples, the shear layers, which are subject to KH instability, periodically shed vortices that are either entrained by the wake recirculation region, or are convected downstream. Entrained vortices (of both signs) by the wake recirculation region result in the upstream jet being characterized by concentric layers of alternating vorticity sign (visible from $t^* = 0.435$–0.790 in Fig. 6.9). Entrainment of shed vortices is also associated with a temporary increase in upstream jet velocity that results in a cyclic pumping of fluid onto the back side of the droplet. Downstream-convected vortices, that are not entrained, quickly lose their initial axisymmetry due to the instability of vortex rings, and subsequently develop into fully 3D flow features. In time, as the liquid sheet is drawn downstream and the coherent droplet diameter expands laterally, the flow within the enveloped cavity at the back of the droplet, encompassing the wake recirculation region and the upstream jet, correspondingly grows in size and complexity. Loss of axisymmetry is observed to first occur in the core region of wake, i.e., small r. However, before it radially expands to encompass the entire wake region, another instability is observed to emerge along the still-axisymmetric positive vorticity sheet (located just inside the equatorial liquid sheet). From $t^* = 0.754$–0.790 in Fig. 6.9, we see what appear to be RT fingers or mushroom-like features propagating inwards towards the core that cause azimuthal rippling in the previously-axisymmetric vorticity sheet. This instability, further discussed in Section 6.3.4, generates the transverse azimuthal modulations observable on the liquid sheet visible for $t^* \geq 0.763$ in Fig. 6.2. As the entire wake region devolves into chaotic, turbulent-like flow, the general coherence of the aforementioned phenomena is lost, as seen for $t^* \geq 1.008$ in Fig. 6.9. At these late times, the coherent droplet body presents an essentially blunt body to the oncoming freestream flow such that the highest pressures are found on the upstream side of the flattened disk-like droplet.

6.3.4 Surface instabilities

As discussed in Section 1.2.1.2, the upstream side of a droplet undergoing aerobreakup is susceptible to RT instability waves that arise from the acceleration of the lighter gas into the denser liquid. In the classical catastrophic breakup regime, "fingers of hot air" were thought to penetrate the droplet, leading to an explosive disintegration [43]. In contrast stands the recent of work of Theofanous and Li [88] who observed that "[t]here are no RT waves piercing the drop. . . ." Indeed, no RT waves are seen on the droplet in our numerical simulation. This is shown in Fig. 6.10 where the upstream side of the drop for various isopleths of α_l remains smooth for the entirety of the simulation. Our numerical results thus support Theofanous and Li's claim of SIE being the terminal breakup regime. The suppression of the RT instability waves was initially explained by Theofanous and Li [88] to be a consequence of the stability of the stagnation flow (reminiscent of the lenticular shape of a gas bubble rising through liquid [5]). More recently, an analysis of the viscous KH instability by Theofanous et al. [90] found that "[w]ave numbers and growth factors of [KH] instability are consistently greater

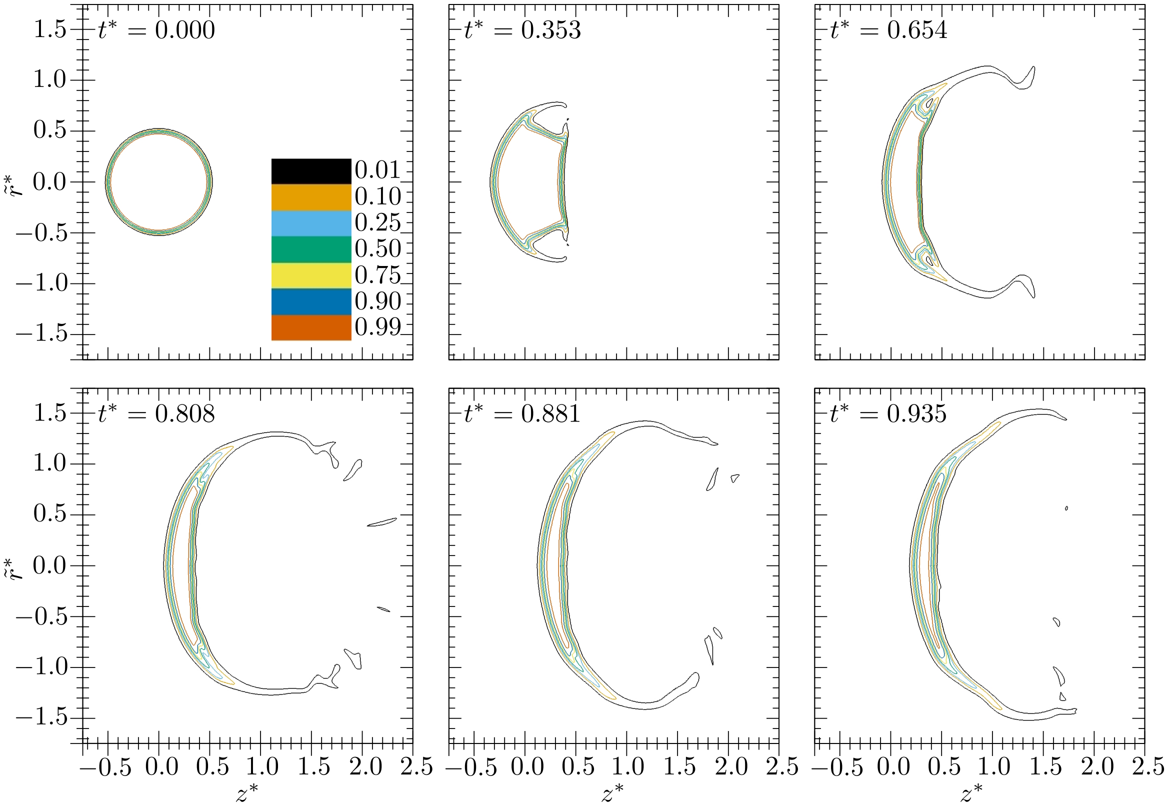

Figure 6.10: Sliced isopleths of α_l showing droplet profiles.

than those of [RT] instability by more than an order of magnitude. . . . [T]he stretching further contributes to keeping this area mollified and free of any instability all the way to the end."

In describing the instabilities that arise on the liquid sheet that lead to its disintegration, Liu and Reitz [54] proposed the "stretched streamwise ligament breakup" mechanism of Stapper and Samuelsen [82]. This breakup mechanism is characterized by the dominant formation and growth of streamwise vortical waves on the sheet, with thin membranes formed between them. "Breakup occurs as the membranes are stretched thin by the rotation of the streamwise vortices and burst into small droplets. The streamwise vortical waves separate as streamwise ligaments, stretch and spin faster in the presence of the air shear, and eventually break up, contributing the larger drops to the final drop size distribution" [82]. From Fig. 6.11, which plots transverse slices of the liquid sheet at various streamwise locations, we see that our numerical results do not support this mechanism as the reason for sheet disintegration. Instead of a liquid sheet with variable thickness in the azimuthal coordinate, we observe relatively constant sheet thickness, and a rippling-type instability.

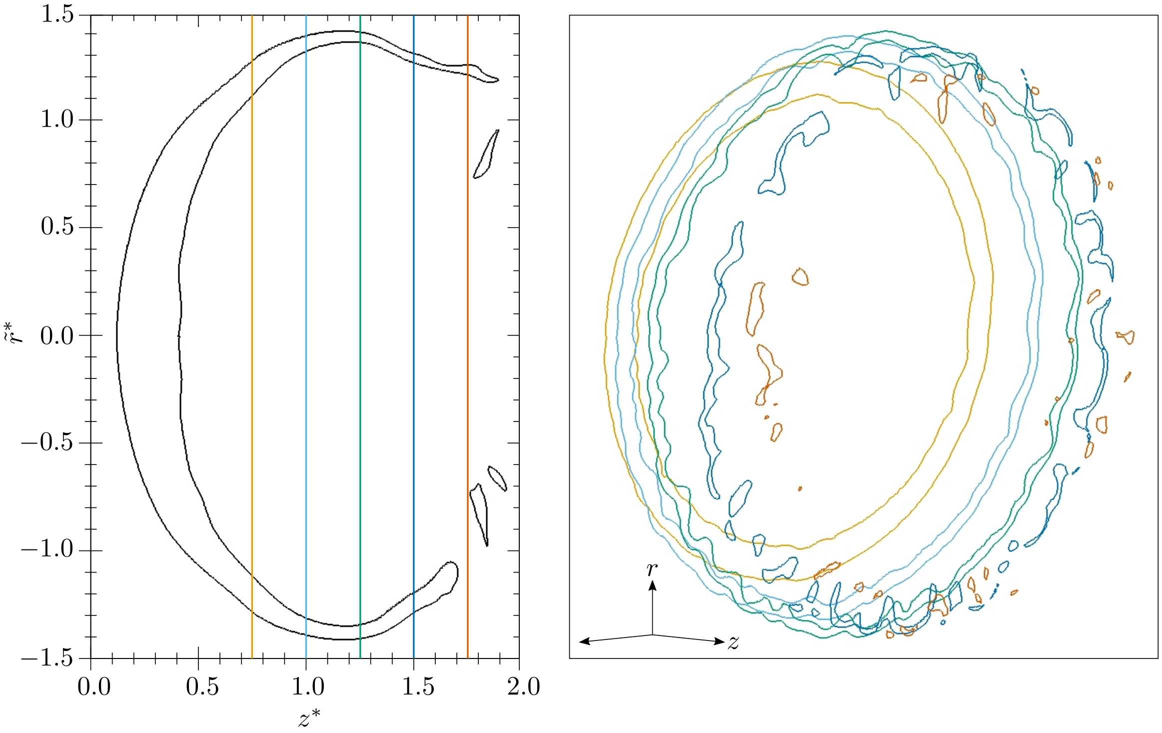

Figure 6.11: Transverse slices of the liquid sheet at $t^* = 0.881$, defined by $\alpha_l = 0.01$, at various streamwise locations.

Additionally, isosurfaces of the liquid sheet colored by axial and radial vorticity, $\omega^*_{z,r} = \omega_{z,r}\dfrac{D_0}{u_s}$, (as shown in Fig. 6.12) suggest that streamwise (axial) vorticity (with its smaller magnitude) does not play a dominant role in the sheet breakup. In addition to the "stretched streamwise ligament" mechanism of sheet breakup, Liu and Reitz [54] also proposed another rippling mechanism based on mass conservation arguments (see Section 1.2.1.4). Though this remains a possibility, the observed phenomena are most likely the net result of several mechanisms. Jalaal and Mehravaran [39] proposed the RT instability as the source of the transverse azimuthal modulations. Arguing that the accelerated liquid sheet is subject to the same instability as that which forms streamwise ligaments in the case of a round liquid jet in coaxial flow, Jalaal and Mehravaran [39] attempted a quantitive comparison with theory, but found only marginal agreement. The general concept, though, of RT instability on the liquid sheet may, indeed, have merit, and supporting (qualitative) evidence can be found in our numerical results. As noted at the end of Section 6.3.3, RT fingers or mushroom-like features are seen emerging along the positive vorticity sheet that lies just inside the equatorial liquid

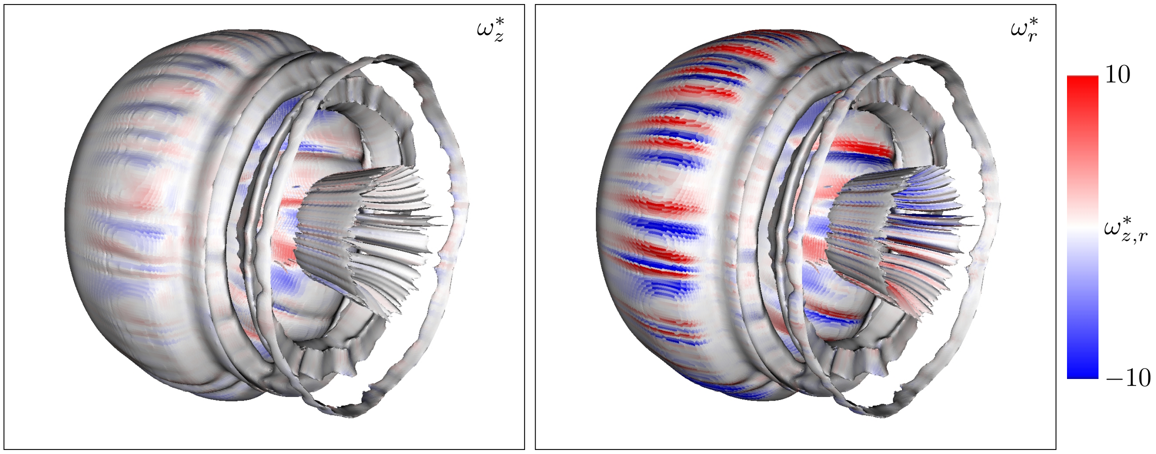

Figure 6.12: The liquid sheet colored by axial and radial vorticity, $\omega_{z,r}^*$, at $t^* = 0.808$.

sheet. To relate these features to the RT instability, we plot filled contours and isopleths of the gas partial density for late times in Fig. 6.13. At $t^* = 0.726$, the axisymmetry of the outer regions of the wake is still preserved, as evidenced by the circular isopleths. From $t^* = 0.744$–0.790, however, the axisymmetry is broken by multiple fingers of denser gas propagating towards the axis into the lighter gas (darker colors correspond to larger densities). These fingers correspond exactly with the indentations generated on the liquid sheet. Not long after this loss of outer axisymmetry, the entire wake region degenerates into a chaotic, turbulent-like flow with complete loss of flow feature coherence.

6.4 Azimuthal Fourier decomposition

Motivated by the observed azimuthal modulations, we perform a Fourier decomposition of the velocity flow field to determine if a particular mode(s) or wavenumber(s) is associated with the loss of axisymmetry. To do this, we take a Fourier transform in the inherently periodic θ-coordinate to obtain the Fourier coefficients of each of the azimuthal modes, $\hat{\mathbf{u}}_m(z, r, t)$. We then calculate an energy metric, reminiscent of the kinetic energy, for each mode, which is defined as

$$\hat{\kappa}_m = |\hat{u}_{z,m}|^2 + |\hat{u}_{r,m}|^2 + |\hat{u}_{\theta,m}|^2, \tag{6.2}$$

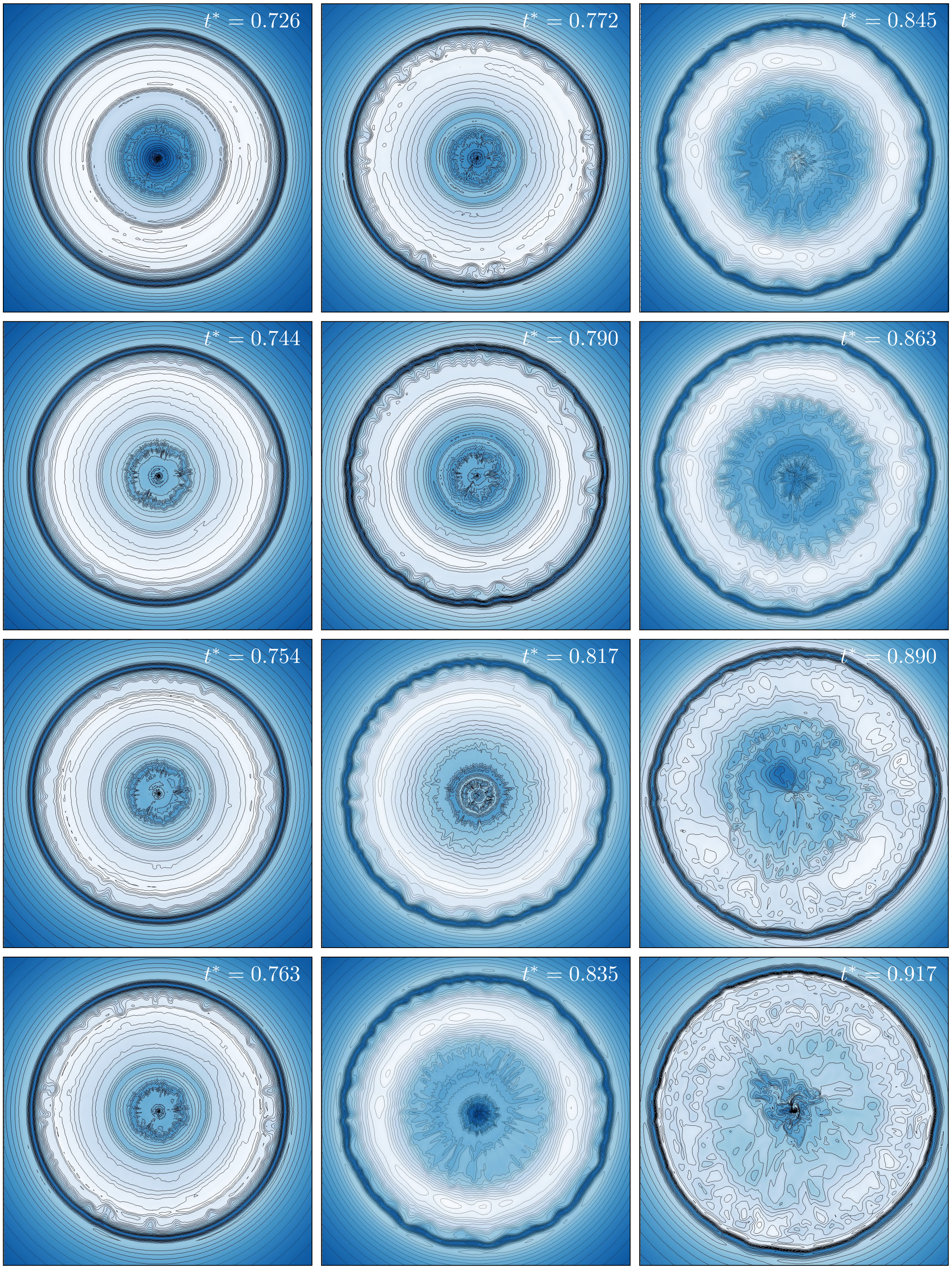

Figure 6.13: Filled contours and isopleths of gas partial density, $\alpha_g \rho_g$, at $z^* = 1$. Darker colors correspond to larger densities (coloring and isopleth values vary between frames).

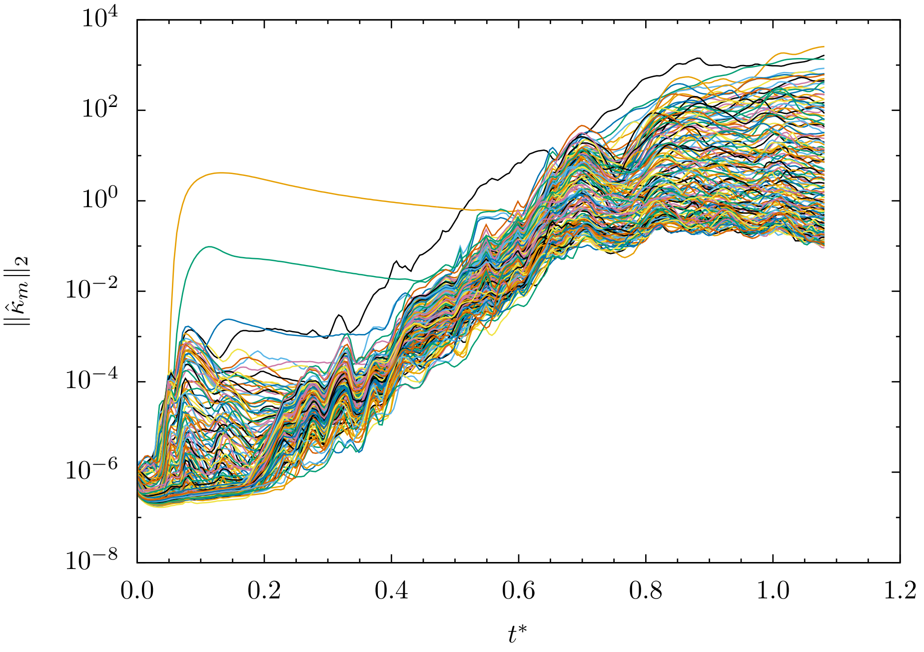

Figure 6.14: L_2-norm of the (kinetic) energy for $N_\theta/2$ modes from the azimuthal Fourier decomposition.

where the hat denotes the Fourier transform in the θ-coordinate. Taking an L_2- and L_∞-norm of $\hat{\kappa}_m$ over the entire computational domain, we plot the time histories of $\|\hat{\kappa}_m\|$ for each of the $\frac{N_\theta}{2}$ modes (excluding the mean) in Figs. 6.14 and 6.15. Notably, the frequency response of the system shows broadband instability growth for all modes. The impulsively-excited modes, which, at first glance, appear to be significant, are actually artifacts of the random velocity perturbations seeded in the initial condition that are picked up by the p-norms (see Fig. 6.16). If we view the interaction of the incident shock with the droplet as an impulsive force applied to the system, the broadband instability response is not surprising. Unfortunately, due to the unsteady, nonstationary, and nonlinear nature of the aerobreakup problem, this type of instability analysis is unable to pick out a dominant mode or wavenumber associated with the loss of axisymmetry. Despite the broadband response, visualization of the first few modes transformed back into θ-space, $\kappa_m = u_{z,m}^2 + u_{r,m}^2 + u_{\theta,m}^2$, reveals some interesting observations about the development of the wake, and offers some general intuition about the physical spatial structure of κ_m. We first plot in Fig. 6.16 the isosurfaces of the impulsively-excited modes at two early times in the breakup process. From Fig. 6.16 we see

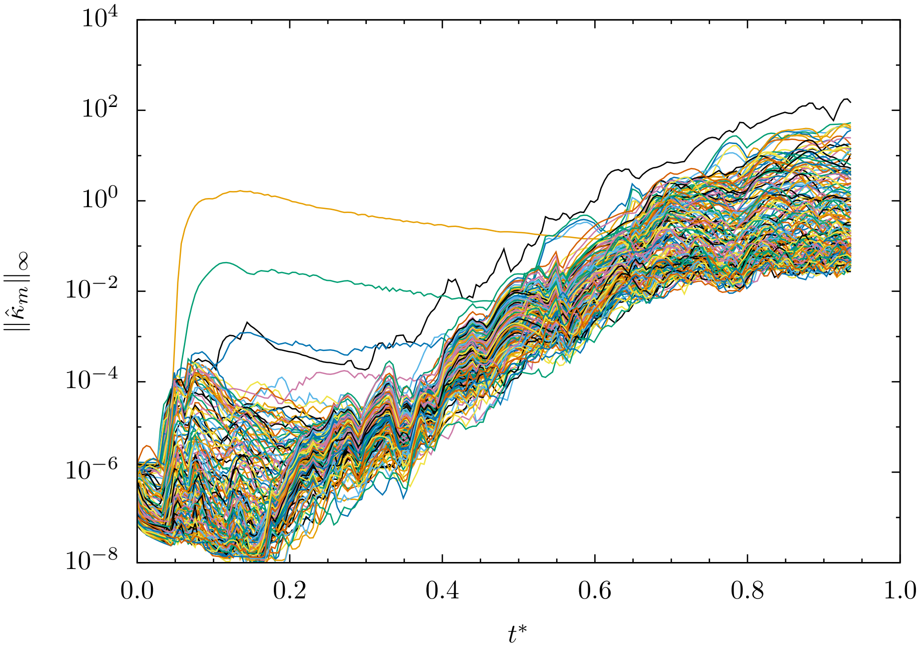

Figure 6.15: L_∞-norm of the (kinetic) energy for $N_\theta/2$ modes from the azimuthal Fourier decomposition.

that not only are the kinetic energies associated with these modes small in magnitude, but they are also physically located away from the droplet, and are not associated with asymmetry of the aerobreakup process at these early times. They are, as mentioned above, artifacts of the random velocity perturbations added to the IC. Next, we show in Fig. 6.17 isosurfaces of the same modes, but at much later times in the simulation when all frequencies have saturated (see Fig. 6.14). From the head-on views of the structures, we are able to confirm that the grid effects described in Section 3.3.2 are absent in this simulation as the structures are oriented at various θ. It is also fairly obvious to see that the structures associated with the loss of axisymmetry are located in the region of the near wake. Structures are initially clustered around the location of the liquid sheet, and subsequently grow in size and complexity. Even at late times, the structures remain bounded by the wake region (associated with nonzero azimuthal vorticity). Streaky streamwise-oriented flow structures near the wake core, visible for $\kappa_{6,8}$ at $t^* = 0.808$, appear to be related to the loss of axisymmetry in the upstream jet region, while the outer structures are linked to the liquid sheet and shear layers. As this broadband instability is not directly associated with any classical hydrodynamic instability, we

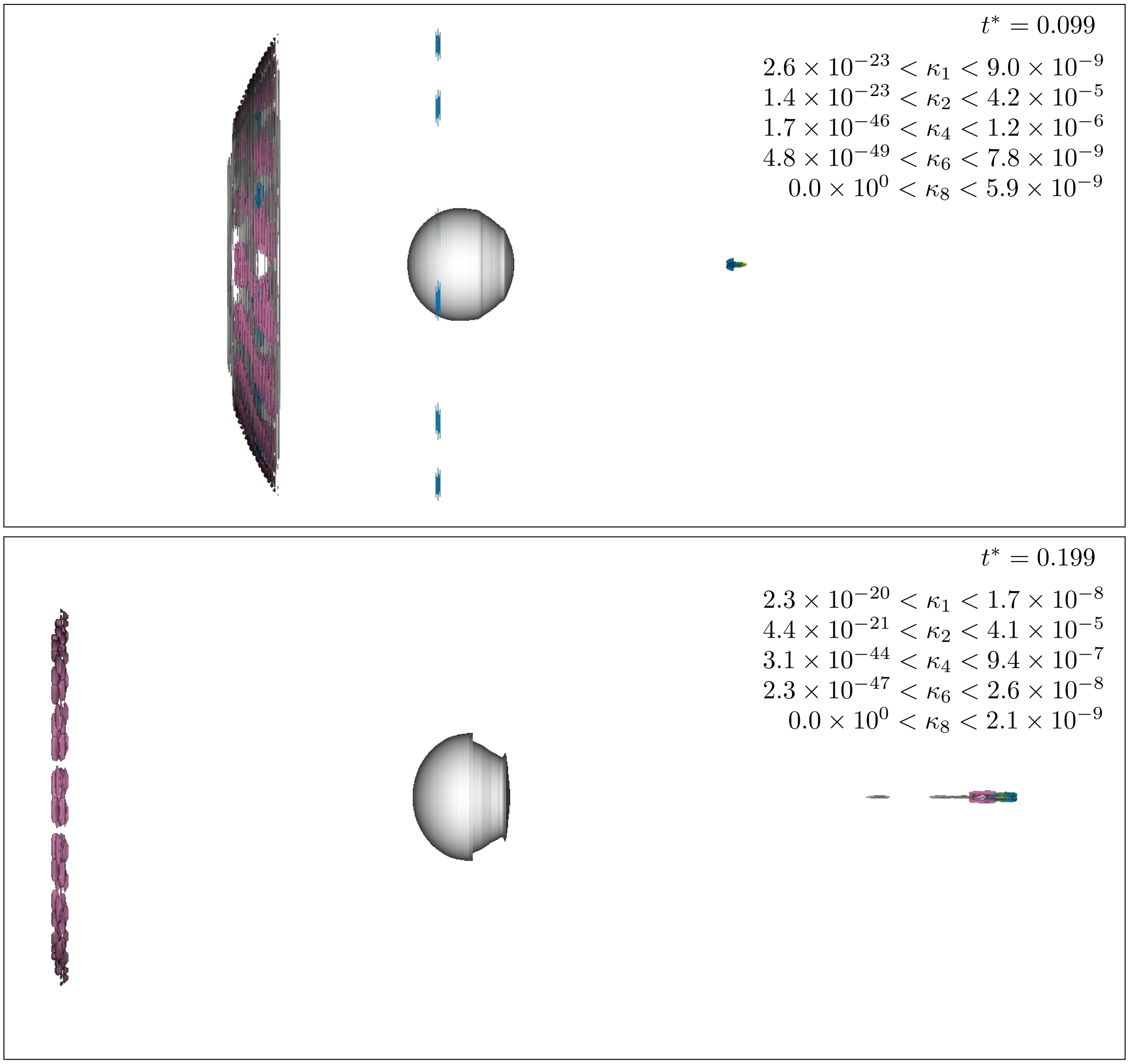

Figure 6.16: Isosurfaces of κ_m, $m = 1, 2, 4, 6, 8$ (gray, orange, green, blue, pink) at $t^* = 0.099, 0.199$. Also shown is the liquid sheet visualized using $\alpha_l = 0.01$. Isosurface values change between frames, and flow is from left to right.

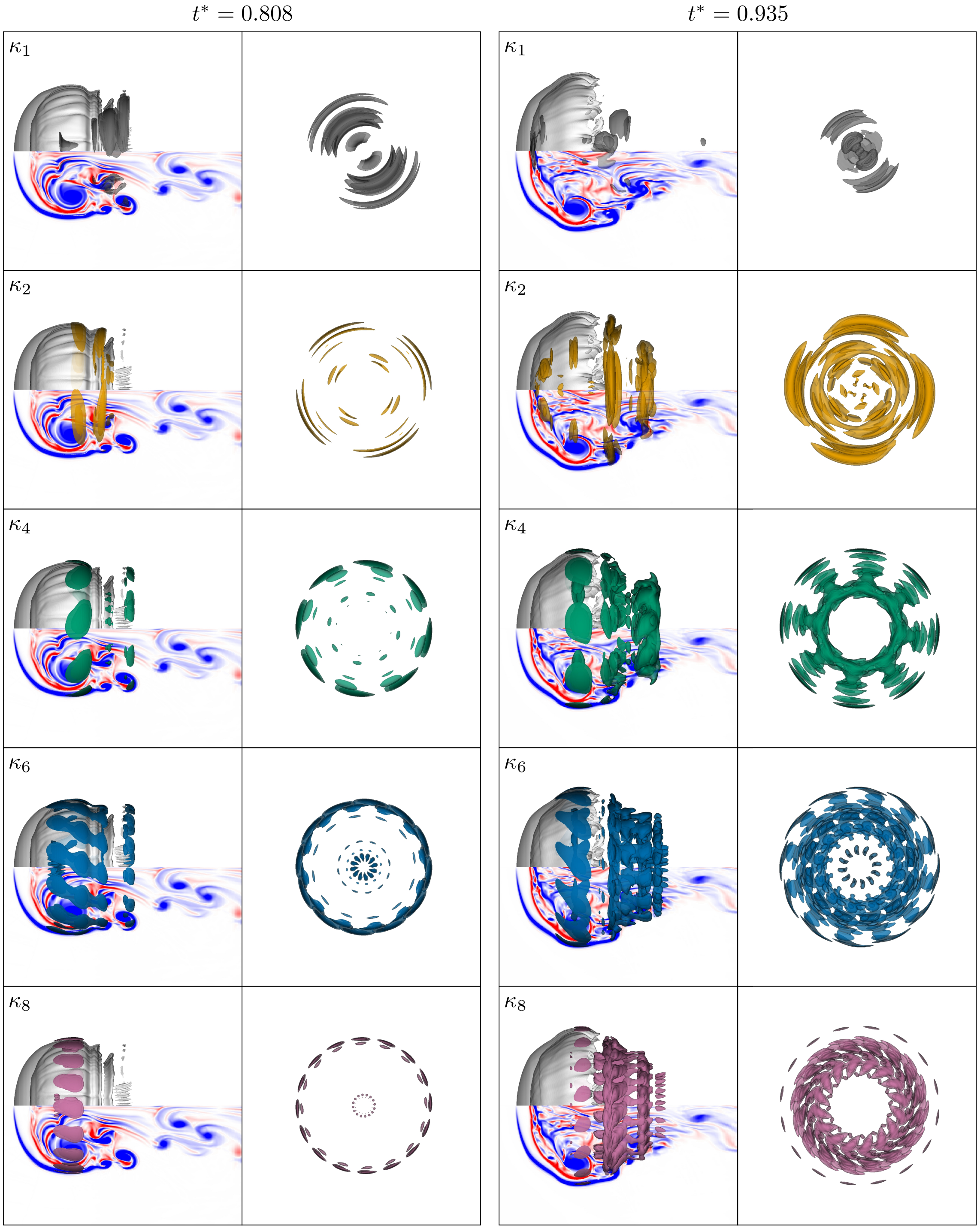

Figure 6.17: Isosurfaces of κ_m, $m = 1, 2, 4, 6, 8$ at $t^* = 0.808, 0.935$. Also shown is the liquid sheet visualized using $\alpha_l = 0.01$, and a filled contour slice of azimuthal vorticity. Front and side views are shown, and isosurface values change between frames.

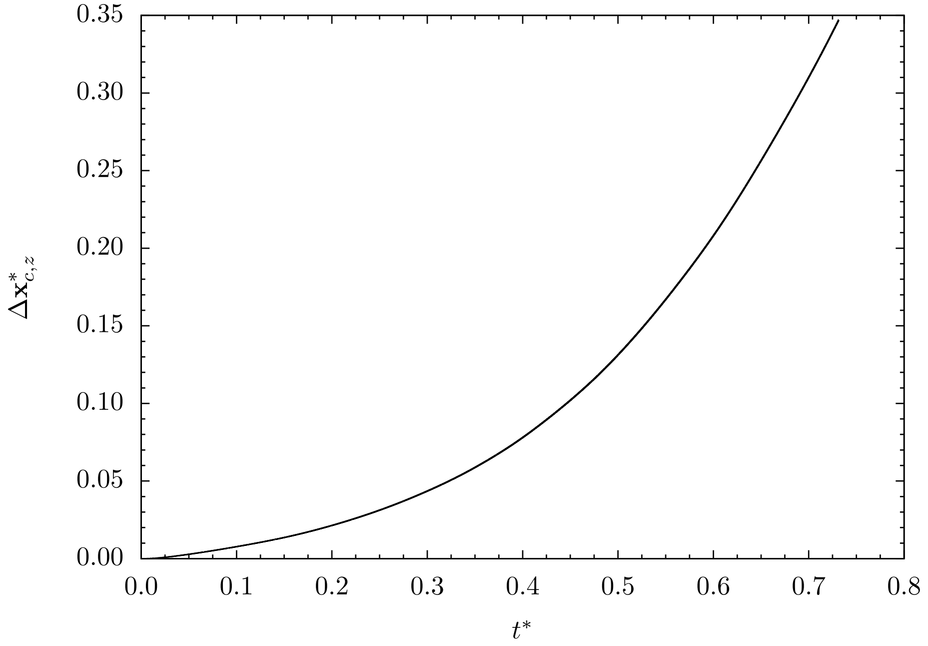

Figure 6.18: Droplet streamwise center-of-mass drift, $\Delta\mathbf{x}^*_{c,z}$.

are unable to relate these κ_m-structures to other recognizable flow features.

6.5 Integral quantities and metrics

In the following section, we show various integral metrics of the droplet's behavior and deformation. The drop's center-of-mass properties, Eqs. (3.10), (3.12) and (3.15), and unsteady drag coefficient, Eq. (5.2), calculated using the deformed diameter, D_d, are shown. Unfortunately, there is no experimental data available in the literature to make a quantitative comparison. We also use the droplet's coherent body mass, i.e., the 3D version of Eq. (5.4), to approximate the total breakup time, t_{br}, and make a few brief comments on t_{br} in secondary atomization modeling.

6.5.1 Center-of-mass properties

The droplet's center-of-mass drift, velocity, and acceleration in the streamwise (axial) direction are plotted, respectively, in Figs. 6.18 to 6.20. While the drift and velocity curves are similar to their 2D counterparts, Figs. 5.11 and 5.12, slight differences are observed in the acceleration plot.

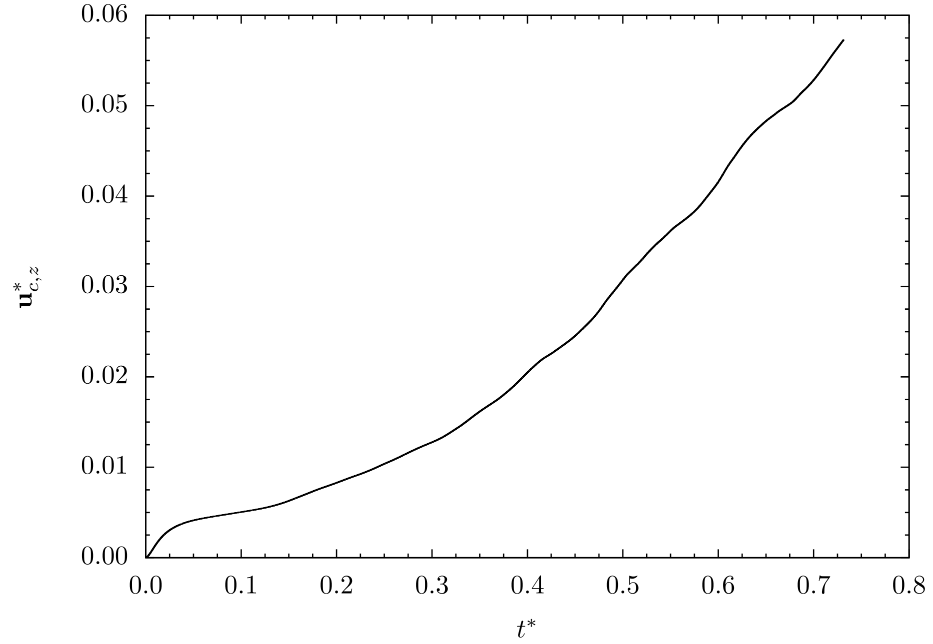

Figure 6.19: Droplet streamwise center-of-mass velocity, $\mathbf{u}^*_{c,z}$.

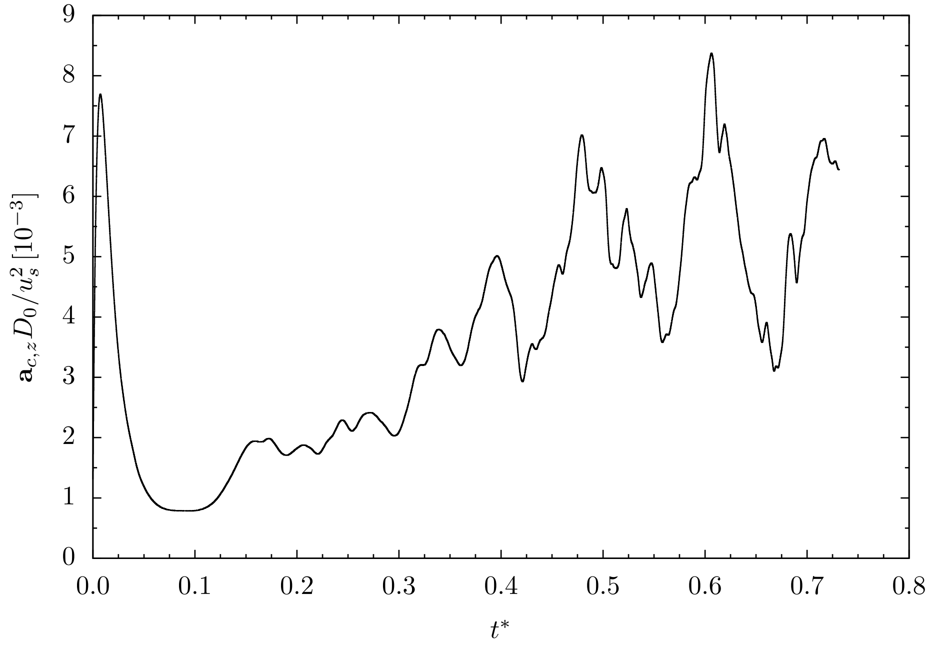

Figure 6.20: Droplet streamwise center-of-mass acceleration, $\mathbf{a}_{c,z}D_0/u_s^2$.

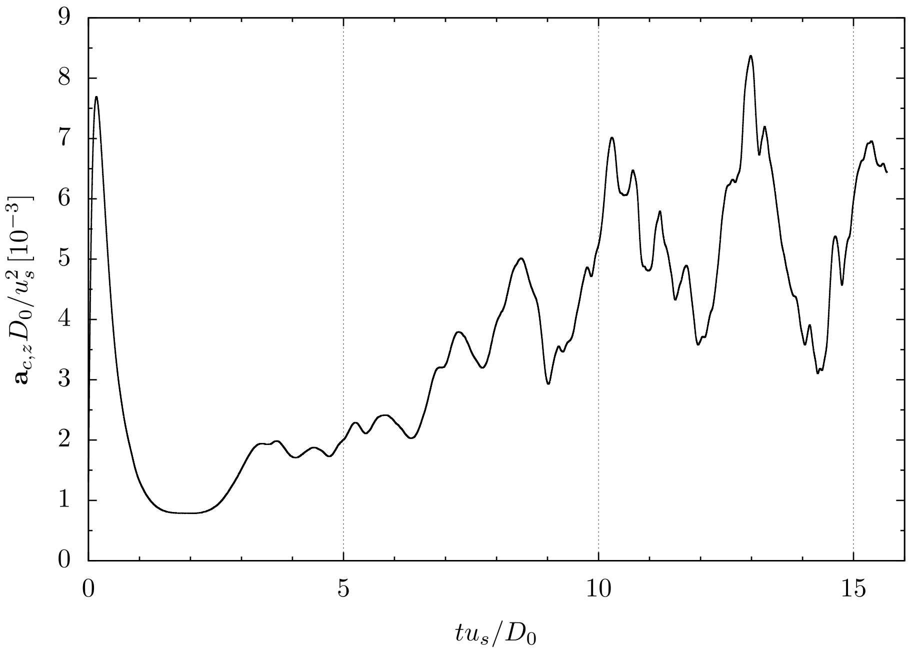

Figure 6.21: Droplet streamwise center-of-mass acceleration in convective time units.

Firstly, in contrast to the immediate fluctuating acceleration of the cylinder in Fig. 5.13, there is a brief period immediately following the passage of the shock when the droplet is subject to constant acceleration. During this time period, the droplet is initially adjusting to the step change in ambient flow conditions, and is still well-approximated as a rigid sphere. This delay, perhaps related to the flow-relieving effect of the third dimension, ceases when the droplet begins to pancake and its drag properties substantially change. Secondly, while it is difficult to see a dominant low-frequency oscillation in the cylinder's acceleration shown in Fig. 5.13, one is observed in the droplet acceleration curve. Again re-nondimensionalizing time to obtain standard convective time units, we check to see if this frequency matches with the well-known $St \approx 0.2$ associated with sphere wake instability. While interesting to note that the last two large oscillations captured in Fig. 6.21 appear to coincide well with an expected period of $\frac{5D_0}{u_s}$, we do not have sufficient data to concretely correlate these low-frequency oscillations to the wake instability. Finally, in Fig. 6.22, we plot the droplet's unsteady drag coefficient, where, following the discussion in Section 5.3.3.2, the frontal area is based on the droplet's deformed diameter, D_d. During the period of constant acceleration, and before the droplet has had sufficient time to significantly deform, we observe that the drag coefficient for a rigid

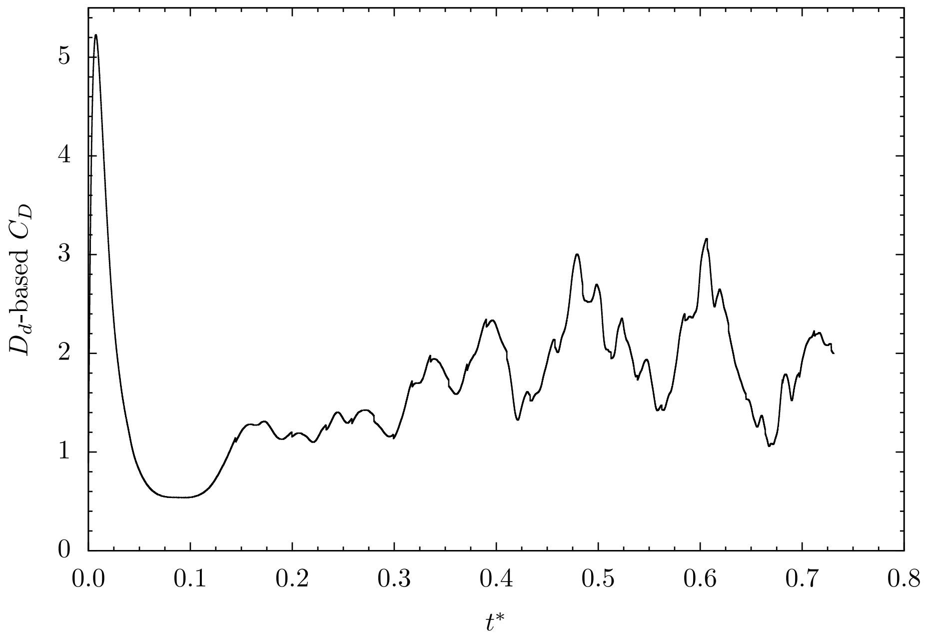

Figure 6.22: Droplet unsteady drag coefficient, C_D, based on D_d.

sphere, $C_D = 0.5$, is approximately recovered. As the droplet begins pancaking, the drag coefficient transitions to be comparable to that for a flat disk, which has $C_D \approx 1$. Unsteady effects, however, quickly take over and the drag coefficient subsequently exhibits fluctuations about an increasing average value.

6.5.2 Breakup time

Historically speaking, there has been no clear consensus in the literature on the time required for breakup, t^*_{br}. Experimental investigations of aerobreakup have often attempted to measure the time required for complete loss of the coherent drop. However, these timings are often complicated by the fact that the coherent drop is typically obscured from view by the generated mist. Models of aerobreakup, used in, e.g., LES-type simulations of primary atomization, typically use breakup times correlated from multiple experiments, or derived from the underlying assumptions of their model. A few of these secondary atomization models are listed in Eq. (6.3), along with their corresponding value for t^*_{br}.

$$t^*_{br} = \begin{cases} \frac{1}{\sqrt{3}} \approx 0.577, & \text{Stochastic modeling [3]}, \\ \frac{\sqrt{3}}{2} \approx 0.866, & \text{Taylor analogy breakup model [64]}, \\ \frac{4.5}{\sqrt{8}} \approx 1.591, & \text{Enhanced Taylor analogy breakup model [84]}, \\ 5, & \text{Wave model [71]}. \end{cases} \tag{6.3}$$

A well-known correlation from Pilch and Erdman [66] for liquids with $Oh < 0.1$ is given as

$$t^*_{br} = \begin{cases} 6(We - 12)^{-0.25} & 12 < We < 18, \\ 2.45(We - 12)^{0.25} & 18 < We < 45, \\ 14.1(We - 12)^{-0.25} & 45 < We < 351, \\ 0.766(We - 12)^{0.25} & 351 < We < 2670, \\ 5.5 & 2670 < We < 10^5, \end{cases} \tag{6.4}$$

which results in values of $3 < t^*_{br} < 8$ (note that a typographical error has been fixed [20]). Most recently, experimental measurements of t^*_{br} for the SIE regime have been given as $t^*_{br} = 1$–2 [88], and $t^*_{br} \sim 1$ (claimed valid for all Newtonian liquids of any viscosity) [87]. Just from Eqs. (6.3) and (6.4), the large disparity in the documented values for t^*_{br} is obvious.

Using the corresponding 3D mass calculation as that from Section 5.4.2, we plot the coherent body mass of the droplet using $\alpha_{cr} = 0.99$ in Fig. 6.23. From the zoomed inset plot, we see that the coherent droplet mass has decreased by 90% at $t^* = 1.01$, and drops another 7.5% by $t^* = 1.09$. A simple extrapolation gives $t^*_{br} \approx 1.15$, which compares well with the experimentally measured values. While our single data point for t^*_{br} is not groundbreaking, it is encouraging that it matches as well as it does with the experiments, and provides additional support for SIE as the terminal regime. At this point, it is also fairly safe to say that historical values of $t^*_{br} \gtrsim 5$ are too large. Conversely, the finite time required for aerobreakup suggests that secondary atomization models would do well to

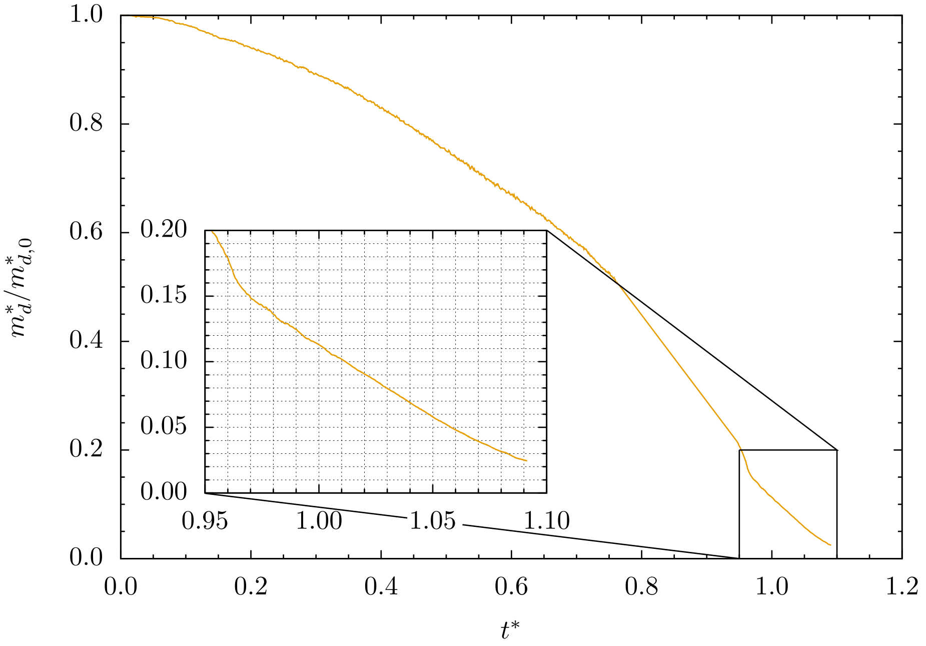

Figure 6.23: Normalized coherent body mass, $m_d^*/m_{d,0}^*$, using $\alpha_{cr} = 0.99$.

not assume instantaneous (i.e., within one computational time step) aerobreakup above We_{cr}.

6.6 Summary

In this chapter, we present the first detailed description of the underlying flow physics associated with droplet deformation during 3D stripping aerobreakup. The droplet morphology is first described, and compared to experimental visualizations of the SIE process. Good qualitative agreement is found in terms of the droplet's initial deformation into a muffin-like shape, followed by the disintegration of a liquid sheet that envelops a cavity in the near-field wake region. Numerical visualizations of the surrounding flow behavior provide novel insight into the experimentally observed drop morphology. At early times, the existence of the equatorial recirculation region, comprised of two counter-rotating vortices, explains both the muffin-like shape, and the pulling of liquid sheets from both the droplet's equator and its flattened back. The enveloped cavity attached to the downstream side of the deforming droplet is associated with a recirculation region that entrains fluid and jets it upstream to impinge on the rear stagnation point. The shear layers that form on both sides of the liquid sheet are subject to KH instability, and shed vortices that are either convected downstream or entrained by the wake recirculation region. RT instability waves on the upstream side of the droplet are noticeably absent, providing support for SIE as the terminal breakup regime. Analyses of the instabilities arising on the liquid sheet reveal discrepancies with the proposed "stretched streamwise ligament breakup" mechanism, while some qualitative evidence for the rise of RT instability along the accelerated sheet can be found. An attempt is made to find particular modes associated with the loss of axisymmetry by performing an azimuthal Fourier decomposition of the flow field. Unfortunately, due to the unsteady and nonlinear nature of the aerobreakup problem, this analysis is limited in its efficacy, and instead shows broadband instability growth of all modes, as would be expected from impulsive forcing of the system. Finally, the droplet's center-of-mass properties and unsteady drag coefficient are shown, and the time required for breakup is found to compare well with values available in the literature.

Chapter 7

Concluding remarks

7.1 Summary and conclusions

In this thesis, we have presented novel DNS results for stripping aerobreakup that constitute a significant advancement in the overall understanding of the flow physics driving the observable phenomena. While the generalized aerobreakup problem has been studied experimentally for decades, limitations on the attainable spatial and temporal resolutions of experimental visualization techniques have hampered a complete understanding of the breakup physics. Similarly, computational investigations of the aerobreakup problem have often had to make simplifying geometrical or modeling assumptions to decrease computational costs. In an attempt to resolve a few outstanding questions regarding the physics of aerobreakup, we have examined the underlying fluid dynamics associated with stripping aerobreakup. This thesis work thus constitutes an attempt to begin to fill a gap in the current state of aerobreakup knowledge associated with the fundamental fluid dynamics responsible for the phenomena observed in the aerobreakup process.

The physical model and the numerical framework utilized to solve the compressible multicomponent Navier-Stokes equations in our simulations were first outlined in Chapters 2 and 3. After a description of the idealized version of the aerobreakup problem, the governing equations were presented in the five-equation model [2, 65]. The stiffened gas EOS was used to model all fluids of interest, and mixture relationships were presented for the nonphysical mixture regions that arise in our diffuse interface framework due to numerical diffusion. Building upon the computational work of Coralic and Colonius [13], the governing equations were solved in a finite-volume framework using a Godunov-type scheme. Formally third-order WENO schemes and the approximate HLLC Riemann solver were used for spatial reconstructions, while a TVD Runge-Kutta scheme was used for temporal integration. After the documentation of two challenging issues associated with the numerical method in Cartesian coordinates, the flow solver was expanded and improved in Chapter 4. The adaptation of MFC from Cartesian to cylindrical coordinates systems, as well as the implementation of a capillary model, was documented and verified via benchmark test cases. Convergence tests for both code extensions showed method convergence with approximately second-order accuracy.

Our numerical results began in Chapter 5 with the investigation of 2D water cylinder aerobreakup. In addition to qualitative and quantitative comparisons with available experimental data, a description of the aerobreakup flow physics was presented, along with characterizations of the water cylinder's unsteady acceleration and drag properties. Across a range of freestream velocities spanning subsonic to slightly supersonic flow, the unsteady drag coefficient was reasonably approximated by a constant for a significant portion of the breakup. Viscous results were used to estimate the numerical viscosity associated with the employed spatial resolution, as well as to quantitatively test the boundary layer stripping mass loss rate equation of Ranger and Nicholls [69]. Contrary to the boundary layer stripping theory, numerical results showed Re-independence of mass stripping rates at early times in the breakup process, followed by the retardation of mass loss with decreasing Re. In Chapter 6, we presented the results of a 3D nonaxisymmetric simulation of a spherical water droplet in the flow behind a $M_s = 1.47$ shock wave. Numerical and experimental visualizations of the SIE phenomenology were compared and showed good agreement. The drop was observed to initially deform into a muffin-like shape, with a spherical upstream side and a flattened back. A thin liquid sheet was drawn from the droplet periphery and enveloped a cavity in the near-field wake region directly behind the coherent body of the deforming droplet. While our simulation results, in the absence of surface tension, were unable to capture the physical disintegration of this liquid sheet, we were able to examine the behavior of the surrounding gas in and around the enveloped cavity. The near-field wake region was characterized by a large recirculation region that entrained surrounding fluid and created a persistent upstream jet of fluid onto the rear stagnation point of the deforming droplet. Parallel shear layers were created on either side of the downstream-drawn liquid sheet that were subject to KH instability and shed vortices of both positive and negative sign. These vortices were either convected downstream where they quickly developed 3D instabilities, or were entrained by the wake recirculation region back into the enveloped cavity area. At late times in the breakup process, symmetry-breaking instabilities, potentially related to RT instability, arose on the accelerated liquid sheet and generated azimuthal modulations. The entire wake region quickly devolved into a nonaxisymmetric chaotic flow. A Fourier decomposition of the flow field in the inherently-periodic azimuthal coordinate revealed broadband instability growth of all modes. Finally, an estimate of breakup time was obtained from our numerical results. While breakup times recorded in the literature span a large range of values, our results suggested that $t^*_{br} \approx 1$. This value was shown to be consistent with experimental measurements of t^*_{br} for SIE breakup, and its finite value suggests that models of secondary atomization should not assume instantaneous breakup once a critical breakup Weber number is reached.

7.2 Suggestions for future work

While a first step towards bridging the aforementioned gap in the current state of aerobreakup knowledge, the work presented in this thesis represents only a small portion of the work that needs to be done before a complete and thorough understanding of the diverse phenomena associated with aerobreakup is achieved. The results presented herein have focused specifically on the stripping or SIE regime of breakup, but the same remark, about the scarcity of knowledge pertaining to the underlying fluid dynamics, applies to the other well-established breakup regimes, e.g, bag or bag-and-stamen breakup. Given the current limitations of experimental methods, especially in visualization of the gaseous phase, numerical simulations are and will continue to be a valuable investigation tool. With advancements in computational capabilities continually decreasing the effective cost of large simulations, DNS of complicated fluid dynamics problems, including that of aerobreakup, will hopefully shed light on previously unexaminable phenomena.

Specifically in the context of the MFC flow solver, the extension of the capillary model to the cylindrical coordinate system would facilitate investigations of the breakup regimes that are observed at lower We. Further investigations of the SIE regime would also be informative, especially if the simulations included both viscous and capillary effects, and perhaps utilized the interface-sharpening method shown in Section 3.3.2.2. While it is believed the overall phenomenology would remain similar to that described in this thesis, the inclusion of capillary effects would enable the simulation to capture the capillary instability that arises on the liquid sheet. As a final note, the numerical issues described in Section 3.3 deserve further attention and examination to determine their exact origins and find rigorous solutions.

Appendix A

State variables, fluxes, and source terms

A.1 Cartesian coordinates

The vector of conservative variables, $\mathbf{q}$:

$$\mathbf{q} = \begin{pmatrix} \alpha_1\rho_1 \\ \alpha_2\rho_2 \\ \rho u \\ \rho v \\ \rho w \\ E \\ \alpha_1 \end{pmatrix}. \tag{A.1}$$

The advective fluxes, $\mathbf{f}^a(\mathbf{q}), \mathbf{g}^a(\mathbf{q})$, and $\mathbf{h}^a(\mathbf{q})$:

$$\mathbf{f}^a(\mathbf{q}) = \begin{pmatrix} \alpha_1\rho_1 u \\ \alpha_2\rho_2 u \\ \rho u^2 + p \\ \rho v u \\ \rho w u \\ (E+p)u \\ \alpha_1 u \end{pmatrix}, \quad \mathbf{g}^a(\mathbf{q}) = \begin{pmatrix} \alpha_1\rho_1 v \\ \alpha_2\rho_2 v \\ \rho u v \\ \rho v^2 + p \\ \rho w v \\ (E+p)v \\ \alpha_1 v \end{pmatrix}, \quad \mathbf{h}^a(\mathbf{q}) = \begin{pmatrix} \alpha_1\rho_1 w \\ \alpha_2\rho_2 w \\ \rho u w \\ \rho v w \\ \rho w^2 + p \\ (E+p)w \\ \alpha_1 w \end{pmatrix}. \tag{A.2}$$

The diffusive fluxes, $\mathbf{f}^d(\mathbf{q}), \mathbf{g}^d(\mathbf{q})$, and $\mathbf{h}^d(\mathbf{q})$:

$$\mathbf{f}^d(\mathbf{q}) = \begin{pmatrix} 0 \\ 0 \\ \mathbf{T}_{\mu,xx} \\ \mathbf{T}_{\mu,xy} \\ \mathbf{T}_{\mu,xz} \\ u\mathbf{T}_{\mu,xx} + v\mathbf{T}_{\mu,xy} + w\mathbf{T}_{\mu,xz} \\ 0 \end{pmatrix},$$

$$\mathbf{g}^d(\mathbf{q}) = \begin{pmatrix} 0 \\ 0 \\ \mathbf{T}_{\mu,yx} \\ \mathbf{T}_{\mu,yy} \\ \mathbf{T}_{\mu,yz} \\ u\mathbf{T}_{\mu,yx} + v\mathbf{T}_{\mu,yy} + w\mathbf{T}_{\mu,yz} \\ 0 \end{pmatrix},$$

$$\mathbf{h}^d(\mathbf{q}) = \begin{pmatrix} 0 \\ 0 \\ \mathbf{T}_{\mu,zx} \\ \mathbf{T}_{\mu,zy} \\ \mathbf{T}_{\mu,zz} \\ u\mathbf{T}_{\mu,zx} + v\mathbf{T}_{\mu,zy} + w\mathbf{T}_{\mu,zz} \\ 0 \end{pmatrix}. \quad \text{(A.3)}$$

The vector of advective source terms, $\mathbf{s}^a(\mathbf{q})$:

$$\mathbf{s}^a(\mathbf{q}) = \begin{pmatrix} 0 \\ 0 \\ 0 \\ 0 \\ 0 \\ 0 \\ \alpha_1 \nabla \cdot \mathbf{u} \end{pmatrix}. \quad \text{(A.4)}$$

The components of the viscous stress tensor, $\mathbf{T}_\mu$:

$$\mathbf{T}_{\mu,xx} = \mu\left(\frac{4}{3}\frac{\partial u}{\partial x} - \frac{2}{3}\left(\frac{\partial v}{\partial y} + \frac{\partial w}{\partial z}\right)\right) + \mu_v\left(\frac{\partial u}{\partial x} + \frac{\partial v}{\partial y} + \frac{\partial w}{\partial z}\right), \tag{A.5a}$$

$$\mathbf{T}_{\mu,xy} = \mathbf{T}_{\mu,yx} = \mu\left(\frac{\partial u}{\partial y} + \frac{\partial v}{\partial x}\right), \tag{A.5b}$$

$$\mathbf{T}_{\mu,xz} = \mathbf{T}_{\mu,zx} = \mu\left(\frac{\partial u}{\partial z} + \frac{\partial w}{\partial x}\right), \tag{A.5c}$$

$$\mathbf{T}_{\mu,yy} = \mu\left(\frac{4}{3}\frac{\partial v}{\partial y} - \frac{2}{3}\left(\frac{\partial u}{\partial x} + \frac{\partial w}{\partial z}\right)\right) + \mu_v\left(\frac{\partial u}{\partial x} + \frac{\partial v}{\partial y} + \frac{\partial w}{\partial z}\right), \tag{A.5d}$$

$$\mathbf{T}_{\mu,yz} = \mathbf{T}_{\mu,zy} = \mu\left(\frac{\partial v}{\partial z} + \frac{\partial w}{\partial y}\right), \tag{A.5e}$$

$$\mathbf{T}_{\mu,zz} = \mu\left(\frac{4}{3}\frac{\partial w}{\partial z} - \frac{2}{3}\left(\frac{\partial u}{\partial x} + \frac{\partial v}{\partial y}\right)\right) + \mu_v\left(\frac{\partial u}{\partial x} + \frac{\partial v}{\partial y} + \frac{\partial w}{\partial z}\right). \tag{A.5f}$$

A.2 Cylindrical coordinates

The vector of conservative variables, $\mathbf{q}$:

$$\mathbf{q} = \begin{pmatrix} \alpha_1\rho_1 \\ \alpha_2\rho_2 \\ \rho u_z \\ \rho u_r \\ \rho u_\theta \\ E \\ \alpha_1 \end{pmatrix}. \tag{A.6}$$

The advective fluxes, $\mathbf{f}^a(\mathbf{q}), \mathbf{g}^a(\mathbf{q})$, and $\mathbf{h}^a(\mathbf{q})$:

$$\mathbf{f}^a(\mathbf{q}) = \begin{pmatrix} \alpha_1\rho_1 u_z \\ \alpha_2\rho_2 u_z \\ \rho u_z^2 + p \\ \rho u_r u_z \\ \rho u_\theta u_z \\ (E+p)u_z \\ \alpha_1 u_z \end{pmatrix}, \qquad \mathbf{g}^a(\mathbf{q}) = \begin{pmatrix} \alpha_1\rho_1 u_r \\ \alpha_2\rho_2 u_r \\ \rho u_z u_r \\ \rho u_r^2 + p \\ \rho u_\theta u_r \\ (E+p)u_r \\ \alpha_1 u_r \end{pmatrix}, \qquad \mathbf{h}^a(\mathbf{q}) = \frac{1}{r}\begin{pmatrix} \alpha_1\rho_1 u_\theta \\ \alpha_2\rho_2 u_\theta \\ \rho u_z u_\theta \\ \rho u_r u_\theta \\ \rho u_\theta^2 + p \\ (E+p)u_\theta \\ \alpha_1 u_\theta \end{pmatrix}. \tag{A.7}$$

The diffusive fluxes, $\mathbf{f}^d(\mathbf{q}), \mathbf{g}^d(\mathbf{q})$, and $\mathbf{h}^d(\mathbf{q})$:

$$\mathbf{f}^d(\mathbf{q}) = \begin{pmatrix} 0 \\ 0 \\ \mathbf{T}_{\mu,zz} \\ \mathbf{T}_{\mu,zr} \\ \mathbf{T}_{\mu,z\theta} \\ u_z\mathbf{T}_{\mu,zz} + u_r\mathbf{T}_{\mu,zr} + u_\theta\mathbf{T}_{\mu,z\theta} \\ 0 \end{pmatrix},$$

$$\mathbf{g}^d(\mathbf{q}) = \begin{pmatrix} 0 \\ 0 \\ \mathbf{T}_{\mu,rz} \\ \mathbf{T}_{\mu,rr} \\ \mathbf{T}_{\mu,r\theta} \\ u_z\mathbf{T}_{\mu,rz} + u_r\mathbf{T}_{\mu,rr} + u_\theta\mathbf{T}_{\mu,r\theta} \\ 0 \end{pmatrix},$$

$$\mathbf{h}^d(\mathbf{q}) = \frac{1}{r}\begin{pmatrix} 0 \\ 0 \\ \mathbf{T}_{\mu,\theta z} \\ \mathbf{T}_{\mu,\theta r} \\ \mathbf{T}_{\mu,\theta\theta} \\ u_z\mathbf{T}_{\mu,\theta z} + u_r\mathbf{T}_{\mu,\theta r} + u_\theta\mathbf{T}_{\mu,\theta\theta} \\ 0 \end{pmatrix}. \quad \text{(A.8)}$$

The vectors of advective source terms, $\mathbf{s}^a(\mathbf{q})$, and diffusive source terms, $\mathbf{s}^d(\mathbf{q})$:

$$\mathbf{s}^a(\mathbf{q}) = -\frac{1}{r}\begin{pmatrix} \alpha_1\rho_1 u_r \\ \alpha_2\rho_2 u_r \\ \rho u_z u_r \\ \rho(u_r^2 - u_\theta^2) \\ 2\rho u_r u_\theta \\ (E+p)u_r \\ \alpha_1(u_r - r\nabla\cdot\mathbf{u}) \end{pmatrix}, \qquad \mathbf{s}^d(\mathbf{q}) = \frac{1}{r}\begin{pmatrix} 0 \\ 0 \\ \mathbf{T}_{\mu,rz} \\ \mathbf{T}_{\mu,rr} - \mathbf{T}_{\mu,\theta\theta} \\ 2\mathbf{T}_{\mu,r\theta} \\ u_z\mathbf{T}_{\mu,rz} + u_r\mathbf{T}_{\mu,rr} + u_\theta\mathbf{T}_{\mu,r\theta} \\ 0 \end{pmatrix}. \quad \text{(A.9)}$$

The components of the viscous stress tensor, $\mathbf{T}_\mu$:

$$\mathbf{T}_{\mu,zz} = \mu\left(\frac{4}{3}\frac{\partial u_z}{\partial z} - \frac{2}{3}\left(\frac{\partial u_r}{\partial r} + \frac{u_r}{r} + \frac{1}{r}\frac{\partial u_\theta}{\partial \theta}\right)\right) + \mu_v\left(\frac{\partial u_z}{\partial z} + \frac{\partial u_r}{\partial r} + \frac{u_r}{r} + \frac{1}{r}\frac{\partial u_\theta}{\partial \theta}\right), \tag{A.10a}$$

$$\mathbf{T}_{\mu,zr} = \mathbf{T}_{\mu,rz} = \mu\left(\frac{\partial u_z}{\partial r} + \frac{\partial u_r}{\partial z}\right), \tag{A.10b}$$

$$\mathbf{T}_{\mu,z\theta} = \mathbf{T}_{\mu,\theta z} = \mu\left(\frac{1}{r}\frac{\partial u_z}{\partial \theta} + \frac{\partial u_\theta}{\partial z}\right), \tag{A.10c}$$

$$\mathbf{T}_{\mu,rr} = \mu\left(\frac{4}{3}\frac{\partial u_r}{\partial r} - \frac{2}{3}\left(\frac{\partial u_z}{\partial z} + \frac{u_r}{r} + \frac{1}{r}\frac{\partial u_\theta}{\partial \theta}\right)\right) + \mu_v\left(\frac{\partial u_z}{\partial z} + \frac{\partial u_r}{\partial r} + \frac{u_r}{r} + \frac{1}{r}\frac{\partial u_\theta}{\partial \theta}\right), \tag{A.10d}$$

$$\mathbf{T}_{\mu,r\theta} = \mathbf{T}_{\mu,\theta r} = \mu\left(\frac{1}{r}\frac{\partial u_r}{\partial \theta} + \frac{\partial u_\theta}{\partial r} - \frac{u_\theta}{r}\right), \tag{A.10e}$$

$$\mathbf{T}_{\mu,\theta\theta} = \mu\left(\frac{4}{3}\left(\frac{u_r}{r} + \frac{1}{r}\frac{\partial u_\theta}{\partial \theta}\right) - \frac{2}{3}\left(\frac{\partial u_z}{\partial z} + \frac{\partial u_r}{\partial r}\right)\right) + \mu_v\left(\frac{\partial u_z}{\partial z} + \frac{\partial u_r}{\partial r} + \frac{u_r}{r} + \frac{1}{r}\frac{\partial u_\theta}{\partial \theta}\right). \tag{A.10f}$$

Appendix B

Analytical PLIC expressions

B.1 Cut volume

B.1.1 Setup

Following previous work relating piecewise linear interface calculations and volume fractions in rectangular grids [73], we consider a rectangular parallelepiped in 3D Cartesian space of sides h_1, h_2, h_3, and a plane with normal vector $\mathbf{n} = (n_1, n_2, n_3)^T$ given by the equation

$$n_1x_1 + n_2x_2 + n_3x_3 = \eta, \tag{B.1}$$

where the plane constant, η, is a parameter related to the shortest distance to the origin. A schematic of the problem setup is shown in Fig. B.1. We assume that all components of $\mathbf{n}$ are positive, and that we need to determine the "cut volume" ABGHKNML of the rectangular cell, which lies beneath the given plane, IJK. It was previously shown [19] that the volume ABGHKNML is given by

$$V = \frac{1}{6n_1n_2n_3}\left(\eta^3 - \sum_{m=1}^{3}\mathcal{F}_3(\eta - n_mh_m) + \sum_{m=1}^{3}\mathcal{F}_3(\eta - \eta_{\max} + n_mh_m)\right), \tag{B.2}$$

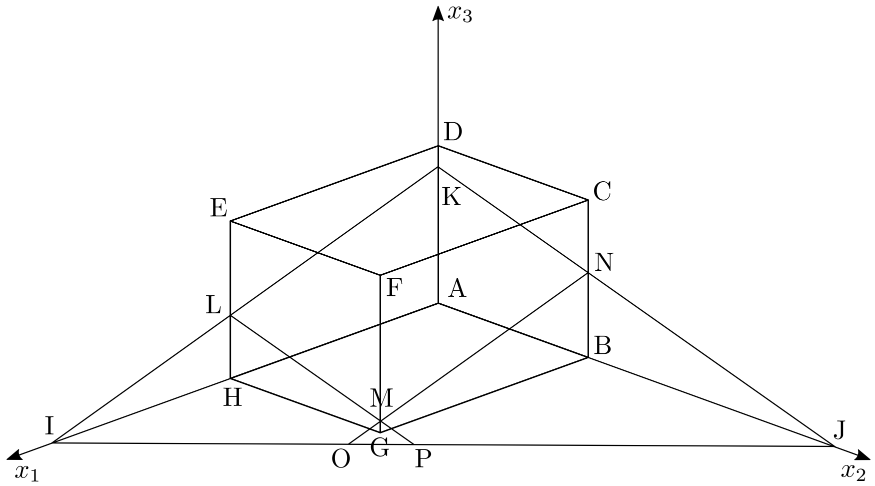

Figure B.1: Schematic of the "cut volume," which is the region inside the parallelepiped ABCDEFGH and below plane IJK. Adapted from Scardovelli and Zaleski [73].

where $\eta_{\max} = \sum_{m=1}^{3} n_m h_m$ and the function $\mathcal{F}_m(\xi)$ is defined as

$$\mathcal{F}_m(\xi) = \begin{cases} \xi^m & \text{for } \xi > 0, \\ 0 & \text{for } \xi \leq 0. \end{cases} \tag{B.3}$$

The cut volume, V, varies from zero, when $\eta = 0$, to the volume of the parallelepiped, $V_0 = h_1 h_2 h_3$, when $\eta = \eta_{\max}$. The volume fraction of the cell is therefore related as $\alpha = \dfrac{V}{V_0}$. We denote the *forward problem* as finding V, given η, and the *inverse problem* as finding η, given V. Scardovelli and Zaleski [73] only showed detailed analysis for the simplified case of a unitary cube ($h_1 = h_2 = h_3 = 1$). Following their analysis, we consider the case of $n_1 h_1 < n_2 h_2 < n_3 h_3$ (since V is invariant with respect to a permutation of the indices) and define $n_{12} = n_1 h_1 + n_2 h_2$ and $\check{n} = \min(n_{12}, n_3 h_3)$. Furthermore, we also restrict our analysis to $\eta \leq \frac{1}{2}\eta_{\max}$. The alternative cases of $\eta > \frac{1}{2}\eta_{\max}$ and cases which include negative components of $\mathbf{n}$ are handled in the same manner as Scardovelli and Zaleski [73]. The rest of Appendix B.1 details the generalized case for a parallelepiped of any size. In practice, we are only concerned with the inverse problem of finding η given $V = \alpha V_0$. The solutions to the forward problems are included, not just for the sake of completeness, but also because they are the starting point for the derivation of the solutions to the inverse problems.

B.1.2 Generalized 3D problem

Forward problem:

$$V = \begin{cases} \dfrac{\eta^3}{6n_1n_2n_3} & \text{for } 0 \leq \eta < n_1h_1, \\ \dfrac{(n_1h_1)^3}{6n_1n_2n_3} + \dfrac{\eta n_1h_1(\eta - n_1h_1)}{2n_1n_2n_3} & \text{for } n_1h_1 \leq \eta < n_2h_2, \\ \dfrac{\eta^2\big(3(n_1h_1 + n_2h_2) - \eta\big) + \displaystyle\sum_{m=1}^{2}(n_mh_m)^2(n_mh_m - 3\eta)}{6n_1n_2n_3} & \text{for } n_2h_2 \leq \eta < \check{n}, \\ \dfrac{\left(\displaystyle\prod_{m=1}^{2} n_mh_m\right) \cdot \left(2\eta - \displaystyle\sum_{m=1}^{2} n_mh_m\right)}{2n_1n_2n_3} & \text{for } \check{n} = n_{12} \leq \eta \leq \dfrac{1}{2}\eta_{\max}, \\ \dfrac{\eta^2(3\eta_{\max} - 2\eta) + \displaystyle\sum_{m=1}^{3}(n_mh_m)^2(n_mh_m - 3\eta)}{6n_1n_2n_3} & \text{for } \check{n} = n_3h_3 \leq \eta \leq \dfrac{1}{2}\eta_{\max}. \end{cases} \tag{B.4}$$

Inverse problem: In some cases, the plane constant, η, is solved for as a root of a polynomial equation. For a general third-order polynomial, $P(\eta) = a_3\eta^3 + a_2\eta^2 + a_1\eta + a_0$, the desired root can be found by first dividing through by a_3, such that $a_3 = 1$ [73]. Then η is calculated as

$$\eta = \sqrt{-\xi_1}\left(\sqrt{3}\sin\xi_3 - \cos\xi_3\right) - \frac{a_2}{3}, \tag{B.5}$$

where

$$\xi_1 = \frac{a_1}{3} - \frac{a_2^2}{9}, \tag{B.6}$$

$$\xi_2 = \frac{a_1a_2 - 3a_0}{6} - \frac{a_2^3}{27}, \tag{B.7}$$

$$\cos(3\xi_3) = \frac{\xi_2}{\sqrt{-\xi_1^3}}. \tag{B.8}$$

For the cases where η is solved for in this manner, we notate η as a "Root of $P_m(\eta)$," where $P_m(\eta)$ is some polynomial with specified coefficients. The solution to the general inverse problem is then

$$\eta = \begin{cases} \sqrt[3]{6n_1n_2n_3V} & \text{for } 0 \le V < V_1, \\ \dfrac{(n_1h_1)^2 + \sqrt{(n_1h_1)^4 + 8n_1n_2n_3(n_1h_1)(V - V_1)}}{2n_1h_1} & \text{for } V_1 \le V < V_2, \\ \text{Root of } P_1(\eta) & \text{for } V_2 \le V < \check{V}, \\ \dfrac{2n_1n_2n_3V + \left(\displaystyle\prod_{m=1}^{2} n_mh_m\right)\left(\displaystyle\sum_{m=1}^{2} n_mh_m\right)}{2\displaystyle\prod_{m=1}^{2} n_mh_m} & \text{for } \check{V} = V_{12} \le V \le \dfrac{1}{2}V_0, \\ \text{Root of } P_2(\eta) & \text{for } \check{V} = V_3 \le V \le \dfrac{1}{2}V_0, \end{cases} \tag{B.9}$$

where

$$V_1 = \frac{(n_1h_1)^3}{6n_1n_2n_3}, \tag{B.10}$$

$$V_2 = V_1 + \frac{(n_2h_2 - n_1h_1)\left(\displaystyle\prod_{m=1}^{2} n_mh_m\right)}{2n_1n_2n_3}, \tag{B.11}$$

$$\check{V} = \begin{cases} V_{12} = \dfrac{\left(\displaystyle\prod_{m=1}^{2} n_mh_m\right)\left(\displaystyle\sum_{m=1}^{2} n_mh_m\right)}{2n_1n_2n_3} & \text{if } \check{n} = n_{12}, \\ V_3 = \dfrac{(n_3h_3)^2\big(3(n_1h_1 + n_2h_2) - n_3h_3\big) + \displaystyle\sum_{m=1}^{2}(n_mh_m)^2(n_mh_m - 3n_3h_3)}{6n_1n_2n_3} & \text{if } \check{n} = n_3h_3. \end{cases} \tag{B.12}$$

The polynomial coefficients in Eq. (B.9) are defined as follows:

$$\left.\begin{aligned} a_0 &= (n_1h_1)^3 + (n_2h_2)^3 - 6n_1n_2n_3V \\ a_1 &= -3\big((n_1h_1)^2 + (n_2h_2)^2\big) \\ a_2 &= 3(n_1h_1 + n_2h_2) \\ a_3 &= -1 \end{aligned}\right\} P_1(\eta), \tag{B.13}$$

$$\left.\begin{aligned} a_0 &= (n_1h_1)^3 + (n_2h_2)^3 + (n_3h_3)^3 - 6n_1n_2n_3V \\ a_1 &= -3\big((n_1h_1)^2 + (n_2h_2)^2 + (n_3h_3)^2\big) \\ a_2 &= 3(n_1h_1 + n_2h_2 + n_3h_3) \\ a_3 &= -2 \end{aligned}\right\} P_2(\eta). \tag{B.14}$$

B.1.3 Generalized 2D problem

If an element of the plane normal, **n**, is identically zero, the generalized 3D problem simplifies to a generalized 2D problem. The 2D version of Eq. (B.2) is

$$V = \frac{1}{2n_1n_2}\left(\eta^2 - \sum_{m=1}^{2} \mathcal{F}_2(\eta - n_mh_m)\right), \tag{B.15}$$

where the indices have been shifted such that n_1 and n_2 refer to the remaining nonzero components of **n**. We also define $\beta = \min(n_1h_1, n_2h_2) = n_1h_1$ given the assumption that $n_1h_1 < n_2h_2$. The solution to the generalized 2D problem is as follows.

Forward problem:

$$V = \begin{cases} \dfrac{\eta^2}{2n_1n_2} & \text{for } 0 \le \eta < \beta, \\ \dfrac{2\eta\beta - \beta^2}{2n_1n_2} & \text{for } \beta \le \eta \le \dfrac{1}{2}\eta_{\max}. \end{cases} \tag{B.16}$$

Inverse problem:

$$\eta = \begin{cases} \sqrt{2n_1n_2V} & \text{for } 0 \le V < V_1, \\ \dfrac{2n_1n_2V + \beta^2}{2\beta} & \text{for } V_1 \le V \le \dfrac{1}{2}V_0, \end{cases} \tag{B.17}$$

where

$$V_1 = \frac{\beta^2}{2n_1n_2}. \tag{B.18}$$

B.1.4 Special cases

For both generalized 2D and 3D problems, there exist special cases that we now deal with. For 2D problems, a special case arises when $n_1h_1 = n_2h_2 = \frac{1}{2}\eta_{\max}$. Similarly, special cases arise in 3D when $n_1 = n_2 = 0$, or when $n_1h_1 = n_2h_2 = n_3h_3 = \frac{1}{3}\eta_{\max}$. We show only the solutions to the forward problems here, as the inverse problem solutions are easily obtained through simple algebraic manipulation. We begin with the special 2D case.

$\mathbf{n_1h_1 = n_2h_2 = \frac{1}{2}}\eta_{\max}$:

$$V = \frac{2h_1h_2\eta^2}{\eta_{\max}^2}. \tag{B.19}$$

Now, the special 3D cases.

$\mathbf{n_1 = n_2 = 0}$:

$$V = \frac{\eta h_1 h_2}{n_3}. \tag{B.20}$$

$\mathbf{n_1h_1 = n_2h_2 = n_3h_3 = \frac{1}{3}}\eta_{\max}$:

$$V = \begin{cases} \dfrac{9h_1h_2h_3\eta^3}{2\eta_{\max}^3} & \text{for } 0 \le \eta < \dfrac{1}{3}\eta_{\max}, \\ \dfrac{h_1h_2h_3\left(-9\eta^3 + \frac{27}{2}\eta_{\max}\eta^2 - \frac{9}{2}\eta_{\max}^2\eta + \frac{1}{2}\eta_{\max}^3\right)}{\eta_{\max}^3} & \text{for } \dfrac{1}{3}\eta_{\max} \le \eta \le \dfrac{1}{2}\eta_{\max}. \end{cases} \tag{B.21}$$

B.2 Plane area in cell

B.2.1 Setup

Once plane IJK in Fig. B.1 has been fully specified with **n** and η, we are interested in finding the area of the plane within the parallelepiped, i.e., area KNML. Aulisa et al. [4] showed that the area of interest can be calculated using

$$A = \frac{\|\mathbf{n}\|}{2n_1n_2n_3}\left(\eta^2 - \sum_{m=1}^{3}\mathcal{F}_2(\eta - n_mh_m) + \sum_{m=1}^{3}\mathcal{F}_2(\eta - \eta_{\max} + n_mh_m)\right), \tag{B.22}$$

where we again assume $n_1h_1 < n_2h_2 < n_3h_3$. Following the same organizational format as for the cut volume derivations (see Appendix B.1), we proceed to document expressions for the desired area for the generalized case of a parallelepiped of any size (the simplified case of a cubic cell was previously considered in [4]).

B.2.2 Generalized 3D problem

$$A = \begin{cases} \dfrac{\eta^2\|\mathbf{n}\|}{2n_1n_2n_3} & \text{for } 0 \le \eta < n_1h_1, \\ \dfrac{\|\mathbf{n}\|n_1h_1(2\eta - n_1h_1)}{2n_1n_2n_3} & \text{for } n_1h_1 \le \eta < n_2h_2, \\ \dfrac{\|\mathbf{n}\|\left(-\eta^2 + 2\eta\displaystyle\sum_{m=1}^{2}n_mh_m - \sum_{m=1}^{2}(n_mh_m)^2\right)}{2n_1n_2n_3} & \text{for } n_2h_2 \le \eta < \check{n}, \\ \dfrac{\|\mathbf{n}\|\displaystyle\prod_{m=1}^{2}n_mh_m}{n_1n_2n_3}, & \text{for } \check{n} = n_{12} \le \eta \le \dfrac{1}{2}\eta_{\max}, \\ \dfrac{\|\mathbf{n}\|\left(-2\eta^2 + 2\eta\eta_{\max} - \displaystyle\sum_{m=1}^{3}(n_mh_m)^2\right)}{2n_1n_2n_3} & \text{for } \check{n} = n_3h_3 \le \eta \le \dfrac{1}{2}\eta_{\max}. \end{cases} \tag{B.23}$$

B.2.3 Generalized 2D problem

In 2D, the desired area is actually the length of a line segment, which is then multiplied by h_3 (recall that $n_3 = 0$) to give an area. The desired line segment length is

$$L = \begin{cases} \dfrac{\eta\|\mathbf{n}\|}{n_1n_2} & \text{for } 0 \le \eta < n_1h_1, \\ \dfrac{n_1h_1\|\mathbf{n}\|}{n_1n_2} & \text{for } n_1h_1 \le \eta \le \dfrac{1}{2}\eta_{\max}. \end{cases} \tag{B.24}$$

B.2.4 Special cases

Once again, special cases arise for the generalized 2D and 3D problems, which are treated below. In 2D,

$\mathbf{n_1 h_1 = n_2 h_2 = \frac{1}{2}}\eta_{\max}$:

$$L = \frac{2\eta h_1 h_2}{\eta_{\max}^2}\sqrt{\left(\frac{\eta_{max}}{h_1}\right)^2 + \left(\frac{\eta_{max}}{h_2}\right)^2}. \tag{B.25}$$

In 3D,

$\mathbf{n_1 = n_2 = 0}$:

$$A = \frac{h_1 h_2 \|\mathbf{n}\|}{n_3}. \tag{B.26}$$

$\mathbf{n_1 h_1 = n_2 h_2 = n_3 h_3 = \frac{1}{3}}\eta_{\max}$:

Let

$$\mathbf{v} = \left(\frac{\eta_{\max}}{h_1}, \frac{\eta_{\max}}{h_2}, \frac{\eta_{\max}}{h_3}\right)^T. \tag{B.27}$$

Then,

$$A = \begin{cases} \dfrac{9\eta^2 h_1 h_2 h_3}{2\eta_{\max}^3}\|\mathbf{v}\| & \text{for } 0 \leq \eta < \dfrac{1}{3}\eta_{\max}, \\ \dfrac{9h_1 h_2 h_3}{2\eta_{\max}^3}\left(2\eta\eta_{\max} - 2\eta^2 - \dfrac{\eta_{\max}^2}{3}\right)\|\mathbf{v}\| & \text{for } \dfrac{1}{3}\eta_{\max} \leq \eta \leq \dfrac{1}{2}\eta_{\max}. \end{cases} \tag{B.28}$$

Appendix C

General center-of-mass derivations

Note that all integrals in the derivations below are over the entire computational domain. For conciseness, we have replaced the subscripted $\int_\Omega \,\mathrm{d}V$ notation with $\int \,\mathrm{d}V$.

C.1 Center-of-mass velocity

We begin with the definition of the center-of-mass location shown below

$$\mathbf{x}_c = \frac{\int \alpha_l \rho_l \mathbf{x} \,\mathrm{d}V}{\int \alpha_l \rho_l \,\mathrm{d}V}. \tag{C.1}$$

Taking a derivative with respect to time, we get

$$\frac{\mathrm{d}\mathbf{x}_c}{\mathrm{d}t} = \frac{\frac{\mathrm{d}}{\mathrm{d}t}\int \alpha_l \rho_l \mathbf{x} \,\mathrm{d}V}{\int \alpha_l \rho_l \,\mathrm{d}V} - \frac{\int \alpha_l \rho_l \mathbf{x} \,\mathrm{d}V}{\left(\int \alpha_l \rho_l \,\mathrm{d}V\right)^2} \frac{\mathrm{d}}{\mathrm{d}t}\left(\int \alpha_l \rho_l \,\mathrm{d}V\right), \tag{C.2}$$

$$= \frac{\int \mathbf{x}\frac{\partial}{\partial t}(\alpha_l \rho_l) \,\mathrm{d}V}{\int \alpha_l \rho_l \,\mathrm{d}V} - \frac{\int \alpha_l \rho_l \mathbf{x} \,\mathrm{d}V}{\left(\int \alpha_l \rho_l \,\mathrm{d}V\right)^2} \frac{\mathrm{d}}{\mathrm{d}t}\left(\int \alpha_l \rho_l \,\mathrm{d}V\right). \tag{C.3}$$

From the continuity equation for the liquid partial density, we have

$$\frac{\partial(\alpha_l \rho_l)}{\partial t} = -\frac{\partial}{\partial \mathbf{x}_j}(\alpha_l \rho_l \mathbf{u}_j). \tag{C.4}$$

Substituting Eq. (C.4) into Eq. (C.2) yields

$$\frac{\mathrm{d}\mathbf{x}_c}{\mathrm{d}t} = \frac{-\int \mathbf{x}\frac{\partial}{\partial \mathbf{x}_j}(\alpha_l\rho_l\mathbf{u}_j)\,\mathrm{d}V}{\int \alpha_l\rho_l\,\mathrm{d}V} - \frac{\int \alpha_l\rho_l\mathbf{x}\,\mathrm{d}V}{\left(\int \alpha_l\rho_l\,\mathrm{d}V\right)^2}\frac{\mathrm{d}}{\mathrm{d}t}\left(\int \alpha_l\rho_l\,\mathrm{d}V\right). \tag{C.5}$$

We can also expand

$$\frac{\partial}{\partial \mathbf{x}_j}(\mathbf{x}\alpha_l\rho_l\mathbf{u}_j) = \mathbf{x}\frac{\partial}{\partial \mathbf{x}_j}(\alpha_l\rho_l\mathbf{u}_j) + \alpha_l\rho_l\mathbf{u}_j\frac{\partial \mathbf{x}}{\partial \mathbf{x}_j}, \tag{C.6}$$

which rearranging yields

$$-\mathbf{x}\frac{\partial}{\partial \mathbf{x}_j}(\alpha_l\rho_l\mathbf{u}_j) = \alpha_l\rho_l\mathbf{u} - \frac{\partial}{\partial \mathbf{x}_j}(\mathbf{x}\alpha_l\rho_l\mathbf{u}_j). \tag{C.7}$$

Substituting into Eq. (C.5) yields

$$\frac{\mathrm{d}\mathbf{x}_c}{\mathrm{d}t} = \frac{\int \alpha_l\rho_l\mathbf{u}\,\mathrm{d}V}{\int \alpha_l\rho_l\,\mathrm{d}V} - \frac{\int \frac{\partial}{\partial \mathbf{x}_j}(\mathbf{x}\alpha_l\rho_l\mathbf{u}_j)\,\mathrm{d}V}{\int \alpha_l\rho_l\,\mathrm{d}V} - \frac{\int \alpha_l\rho_l\mathbf{x}\,\mathrm{d}V}{\left(\int \alpha_l\rho_l\,\mathrm{d}V\right)^2}\frac{\mathrm{d}}{\mathrm{d}t}\left(\int \alpha_l\rho_l\,\mathrm{d}V\right). \tag{C.8}$$

Using the divergence theorem on the second term of Eq. (C.8), we finally arrive at the following expression for the velocity of the liquid center-of-mass:

$$\frac{\mathrm{d}\mathbf{x}_c}{\mathrm{d}t} = \frac{\int \alpha_l\rho_l\mathbf{u}\,\mathrm{d}V}{\int \alpha_l\rho_l\,\mathrm{d}V} - \frac{\int \mathbf{x}\alpha_l\rho_l(\mathbf{u}\cdot\hat{\mathbf{n}})\,\mathrm{d}A}{\int \alpha_l\rho_l\,\mathrm{d}V} - \frac{\int \alpha_l\rho_l\mathbf{x}\,\mathrm{d}V}{\left(\int \alpha_l\rho_l\,\mathrm{d}V\right)^2}\frac{\mathrm{d}}{\mathrm{d}t}\left(\int \alpha_l\rho_l\,\mathrm{d}V\right). \tag{C.9}$$

Defining the mass of the liquid as

$$m_l = \int \alpha_l\rho_l\,\mathrm{d}V, \tag{C.10}$$

we can clean up Eq. (C.9) as

$$\frac{\mathrm{d}\mathbf{x}_c}{\mathrm{d}t} = \frac{\int \alpha_l\rho_l\mathbf{u}\,\mathrm{d}V}{\int \alpha_l\rho_l\,\mathrm{d}V} - \frac{1}{m_l}\int \mathbf{x}\alpha_l\rho_l(\mathbf{u}\cdot\hat{\mathbf{n}})\,\mathrm{d}A - \frac{\mathbf{x}_c}{m_l}\frac{\mathrm{d}m_l}{\mathrm{d}t}. \tag{C.11}$$

C.2 Center-of-mass acceleration

Starting from Eq. (C.8), we can take another derivative in time to get

$$\frac{\mathrm{d}^2\mathbf{x}_c}{\mathrm{d}t^2} = \frac{\int \frac{\partial}{\partial t}(\alpha_l\rho_l\mathbf{u})\,\mathrm{d}V}{m_l} - \frac{\int \alpha_l\rho_l\mathbf{u}\,\mathrm{d}V}{m_l^2}\frac{\mathrm{d}m_l}{\mathrm{d}t} - \frac{\frac{\mathrm{d}}{\mathrm{d}t}\int \frac{\partial}{\partial \mathbf{x}_j}(\mathbf{x}\alpha_l\rho_l\mathbf{u}_j)\,\mathrm{d}V}{m_l}$$
$$+ \frac{\int \frac{\partial}{\partial \mathbf{x}_j}(\mathbf{x}\alpha_l\rho_l\mathbf{u}_j)\,\mathrm{d}V}{m_l^2}\frac{\mathrm{d}m_l}{\mathrm{d}t} - \frac{1}{m_l}\frac{\mathrm{d}\mathbf{x}_c}{\mathrm{d}t}\frac{\mathrm{d}m_l}{\mathrm{d}t} + \frac{\mathbf{x}_c}{m_l^2}\left(\frac{\mathrm{d}m_l}{\mathrm{d}t}\right)^2 - \frac{\mathbf{x}_c}{m_l}\frac{\mathrm{d}^2m_l}{\mathrm{d}t^2}. \quad \text{(C.12)}$$

Using

$$\frac{-1}{m_l}\frac{\mathrm{d}\mathbf{x}_c}{\mathrm{d}t}\frac{\mathrm{d}m_l}{\mathrm{d}t} = \frac{-\int \alpha_l\rho_l\mathbf{u}\,\mathrm{d}V}{m_l^2}\frac{\mathrm{d}m_l}{\mathrm{d}t} + \frac{\int \frac{\partial}{\partial \mathbf{x}_j}(\mathbf{x}\alpha_l\rho_l\mathbf{u}_j)\,\mathrm{d}V}{m_l^2}\frac{\mathrm{d}m_l}{\mathrm{d}t} + \frac{\mathbf{x}_c}{m_l^2}\left(\frac{\mathrm{d}m_l}{\mathrm{d}t}\right)^2, \quad \text{(C.13)}$$

we can rewrite Eq. (C.12) as

$$\frac{\mathrm{d}^2\mathbf{x}_c}{\mathrm{d}t^2} = \frac{\int \frac{\partial}{\partial t}(\alpha_l\rho_l\mathbf{u})\,\mathrm{d}V}{m_l} - \frac{2\int \alpha_l\rho_l\mathbf{u}\,\mathrm{d}V}{m_l^2}\frac{\mathrm{d}m_l}{\mathrm{d}t} - \frac{\frac{\mathrm{d}}{\mathrm{d}t}\int \frac{\partial}{\partial \mathbf{x}_j}(\mathbf{x}\alpha_l\rho_l\mathbf{u}_j)\,\mathrm{d}V}{m_l}$$
$$+ \frac{2\int \frac{\partial}{\partial \mathbf{x}_j}(\mathbf{x}\alpha_l\rho_l\mathbf{u}_j)\,\mathrm{d}V}{m_l^2}\frac{\mathrm{d}m_l}{\mathrm{d}t} + \frac{2\mathbf{x}_c}{m_l^2}\left(\frac{\mathrm{d}m_l}{\mathrm{d}t}\right)^2 - \frac{\mathbf{x}_c}{m_l}\frac{\mathrm{d}^2m_l}{\mathrm{d}t^2}. \quad \text{(C.14)}$$

The first term on the RHS of Eq. (C.14) can be rewritten as

$$\frac{\int \frac{\partial}{\partial t}(\alpha_l\rho_l\mathbf{u})\,\mathrm{d}V}{m_l} = \frac{1}{m_l}\int\left(\alpha_l\rho_l\frac{\partial \mathbf{u}}{\partial t} + \mathbf{u}\frac{\partial(\alpha_l\rho_l)}{\partial t}\right)\mathrm{d}V. \quad \text{(C.15)}$$

Again using the continuity equation, Eq. (C.4), we have

$$\frac{\int \frac{\partial}{\partial t}(\alpha_l\rho_l\mathbf{u})\,\mathrm{d}V}{m_l} = \frac{1}{m_l}\int\left(\alpha_l\rho_l\frac{\partial \mathbf{u}}{\partial t} - \mathbf{u}\frac{\partial}{\partial \mathbf{x}_j}(\alpha_l\rho_l\mathbf{u}_j)\right)\mathrm{d}V, \quad \text{(C.16)}$$
$$= \frac{1}{m_l}\int\left(\alpha_l\rho_l\frac{\partial \mathbf{u}}{\partial t} + \alpha_l\rho_l\mathbf{u}_j\frac{\partial \mathbf{u}}{\partial \mathbf{x}_j} - \frac{\partial}{\partial \mathbf{x}_j}(\alpha_l\rho_l\mathbf{u}\mathbf{u}_j)\right)\mathrm{d}V, \quad \text{(C.17)}$$
$$= \frac{1}{m_l}\int\left(\alpha_l\rho_l\left(\frac{\partial \mathbf{u}}{\partial t} + \mathbf{u}_j\frac{\partial \mathbf{u}}{\partial \mathbf{x}_j}\right) - \frac{\partial}{\partial \mathbf{x}_j}(\alpha_l\rho_l\mathbf{u}\mathbf{u}_j)\right)\mathrm{d}V. \quad \text{(C.18)}$$

Substituting back into Eq. (C.14), and again using the divergence theorem where applicable, we get

$$\begin{aligned}\frac{\mathrm{d}^2\mathbf{x}_c}{\mathrm{d}t^2} &= \frac{\int \alpha_l\rho_l\mathbf{a}\,\mathrm{d}V}{\int \alpha_l\rho_l\,\mathrm{d}V} - \frac{1}{m_l}\left(\int \alpha_l\rho_l\mathbf{u}(\mathbf{u}\cdot\hat{\mathbf{n}})\,\mathrm{d}A + \frac{\mathrm{d}}{\mathrm{d}t}\int \mathbf{x}\alpha_l\rho_l(\mathbf{u}\cdot\hat{\mathbf{n}})\,\mathrm{d}A\right)\\ &\quad - \frac{2}{m_l^2}\frac{\mathrm{d}m_l}{\mathrm{d}t}\left(\int \alpha_l\rho_l\mathbf{u}\,\mathrm{d}V - \int \mathbf{x}\alpha_l\rho_l(\mathbf{u}\cdot\hat{\mathbf{n}})\,\mathrm{d}A\right) + \frac{2\mathbf{x}_c}{m_l^2}\left(\frac{\mathrm{d}m_l}{\mathrm{d}t}\right)^2 - \frac{\mathbf{x}_c}{m_l}\frac{\mathrm{d}^2m_l}{\mathrm{d}t^2}.\end{aligned} \tag{C.19}$$

Appendix D

2D aerobreakup details

D.1 Grid resolution study

The aerobreakup of a 2D water cylinder in the flow behind a $M_s = 1.47$ shock wave is simulated at three different spatial resolutions: $(N_x, N_y) = (600, 300), (1200, 600), (2400, 1200)$. For convenience, let us label the simulations from A to C, with A corresponding to the coarsest resolution, and C corresponding to the finest resolution. All three simulations are run at a fixed CFL number of $\mathcal{C} = 0.25$. We proceed to show qualitative and quantitative comparisons of the numerical results.

D.1.1 Qualitative results

A time history of these simulations is shown in Fig. D.1. Though the wake structure becomes noticeably more detailed as the grid is refined, the overall qualitative features of the breakup process, described in Section 5.3.1, remain similar. Features characteristic of stripping breakup, such as the initial flattening of the cylinder and the formation of tips at the cylinder's periphery, are present at all three grid resolutions. The recirculation regions at the cylinder's equator and the presence of an upstream jet in the wake are also observable at all levels of grid refinement.

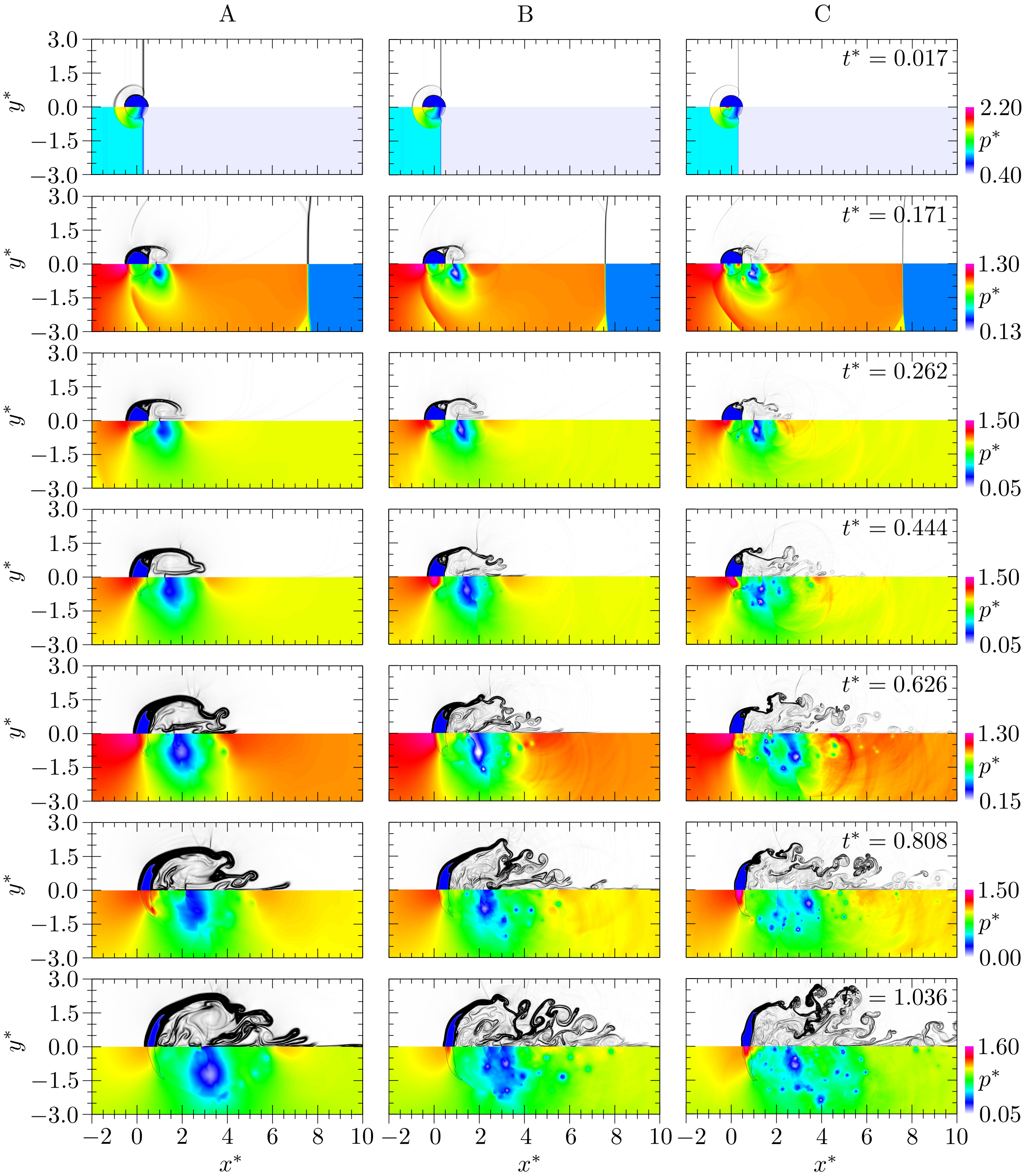

Figure D.1: Numerical schlieren (top) and filled pressure contours (bottom) of the aerobreakup of a $D_0 = 4.8\,\text{mm}$ cylinder behind a $M_s = 1.47$ shock wave for three spatial resolutions. Isopleths are shown for $\alpha_l \geq 0.5$.

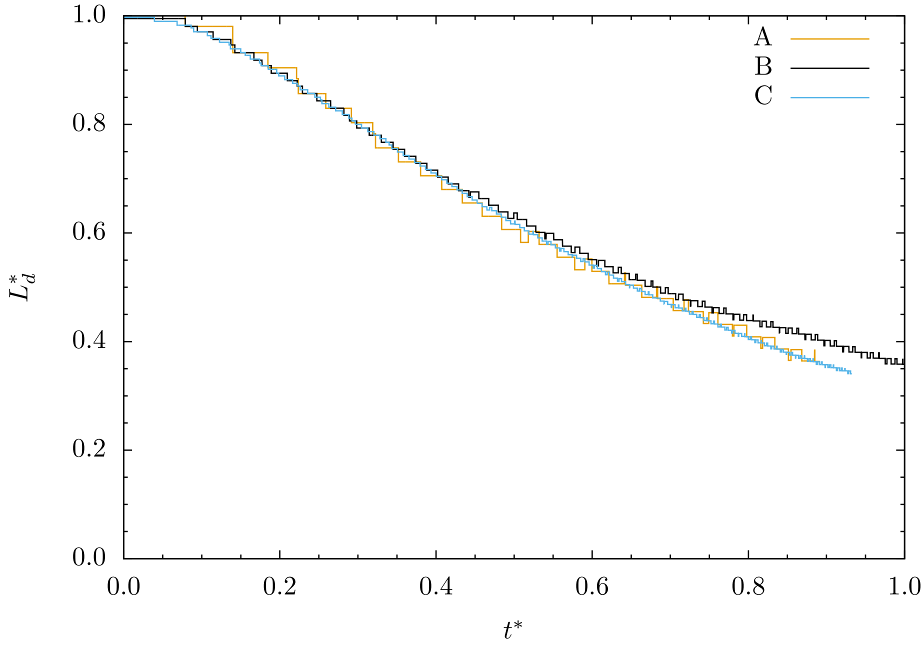

Figure D.2: Cylinder centerline width, L_d^*, for three spatial resolutions.

D.1.2 Quantitative results

The plots for centerline width, deformed diameter, and coherent body area, calculated using the methodology outlined in Section 3.2.1, for the three different spatial resolutions are shown in Figs. D.2 to D.4 using $\alpha_{cr} = 0.5$. The differences between the three curves for L_d^* and D_d^* are small, with the largest deviations occurring at later times. In the plot of A_d, Run A is seen to be insufficiently resolved, while Runs B and C show nearly identical behavior. Finally, the center-of-mass drift, calculated using Eq. (3.10), for the three resolutions is plotted in Fig. D.5. Again, the differences are negligible with Run B doing a slightly better job of tracking Run C. Based on the above results, a spatial resolution of $(N_x, N_y) = (1200, 600)$ is chosen for the results shown in Chapter 5.

D.2 Comparison with experimental visualizations

There exists both inconsistency and uncertainty in the time specifications of the holographic interferograms used in Fig. 5.5. The inconsistency arises from various publications by the same authors

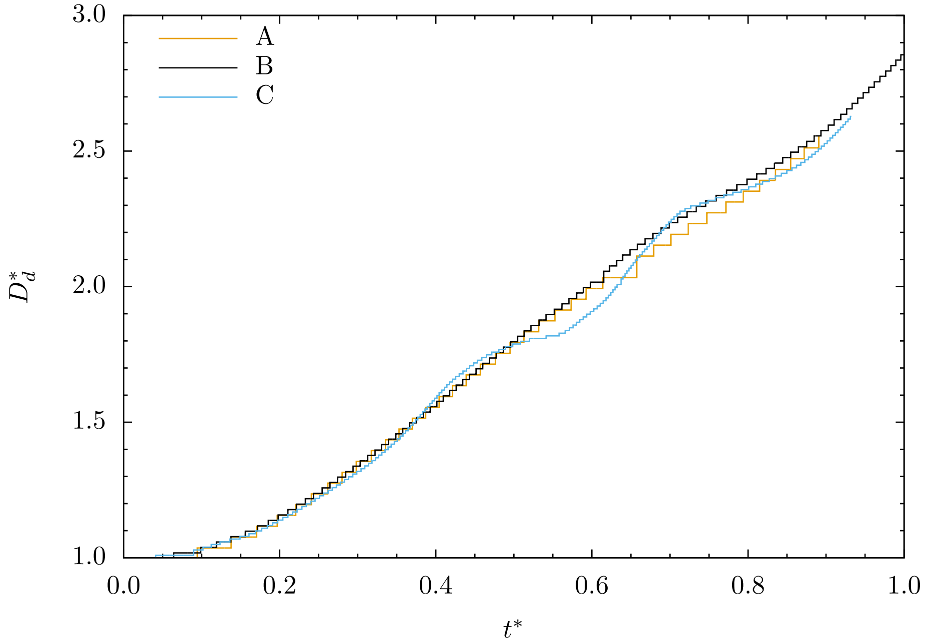

Figure D.3: Cylinder deformed diameter, D_d^*, for three spatial resolutions.

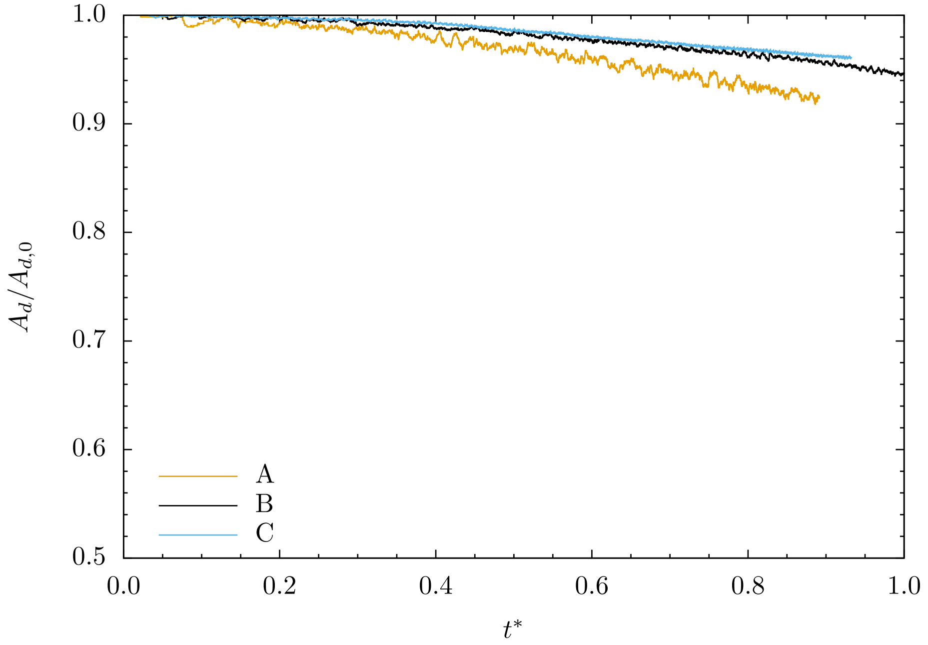

Figure D.4: Cylinder coherent body area, $A_d/A_{d,0}$, for three spatial resolutions.

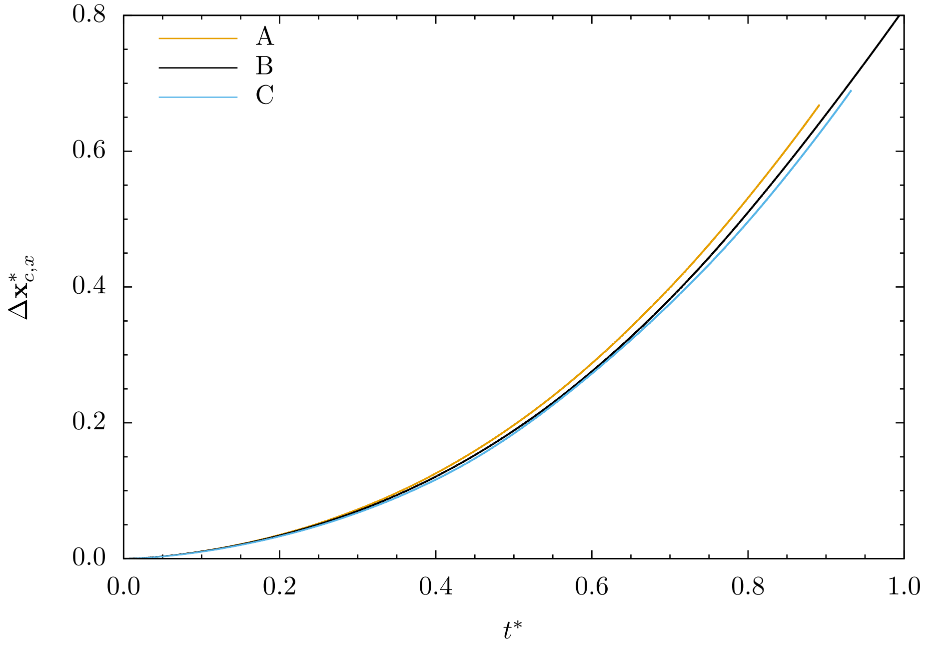

Figure D.5: Cylinder streamwise center-of-mass drift, $\Delta \mathbf{x}^*_{c,x}$, for three spatial resolutions.

([32, 33, 35]), which state different times for the same experimental images. The earliest of these works ([32]) is an internal report that timed the snapshots at $t = 30\,\mu$s and $t = 50\,\mu$s. The same images were then used in two separate publications ([33, 35]). Igra and Takayama [33] kept the original times of $30\,\mu$s and $50\,\mu$s, while Igra and Takayama [35] presented new times of $23\,\mu$s and $43\,\mu$s. All publications [32, 33, 35] stated the times as being after “the interaction between the incident shock wave and the water column” [35]. It is unclear why the discrepancy in timing exists between [35] and [32, 33]. Further complicating the matter is that the phrase “interaction between the shock wave and water column” is inherently ambiguous, and could refer to any time between the shock reaching the leading edge and the shock leaving the trailing edge of the water column.

Let us, for now, take the earlier times of $23\,\mu$s and $43\,\mu$s from [35], and interpret the “shock-column interaction” to mean the arrival of the shock at the leading edge. The comparison of the experimental interferograms and the numerical schlieren images from our simulations is shown in Fig. D.6. It is clear that any comparison is difficult to make since the images appear to be taken at completely different times given the differences in distance traveled by the incident shock. Changing the times to be $30\,\mu$s and $50\,\mu$s, or interpreting the “shock-column interaction” as anything other

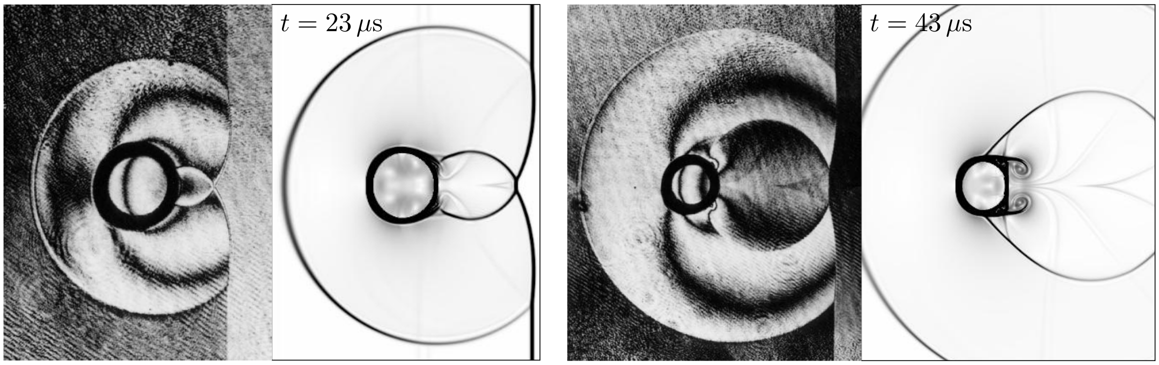

Figure D.6: Comparison of numerical schlieren images (right) to experimental holographic interferograms (left) from Figs. 6 and 9 of [35] at originally stated times. Experimental images reprinted from Igra and Takayama [35] with the permission of Springer. © 2001 by Springer-Verlag.

than the shock's arrival at the leading edge would all result in even worse comparisons than the one shown in Fig. D.6.

In an attempt to reconcile the discrepancy, digital measurements of the distance traversed by the incident shock were taken from the interferograms. Our measurements indicate that the times should perhaps be closer to $16\,\mu$s and $32\,\mu$s. Numerical schlieren images at these modified times are compared to the experimental interferograms in Fig. 5.5, and are seen to match the incident and reflected shock locations. However, even in this method of timing the experimental snapshots, there is an inherent uncertainty in the exact location of the boundary of the water cylinder, owing to the thick ring on the holographic interferograms. Measurements to obtain times of $16\,\mu$s and $32\,\mu$s were taken by assuming the boundary to be located in the middle of the thick ring. Measurements taken from the edge of the ring resulted in alternate times of approximately $22\,\mu$s and $42\,\mu$s, which are close to the reported times in [35], but still significantly different from those reported in [32, 33]. At this point, it is unknown whether this discrepancy in time is a result of reporting errors by the original authors, a misinterpretation, on our part, of what is meant by the "shock-column interaction," or a combination of these factors. The comparison shown in Fig. 5.5 represents our best efforts to faithfully represent both experimental and numerical data.

Bibliography

[1] C. Aalburg, B. Van Leer, and G. M. Faeth. Deformation and drag properties of round drops subjected to shock-wave disturbances. *AIAA J.*, 41(12):2371–2378, 2003.

[2] G. Allaire, S. Clerc, and S. Kokh. A five-equation model for the simulation of interfaces between compressible fluids. *J. Comput. Phys.*, 181:577–616, 2002.

[3] S. V. Apte, M. Gorokhovski, and P. Moin. LES of atomizing spray with stochastic modeling of secondary breakup. *Int. J. Multiphase Flow*, 29:1503–1522, 2003.

[4] E. Aulisa, S. Manservisi, R. Scardovelli, and S. Zaleski. Interface reconstruction with least-squares fit and split advection in three-dimensional Cartesian geometry. *J. Comput. Phys.*, 225:2301–2319, 2007.

[5] G. K. Batchelor. The stability of a large gas bubble rising through liquid. *J. Fluid Mech.*, 184: 399–422, 1987.

[6] V. M. Boiko and S. V. Poplavski. On the dynamics of drop acceleration at the early stage of velocity relaxation in a shock wave. *Combust. Explo. Shock+*, 45(2):198–204, 2009.

[7] R. Bouard and M. Coutanceau. The early stage of development of the wake behind an impulsively started cylinder for $40 < Re < 10^4$. *J. Fluid Mech.*, 101:583–607, 1980.

[8] J. U. Brackbill, D. B. Kothe, and C. Zemach. A continuum method for modeling surface tension. *J. Comput. Phys.*, 100:335–354, 1992.

[9] S. Chandrasekhar. *Hydrodynamic and Hydromagnetic Stability.* International Series of Monographs on Physics. Oxford University Press, 3rd edition, 1961.

[10] H. Chen. Two-dimensional simulation of stripping breakup of a water droplet. *AIAA J.*, 46 (5):1135–1143, 2008.

[11] V. Coralic. *Simulation of shock-induced bubble collapse with application to vascular injury in shockwave lithotripsy.* PhD thesis, California Institute of Technology, Pasadena, CA, 2015.

[12] V. Coralic and T. Colonius. Shock-induced collapse of a bubble inside a deformable vessel. *Eur. J. Mech. B-Fluid*, 40:64–74, 2013.

[13] V. Coralic and T. Colonius. Finite-volume WENO scheme for viscous compressible multicomponent flows. *J. Comput. Phys.*, 274:95–121, 2014.

[14] Z. Dai and G. M. Faeth. Temporal properties of secondary drop breakup in the multimode breakup regime. *Int. J. Multiphase Flow*, 27:217–236, 2001.

[15] G. Della Rocca and G. Blanquart. Level set reinitialization at a contact line. *J. Comput. Phys.*, 265:34–49, 2014.

[16] O. G. Engel. Fragmentation of waterdrops in the zone behind an air shock. *J. Res. Nat. Bur. Stand.*, 60(3):245–280, March 1958.

[17] A. K. Flock, D. R. Guildenbecher, J. Chen, P. E. Sojka, and H. J. Bauer. Experimental statistics of droplet trajectory and air flow during aerodynamic fragmentation of liquid drops. *Int. J. Multiphase Flow*, 47:37–49, 2012.

[18] A. B. Gojani, K. Ohtani, K. Takayama, and S. H. R. Hosseini. Shock Hugoniot and equations of states of water, castor oil, and aqueous solutions of sodium chloride, sucrose, and gelatin. *Shock Waves*, pages 1–6, April 2009. doi: 10.1007/s00193-009-0195-9.

[19] D. Gueyffier, J. Li, A. Nadim, R. Scardovelli, and S. Zaleski. Volume-of-fluid interface tracking with smoothed surface stress methods for three-dimensional flows. *J. Comput. Phys.*, 152:423–456, 1999.

[20] D. R. Guildenbecher, C. López-Rivera, and P. E. Sojka. Secondary atomization. *Exp. Fluids*, 46:371–402, 2009.

[21] J. Han and G. Tryggvason. Secondary breakup of axisymmetric liquid drops. II. impulsive acceleration. *Phys. Fluids*, 13(6):1554–1565, June 2001.

[22] A. R. Hanson, E. G. Domich, and H. S. Adams. Shock tube investigation of the breakup of drops by air blasts. *Phys. Fluids*, 6(8):1070–1080, August 1963.

[23] F. H. Harlow and A. A. Amsden. Fluid dynamics. Technical Report LA-4700, LASL, June 1971.

[24] J. O. Hinze. Critical speeds and sizes of liquid globules. *Appl. Sci. Res.*, A1:273–288, 1949.

[25] J. O. Hinze. Fundamentals of the hydrodynamic mechanism of splitting in dispersion processes. *AIChE J.*, 1(3):289–295, 1955.

[26] H. Hirahara and M. Kawahashi. Experimental investigation of viscous effects upon a breakup of droplets in high-speed air flow. *Exp. Fluids*, 13:423–428, 1992.

[27] H. Honji and S. Taneda. Unsteady flow past a circular cylinder. *J. Phys. Soc. Jpn.*, 27(6): 1668–1677, August 1969.

[28] P. F. Hopkins. A new class of accurate, mesh-free hydrodynamic simulation methods. *Mon. Not. R. Astron. Soc.*, 450:53–110, 2015.

[29] L. P. Hsiang and G. M. Faeth. Near-limit drop deformation and secondary breakup. *Int. J. Multiphase Flow*, 18(5):635–652, 1992.

[30] L. P. Hsiang and G. M. Faeth. Drop deformation and breakup due to shock wave and steady disturbances. *Int. J. Multiphase Flow*, 21(4):545–560, 1995.

[31] J. C. P. Huang. The break-up of axisymmetric liquid sheets. *J. Fluid Mech.*, 43:305–319, 1970.

[32] D. Igra and K. Takayama. Investigation of aerodynamic breakup of a cylindrical water droplet. Technical Report Vol. 11, pp. 123–134, Institute of Fluid Science, Tohoku University, February 1999.

[33] D. Igra and K. Takayama. Investigation of aerodynamic breakup of a cylindrical water droplet. *Atom. Sprays*, 11:167–185, 2001.

[34] D. Igra and K. Takayama. Experimental and numerical study of the initial stages in the interaction process between a planar shock wave and a water column. In *Proc. 23rd Int. Symposium on Shock Waves*, number 5071, Fort Worth, Texas, 2001. The University of Texas at Arlington, Arlington, Texas, USA.

[35] D. Igra and K. Takayama. Numerical simulation of shock wave interaction with a water column. *Shock Waves*, 11:219–228, 2001.

[36] D. Igra and K. Takayama. A study of shock wave loading on a cylindrical water column. Technical Report Vol. 13, pp. 19–36, Institute of Fluid Science, Tohoku University, March 2001.

[37] D. Igra and K. Takayama. Experimental investigation of two cylindrical water columns subjected to planar shock wave loading. *J. Fluid Eng. - T. ASME*, 125:325–331, 2003.

[38] M. Jain, R. S. Prakash, G. Tomar, and R. V. Ravikrishna. Secondary breakup of a drop at moderate Weber numbers. *Proc. R. Soc. A*, 471(20140930), 2015. doi: 10.1098/rspa.2014.0930.

[39] M. Jalaal and K. Mehravaran. Transient growth of droplet instabilities in a stream. *Phys. Fluids*, 26(012101), 2014.

[40] E. Johnsen. *Numerical simulations of non-spherical bubble collapse with applications to shockwave lithotripsy.* PhD thesis, California Institute of Technology, Pasadena, CA, 2007.

[41] E. Johnsen and T. Colonius. Implementation of WENO schemes in compressible multicomponent flow problems. *J. Comput. Phys.*, 219:715–732, December 2006.

[42] E. Johnsen and T. Colonius. Numerical simulations of non-spherical bubble collapse. *J. Fluid Mech.*, 629:231–262, 2009.

[43] D. D. Joseph, J. Belanger, and G. S. Beavers. Breakup of a liquid drop suddenly exposed to a high-speed airstream. *Int. J. Multiphase Flow*, 25:1263–1303, 1999.

[44] G. Jourdan, L. Biamino, C. Mariani, C. Blanchot, E. Daniel, J. Massoni, L. Houas, R. Tosello, and D. Praguine. Attenuation of a shock wave passing through a cloud of water droplets. *Shock Waves*, 20:285–296, 2010.

[45] S. M. Karim and L. Rosenhead. The second coefficient of viscosity of liquids and gases. *Rev. Mod. Phys.*, 24(2):108–116, April 1952.

[46] S. Khosla, C. E. Smith, and R. P. Throckmorton. Detailed understanding of drop atomization by gas crossflow using the volume of fluid method. In *Proc. 19th Annual Conference on Liquid Atomization and Spray Systems*, Toronto, Canada, May 2006. ILASS Americas.

[47] D. Kim, O. Desjardins, M. Herrmann, and P. Moin. Toward two-phase simulation of the primary breakup of a round liquid jet by a coaxial flow of gas. Annual research briefs, Center for Turbulence Research, 2006.

[48] H. J. Kim and P. A. Durbin. Observations of the frequencies in a sphere wake and of drag increase by acoustic excitation. *Phys. Fluids*, 31(11):3260–3265, November 1988. doi: 10.1063/1.866937.

[49] W. R. Lane. Shatter of drops in streams of air. *Ind. Eng. Chem.*, 43(6):1312–1317, June 1951.

[50] R. J. LeVeque. *Numerical Methods for Conservation Laws.* Birkhaüser Verlag, 2nd edition, 1992.

[51] R. J. LeVeque. *Finite Volume Methods for Hyperbolic Problems.* Cambridge Texts in Applied Mathematics. Cambridge Univ. Press, 2002.

[52] S. Li. WENO schemes for cylindrical and spherical geometry. Los Alamos Report LA-UR-03-8922, Los Alamos National Laboratory, Los Alamos, NM, October 2003.

[53] A. B. Liu, D. Mather, and R. D. Reitz. Modeling the effects of drop drag and breakup on fuel sprays. Technical Paper 930072, Society of Automotive Engineers, 1993.

[54] Z. Liu and R. D. Reitz. An analysis of the distortion and breakup mechanisms of high speed liquid drops. *Int. J. Multiphase Flow*, 23(4):631–650, 1997.

[55] A. Lozano, Félix Barreras, Guillermo Hauke, and César Dopazo. Longitudinal instabilities in an air-blasted liquid sheet. *J. Fluid Mech.*, 437:143–173, 2001.

[56] P. Marmottant and E. Villermaux. On spray formation. *J. Fluid Mech.*, 498:73–111, 2004.

[57] C. Mehring and W. A. Sirignano. Nonlinear capillary wave distortion and disintegration of thin planar liquid sheets. *J. Fluid Mech.*, 388:69–113, 1999.

[58] J. C. Meng and T. Colonius. The effects of shock strength on droplet breakup. In R. Bonazza, editor, *Proc. 29th Int. Symposium on Shock Waves*, number 000311, Madison, WI, July 2013.

[59] J. C. Meng and T. Colonius. Droplet breakup in high-speed gas flows. In *Proc. 8th Int. Conf. on Multiphase Flow*, number 488, Jeju, Korea, May 2013.

[60] J. C. Meng and T. Colonius. Numerical simulations of the early stages of high-speed droplet breakup. *Shock Waves*, 25(4):399–414, July 2015. doi: 10.1007/s00193-014-0546-z.

[61] A. Mignone. High-order conservative reconstruction schemes for finite volume methods in cylindrical and spherical coordinates. *J. Comput. Phys.*, 270:784–814, 2014.

[62] K. O. Mikaelian. Rayleigh-Taylor instability in finite-thickness fluids with viscosity and surface tension. *Phys. Rev. E*, 54(4):3676–3680, October 1996.

[63] K. Mohseni and T. Colonius. Numerical treatment of polar coordinate singularities. *J. Comput. Phys. Note*, 157:787–795, 2000.

[64] P. J. O'Rourke and A. A. Amsden. The TAB method for numerical calculation of spray droplet breakup. Technical Paper 872089, Society of Automotive Engineers, 1987.

[65] G. Perigaud and R. Saurel. A compressible flow model with capillary effects. *J. Comput. Phys.*, 209:139–178, 2005.

[66] M. Pilch and C. A. Erdman. Use of breakup time data and velocity history data to predict the maximum size of stable fragments for acceleration-induced breakup of a liquid drop. *Int. J. Multiphase Flow*, 13(6):741–757, 1987.

[67] S. Quan and D. P. Schmidt. Direct numerical study of a liquid droplet impulsively accelerated by gaseous flow. *Phys. Fluids*, 18(102103), 2006.

[68] J. J. Quirk and S. Karni. On the dynamics of a shock-bubble interaction. *J. Fluid Mech.*, 318: 129–163, 1996.

[69] A. A. Ranger and J. A. Nicholls. Aerodynamic shattering of liquid drops. In *Proc. AIAA 6th Aerospace Sciences Meeting*, number 68-83, New York, New York, January 1968. AIAA.

[70] W. G. Reinecke and G. D. Waldman. A study of drop breakup behind strong shocks with applications to flight. Technical Report SAMSO-TR-70-142, Air Force Systems Command, May 1970.

[71] R. D. Reitz. Modeling atomization processes in high-pressure vaporizing sprays. *Atom. Spray Technol.*, 3:309–337, 1987.

[72] H. Sakamoto and H. Haniu. A study on vortex shedding from spheres in a uniform flow. *J. Fluid Eng. - T. ASME*, 112:386–392, December 1990.

[73] R. Scardovelli and S. Zaleski. Analytical relations connecting linear interfaces and volume fractions in rectangular grids. *J. Comput. Phys. Note*, 164:228–237, 2000.

[74] P. K. Senecal, D. P. Schmidt, I. Nouar, C. J. Rutland, R. D. Reitz, and M. L. Corradini. Modeling high-speed viscous liquid sheet atomization. *Int. J. Multiphase Flow*, 25:1073–1097, 1999.

[75] F. S. Sherman. A low-density wind-tunnel study of shock-wave structure and relaxation phenomena in gases. Technical Note 3298, NACA, July 1955.

[76] R. K. Shukla. Nonlinear preconditioning for efficient and accurate interface capturing in simulation of multicomponent compressible flows. *J. Comput. Phys.*, 276:508–540, 2014.

[77] K. M. Shyue. An anti-diffusion based Eulerian interface-sharpening algorithm for compressible two-phase flow with cavitation. In C.-D. Ohl, E. Klaseboer, S. W. Ohl, S. W. Gong, and B. C. Khoo, editors, *Proc. 8th Int. Symposium on Cavitation*. Research Publishing Services, January 2012. doi: 10.3850/978-981-07-2826-7198.

[78] K. M. Shyue and F. Xiao. An Eulerian interface sharpening algorithm for compressible two-phase flow: The algebraic THINC approach. *J. Comput. Phys.*, 268:326–354, 2014.

[79] P. G. Simpkins and E. L. Bales. Water-drop response to sudden accelerations. *J. Fluid Mech.*, 55:629–639, 1972.

[80] K. K. So, X. Y. Hu, and N. A. Adams. Anti-diffusion method for interface steepening in two-phase incompressible flow. *J. Comput. Phys.*, 30:5155–5177, 2011.

[81] H. B. Squire. Investigation of the instability of a moving liquid film. *Brit. J. Appl. Phys.*, pages 167–169, 1953.

[82] B. E. Stapper and G. S. Samuelsen. An experimental study of the breakup of a two-dimensional liquid sheet in the presence of co-flow air shear. In *Proc. AIAA 28th Aerospace Sciences Meeting*, number AIAA-90-0461. AIAA, January 1990.

[83] K. Takayama and K. Itoh. Unsteady drag over cylinders and aerofoils in transonic shock tube flows. Technical Report Vol. 51, Institute of High Speed Mechanics, Tohoku University, Sendai, Japan, 1986.

[84] F. X. Tanner. Liquid jet atomization and droplet breakup modeling of non-evaporating diesel fuel sprays. Technical Paper 970050, Society of Automotive Engineers, 1997.

[85] H. Tanno, K. Itoh, T. Saito, A. Abe, and K. Takayama. Interaction of a shock with a sphere suspended in a vertical shock tube. *Shock Waves*, 13:191–200, 2003. doi: 10.1007/s00193-003-0209-y.

[86] G. I. Taylor. The shape and acceleration of a drop in a high-speed air stream. In G. K. Batchelor, editor, *The Scientific Papers of G.I. Taylor*, volume 3, pages 457–464. Cambridge Univ. Press, 1949.

[87] T. G. Theofanous. Aerobreakup of Newtonian and viscoelastic liquids. *Annu. Rev. Fluid Mech.*, 43:661–690, 2011.

[88] T. G. Theofanous and G. J. Li. On the physics of aerobreakup. *Phys. Fluids*, 20(052103), 2008.

[89] T. G. Theofanous, G. J. Li, and T. N. Dinh. Aerobreakup in rarefied supersonic gas flows. *J. Fluid Eng. - T. ASME*, 126:516–527, 2004.

[90] T. G. Theofanous, V. V. Mitkin, C. L. Ng, C. H. Chang, X. Deng, and S. Sushchikh. The physics of aerobreakup. II. viscous liquids. *Phys. Fluids*, 24(022104), 2012.

[91] K. W. Thompson. Time dependent boundary conditions for hyperbolic systems. *J. Comput. Phys.*, 68:1–24, 1987.

[92] K. W. Thompson. Time dependent boundary conditions for hyperbolic systems, II. *J. Comput. Phys.*, 89:439–461, 1990.

[93] A. Tiwari, J. B. Freund, and C. Pantano. A diffuse interface model with immiscibility preservation. *J. Comput. Phys.*, 252:209–309, 2013.

[94] E. F. Toro, M. Spruce, and W. Speares. Restoration of the contact surface in the HLL-Riemann solver. *Shock Waves*, 4:25–34, 1994.

[95] A. R. Wadhwa, V. Magi, and J. Abraham. Transient deformation and drag of decelerating drops in axisymmetric flows. *Phys. Fluids*, 19(113301), 2007. doi: 10.1063/1.2800038.

[96] S. Wang and E. Johnsen. High-order schemes for cylindrical/spherical geometries with cylindrical/spherical symmetry. In *Proc. 21st AIAA Computational Fluid Dynamics Conference*, number AIAA 2013-2430, San Diego, CA, June 2013. AIAA.

[97] A. Wierzba. Deformation and breakup of liquid drops in a gas stream at nearly critical Weber numbers. *Exp. Fluids*, 9:59–64, 1990.

[98] A. Wierzba and K. Takayama. Experimental investigation of the aerodynamic breakup of liquid drops. *AIAA J.*, 26(11):1329–1335, 1988.

[99] H. Zhao, H. F. Liu, X. K. Cao, W. F. Li, and J. L. Xu. Breakup characteristics of liquid drops in bag regime by a continuous and uniform air jet flow. *Int. J. Multiphase Flow*, 37:530–534, 2011.

[100] H. Zhao, H. F. Liu, J. L. Xu, and W. F. Li. Experimental study of drop size distribution in the bag breakup regime. *Ind. Eng. Chem. Res.*, 50:9767–9773, 2011.